





Colloïdale 'Quantum Dots' voor geïntegreerde fotonica:  
van optische winst tot ultrasnelle modulatie

Colloidal Quantum Dots for Guided Wave Photonics:  
from Optical Gain to Ultrafast Modulation

Pieter Geiregat

Promotoren: prof. dr. ir. D. Van Thourhout, prof. dr. ir. Z. Hens  
Proefschrift ingediend tot het behalen van de graad van  
Doctor in de Ingenieurswetenschappen: Toegepaste Natuurkunde

Vakgroep Informatietechnologie  
Voorzitter: prof. dr. ir. D. De Zutter  
Faculteit Ingenieurswetenschappen en Architectuur

Vakgroep Anorganische en Fysische Chemie  
Voorzitter: prof. dr. I. Van Driessche  
Faculteit Wetenschappen

Academiejaar 2014 - 2015



ISBN 978-90-8578-766-2  
NUR 926, 965  
Wettelijk depot: D/2015/10.500/10



Universiteit Gent  
Faculteit Ingenieurswetenschappen en  
Architectuur  
Vakgroep Informatietechnologie  
Faculteit Wetenschappen  
Vakgroep Anorganische en Fysische Chemie

Promotoren:

prof. dr. ir. Dries Van Thourhout  
prof. dr. ir. Zeger Hens

Jury:

prof. dr. ir. Rik Van de Walle (chairman)	Ghent University
prof. dr. ir. Dries Van Thourhout (promotor)	Ghent University
prof. dr. ir. Zeger Hens (promotor)	Ghent University
prof. dr. ir. Günther Roelkens (secretary)	Ghent University
prof. dr. ir. Edouard Brainis	Ghent University
prof. dr. Christophe Delerue	Université de Lille 1
dr. Arjan Houtepen	Delft University of Technology
prof. dr. Philippe Smet	Ghent University

Universiteit Gent  
Faculteit Ingenieurswetenschappen en Architectuur

Vakgroep Informatietechnologie  
Sint-Pietersnieuwstraat 41, B-9000 Gent, België

Tel.: +32-9-2643316

Fax.: +32-9-2643593



Proefschrift tot het behalen van de graad van  
Doctor in de Ingenieurswetenschappen:  
Toegepaste Natuurkunde  
Academiejaar 2014-2015



## Dankwoord

The thank-you note. The part you probably started reading before the rest of this thesis, and I can't blame you, I always do the same thing. It's been a long journey starting in the technicum office with Bram discussing core/shell quantum dots and searching for chairs in the S3 building as the PCN group had just moved to their new location. From being a quiet and ever-amazed thesis student at Herodot meetings to the wonderful summer school in Corsica. From the work benches all across university (where haven't I been in these 5 years ?) to the mysterious white-light setup in Delft. From the monday morning meetings to posters in Santa Fe and the stage at CLEO in San Francisco, or presenting in front of the scientific celebrity crowd at '30 years of Colloidal Quantum Dots' in Paris.

I have met amazing people during these, some of whom I even dare to call friends by now. Stijn (and Katrien), thanks for being the best office mate ever. I hope you have a wonderful life together, the bachelor party was an amazing cherry on the cake and the wedding even more so. Isabelle, thanks for being a great colleague and even better friend throughout these years.

The old crew, Yolanda (thanks for all the great times and for all the work you have done to make this thesis a reality), Marco and Antti (You guys probably wont read this ever, but still), Raquel, Karel and Iwan. Abdoulghafar, at some point we were the brave last engineers at the chemistry department and we had a great time in Santa Fe in the somewhat overluxurious hotel (we can admit it now we both have finished the thesis). I hope you fare well in your new career. The new crew: Antoine, Tangi, Suzanne and of course Kim: you truly are the best colleagues. From outside PCN (yes, there is a world outside) I would like to thank everyone for the great atmosphere, not the least at the regular parties and drinks.

I probably wouldn't be writing this thesis if it were not for Bram De Gey-

ter. Going from a shy and inexperienced thesis student to the critical and enthusiastic scientist that I am today is in large due to his support and friendship, which I value very much. I wish all the best to you and your family, I'm absolutely sure your company will be the next Google any time soon (I better start buying stock asap...).

Going to Delft for the ultrafast measurements was and will always be a treat for me (even though I was locked up in a dark room with high power lasers most of the time), not only because of science but because of the many great people I met over there. My thanks and respect go out to all the people that helped me feel at home there: Michiel, Simon, Lucas, Wiel, Frank, Nathalie, Sandeep, ... Special thanks to Laurens for having me in the group, it has been a privilege. A special paragraph in this 'Dankwoord' should definitely be addressed to Arjan: I have always been amazed by your enthusiasm for science and it definitely was a big part of my decision to stay in the field. But more than a scientist I always enjoyed our little talks about nothing much, they were a great support and made me feel right at home in Delft. It was my absolute pleasure collaborating all these years.

Being in 2 (or 3, or 4 ?) research groups at the same time is sometimes difficult as (for now) I cannot split myself in that many parts. Spending most of my time in Ghent at the PCN group, I still have to thank a lot of people in the Photonics Research Group for their support: Steven (without you my crazy processing ideas would never see the light of day), Kasia and Zhechao (for showing me how to work properly in the cleanroom), Ilse (for being patient with my endless expense notes). Of course, a special reference to the guys from CLEO: Bart, Raphael, Frederic, Pieter, Francois and Suzanne. We definitely made San Jose into a much more fun place than it actually is !

Furthermore, I would like to thank all the people that found time and patience to collaborate with me over the years: Christophe (for the ever amazing tight binding calculations), the people at Lumilab (especially Philippe for teaching me everything on luminescence and general enthusiasm on science), ELIS (Wouter, Mohammad and Aimi), DRAFT (Diederik, Francis and Wouter), COCOON (Cristophe and Kilian). Special thanks to my thesis students aswell, Lu Qi, Floris and Joachim. Hope you guys are doing well out there, it was great working together.

Of course, this work would not (literally, at all) have been possible without the support and ever-patient guidance of Zeger and Dries. It was a great privilege to start working with you 5 years ago and it still is very much so today. In these 5 years I have learned so much from you that I cannot possibly write it down in words so I'll keep it simple: Thanks for your support and guidance, and thanks for believing in me and my work. Special thanks aswell to Isabelle van den Driessche and Roel Baets for having me in their respective research groups for these 5 years. Roel, my special thanks for the continued support after my PhD.

Of course finishing a PhD doesn't only rely on the people at work. I would like to thank all my friends (the 'copains') for being there all those years, through good and bad I have always valued your friendship and support: Sandy, Eddy, Ameye, Koen, Duif, Bino, Bijlke, Tine, Herman en Nookie. And of course Tom, thanks for sticking out with me for the last 25 years or so, it's amazing to have such a good friend.

Save the best for last: Julie, schattiebol, bedankt om er te zijn voor mij, voor jouw liefde en warmte, elke dag opnieuw. Ik zie je graag en kijk reikhalzend uit naar onze toekomst samen, een avontuur dat we samen gaan beleven, jij en ik !

The final word on this thank-you note is maybe the most important as it relates to my parents. Thanks for being there for me during the past 27 years, giving me my freedom and showing me the right path in life. Thanks for always supporting me although you probably still have no idea what I actually do for a living. I am very lucky to have you and I do realize that more and more each day.

*Gent, januari 2014*  
*Pieter Geiregat*



# Table of Contents

<b>Dankwoord</b>	<b>i</b>
<b>Nederlandse samenvatting</b>	<b>xv</b>
<b>English summary</b>	<b>xxi</b>
<b>1 Introduction</b>	<b>1</b>
1.1 Problem Definition . . . . .	1
1.2 Thesis Outline . . . . .	3
1.3 Publications . . . . .	5
<b>2 Physics of Nanocrystals for Integrated Photonics</b>	<b>11</b>
2.1 Light-Matter Interaction . . . . .	11
2.1.1 Light . . . . .	11
2.1.2 Matter . . . . .	12
2.1.3 Light-Matter Interaction . . . . .	14
2.1.3.1 Basics: The Einstein Coefficients . . . . .	14
2.1.3.2 A Quantum Picture . . . . .	15
2.2 Photonics . . . . .	16
2.2.1 Long Range Data Communication . . . . .	17
2.2.1.1 Fibers . . . . .	18
2.2.1.2 Amplifiers . . . . .	19
2.2.1.3 Modulation and Conversion . . . . .	19
2.2.2 Integrated Photonics for Optical Interconnects . . . . .	20
2.3 Colloidal Quantum Dots . . . . .	23
2.3.1 Historical Perspective . . . . .	24
2.3.2 Synthesis and Deposition . . . . .	26
2.3.3 Linear Optical Properties . . . . .	29
2.3.3.1 Size Dependence of the Optical Band Gap . . . . .	29
2.3.3.2 Maxwell-Garnett Effective Medium . . . . .	30
2.3.3.3 Intrinsic Absorption Coefficient . . . . .	31

---

2.3.3.4	Oscillator Strength . . . . .	32
2.3.3.5	Photoluminescence of QDs . . . . .	33
2.3.4	Ultrafast Properties . . . . .	34
2.3.4.1	Auger Recombination . . . . .	35
2.3.4.2	Statistics of Multi-Excitons . . . . .	36
2.3.4.3	Carrier Cooling . . . . .	37
2.3.4.4	Multiple Exciton Generation . . . . .	38
2.3.4.5	Intraband Absorption . . . . .	39
2.3.5	Colloidal Nanocrystal Lasers . . . . .	40
2.4	Ultrafast Spectroscopy . . . . .	45
2.4.1	White Light Pump-Probe Spectroscopy . . . . .	45
2.4.2	Spectroscopy of Colloidal Quantum Dots . . . . .	46
2.4.3	Pump-Repump Experiments . . . . .	49
<b>3</b>	<b>Advanced Optical Properties of Lead-Chalcogenide Heterostructures</b>	<b>57</b>
3.1	PbS/CdS Core/shell Nanocrystals . . . . .	57
3.1.1	Introduction . . . . .	57
3.1.2	Synthesis and Core Size Determination . . . . .	59
3.1.3	Absorption Coefficient . . . . .	61
3.1.4	Oscillator Strength . . . . .	63
3.2	Optical Properties of Anisotropic Lead-Chalcogenide Nanocrystals . . . . .	67
3.2.1	Introduction . . . . .	67
3.2.2	Synthesis . . . . .	68
3.2.3	Spontaneous Emission and Morphology . . . . .	68
3.2.4	Interdot Coupling . . . . .	69
3.3	Ultrafast Optical Properties of Lead-Salts for Optical Gain	74
3.3.1	Spherical PbS Quantum Dots . . . . .	74
3.3.2	PbS Nanorods . . . . .	75
<b>4</b>	<b>Coulomb Shifts</b>	<b>85</b>
4.1	Introduction . . . . .	86
4.2	Concepts . . . . .	87
4.2.1	Exciton Addition Energies and Coulomb Shifts . . . . .	87
4.2.2	Determination of Spectral Shifts . . . . .	89
4.3	Experimental Section . . . . .	90
4.4	Results and Discussion . . . . .	91
4.4.1	Near - Band Gap Probing . . . . .	91
4.4.2	Above Band Gap Probing . . . . .	93

---

4.5	Discussion . . . . .	96
4.6	Conclusion . . . . .	99
<b>5</b>	<b>Phonon Bottleneck</b>	<b>103</b>
5.1	Introduction . . . . .	103
5.2	Experiments . . . . .	105
5.3	Kinetic Analysis: a 3 Level Model . . . . .	109
5.4	Spectral Analysis: the Relevance of the Bottleneck . . . . .	112
5.5	Relaxation Modeling . . . . .	114
5.6	Tight Binding Calculations . . . . .	115
5.6.1	PbS Band Structure around Critical Points . . . . .	115
5.6.2	Carrier Cooling in Polar Semiconductors . . . . .	117
5.7	Phonon Scattering . . . . .	119
5.7.1	Cascade Model . . . . .	120
5.7.2	Four Level Approximation . . . . .	121
5.8	From Bulk to Nanocrystals . . . . .	125
5.9	The Role of Saddle Points . . . . .	126
5.10	Relevance of Bottleneck for Multiple Exciton Generation . . . . .	127
5.11	Conclusion . . . . .	129
<b>6</b>	<b>Wavelength Conversion</b>	<b>135</b>
6.1	Introduction . . . . .	136
6.2	Light Absorption by Photo-Excited Quantum dots . . . . .	137
6.3	Matching State Filling and Intraband Transitions . . . . .	139
6.4	Strength and Dynamics . . . . .	142
6.4.1	Refresh Timescale . . . . .	142
6.4.2	Interaction Lengths . . . . .	145
6.5	Technological Relevance . . . . .	146
6.5.1	Competitive Technologies for Wavelength Conversion . . . . .	146
6.5.2	Integration on SOI . . . . .	147
6.5.3	Conversion Bandwidth . . . . .	149
6.5.4	Other Materials . . . . .	150
6.6	Conclusion . . . . .	153
<b>7</b>	<b>Thresholdless Optical Gain</b>	<b>157</b>
7.1	Introduction . . . . .	157
7.2	Synthesis and Linear Optical Properties . . . . .	159
7.2.1	Synthesis . . . . .	159
7.2.2	Absorbance . . . . .	160

---

7.2.3	Photoluminescence . . . . .	162
7.2.4	Low Temperature . . . . .	164
7.3	Theoretical Description of Energy Level Structure of HgTe Quantum Dots . . . . .	164
7.3.1	Methods . . . . .	164
7.3.2	Band Structure and Absorption Spectra . . . . .	166
7.4	Nearly Thresholdless Optical Gain . . . . .	167
7.4.1	Methods . . . . .	167
7.4.2	Band Edge Dynamics . . . . .	169
7.4.3	Fluence Dependence of Gain Threshold . . . . .	169
7.4.4	Exciton Dynamics and Gain Lifetime . . . . .	172
7.4.5	High Fluence Regime . . . . .	174
7.5	Theoretical Models for Thresholdless Optical Gain . . . . .	175
7.5.1	Excited State Relaxation . . . . .	177
7.5.2	Four Level System . . . . .	183
7.6	HgTe for Integrated Photonics . . . . .	187
7.6.1	Thin Film Formation . . . . .	187
7.6.2	Performance . . . . .	188
7.6.3	Intrinsic Material Gain . . . . .	191
7.6.4	Benchmarking HgTe for Optical Interconnects . . . . .	192
7.7	Conclusion . . . . .	194
<b>8</b>	<b>Absorption Enhancement</b>	<b>201</b>
8.1	Introduction . . . . .	202
8.2	Experiment . . . . .	203
8.2.1	Thin Film Formation . . . . .	203
8.2.2	Determination of the Absorption Cross Section . . . . .	205
8.3	Observation of Enhancement . . . . .	207
8.4	Maxwell-Garnett Model . . . . .	209
8.5	Beyond Maxwell-Garnett: The Coupled Dipole Model . . . . .	210
8.6	Coupled Dipole Model and the Experiment . . . . .	217
8.6.1	Nanocrystal Size and Ligand Length . . . . .	217
8.6.2	The Wavelength Dependence of the Enhancement . . . . .	218
8.6.3	Core/Shell Nanocrystals . . . . .	219
8.7	Beyond Single Component Monolayer . . . . .	220
8.7.1	Multilayers . . . . .	221
8.7.2	Polarization Dependence . . . . .	221
8.7.3	Dipolar Coupling and Spontaneous Emission . . . . .	222
8.7.4	Phonon Dipolar Coupling . . . . .	223

---

8.8	Conclusion . . . . .	225
<b>9</b>	<b>Silicon Photonics with Colloidal Nanocrystals</b>	<b>229</b>
9.1	Introduction . . . . .	229
9.2	Hybrid Plasmonic-Dielectric Waveguides . . . . .	230
9.2.1	Simulations . . . . .	231
9.2.2	Hybrid structures . . . . .	233
9.3	Colloidal Nanocrystals on SOI Waveguides . . . . .	237
9.4	Microcavities . . . . .	240
9.4.1	DBR cavities . . . . .	241
9.4.2	Microdisks . . . . .	242
9.5	Incorporation of Nanocrystals in Functional Oxides . . . . .	243
9.6	Conclusion . . . . .	245
<b>10</b>	<b>General Conclusion</b>	<b>253</b>
10.1	Conclusion . . . . .	253
10.2	Perspectives . . . . .	255
10.2.1	Light Conversion and Modulation . . . . .	256
10.2.2	Optical Gain . . . . .	256
10.2.3	Hot Carrier Cooling . . . . .	258
10.2.4	Absorption Enhancement . . . . .	258
10.2.5	SOI integration . . . . .	258



# List of Acronyms

## **A**

A	Absorbance
AFM	Atomic Force Microscopy
ASE	Amplified Spontaneous Emission

## **C**

CVD	Chemical Vapour Deposition
CW	continuous wave

## **D**

DBR	Distributed Bragg Reflector
DFB	Distributed Feedback
DIR	Dot-in-Rod
DLS	Dynamic Light Scattering
DOS	Density of States

## **E**

EDX	Energy Dispersive X-ray spectroscopy
-----	--------------------------------------

## **F**

FWHM	Full Width at Half Maximum
------	----------------------------

## **H**

HAADF	High Angular Annular Dark Field
HOMO	Highest Occupied Molecular Orbital

## **I**

ICP-MS	Inductively Coupled Plasma Mass Spectrometry
--------	--

## **L**

LUMO	Lowest Unoccupied Molecular Orbital
<b>M</b>	
MEG	Multiple Exciton Generation
<b>O</b>	
OLED	Organic Light Emitting Diode
OPA	Optical Parametric Amplifier
<b>P</b>	
PA	Photoinduced Absorption
PbX	Abbreviation for the most common lead chalcogenide QDs. X replaces either S (sulphur), Se (selenium) or Te (tellurium)
PECVD	Plasma Enhanced Chemical Vapour Deposition
PL	photoluminescence
<b>Q</b>	
QD	Quantum Dot
QR	Quantum Rod
QY	Quantum Yield
<b>R</b>	
RF	Radio Frequent
<b>S</b>	
SEM	Scanning Electron Microscope
SILAR	Successive Ionic Layer Adsorption and Reaction
SOI	Silicon-On-Insulator
<b>T</b>	
TA	Transient Absorption spectroscopy
TE	Transverse Electric
TEM	Transmission Electron Microscopy
TM	Transverse Magnetic
<b>X</b>	
X	Exciton





# Nederlandse samenvatting

## –Summary in Dutch–

Het onderzoek in deze thesis bevindt zich op de kruising tussen geïntegreerde fotonica (die licht gebruik in plaats van elektriciteit om informatie over te dragen) en nanotechnologie (die materie op de nanoschaal manipuleert, een duizendste van een micrometer), twee onderzoeksgebieden die aanzienlijke aandacht krijgen vanuit zowel de industrie als de academische wereld. Zo werd nanotechnologie recent door de Europese Commissie benoemd als een 'Key Enabling Technology': een technologische sector die zowel de Europese economie als kennis zal vergroten. Bovendien koos UNESCO 2015 uit als jaar van het 'licht'.

Fotonica is een relatief nieuwe technologie die licht wenst te gebruiken (*i.e.* fotonen in plaats van *elektronen*) in een brede waaier van toepassingen waar de elektronica vandaag tekort schiet: energie-efficiënte en breedbandige (data)communicatie, hoge bandbreedte interconnecties tussen de kernen van processoren op een computer-chip, detectie van virussen en chemische componenten door goedkope sensoren (lab-on-a-chip), ... De miniaturisatie van die 'fotonische' functies op een chip (zogenaamde integratie ofwel geïntegreerde micro -en nanofotonica) is een route die sterk kopieert van de ontwikkeling van de micro-elektronica in de voorbije decennia: door miniaturisatie kunnen veel meer functies op een kleiner oppervlak gecombineerd worden waardoor componenten niet alleen kleiner worden, maar ook sneller en energiezuiniger. Veel bedrijven (Intel, IBM, ST, Huawei, ...) zien silicium als het materiaal bij uitstek om dit te realiseren vermits de huidige micro en nano-elektronica faciliteiten de wereld rond reeds dit materiaal gebruiken met een indrukwekkende know-how en precisie waardoor de kosten voor ontwikkeling kunnen dalen en producten sneller geïmplementeerd kunnen worden. Hoewel het silicium-platform zeer goed is in het geleiden en filteren van licht op micrometer ( $10^{-6}$  meter) schaal, schiet het materiaal te kort op gebied van licht generatie en modulatie. Zo wordt het vinden van een efficiënte, energiezuinige en compacte lichtbron (*i.e.* in

essentie een goedkope laser op een micro-chip) ook wel eens smalend de 'heilige graal' van de silicium fotonica genoemd.

Nanotechnologie, 'what's in a name', is een tak van de toegepaste wetenschappen die zich bezig houdt met de synthese, karakterisatie en manipulatie van materialen op de nanoschaal, *i.e.* structuren met de afmetingen van een duizendste van een menselijk haar. De nanoschaal is een gebied waar de klassieke wetten van de fysica in vraag worden gesteld en de vuistregels bepaald worden door de kwantummechanica. Hierdoor worden voortdurend nieuwe en vaak onverwachte materiaaleigenschappen en functies ontdekt, die op hun beurt dan weer worden gebruikt om meer performante en energiezuinige producten op de markt te brengen, zoals zonnecellen met hoger rendement of batterijen met langere levensduur. Een aanzienlijk deel van de nanowetenschap bestudeert materialen die toepassingen vinden in de manipulatie van licht (*i.e.* dus in de fotonica) zoals de absorptie (bv. een zonnecel, een lichtgevoelige chip in een reflex camera, ..) of generatie (bv. LED schermen en verlichting) van licht. De combinatie van nanotechnologie en fotonica wordt ook 'nanofotonica' genoemd en het is precies in dat gebied dat het werk van deze thesis zich situeert: een poging om de kracht van nanotechnologie, die materie op de nanoschaal kneedt tot nieuwe onverwachte eigenschappen, te combineren met nanofotonica, die licht kan manipuleren op de nanoschaal maar beperkingen kent door de limieten van silicium als technologie-platform.

De nanomaterialen bij uitstek om licht te manipuleren zijn zogenaamde nanokristallen (of 'quantum dots'): kristallen van halfgeleider materiaal van slechts enkele nanometer in afmeting, gestabiliseerd in een colloïdale oplossing. Ze worden gemaakt via lage temperatuur chemische processen in grote volumes, wat de productie bijzonder goedkoop en opschaalbaar maakt. Door de bijzonder kleine schaal van de deeltjes treedt een grote waaier aan kwantumeffecten op zoals de grootte-afhankelijkheid van hun lichtabsorptie en emissiespectrum. Wij combineren deze nanokristallen met silicium (fotonica) met als doel hun lineaire en vooral hun niet-lineaire eigenschappen uit te buiten om de optische functionaliteit van silicium uit te breiden. Het onderzoek is dan ook op te delen in drie stukken:

- Studie van de lineaire en (ultrasnelle) niet-lineaire optische eigenschappen van nanokristallen in oplossing en in dunne filmen.
- Analyse van de interacties tussen nanokristallen in een dichtgepakte film.
- De combinatie van die dunne filmen met componenten uit de silicium fotonica.

Het onderzoek in deze thesis start met een basis karakterisatie van de lineaire optische eigenschappen (zoals de absorptie en spontane emissie van licht) van lood-chalcogenide (PbX, X=S,Se,Te) nanokristallen en meer geavanceerde multi-laags nanosystemen (PbX/CdX). Goede overeenkomst met theoretische modellen toont aan dat de deeltjes type I gedrag vertonen waarbij de elektronen en gaten in de kern gelokaliseerd zijn. Hun excellente stabiliteit en hoge efficiëntie voor licht emissie maken hen geschikt voor toepassingen in devices zoals LEDs (licht-emitterende diodes), fotodetectoren en zonnecellen, al dan niet geïntegreerd op het silicium fotonica platform.

Vervolgens werden de ultrasnelle eigenschappen van ladingsdragers in nanokristallen bekeken. Wanneer een halfgeleidend materiaal (met een 'bandkloof' of verboden zone in energie die een valentieband scheidt van een conductieband) wordt geëxciteerd met een hoog energie foton (kwantum van licht), ontstaat er een elektron-gat paar (een zogenaamd 'exciton') met exces energie, ook wel een 'heet' exciton genoemd. Die energie wordt snel (in een paar picoseconden, *i.e.*  $10^{-12}$ s) gedissipeerd (typisch als warmte door verstrooiing aan roostervibraties) waarna het elektron-gat paar 'koud' is, *i.e.* het elektron bevindt zich in het laagste conductie-band niveau en het gat in het laagste valentieband niveau. Dit verlies van energie als warmte wordt vaak gezien als nefast vermits de exces energie kon gebruikt worden in een aantal omzettingsprocessen zoals multi-exciton generatie of transfer naar elektrodes in een zonnecel. In multi-exciton generatie creëert een enkel heet elektron-gat paar door impact ionisatie een tweede exciton. Zo krijg je voor een enkel foton, twee elektron-gat paren wat de kortsluitstroom en dus de efficiëntie van een zonnecel drastisch kan verbeteren. Anderzijds geeft de snelle dynamica (op een picoseconde tijdschaal) van het koelingsproces een excellent platform voor ultrasnelle modulatie van licht. Immers, door de snel veranderende optische eigenschappen van het materiaal (bv. de absorptie) in die paar picoseconden van koeling, kan ook de propagatie van een externe lichtbundel snel beïnvloed (*i.e.* 'gemoduleerd') worden. In beide gevallen is een studie van de dynamica van zulke hete ladingsdragers in nanostructuren een must voor de uitbouw van nieuwe toepassingen.

Om de dynamica te bestuderen gebruiken we een pomp-probe opstelling waarbij 180 femtoseconde (een tiende van een picoseconde) lichtpulsen het sample (een colloïdale oplossing van de nanokristallen of een dunne film ervan) 'pompen' (*i.e.* elektron-gat paren creëren) en vervolgens een korte 'probe' puls met een variabele vertraging ten opzichte van de pomp,

de verandering in absorptie van het staal opmeet. De focus hier ligt vooral op lood-chalcogenide nanokristallen (zoals lood-sulfide of lood-selenide) vermits die optisch actief zijn in het nabije infrarood, precies dat deel van het elektromagnetisch spectrum waar de silicium fotonica werkzaam is.

Een waaier aan fenomenen treedt op in een pomp-probe meting, afhankelijk van de tijdsvertraging tussen de pomp en de probe en de energie van de pomp puls (relatief tot de energie van de verboden zone van de nanokristallen). Rond de energie van de verboden zone, waar de ladingen koud zijn, wordt het probe-spectrum gedomineerd door spectrale verschuivingen (zogenaamde 'Coulomb' effecten) en vermindering van absorptie door opvullen van elektronische toestanden met ladingsdragers. Bij hoge energie, ver boven de verboden zone, treedt een picoseconde absorptievermindering op in een nauw energiebereik rond het kritische  $\Sigma$ -punt, karakteristiek voor alle lood-chalcogenide nanokristallen evenals het bulk materiaal. Wij observeren de absorptievermindering in nanokristallen van verschillende grootte en schrijven het toe aan het vertragen van het koeltempo van ladingen. Een theoretisch model werd opgesteld dat deze vertraging verklaart als een flessenhals-effect: koeling van hoog energetische lading kan alleen plaatsvinden rond  $\Sigma$  door verstrooiing met specifieke fononen (roostervibraties). Bovendien werd aangetoond dat quasi alle lading koelt via die flessenhals zodat het waargenomen effect zeer relevant is voor toepassingen waaring hete lading van belang is. Vermits we ook de dynamica van de vertraging kunnen opmeten, kunnen we (voor het eerst) het koeltempo van hete lading opmeten, een cruciale parameter in veel theoretische modellen.

Bij energieën van de probe puls lager dan de verboden zone wordt een toename van absorptie waargenomen, zogenaamde foto-geïnduceerde absorptie. Deze absorptietoename voor energieën onder de bandkloof wordt toegeschreven aan 'intraband'-absorptie: absorptie van licht door elektronen (of gaten) waarna het elektron wordt gepromoveerd tot energieniveaus binnen dezelfde band (in plaats van valentie-conductie, hier dus conductie-conductie of valentie-valentie). Vermits zowel de vermindering van absorptie voor energieën aan de bandrand als de toename bij energieën erboven schalen met het aantal elektron-gat paren in de nanokristallen, bestaat er een groot bereik van pompvermogen waar het absorptieverlies (door het opvullen van discrete energieniveaus met ladingsdragers) en de absorptietoename (door intraband absorptie) elkaar perfect compenseren. Wij noemen de golflengte waarbij dit gebeurt de compensatie-golflengte en net bij deze compensatie-golflengte ontstaat een uitermate interessante dynamica: hete lading geeft een sterke absorptietoename (door intraband absorptie) in

de eerste paar picoseconden van het koelproces vermits er dan nog geen compensatie is door absorptievermindering (lading is nog niet aangekomen in de koude niveaus). Wanneer de lading dan eindelijk koud is (na 1-2 picoseconden) treedt de compensatie op waardoor de absorptie-toename weer verdwijnt en de dots zich gedragen als ware er nooit een pomp puls geweest. Er is dus met andere woorden geen residuele achtergrond aan het snelle proces, een vaak voorkomend probleem bij andere mechanismes voor snelle lichtmodulatie. Het proces is lineair in het pompvermogen, uitermate sterk en ultrasnel: modulaties tot 23 dB zijn haalbaar op een sub 1-exciton niveau (*i.e.* met een laag vermogen voor de pomp) aan snelheden van 225 en 450 Gb/s waardoor toepassingen in optische golflengte conversie en modulatie zeker realistisch zijn.

De sterke foto-geïnduceerde absorptie die ons aan de snelle en sterke modulatie helpt, is helaas ook de limiterende factor om optische transparantie van de quantum dots (een premise voor optische winst) te bekomen vermits we in dergelijke toepassingen zoveel mogelijk absorptievermindering onder invloed van de pomp wensen. In de praktijk moet voor de meest courant gebruikte nanokristallen minstens één elektron-gat paar aanwezig zijn per dot en dat liefst voor een lange periode (*i.e.* niet beperkt door niet-radiatieve verliesmechanismen). Die voorwaarden leiden tot grote drempels voor het bereiken van optische winst (versterking van licht). Dat laatste is een voorwaarde voor het bouwen van elektrisch aangestuurde lasers op basis van nanokristallen, een mogelijke oplossing voor de vermelde 'heilige graal' van de silicium fotonica. Twee nieuwe routes om die transparantie te bekomen werden uitgewerkt in deze thesis: structurele relaxatie van de foto-geëxciteerde toestand en meer-niveau systemen door formatie van optisch actieve mid-gap toestanden. Beide aanpakken kunnen in theorie leiden tot drempelloze versterking van licht. HgTe (kwik-telluride) nanokristallen werden onderzocht voor dit doeleinde en een uitzonderlijk lage drempel (tot 3 grootte-orde lager dan de state-of-the-art) gecombineerd met een onverwacht lange levensduur werden waargenomen. Bovendien zijn de winstcoëfficiënten voldoende groot om licht te versterken over relatief korte afstand wat het materiaal geschikt maakt voor toepassingen in geïntegreerde fotonica.

Het opmeten en begrijpen van de lineaire en niet-lineaire optische eigenschappen van nanokristallen in oplossing is maar een eerste stap in het uitbouwen van een technologieplatform voor (silicium) fotonische toepassingen vermits, voor die doeleinden, nanokristallen steeds in dunne filmen zullen afgezet worden. In deze thesis werd aangetoond dat een simpele ver-

taling van de eigenschappen van oplossing naar dunne film (zoals bijvoorbeeld met een effectieve medium theorie) niet altijd correct is. Zo werd een dichtgepakte monolaag van nanokristallen (waarbij de afstand tussen de kristallen maar enkele nanometer bedraagt) als modelsysteem gebruikt om de interacties tussen de deeltjes beter te begrijpen en we vonden dat de absorptie per dot tot 5 maal sterker is in de dunne film dan in oplossing. Deze versterking werd kwalitatief en kwantitatief uitgelegd door een gekoppeld dipool-model waarbij nabije-veld elektrostatische interacties tussen de dipolen (een fenomeen dat in verdunde oplossingen niet optreedt) kan leiden tot interne versterking van het elektrische veld dat de dipool aanstuurt. Niet alleen de absorptie, maar de spontane emissie (levensduur) van de nanokristallen in de dichtgepakte lagen wordt aangepast door dit effect. Naast de theoretische relevantie, kunnen beide effecten (versterking van absorptie en verkorting van de radiatieve levensduur) ook gebruikt worden in toepassingen, bv. om dunnere absorberende lagen voor zonnecellen te maken of LEDs met grotere helderheid.

Ten slotte werden de nanokristallen geïntegreerd in fotonische structuren zoals golfgeleiders en micro-resonatoren met als doel aan te tonen dat de dots interageren met de optische modes van die structuren, een voorwaarde om de interessante lineaire (spontane licht emissie en absorptie) en vooral de niet-lineaire (licht modulatie en optische winst) uit te buiten in die structuren. Ook werden theoretische modellen opgesteld om die interacties te begrijpen op basis van het ontwikkelde gekoppelde dipool-model.

## English summary

The research in this thesis is at the crossroads of integrated photonics (which uses light instead of electricity to carry information) and nanotechnology (which manipulates matter on the nano-scale, a millionth of a millimeter), two scientific fields that receive appreciable industrial and academic interest as both were identified by the European Commission as a Key Enabling Technology for Europe and are as such, vibrant areas of the European economy and research in global. Given the importance of integrated photonics and nanotechnology across a wide range of industries and services, ranging from biomedical to data-communication, investment in related technologies can have a substantial impact on Europe's economy and society as a whole. Moreover, as was put forward by the European Commission in the Horizon 2020 program, future research in the European Union should focus on sustainable development (flexible manufacturing and energy efficiency) through nanotechnologies and advanced materials offering new functionalities and improved performance.

Silicon photonics is considered by many major industrial players (IBM, Intel, Luxtera, Huawei, ST, ...) as an enabling technology for a variety of next-generation devices in datacommunication, on-chip interconnects, (bio-)sensing and even quantum computing. As an example, the electrical interconnects between microprocessors (*i.e.* the multi-core concept) are approaching their limits both in terms of bandwidth and power consumption. The use of light to transfer the information on-chip instead of electrons, is considered the best solution by all industrial players and at least for now, silicon photonics is considered by many the only way forward. Recent reports indicate the chip-to-chip interconnect market to reach a staggering 1 billion dollar by 2020. Although silicon is great at guiding and routing light on a chip, it is actually quite bad at generating or modulating light, to the extent that a cost-effective and efficient silicon-compatible light source is called by many the 'holy grail' of silicon photonics.

Nanotechnology, what's in a name, is the manipulation of matter on the nanoscale, a size regime where classical physics breaks down and the rules

of thumb are dictated by quantum mechanics. This booming and peculiar realm of applied physics gives us new and unexpected material properties to make more performant and energy-efficient materials and devices, ranging from better light harvesting in solar cells to increased battery capacity and more efficient light sources. A subdivision of nanotechnology occupies itself with the application of nanomaterials for photonic applications such as light emission, detection and/or modulation. Often referred to as 'nanophotonics', it aims at combining specifically designed nanomaterials (such as colloidal quantum dots, 2D materials (graphene), perovskites, ...) with state-of-the-art photonic structures (photonic crystals, dielectric and plasmonic waveguides and antennas, ...).

In an attempt to combine the strengths of both nanotechnology, capable of designing materials with on-demand optical properties, and silicon photonics, capable of manipulating light-matter interaction with an industrially relevant CMOS fabrication backbone, our research aims at remedying the limitations of silicon photonics through hybridization with novel nanomaterials: 'colloidal quantum dots' (QDs). QDs are nanometer size pieces of (inorganic) semiconductor crystals obtained through a wet chemical synthesis which offer size-tunable optical properties. Combining the QDs with silicon photonics, we aim at understanding the potential and the inevitable limitations of QDs for on-chip optical gain, wavelength conversion and photodetection.

Based on this rationale, we conducted our research in three main directions:

- Study of ultrafast linear and non-linear optical properties of quantum dots in solution phase
- Understanding QD-QD interaction in close packed thin films of QDs
- Combining QDs with silicon photonics on a device-scale level

The research in this thesis starts with the basic characterization of the linear optical properties (absorption and spontaneous emission) of lead-chalcogenide (PbX, X=S,Se,Te) QDs and more advanced core/shell (PbX/CdX) systems. Good correspondence with theory is found to reveal the type I nature of the QDs, a configuration where both electron and hole are confined to the core. Their excellent stability and high luminescence efficiency make them ideal for light emitting and absorbing functionalities such as solar cells, light emitting diodes (LEDs) or photodetectors, possibly integrated on the silicon photonics platform.

Following above band gap photoexcitation of semiconductor materials (*i.e.* materials with an energy gap (so-called 'band gap') between a valence band and a conduction band), a high energy electron-hole pair (an exciton) rapidly dissipates its excess energy to end up as a band edge exciton with the electron and the hole occupying the lowest conduction band and highest valence band levels. Very often, hot exciton relaxation is seen as a loss channel, competing with processes that better preserve the free energy of the high energy exciton such as multiple exciton generation or charge transfer of hot charge carriers. On the other hand, the high rate of intraband relaxation may render the process useful for applications relying on a fast change or modulation of materials properties. In both cases, application development would benefit from a better understanding of the properties and dynamics of cooling charge carriers.

Hyperspectral and ultrafast transient absorption spectroscopy is used to map the properties of cooling charge carriers in lead sulfide quantum dots. In such an experiment, a temporally short (180 femtoseconds) pump pulse photoexcites the sample (a colloidal dispersion of QDs or a thin film of the latter) creating excitons, after which the sample is probed with a temporally delayed short pulse at different energies. First, we show that, depending on the energy of pump and probe photons and on the pump-probe time delay, different phenomena dominate the transient absorption spectrum. Whereas around the bandgap transition, the well-documented bleach and Coulomb-shift of the bandgap exciton dominate, a short lived transient bleach feature appears at probe photon energies corresponding to the critical point in the energy band diagram along the  $\Sigma$  direction. This temporary slowing-down of the cooling exciton is present in PbX (X=S,Se) nanocrystals of different sizes, suggesting that this cooling bottleneck is intrinsically related to the PbS band structure. In fact, as the critical point along the  $\Sigma$  direction is a saddle point, the cooling exciton arriving at the critical point must change the direction of its momentum to continue cooling towards the band edges around the L point. Apparently, this results in a temporary accumulation of the exciton around the critical point. Moreover, we argue that this slow cooling via the  $\Sigma$  direction saddle point is the dominant cooling pathway for high energy excitons. This conclusion stresses the importance of the bulk band structure for understanding cooling dynamics of hot charges in semiconductor nanocrystals. At probe wavelengths below the bandgap, we observe an ultrafast and broadband photo-induced absorption feature that reflects the changing cross section for intraband absorption of the cooling exciton. Interestingly, the wavelength at which this photoinduced absorp-

tion matches the bleach of the bandgap transition stays put after exciton cooling. Hence, at this matching wavelength, photo-excitation results in a short, 1-2 ps burst of photoinduced absorption after which the sample has the same absorbance as the original, unexcited sample. We find that this burst photoinduced absorption is linear in the excitation power, both in the single and multi-exciton regime. Moreover, excitation pulses separated by only 2.2 ps give rise to a sequence of absorption bursts, showing that PbS quantum dots could be used for the ultrafast (225 and 450 Gb/s), all-optical conversion of data signals between two wavelengths.

The strong photo-induced absorption close to the band edge observed in lead-chalcogenides impedes their use in applications where stimulated emission is required such as lasers or amplifiers. Routes followed in the visible part of the spectrum (using cadmium based compounds) are not readily transferable to the near-infrared: interfacial alloying and/or giant shell quantum dots in the near-infrared have been proven less efficient at suppressing the non-radiative Auger rate and/or lifting the threshold for population inversion, a premise for stimulated emission to dominate over absorption and eventually give lasing action.

Novel paradigms are required to push colloidal nanocrystals in the near-infrared range to become efficient lasing dyes. Two of these concepts are explored in this work: multi-level systems through mid-gap state formation and structural relaxation of the excited-state. Both approaches could lead to 'thresholdless' amplification. In particular, HgTe QDs were explored as a new class of near-infrared active QDs showing near-thresholdless optical gain with remarkably long gain-lifetimes. The combination of the low gain threshold, long gain lifetime and substantial gain coefficients of  $100\text{cm}^{-1}$  make HgTe QDs a very promising gain material for integrated photonics, where in particular electrically pumped devices become feasible for the first time.

Understanding the linear and non-linear response of QDs in solution is only a first step towards functional photonic devices. Indeed, in a device context, QDs will always be used in a thin film (*e.g.* cladding a waveguide or combined with a microcavity). A simple translation of the properties measured in solution to the thin film case was shown to be inadequate. A close-packed monolayer of QDs (with interdistances on the order of the QD size, *i.e.* a few nanometer) was used as a model system to study the near-field interactions between QDs. It was found experimentally that the absorption cross section could be increased with a factor of 4 (CdSe) to 5 (PbS) compared to the solution case. The observed *absorp-*

*tion enhancement* was explained both qualitatively and quantitatively by a coupled dipole model. As such, this model provides a general toolbox for understanding QD-QD interactions in thin films. Modification of the spontaneous emission was also observed (through shortening of the radiative lifetime).

Finally, the QDs were combined with the building blocks of the silicon photonics platform: waveguides and microcavities. Through absorption and photoluminescence measurements, interaction of the QDs with the optical modes of the waveguides and microcavities were shown experimentally and modeled using the developed coupled dipole model.



# 1

## Introduction

### 1.1 Problem Definition

Silicon photonics holds great promise for future integrated optical networks, where light instead of electrons are used to carry information across the globe. Using silicon, it can rely on the immense CMOS fabrication expertise and infrastructure developed since the 1970's. Although the race is far from over, some first commercializations have been shown gradually over the past decades, going from simple gyroscopes to full Fibre-To-The-Home (FTTH) modules or even on-chip interconnects. Not the least at Ghent University, where a number of spin-off companies have been successfully started such as Caliopa and Luceda Photonics. Also major industrial players (IBM, Alcatel-Lucent, Intel, ...) show great interest in the silicon photonics platform. The possibility to interface small footprint modules with standard long-range telecom facilities (e.g. glass fiber) is not the only application imaginable since on-going research shows great promise in disposable lab-on-a-chip sensors, quantum computing and on-chip interconnects.

Using silicon has its merits in terms of commercialization and manufacturing, but the material itself presents considerable limitations as a 'photonic' backbone. Although it is excellent at passive functionalities such as guiding and routing of light, its indirect band gap, limited carrier mobility and centro-symmetric crystal structure make for very inefficient light gener-

ation and/or modulation. Light generation for simple light-emitting-diodes or single photon sources (relying on spontaneous emission) or lasers (relying on stimulated emission) are far from trivial using only silicon (refs), as is the modulation of light at speeds in excess of 100 Gbit/s, the standard these days.

To accommodate these shortcomings, two routes are followed to extend the silicon photonics platform: either direct modification of silicon through doping or straining or hybridization with novel materials. The latter is done either through 'bonding' or growing (so-called hetero-epitaxy) of functional III-V materials on silicon or through the use of novel materials typically deposited from a solution phase such as colloidal quantum dots (QDs).

QDs are nanometer sized pieces of (inorganic) semiconductor crystals obtained through a solution-based chemical synthesis at relatively low temperatures. The benefits of combining QDs with (silicon) photonics are immense:

- Large scale and cost-effective production of QDs has been shown feasible due to the solution-based approach.
- Deposition in thin films is straightforward through solution based techniques as spincoating, dropcasting or doctor-blading.
- Due to their inorganic nature and specific energy level structure, QDs can be made stable against aging, oxidation and temperature induced effects.
- Size dependent optical properties allow end users to choose the material based on the application, and not vice versa.

QDs are very efficient at light emission and absorption in a linear regime, making them great candidates for on-chip light sources (e.g. for single photon sources) and detectors. However, pushing these particles to regimes of high carrier densities required for e.g. fast modulation or light amplification, presents some difficulties:

- Fast non-radiative Auger recombination in regimes of high carrier density quickly diminishes the population inversion required to sustain lasing action.
- Carrier based light modulation using QDs will be limited by relatively slow interband exciton dynamics (either radiative or non-radiative).
- QDs are typically obtained and characterized in solution. It is not clear to what extent, either beneficial or not, these properties are retained in close packed films, a situation more relevant for actual QD based devices.

- To combine QDs with the existing silicon photonics framework, we need to investigate whether the QDs can interact with that framework, *i.e.* whether the exciting optical properties can be coupled to *e.g.* photonic waveguides, resonators, etc. ...

As such, the work in this thesis strives to uplift the limitations of QDs for more advanced photonic functionalities such as on-chip lasing and ultrafast light modulation to complete the silicon photonics platform.

## 1.2 Thesis Outline

In this multidisciplinary thesis, we aimed at understanding, remedying and applying the linear and non-linear ultrafast properties of colloidal quantum dots to enhance the silicon photonics platform. More specifically, we strived to resolve the aforementioned problems of QDs for silicon photonics (and guided wave optics in general), by studying:

- The linear optical properties (absorption, photoluminescence) of near-infrared emitting PbS and PbS/CdS heterostructure QDs (both spherical and anisotropic in shape)
- The ultrafast non-linear properties of hot and cold excitons (electron-hole pairs) in near-infrared active QDs (either in solution or in thin films) for fundamental studies (excitons shifts, phonon assisted cooling, ...) and applications in hot carrier devices, all-optical light conversion and low threshold optical gain.
- Novel collective optical properties of QDs in close-packed thin films through a near-field dipolar coupling mechanism.
- A framework for simulation and practical integration of QDs on the silicon photonics platform (from simple waveguides to subwavelength nanopatch cavities).

Chapter 2 starts off with a general introduction to the exciting field of nanoscale semiconductor physics and (non-)linear photonics with colloidal quantum dots. A general overview of both fields is given which should allow the reader to grasp and situate the more advanced discussions in the following chapters. In chapter 3, an overview of the linear (spontaneous emission and linear absorption) and non-linear (Auger recombination, optical gain) of the widely used near-infrared emitting QDs (spherical PbS and PbS/CdS core/shell QDs) is presented. A sizing curve, relating the first excitonic absorption feature to the particle size, is determined through a

combination of ICP-MS and absorption spectroscopy for the core/shell system and the nature of the electronic states is determined to be type I. More advanced anisotropic heterostructures are studied in terms of structural and (ultrafast) optical properties where it is concluded that Pb-chalcogenide are not suitable for light amplification, but could find applications in light modulation or conversion as discussed in chapter 6.

Next, in chapters 4 to 7, the ultrafast non-linear properties of hot and cold excitons in colloidal quantum dots are investigated where each time, a relevant application or theoretical perspective was put forward. In chapter 4, the spectral shifts of the absorption spectrum due to hot and cold excitons are studied: a general toolbox was developed to analyze these shifts induced by hot and cold (multi-)excitons ( $X$ ), which is relevant for analysis of any kind of pump-probe experiment or for detailed theoretical studies of the  $X$ - $X$  interactions in nanoscale structures. The analysis was carried out on PbS QDs and led to a theoretical picture where carrier wavefunction overlap is the crucial parameter determining the magnitude of the Coulomb interactions leading to the spectral shifts. Next, chapter 5 deals with the cooling of hot carriers where the cooling of truly hot excitons (with energies far above the band gap) is studied for different sizes of lead-chalcogenide (PbS and PbSe) QDs. Although extremely relevant for applications such as MEG (Multiple Exciton Generation) solar cells or hot carrier extraction in photodetection, these results are the first that address this issue by directly looking at the hot excitations instead of indirect band edge dynamics. A slowdown of hot carrier cooling was found and explained (both experimentally and theoretically) in terms of a 'phonon scattering bottleneck' associated with a saddle point in the energy dispersion of lead-chalcogenides. These results shed a new light on the role such saddle points for carrier cooling in polar materials, or custom made materials in general. The bottleneck allows us to quantify hot carrier cooling rates and the implications for theoretical models of multiple-exciton generation are discussed. In chapter 6, the intraband absorption of hot and cold carriers is studied for applications in light modulation and conversion. We demonstrate that a specific wavelength range exist where the effects of photobleaching, photoinduced absorption and spectral shifts cancel, apart from the first picosecond following photoexcitation by a pump pulse. This results in an intense, linear and ultrafast optical response that maintains its characteristics under excitation sequences of 450 and 225 Gb/s pulse trains. We argue that this makes colloidal QDs an ideal material for low power, picosecond wavelength conversion that can be used in small footprint, integrated photonic devices. In addition, it sheds a new light on intraband absorption as a useful material property of colloidal QDs. In chapter 7,

HgTe QDs are studied for applications in low threshold optical gain. We show that HgTe QDs exhibit size-tuneable stimulated emission throughout the near-infrared telecom window at a threshold 2 orders of magnitude lower than ever reported for QDs. We demonstrate that stimulated emission involves a high oscillator strength transition to a gap state, making HgTe QDs an effective 3-level system. Since the combination of gain coefficient, threshold and gain lifetime of HgTe QDs meet the requirements for DC electrical pumping, this result could make the formation of effective 3-level systems a new paradigm for developing QD-based gain media. In chapter 8, the QDs are transferred from solution to a close-packed thin film. The linear optical properties (such as spontaneous emission and absorption) are re-evaluated using a simple monolayer model system. Deviations from the solution phase are found in the absorption strength (*i.e.* the absorption cross section) and spontaneous emission lifetime of the QDs: the former is enhanced and the latter decreased compared to the solution case. These deviations can be quantitatively explained using a dipolar coupling model indicating the importance of near-field electrostatic coupling between adjacent dots on the nanometre scale, which is present in close-packed films but not in dilute liquid dispersions. This is one of the first demonstrations of a collective optical effect for arrays of semiconducting colloidal quantum dots and offers a new design paradigm for *e.g.* overcoming the absorption-extraction compromise of thin film solar cells. Having transferred the QDs from solution to thin films, we are now ready to incorporate them into actual photonic devices. In chapter 9, the possibility for hybridisation of silicon photonics with QDs is investigated through simulations and experiments. We shown that the QDs can interact with the optical modes of the silicon platform, both in simple waveguides as in optical micro - and nano-cavities). As such, the enormous wealth of interesting linear and ultrafast non-linear properties of QDs are transferable to the silicon photonics framework to create next-generation photonic devices with reduced device footprints and energy consumption. A short prospect for this exciting route to become reality and inevitable hurdles are provided in chapter 10.

### 1.3 Publications

## List of Articles

- [1] Geiregat, P.; Delerue, C.; Justo, Y.; Aerts, M.; Spoor, F.; Thourhout, D. V.; Siebbeles, L. D. A.; Allan, G.; Houtepen, A. J.; Hens, Z. A Phonon Scattering Bottleneck for Carrier Cooling in Lead Chalcogenide Nanocrystals. *ACS Nano* **2015**, ASAP, year.
- [2] Geiregat, P.; Houtepen, A.; Justo, Y.; Grozema, F. C.; Van Thourhout, D.; Hens, Z. Coulomb Shifts upon Exciton Addition to Photoexcited PbS Colloidal Quantum Dots. *The Journal of Physical Chemistry C* **2014**, *118*, 22284–22290.
- [3] Omari, A.; Xie, W.; Geiregat, P.; Van Thourhout, D.; Hens, Z. Modeling the Optical Properties of Low-cost Colloidal Quantum Dot Functionalized Strip SOI Waveguides. *IEEE Journal of Selected Topics in Quantum Electronics* **2014**, *20*, 4400306.
- [4] Justo, Y.; Geiregat, P.; Hoecke, K. V.; Vanhaecke, F.; Donega, C. D. M.; Hens, Z. Optical Properties of PbS / CdS Core / Shell Quantum Dots. *Journal of Physical Chemistry C* **2013**, *117*, 20171–20177.
- [5] Omari, A.; Geiregat, P.; Van Thourhout, D.; Hens, Z. Light Absorption in Hybrid Silicon-on-Insulator/Quantum Dot Waveguides. *Optics Express* **2013**, *21*, 23272.
- [6] Geiregat, P.; Justo, Y.; Abé, S.; Flamee, S.; Hens, Z. Giant and Broadband Absorption Enhancement in Colloidal Quantum Dot Monolayers through Dipolar Coupling. *ACS Nano* **2013**, *7*, 987–993.
- [7] De Geyter, B.; Komorowska, K.; Brainis, E.; Emplit, P.; Geiregat, P.; Hassinen, A.; Hens, Z.; Van Thourhout, D. From Fabrication to Mode Mapping in Silicon Nitride Microdisks with Embedded Colloidal Quantum Dots. *Applied Physics Letters* **2012**, *101*, 161101.
- [8] De Geyter, B.; Houtepen, A. J.; Carrillo, S.; Geiregat, P.; Gao, Y.; Ten Cate, S.; Schins, J. M.; Van Thourhout, D.; Delerue, C.; Siebbeles, L. D.; Hens, Z. Broadband and Picosecond Intraband Absorption in Lead-Based Colloidal Quantum Dots. *ACS Nano* **2012**, *6*, 6067–6074.
- [9] Justo, Y.; Goris, B.; Kamal, J. S.; Geiregat, P.; Bals, S.; Hens, Z. Multiple Dot-in-Rod PbS/CdS Heterostructures with High Photoluminescence Quantum Yield in the Near-Infrared. *Journal of the American Chemical Society* **2012**, *134*, 5484–5487.

## List of Conference Contributions

- [1] Lu, Q.; Geiregat, P.; Hens, Z.; Thourhout, D. V. Design of Integrated Nanocrystal Light Sources. *Photonics Conference (PHO)*, 2011; pp 527–528.
- [2] Devloo-casier, K.; Dendooven, J.; Geiregat, P.; Ludwig, K.; Detavernier, C. In-situ synchrotron based XRF and GISAXS study of ALD encapsulation of supported nanocrystals. *Baltic Conference on Atomic Layer Deposition*, 2011.
- [3] De Geyter, B.; Geiregat, P.; Houtepen, A. J.; Van Thourhout, D.; Siebbeles, L. D.; Hens, Z. Ultrafast Photoinduced Absorption in PbS, PbSe and PbSe/CdSe Core/Shell Nanocrystals for near-Infrared to Mid-infrared All-Optical Signal Processing. *MRS Fall Meeting*, 2012.
- [4] Devloo-Casier, K.; Dendooven, J.; Ludwig, K. F.; Geiregat, P.; Hens, Z.; Detavernier, C. Nanoscale Area Selective ZnO Growth between a Monolayer of Nanocrystals. *12th International conference on Atomic Layer Deposition (ALD 2012)*, 2012.
- [5] Geiregat, P.; Justo, Y.; Hens, Z. Giant absorption enhancement in colloidal quantum dot supercrystals through dipolar coupling. *7th International Conference on Quantum Dots (QD-2012)*, 2012; p 78.
- [6] De Geyter, B.; Geiregat, P.; Houtepen, A. J.; Van Thourhout, D.; Siebbeles, L. D.; Hens, Z. Ultrafast Intraband Absorption in Lead-Chalcogenide Core and Core/Shell Nanocrystals for Near-to Mid-IR All-Optical Signal Processing. *7th International Conference on Quantum Dots (QD-2012)*, 2012.
- [7] Omari, A.; Hiroyuki, S.; Geiregat, P.; Van Thourhout, D.; Hens, Z. Characterization of Pbs/CdS Qdot Absorption on SOI Waveguides. *17th Annual Symposium of the IEEE Photonics Benelux Chapter*, 2012; pp 295–298.
- [8] De Geyter, B.; Houtepen, A. J.; Carrillo, S.; Geiregat, P.; Gao, Y.; ten Cate, S.; Schins, J. M.; Van Thourhout, D.; Delerue, C.; Siebbeles, L. D. a.; Hens, Z. Broadband and Picosecond Intraband Absorption in Lead-Based Colloidal Quantum Dots. *14th International Conference on Transparent Optical Networks (ICTON)*, 2012; p Th.A5.4.

- [9] Geiregat, P.; Justo, Y.; Abe, S.; Flamee, S.; Hens, Z. Giant and broad-band absorption enhancement in colloidal quantum dot monolayers through dipolar coupling: a Novel Optical Phenomenon at the Nanoscale. *CLEO: QELS Fundamental Science*, 2013; p QTu1A.7.
- [10] Devloo-Casier, K.; Dendooven, J.; Ludwig, K. F.; Geiregat, P.; Hens, Z.; Detavernier, C. In situ GISAXS during atomic layer deposition of oxides on ordered quantum dots. *GISAXS 2013 Workshop*, 2013.
- [11] De Geyter, B.; Komorowska, K.; Brainis, E.; Emplit, P.; Geiregat, P.; Hassinen, A.; Hens, Z.; Van Thourhout, D. Embedding Colloidal Nanocrystals in Silicon Nitride Micro-Disk Resonators: From Mode-Mapping to Single Dot Spectroscopy. *E-MRS 2013 Spring & Bilateral*, 2013.
- [12] Omari, A.; Geiregat, P.; Van Thourhout, D.; Hens, Z. Assessing Colloidal Quantum Dot Optical Properties through Free Standing Layers on Photonic Waveguides. *E-MRS 2013 Spring & Bilateral*, 2013.
- [13] Omari, A.; Geiregat, P.; Van Thourhout, D.; Hens, Z. Modelling Colloidal Quantum Dots on SOI Photonic Waveguides. *E-MRS 2013 Spring & Bilateral*, 2013.
- [14] Omari, A.; Geiregat, P.; Van Thourhout, D.; Hens, Z. Probing the Optical Constants at the Nanoscale of Colloidally Prepared Films through Optical Waveguides. *NWO Scientific Meeting*, 2013.
- [15] Omari, A.; Geiregat, P.; Van Thourhout, D.; Hens, Z. Optical Properties of SOI Waveguides Functionalized with Close-Packed Quantum Dot Films. *15th International Conference on Transparent Optical Networks (ICTON)*, 2013.
- [16] Geiregat, P.; Houtepen, A. J.; Sagar, L. K.; Delerue, C.; Thourhout, D. V. Thresholdless Optical Gain using Colloidal HgTe Nanocrystals. *CLEO: QELS Fundamental Science*, 2014; p FTh4C.4.
- [17] Geiregat, P.; Houtepen, A.; Aerts, M.; Van Thourhout, D.; Delerue, C.; Hens, Z. Properties and Dynamics of Cooling Charge Carriers in Lead Sulfide Quantum Dots. *Nanax*, 2014.

- [18] Geiregat, P.; Houtepen, A. J.; Sagar, L. K.; Delerue, C.; Grozema, F. C.; Thourhout, D. V.; Hens, Z. Near-Thresholdless Optical Gain using Colloidal HgTe Quantum Dots. *30 Years of Colloidal Quantum Dots*, 2014.
- [19] Geiregat, P.; Houtepen, A.; Aerts, M.; Delerue, C.; Hens, Z. Hyperspectral Analysis of Ultrafast Hot Carrier Dynamics in Pb-chalcogenide Nanocrystals : a Case for Slow Cooling. *8th International Conference on Quantum Dots (QD-2014)*, 2014.
- [20] Geiregat, P.; Houtepen, A. J.; Van Thourhout, D.; Delerue, C.; Hens, Z. Properties and Dynamics of Cooling Charge Carriers in Lead Sulfide Quantum Dots. *International Conference on Fundamental Processes in Semiconductor Nanocrystals*, Oxford, UK, 2014.



# 2

## Physics of Nanocrystals for Integrated Photonics

### 2.1 Light-Matter Interaction

#### 2.1.1 Light

Light as we perceive it (*i.e.* visible light) is only a fraction of a much larger spectrum of electromagnetic radiation going from short wavelength UV and Gamma radiation up to long wavelength infrared, microwaves and radiowaves. Surprisingly, all these phenomena can be described by a single set of equations known as 'Maxwell's equations' which describe light as a vector wave with an electric ( $\mathbf{E}$ ) and magnetic ( $\mathbf{H}$ ) component<sup>1</sup>.

Assuming a monochromatic wave with angular frequency  $\omega$  propagating in a homogeneous and linear dielectric medium with a (complex) refractive index  $n(\omega) = n_r(\omega) + jn_i(\omega)$ , we can write<sup>1</sup>:

$$\mathbf{E}(\mathbf{r}, \omega) = \mathbf{E}_0 e^{-j\omega t} e^{j\mathbf{k} \cdot \mathbf{r}} \quad (2.1)$$

The wavevector  $\mathbf{k}$  can be written as:  $\mathbf{k} = \mathbf{1}_e k_0 n$ , with  $k_0 = \frac{2\pi}{\lambda_0}$ , where  $\lambda_0$  is the wavelength in vacuum. Plugging this expression into equation 2.1, we can see that the imaginary part of  $n$  will give rise to extinction and the real part to periodic oscillations in space (with a period of  $\lambda_0/n_r$ ). As such, we can define an extinction coefficient<sup>2</sup>:  $\mu = \frac{4\pi n_i}{\lambda}$ .

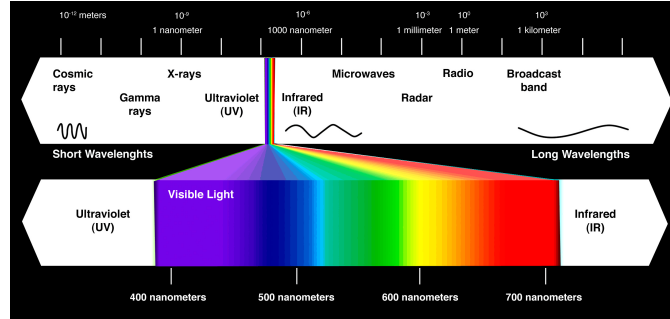


Figure 2.1: Overview of the electromagnetic spectrum. Note that the 'visible' part of the spectrum (what we often call 'light') composes only a small fraction of the total spectrum.<sup>1</sup>

Since  $n$  is an expression of the material's response to different frequencies (inherently linked to the susceptibility  $\chi$  and the polarizability of the material at hand, see Saleh *et al.*<sup>1</sup>), the propagation of short pulses (which are spectrally broad, Fourier principle<sup>1</sup>) is subject to dispersion. A phenomenon very similar to the formation of a rainbow, light at different frequencies experiences different (phase) velocities  $\frac{c}{n_r(\omega)}$  (with  $c$  the speed of light in vacuum). As such, the different frequency components of a spectrally broad pulse propagate at different speeds (*e.g.* in a glass fiber or an integrated silicon waveguide) leading to pulse broadening.

### 2.1.2 Matter

The atoms making up solids lie in close proximity to each other and typically combine themselves into a periodic arrangement known as a crystal lattice. The energy levels of solids are therefore determined by the periodicity of the individual atomic potentials and the interaction with neighbouring lattice atoms<sup>3</sup>. In the context of nanocrystals, it is instructive to see how energy levels change when going from isolated atoms to infinitely extending solids (so-called 'bulk'). Nanocrystals are somewhere between the molecular (1-100 atoms) and the bulk ( $> 100.000$  atoms) case and their energy levels structure inherits from both extremes. Isolated atoms and even molecules exhibit discrete energy levels. As atoms are brought closer to form solids, exchange interactions (due to the Pauli principle) and different sorts of short - and long range interactions between the atoms become increasingly important. The initially sharp levels associated with the valence electrons of isolated atoms gradually broaden into collections of numer-

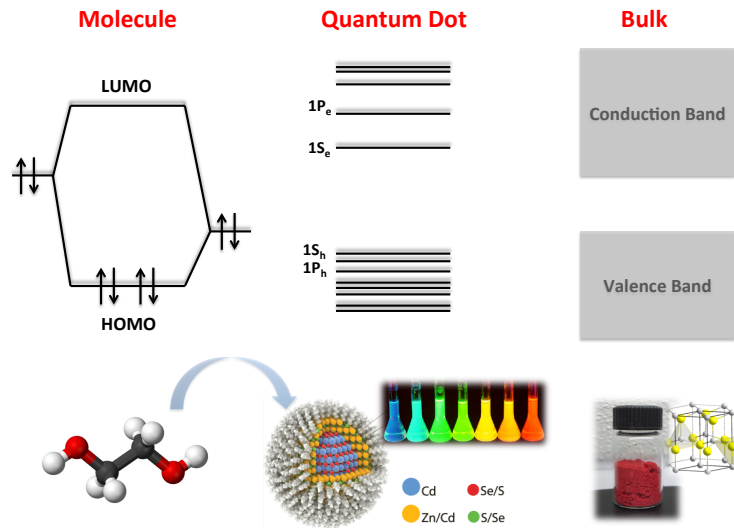


Figure 2.2: Schematic depicting crossover from molecules to quantum dots to bulk semiconductors.

ous densely spaced energy levels that form energy bands. This process is depicted in Figure 2.2.

The lowest lying energy levels remain sharp because the electrons in the inner subshells are shielded from the influence of nearby atoms while the sharp energy levels associated with the outer electrons become bands as atoms enter into close proximity. The formation of such energy bands is the essence of solid state theory<sup>3</sup>, where different materials can be classified according to how these bands are filled: metals, insulators and semiconductors. The lowest lying unoccupied (or partially occupied) band is called the 'conduction band' (inheriting from the LUMO, Lowest Unoccupied Molecular Orbital) and the highest (in energy) fully occupied band is called the valence band (inheriting from the HOMO, Highest Occupied Molecular Orbital). These bands are separated by a forbidden gap, the band gap of the material, denoted by  $E_g$ . Depending on the size of this gap and position of the Fermi level, a material will be classified conducting (Fermi level inside a band, mobile carriers available for conduction), semiconducting (Fermi level inbetween two bands with a moderate gap, mobile carriers available only after excitation (*e.g.* optical, thermal, ...)), or insulating (Fermi level inbetween two bands with a huge energy gap, typically a few electron-volt (eV) or more).

### 2.1.3 Light-Matter Interaction

Light interacts with matter because matter contains electric charges. The time-varying electric field of light exerts forces on the electric charges and dipoles in atoms, molecules and solids, causing them to oscillate so that they undergo acceleration dissipating the energy of the field into matter: oscillating electric charges absorb and emit light (or more general, electromagnetic radiation). In a quantum mechanical picture, atoms, molecules and solids have specific energy levels and bands that are determined by the laws of quantum mechanics. A photon may interact with an atom if its energy matches the difference between two atomic energy levels (see previous).

#### 2.1.3.1 Basics: The Einstein Coefficients

In 1917 Einstein introduced a model for the interaction of light with matter<sup>4</sup>. Although superseded by developments in quantum theory, his approach is still used quite often due to its simplicity and the additional insights it provides. Einstein considered two energy levels of an atom: an upper level 2 with energy  $E_2$  (occupation  $n_2$ ) and a lower level 1 with energy  $E_1$  (occupation  $n_1$ ), and identified 3 fundamental processes by which radiation could interact with atoms in these levels (see Figure 2.3): spontaneous emission, absorption and stimulated emission.

**Absorption** Absorption is the process by which a photon is absorbed by the 2-level system, causing an electron to jump from a lower energy level to a higher one. The process is described by the Einstein coefficient  $B_{12}$  ( $J^{-1}m^3s^{-2}$ ), which gives the probability per unit time and per unit spectral energy density of the radiation field that an electron in state 1 with energy  $E_1$  will absorb a photon with an energy  $E_2 - E_1 = \hbar\omega$  and jump to state 2 with energy  $E_2$ .  $\rho(\hbar\omega)$  is the spectral energy density of the isotropic radiation field at the frequency of the transition (derived in Planck's law).

$$\frac{dn_2}{dt} = B_{12}n_1\rho(\hbar\omega) \quad (2.2)$$

**Spontaneous Emission** Spontaneous emission is the process by which an electron "spontaneously" (*i.e.* without any outside influence) decays from a higher energy level to a lower one. The process is described by the Einstein coefficient  $A_{21}$  ( $s^{-1}$ ) which gives the probability per unit time that an electron in state 2 with energy  $E_2$  will decay spontaneously to state 1 with energy  $E_1$ , emitting a photon with an energy  $E_2 - E_1 = \hbar\omega$ .

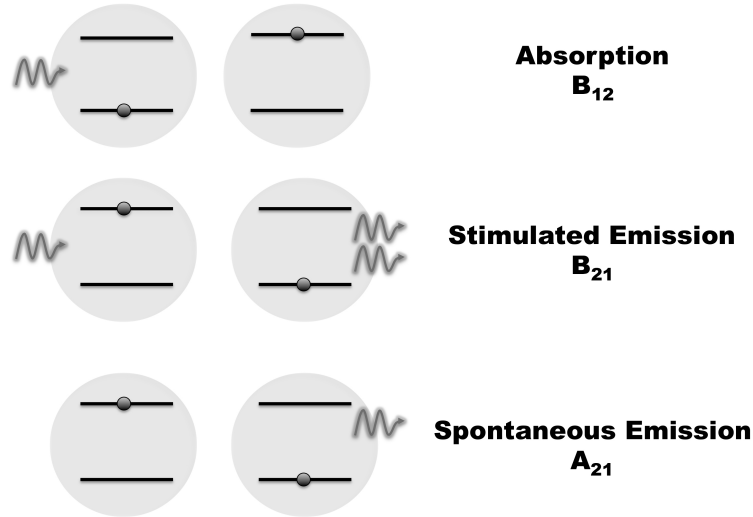


Figure 2.3: Schematic depicting the fundamental light-matter interactions: absorption, stimulated emission and spontaneous emission.

$$\frac{dn_2}{dt} = -A_{21}n_2 \quad (2.3)$$

**Stimulated Emission** Stimulated emission is the process by which an electron is 'stimulated' to jump from a higher energy level to a lower one by the presence of electromagnetic radiation (*i.e.* a photon) at the frequency of the transition. From the thermodynamic viewpoint, this process could be regarded as "negative absorption". The process is described by the Einstein coefficient  $B_{21}$  ( $J^{-1}m^3s^2$ ), which gives the probability per unit time and per unit spectral energy density of the radiation field that an electron in state 2 with energy  $E_2$  will decay to state 1 with energy  $E_1$ , emitting a photon with an energy  $E_2 - E_1 = \hbar\omega$ .

$$\frac{dn_2}{dt} = -B_{21}n_2\rho(\hbar\omega) \quad (2.4)$$

### 2.1.3.2 A Quantum Picture

Explicit expressions for the Einstein coefficients can be obtained using a quantum mechanical approach. The absorption of light with angular fre-

quency  $\omega$  is modeled as the removal of an energy quantum  $\hbar\omega$  (the photon) from a radiation field, accompanied with a transition in the absorbing system (the electron) from an initial state ' $i$ ' to a final state, labeled ' $f$ '. The transition rate can be calculated using time dependent perturbation theory, *i.e.* Fermi's Golden Rule<sup>2</sup>:

$$W_{if} = \frac{e^2\pi}{\hbar} |\langle f | \mathbf{e} \cdot \mathbf{r} | i \rangle|^2 \frac{E_{loc}(E)^2}{2} \quad (2.5)$$

where  $\mathbf{e}$  is the polarization vector of the incident light field and  $\mathbf{r}$  is the position operator of the electron making the transition between levels 1 and 2. For spherical particles in a dielectric medium, the local field  $E_{loc}$  is related to the spectral density  $\rho(E)$  of the radiation field at energy  $E$  through the local field factor  $f_{LF}$ :

$$W_{if} = \frac{e^2\pi}{\hbar\epsilon_0\epsilon_s} |\langle f | \mathbf{e} \cdot \mathbf{r} | i \rangle|^2 |f_{LF}|^2 \rho(E) \quad (2.6)$$

As such, we can derive the following expression for the (A,B) coefficients using the oscillator strength  $f_{12}$  and level degeneracies  $g_{1,2}$  (see 2.3.3):

$$A_{21} = \frac{2\pi\nu^2 c^2}{\epsilon_0 m_e c^3} \times \frac{g_1}{g_2} \times f_{12} \quad (2.7)$$

$$B_{12} = \frac{4\pi^2 e^2}{m_e h\nu c} \times f_{12} \quad (2.8)$$

$$B_{21} = \frac{4\pi^2 e^2}{m_e h\nu c} \times \frac{g_1}{g_2} \times f_{12} \quad (2.9)$$

## 2.2 Photonics

Photonics could be defined as a field of science and engineering that pre-occupies itself with the generation, detection and manipulation of light for applications in telecommunication, sensing, computing, imaging, ... The word is derived from 'photon', the elementary particle constituting light, much as electronics is derived from the 'electron'. We will focus in this section (and thesis) on two main research directions: long range data-communication through optical fibers and integrated photonics for on-chip short range interconnects. A good overview of the extensive field can be found in Saleh *et al.*<sup>1</sup>.

### 2.2.1 Long Range Data Communication

Until the 1970s data communication relied on the transmission of electrical signals over copper wire or in free space using micro- and radio frequency waves. At first, light (here seen as electromagnetic radiation in the visible and near-infrared part of the spectrum) was not considered a good candidate for replacing the electrical signals: it can easily be obstructed or absorbed by solid objects or clouds and no adequate sources and detectors were available at that time. However, the advent of two photonic inventions was to quickly change this underappreciation of light as information carrier: the development of efficient and compact light sources (solid state LEDs and lasers) and the development of low-loss optical fibers to conduct the light. It opened up the exciting possibilities of light as means of information carrier:

- The capacity of fibers for data transmission is huge: a single silica fiber can carry hundreds of thousands of telephone channels, utilizing only a small part of the theoretical capacity (which is close to 100 Tbit/s). In the last 30 years, the progress concerning transmission capacities of fiber links has been significantly faster than e.g. the progress in the speed or storage capacity of computers.
- The losses for light propagating in fibers are amazingly small: *ca.* 0.2 dB/km for modern single-mode silica fibers, so that many tens of kilometers can be bridged without amplifying the signals.
- A large number of channels can be reamplified in a single fiber amplifier, if required for very large transmission distances. Due to the huge transmission rate achievable, the cost per transported bit can be extremely low.
- Compared with electrical cables, fiber-optic cables are very lightweight and are immune to problems that arise with electrical cables, such as ground loops or electromagnetic interference (EMI). Such issues are important, for example, for data links in industrial and demanding environments.

A typical optical fiber communication system or network consists of a

- Light source, to generate light, comparable to a power source in electronics.
- Modulator/Convertor, with the ability to encode information onto a light stream, either between electrical and optical data-streams or all-optical.
- Amplifier, to compensate inevitable losses in the communication link.
- Detector, to read-out the information.

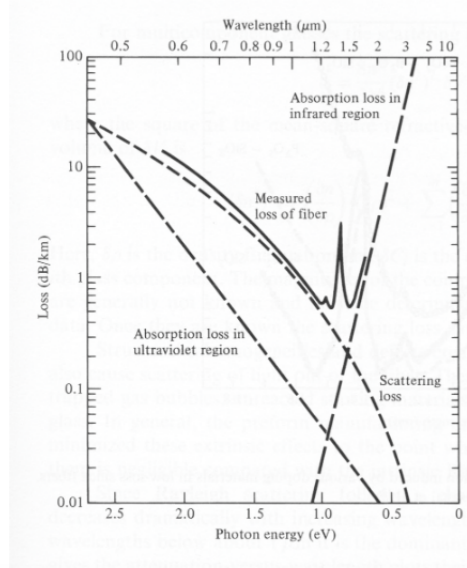


Figure 2.4: Typical propagation loss (in dB/km) for a silica optical fiber as function of photon energy (wavelength).<sup>1</sup>

- Optical fiber, the transport channel of the optical connection.

To design and evaluate the potential of new materials (such as colloidal quantum dots) for use in these modern telecom networks, we should understand the limitations and rules of the current optical data communication toolbox. We will discuss three components in detail: the fiber link, the amplifier and the modulator/convertor.

### 2.2.1.1 Fibers

An optical fiber is a cylindrical dielectric waveguide, a few tens of microns wide, usually made of materials with sufficiently low optical loss such as fused silica glass of high chemical purity. Light is confined in the fiber through total internal reflection as the core refractive index is higher than that of the cladding material. Fibers, although excellent light guides, present some limitations to high speed and low-loss datacommunication. These limitations can be split up in two categories: attenuation and dispersion.

When light propagates through a glass fiber it attenuates due to various loss mechanisms (Rayleigh scattering, impurity absorption (mainly resid-

ual hydroxyl groups -OH, ...). All of these mechanisms show a particular wavelength dependence resulting in so-called 'bands' or 'windows' of low optical loss (see Figure 2.4). The lowest optical loss is obtained in the second window around 1300 nm and the third window around 1550 nm. The first window around 800-900 nm was historically the first to be used as GaAs/AlGaAs LEDs were initially used as sources and cheap silicon photodiodes as means of detection. However, optical loss is quite significant in this region, limiting it to short-range transmission only. Although initially the second window around 1300 nm was preferred due to relatively low loss and zero dispersion, the standard has shifted more towards the third window where more efficient rare-earth doped amplifiers are available (see further).

Short pulse packets propagating through a fiber undergo pulse broadening<sup>1</sup>, limiting the data rates that can be sent through these fibers. The broadening is a direct consequence of 'dispersion' in the silica (see figure) expressed through a dispersion coefficient  $D_\lambda$ . The sign (positive (anomalous) or negative (normal)) does not influence the amount of broadening, but can be used to create dispersion compensated fibers alternating for example positive and negative dispersion to create an average zero dispersion.

### 2.2.1.2 Amplifiers

Although fibers present ultra-low loss, long distance communication over several 1000's of km is only possible using intermediate or final stage amplification of the optical signal. The main<sup>5</sup> component is the EDFA (Erbium Doped Fiber Amplifier), which uses a relatively cheap pump laser (980 nm or 1480 nm) to excite electrons to a higher energy level in Erbium ( $Er^{3+}$ ) ions, typically embedded in a sapphire (*i.e.* a glass fiber) host. Rapid depopulation of this excited state to a lower energy state results in a net gain band around 1500 nm (depending on doping concentration and host material). Not only is the gain spectrum quite narrow, the small gain cross section and inter-species quenching leads to long fiber lengths and high input powers for operation, limiting the use of EDFAs to long distance communication only.

### 2.2.1.3 Modulation and Conversion

To encode information on a light beam, both the phase (Field Modulation) and the amplitude (Amplitude Modulation) can be used. Since individual wavelengths are 'independent' of each other (in linear materials), this encoding can happen on practically every single wavelength (or frequency)

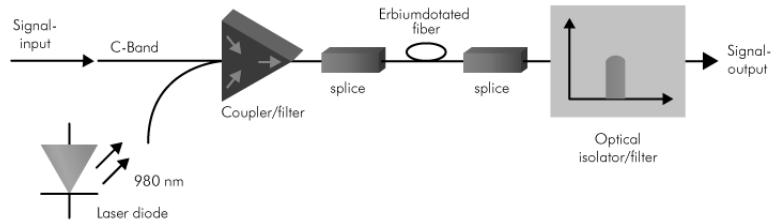


Figure 2.5: Schematic depiction of Erbium-Doped-Fiber-Amplifier (EDFA), pumped by a 980 laser diode. C-band refers to one of the optical communication bands, more specifically from 1530 to 1565 nm).<sup>1</sup>

within the operational spectrum of the communication link. The latter is dictated by the loss spectrum of the fiber and the emission and detection range of sources and detectors respectively. This method is called 'wavelength division multiplexing' (WDM). Alternatives are time-domain multiplexing (TDM) or code-division multiplexing (CDM) (see Saleh *et al.* for more information). Combining (muxing) and splitting (demuxing) the datastreams on the different wavelengths is done using dispersive structures such as optical gratings (such as AWGs (arrayed waveguide-gratings), see Figure 2.6c). Transferring information (from a so-called 'carrier' to a 'target') between different frequencies is not trivial as they do not interact in linear dielectric materials such as the silica fiber or silicon waveguides (see further) used to guide the light. More advanced non-linear approaches are required that use the phase -or intensity modulations induced by a carrier wave to transfer the information to a target wavelength. This concept of 'wavelength conversion' is further explored in chapter 6 where the use of QDs as the functional non-linear material is considered.

## 2.2.2 Integrated Photonics for Optical Interconnects

Following the success of miniaturization of electrical circuits using the CMOS (Complementary Metal-Oxide-Semiconductor) platform, major efforts are now put in combining several photonic functionalities such as generating, routing, detecting and manipulating light on a single photonic integrated circuit (PIC). Apart from size reduction and cost-effective fabrication due to batch production, miniaturization offers advantages in terms of alignment tolerance (no bulk optical components), energy consumption (due to increased light-matter interaction) and functionality (*e.g.* lab-on-a-chip). The material system of choice to do this is that of silicon-on-insulator (SOI): silicon structures built on a buried oxide ( $\text{SiO}_2$ ) layer (see Figure

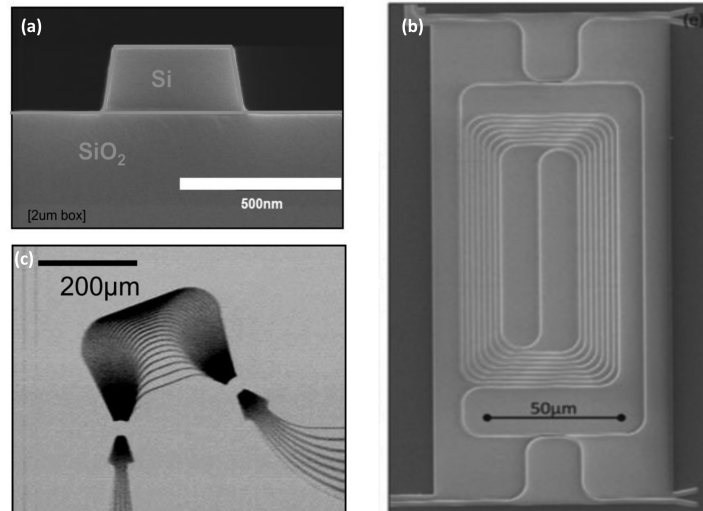


Figure 2.6: Passive devices in SOI (Silicon-On-Insulator) (a) SEM image of a cross-section of a single mode waveguide in silicon. The width of the waveguide is 450 nm and the height is 220 nm. Picture from Dumon *et al.*<sup>6</sup>, (b) large folded-spiral ring<sup>7</sup> and (c) arrayed waveguide grating (AWG)<sup>6</sup>.

2.6a). A group IV semiconductor with indirect band gap, silicon has the advantage of being earth-abundant and processable within a standard CMOS fab, *e.g.* the extensive facilities available worldwide for nano-electronic fabrication, such as *IMEC* in Leuven (Belgium). Moreover, the high refractive index ( $n_{Si}=3.48$ ) contrast with its native oxide silica ( $SiO_x, n=1.45$ ) and air ( $n=1$ ) allows for tight confinement of light leading to dense miniaturization and micrometre scale devices with versatile optical functionalities (*e.g.* a sensor or fiber-to-the-home (FTTH) module) on a millimetre square PIC-chip.

**Short-Range Interconnects** The use of light as information carrier is not only limited to long haul datacommunication but starts to see its uses in datatransfer between racks, boards and even discrete chips in server infrastructures. The optical computer is not for anytime soon, but using light to transfer data between the cores of a microprocessor is a very realistic goal for the near future. As it is subject to completely different physics than electronics, optics could offer advantages over electronics both in interconnect

density, bandwidth and clocking (timing)<sup>8</sup>.

The requirements for long-haul datacommunication are of course different than those imposed by short-range optical interconnects for *e.g.* intra-rack or even between different processor cores on-chip. Losses can be higher but the footprint of devices should be small as to be compatible with dense integration on- or intra-chip. There is a bandwidth-length trade-off for communication links<sup>8</sup> such that when the bandwidth increases, the length at which optical interconnects perform better compared to electrical interconnects decreases. Rack-to-rack optical interconnects are already being deployed in data centers since a few years and even board-to-board optical interconnects, with lengths in the order of a few tens of centimeters found their way to the market. Research is now focusing on realizing optical interconnects for chip-to-chip and on-chip communication. To set targets for optical interconnects on this short distance scale we need to distinguish between the inter-chip and intra-chip optical interconnects, where typical lengths are in the order of several centimeters for inter-chip and below 2 centimeter for intra-chip interconnects. For inter-chip optical interconnects the energy efficiency should be  $< 1\text{pJ/bit}$  to be competitive with the current state-of-the-art electrical interconnects and even around  $100\text{fJ/bit}$  in order to offer an energy advantage over the latter<sup>8;9</sup>. Note that this is the energy of the total interconnect, including the source, modulator and receiver. The latter implies that the energy cost of each individual component should be substantially less than the presumed targets of  $0.1 - 1\text{pJ/bit}$ .

**Integrated Light Source** Although silicon is excellent at passive functionalities such as guiding and filtering of light, more advanced functionalities such as light generation (for lasers and LEDs) or non-linear wavelength conversion are difficult to achieve in silicon because of its indirect band gap and centrosymmetric crystal lattice respectively. Especially the efficient light source is a bottleneck for silicon integrated photonics, to the extent that it is called 'the holy grail' of silicon photonics. The answer seems simple: combine other materials (*e.g.* direct gap III-V semiconductors) with silicon to provide these extra features, so-called *hybridization* of silicon.

The main routes towards on-chip lasing are:

- *Direct hetero-epitaxy of direct gap III-V semiconductors on silicon*<sup>10-12</sup>  
Due to the large lattice mismatch of III-V materials with silicon, it is very difficult to grown high quality epitaxial layers directly on silicon as dislocations are easily formed under the high lattice stress. These dislocations are detrimental for the optical performance as they often

trap carriers or scatter and absorb light. To avoid these dislocations buffer layers or epitaxial overgrowth (ELOG) are used.

- *Bonding of III-V dies*<sup>13;14</sup>  
Bonding of III-V on silicon is possible through either molecular bonding or adhesive bonding using an optically thin and transparent adhesive where the die should be sufficiently close to the silicon platform to enable evanescent coupling.
- *Strained silicon*<sup>15</sup> and *germanium (Ge) on silicon*. Straining silicon could remedy its indirect band gap and the use of (strained) germanium is possible due to the limited lattice mismatch with silicon (4.7%).
- *Rare-earth*<sup>16</sup> *doped glasses and silicon nanocrystals*<sup>17</sup> Although compatible with silicon through epitaxial growth, the material cross sections for optical gain or other non-linear effects are small, making them difficult to use in short-range interconnects requiring small device footprints with low energy consumption.
- *Novel (nano-)materials (organics, perovskites, QDs)*<sup>18</sup> Combining these new types of materials with silicon is a rather new field of research. Organic materials (small molecule, polymers, ...) offer rather interesting non-linear properties but are limited in terms of stability and wavelength range (typically in the visible part of the spectrum). Perovskites are a new class of solution-processable inorganic semiconductors which have shown great potential in photovoltaics.
- *Raman laser*<sup>19</sup> Although not strictly a 'laser', the amplification of light through a Raman scattering process can be used to amplify light on a chip. The light intensities required to do so are quite high (due to the second order nature of the effect) and the required device lengths are large as well.

All the epitaxial approaches (direct growth, Ge-on-Si, bonding) require expensive vacuum epitaxy and are difficult to scale up. Having a solution-processable, cheap and stable laser dye that operates in the near-infrared region is the ultimate goal.

### 2.3 Colloidal Quantum Dots

What's in a name, colloidal nanocrystals (or quantum dots, QDs) are nanometer sized pieces of crystalline semiconductor (or metal) consisting of a few hundred to a few thousand atoms each (see Figure 2.7). Their surface is typically passivated by long chain organic molecules (so-called ligands) such as fatty acids, which keeps them stable in a colloidal dispersion. They

find themselves between the worlds of atoms and molecules on one side and the 'bulk' on the other side. Their electronic and optical properties depend strongly on size and shape as opposed to the 'bulk' regime where only composition (*i.e.* the type of atoms forming the crystal) is of importance. These additional degrees of freedom combined with new quantum effects emergent from their nanoscale nature, allow for unique properties<sup>20</sup> such as exceptionally strong superparamagnetism in magnetic nanocrystals, localised plasmon resonances in metallic particles and, of our great interest, a size-dependent optical band gap for tunable light emission and absorption. The nanoscale size regime allows us to discover new and exciting phenomena not observed in higher dimensional systems. They are at the forefront of quantum confinement and are referred to as zero-dimensional, *i.e.* no dimension is left macroscopic which is still the case for e.g. 2D quantum wells or 1D quantum wires.

Nanocrystals or 'colloidal quantum dots' are, as opposed to their epitaxially grown counterparts, obtained through wet chemical synthesis (see further). This solution based approach offers scalability and cost-effective deposition (e.g. spincoating or dropcasting instead of vacuum epitaxy) on practically any kind of substrate allowing quite straightforward device fabrication and integration on existing technology platforms (e.g. silicon photonics). Owing to their inorganic nature, they offer increased thermal stability under extreme conditions, making them ideal for high end applications such as lasers or solar cells.

### 2.3.1 Historical Perspective

About 30 years ago in the former Soviet Union, Aleksey Ekimov, experimenting with semiconductor-doped glasses<sup>21</sup>, was seeking the help of theoretician Alexander Efros<sup>22</sup> to explain apparent color changes of what appeared to be tiny particles of variable sizes. At the same time, Louis Brus<sup>23</sup> in the United States and Arnim Henglein<sup>24</sup> in Germany discovered striking color changes of semiconductor nanoparticles grown as aqueous colloidal suspensions, giving rise to the simple description of the band gap dependence on size that is now familiar to students as the Brus formula<sup>25</sup>. These publications are widely considered to be the inception of what is now the flourishing field of colloidal quantum dots (QDs).

QDs are now used in bio-imaging applications for a number of years, and researchers have recently developed methods to stop the fluorescence from quantum dots switching on and off in a random manner<sup>26</sup> (a problem known as 'blinking'). More recently, the optical properties of colloidal quantum dots have been exploited in lighting to improve energy efficiency

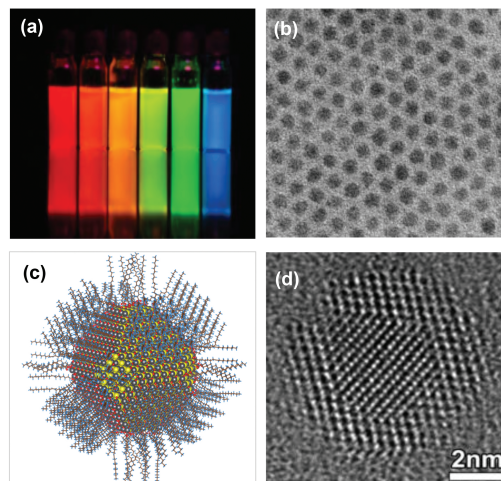


Figure 2.7: Overview of QD properties: (a) Size series of CdTe QDs under UV excitation, (b) TEM image of QDs showing size monodispersity, (c) depiction of individual QD with inorganic core and organic ligand shell and (d) HR-TEM image of a core/shell PbTe/CdTe particle showing the stacking of individual atoms building up the QD.

and make the output of light-emitting diodes seem more natural, and applications in digital cameras, displays and solar power are also being investigated.

Indeed, as of 2013 Sony and 3M, working with technology from QDvision and Nanosys respectively, have brought display products to the market with higher color purity and energy efficiency than the competitive OLED technology. Due to the inorganic nature of the nanocrystals, longer lifetimes and reduced packaging costs are claimed.

A challenge facing all companies (QDvision (Sony), Philips, Nexdot, Nanosys(3M), ...) building products with colloidal quantum dots is to move away from toxic materials such as cadmium. Although this seems problematic, recent EU RoHS directive changes allowed Sony to build a first quantum dot enabled 4K - display with high color purity and energy efficiency, based on Cd-compounds in low amounts embedded in a glass sealed resin. In a different approach Dow Electronic licensed technology from Nanoco to produce Cd-free nanocrystals based on more earth-abundant copper and zinc compounds for future display applications.

Up till now, only the linear optical properties (light absorption and/or emission) of nanocrystals have seen the first signs of commercialization. A new field, explored in this thesis, is the integration of colloidal quantum dots with micro - and nanophotonic chips exploiting the ultrafast non-linear behaviour offered by nanocrystals, pushing the application scope to new and unexpected directions.

### 2.3.2 Synthesis and Deposition

In this section we will discuss the wet chemical synthesis of colloidal QDs and their film formation.

**Wet chemical synthesis** The synthesis of colloidal nanocrystals has experienced enormous development since the introduction of the hot injection (HI) synthesis developed by Murray, Norris and Bawendi in 1993<sup>27</sup>. Moving away from the doped glasses and electrochemical techniques used in the 1980s to ligand-stabilized colloidal dispersions in organic solvents offered new degrees of freedom in designing nanocrystal size, shape, composition and surface functionalization.

The HI synthesis is based on the pyrolysis of metal-organic precursors in hot solvents (50°C-360°C) in the presence of coordinating species. Based on the concept put forward by La Mer and Dinegar, the method relies on the formation of a supersaturated reaction mixture by rapid generation of solution-phase monomers out of the injected precursors. The su-

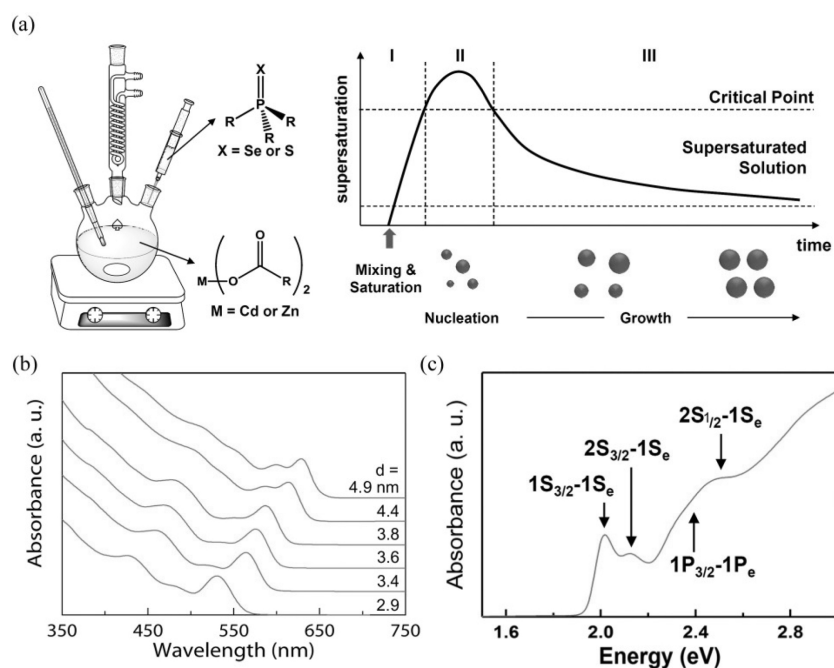


Figure 2.8: Hot injection synthesis of CdX (X=S,Se) nanocrystals (a) A schematic of a hot injection setup typically used in our labs and a scheme illustrating the La Mer and Dinegar model for nucleation and growth of monodisperse particles (b) Typical absorption spectra of CdX nanocrystals and (c) a labeling of the electronic transition involved.

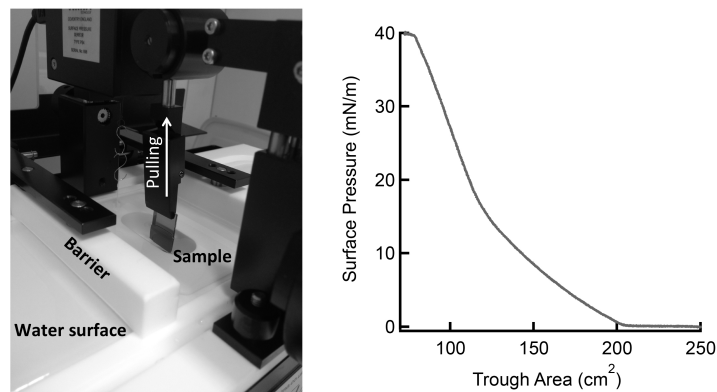


Figure 2.9: Overview of Langmuir-Blodgett deposition trough with water surface, barriers to compress the layer and a vertical sample pull to transfer the formed layer from the water surface to a sample. On the right, a typical isotherm is shown, relating surface pressure to the compressed area (or trough area).

persaturation initiates a homogeneous nucleation and growth process that results in monodisperse (nanocrystal) colloids capped with organic ligands. A schematic of such a typical hot-injection process and setup is shown in Figure 2.8.

**Layer formation with Langmuir-Blodgett** Since QDs are obtained through a wet chemical synthesis, they are available for film formation as a colloidal dispersion, typically in apolar solvents (although transfer to *e.g.* water is possible in some cases). As such, typical solution based deposition methods are applicable: dropcasting, spincoating, doctor blading, inkjet printing. Although these techniques allow for uniform deposition over large areas, it remains difficult to control the morphology of the formed layers. For example, the formation of a perfect hexagonally packed monolayer using spincoating is near-impossible to achieve. Other methods such as evaporation-induced self-assembly or template patterning allow more control, yet the most controllable technique is that of the Langmuir-Blodgett (or Langmuir-Schaeffer<sup>28</sup>) deposition. The latter is compatible with any type of substrate (from hydrophobic silicon to hydrophilic silica), a large variety of QDs. Moreover, it allows for the formation of perfectly packed layers with monolayer precision on 2D and 3D substrates (*e.g.* photonic structures such as micron sized waveguides and resonators).

The basis of Langmuir-Blodgett is the contrast between the organic hydrophobic ligand shell of the QDs and a water surface. When a drop of QD dispersion in a volatile solvent is put on such a surface, the QDs spread to form islands of close packed (*e.g.* hexagonally or cubic) nanocrystals. Subsequently, these islands are compressed into a continuous single monolayer on the water surface. This layer is transferred to a desired substrate using dipping or pulling of the substrate respectively on or through the layer. The change in surface pressure (so-called isotherm) associated with the transition from a water-air interface to a water-QDs-air interface is monitored during film formation to monitor the deposition in-situ. Figure 2.9 (left) shows a schematic of a typical Langmuir-Blodgett deposition routine and (right) a typical surface pressure isotherm.

### 2.3.3 Linear Optical Properties

In this section, a limited overview of the linear optical properties of colloidal QDs is presented as a short guideline for future chapters. A more thorough review is provided by Hens *et al.*<sup>2</sup>.

#### 2.3.3.1 Size Dependence of the Optical Band Gap

Historically, the first description of quantum confinement can be traced back to the work of Brus<sup>25</sup> who considered a spherical semiconductor nanocrystal of radius  $R$  occupied by an electron and hole of opposite charge, interacting through a screened Coulomb interaction. Using infinite potential well boundary conditions, he obtained the famous 'Brus' formula for the (optical) band gap:

$$E_g = E_{g,bulk} + \frac{\hbar^2 \pi^2}{8m_r R^2} - \frac{1.786e^2}{\epsilon R} \quad (2.10)$$

Here,  $m_r$  is the reduced electron mass and  $\epsilon$  is the dielectric constant of the semiconductor material. Although only an approximate solution to the full many-body Schrödinger equation, it captures the essence of quantum confinement: size reduction leads to an energy increase of the material band gap over its bulk value or equivalently a blueshift in the optical absorption and emission spectra. This teaches us two important lessons: we have to start with a bulk material that has a sufficiently low energy gap to reach *e.g.* the near-infrared part of the optical spectrum and size control (*i.e.* the chemical synthesis) is crucial to obtain narrow emission and absorption features.

The strong correlation between size and optical band gap, allows to construct 'sizing curves', typically linking the first exciton transition  $E_1$  (in

eV) to the particle diameter  $d$  (in nm) (obtained from TEM analysis). As an example, Moreels *et al.*<sup>29</sup> determined the sizing curve for PbS (with the size  $d$  in nm and the energy  $E$  in eV):

$$E_1 = 0.41 + \frac{1}{0.0252d^2 + 0.283d} \quad (2.11)$$

Using these sizing curves, a simple absorption experiment can give quick feedback on both size and size dispersion.

### 2.3.3.2 Maxwell-Garnett Effective Medium

To describe the optical properties of a composite medium such as a colloidal dispersion of nanocrystals in an organic solvent, effective medium theories can be used. In such a theory, the geometry and (complex) dielectric constants of the dielectric inclusions ('d') and surrounding host material ('h'),  $\epsilon_d$  and  $\epsilon_h$  respectively, are replaced by effective quantities such as the 'effective dielectric constant'  $\epsilon_{eff}$ . A common approach is that of the Maxwell-Garnett (MG) mixing rule where the quantum dot (QD) volume fraction  $f$  (the volume occupied by QDs per unit of sample volume) is used:

$$\epsilon_{eff} = \frac{1 + 2\beta f}{1 - \beta f} \epsilon_d \quad (2.12)$$

with  $\beta = \frac{3\epsilon_h}{\epsilon_d + 2\epsilon_h}$ . The MG approach is based on the assumption that point dipoles in a homogeneous host medium do not interact (*e.g.* through near- or far-field electrostatic interactions). Note that when nanocrystals are put in thin films, their interparticle spacing is on the order of their own size (3-10 nm) which makes the applicability of MG questionable as will be discussed in chapter 7 of this thesis. MG is thus valid in the limit for  $f \rightarrow 0$ , resulting in a more elegant form for the real (Re) and imaginary (Im) parts of  $\epsilon_{eff}$ :

$$\epsilon_{eff,Re} = \epsilon_{h,Re} \quad (2.13)$$

$$\epsilon_{eff,Im} = \frac{9\epsilon_h^2}{|\epsilon_d + 2\epsilon_h|^2} \times f\epsilon_{d,Im} = |f_{LF}|^2 f\epsilon_{d,Im} \quad (2.14)$$

Equation 2.14 introduces the concept of screening by means of the quantity  $f_{LF}$ . Indeed, when a dielectric inclusion (*e.g.* a nanocrystal with  $\epsilon_d$ ) in a 'host' (*e.g.* organic solvent with  $\epsilon_h$ ) is subject to an external electric field, the field inside the particle (called the 'local field') is reduced or

'screened' relative to the external field by a factor  $f_{LF}$ , the so-called local field factor:

$$f_{LF} = \frac{E_{local}}{E_{external}} = \frac{3\epsilon_h}{\epsilon_d + 2\epsilon_h} \quad (2.15)$$

In general,  $f_{LF} \ll 1$  because  $\epsilon_{h,Re} \ll \epsilon_{d,Re}$ , which confirms the idea of 'screening', *i.e.* reducing the local field relative to the external driving field (see Figure 2.10).

### 2.3.3.3 Intrinsic Absorption Coefficient

The intrinsic absorption coefficient  $\mu_i$  is a convenient quantity to describe light absorption by a dilute dispersion of nanocrystals.<sup>2</sup> It relates the volume fraction  $f$  of the QDs in dispersion, *i.e.*, the ratio between the volume of the QDs and the total volume of the dispersion, to the absorbance  $A$  of that dispersion. With  $L$  the length of the optical path through the sample, it is defined as:

$$\mu_i = \frac{A \ln(10)}{fL} \quad (2.16)$$

In the case of point-like and dispersed particles at low volume fractions, the Maxwell-Garnett effective medium theory provides an expression for  $\mu_i$  that only depends on the dielectric function of the particles ( $\tilde{\epsilon} = \epsilon_R + i\epsilon_I$ ) and the surroundings ( $\epsilon_s$ ):

$$\mu_i = \frac{2\pi}{\lambda n_s} |f_{LF}|^2 \epsilon_I \quad (2.17)$$

For core/shell particles, this expression complicates due to additional screening of the shell material. Still a compact expression was derived by Neeves *et al.*<sup>30</sup>, where the indices  $c$  and  $sh$  refer to core and shell, respectively:

$$\begin{aligned} \mu_i &= \frac{2\pi}{\lambda n_s} \text{Im}(3\epsilon_s \beta) \\ \text{with } \beta &= \left( \frac{\epsilon_{sh}\epsilon_a - \epsilon_s\epsilon_b}{\epsilon_{sh}\epsilon_a + 2\epsilon_s\epsilon_b} \right) \\ \epsilon_a &= \epsilon_c \left( 3 - 2 \frac{V_{sh}}{V_{QD}} \right) + 2\epsilon_{sh} \frac{V_{sh}}{V_{QD}} \\ \epsilon_b &= \epsilon_c \frac{V_{sh}}{V_{QD}} + \epsilon_{sh} \left( 3 - \frac{V_{sh}}{V_{QD}} \right) \end{aligned} \quad (2.18)$$

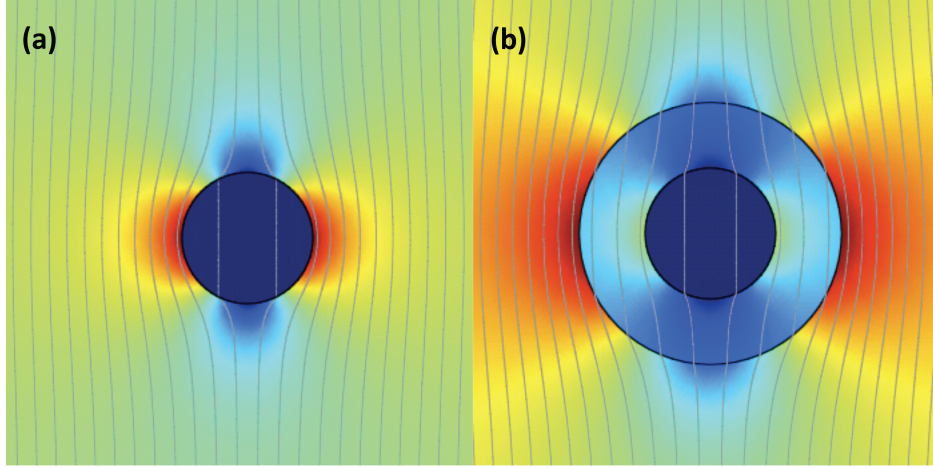


Figure 2.10: Normalized electric field strength for a core (a) and core/shell (b) particle showing the 'local field' effect: the electric field outside the particle is larger than inside due to dielectric screening (see text).

For various core QDs, it has been demonstrated that the experimental intrinsic absorption coefficient at short wavelengths coincides with a theoretical value obtained using the dielectric function of the bulk material in eq. 2.17. This observation indicates that states at higher energy are bulk-like and not subject to quantum confinement. As such, the concentration of QDs in a dispersion  $[QD]$  (typically in  $\mu\text{M}$ ) can be determined from the absorbance  $A$  at high energies (*e.g.* 400 nm for PbX compounds) using the Beer-Lambert law and  $\mu_i$ :

$$[QD] = \frac{A}{\epsilon L} = \frac{A \ln(10)}{\mu_i N_A V_{QD} L} \quad (2.19)$$

Here,  $\epsilon$  is the molar extinction coefficient (in  $\mu\text{M}^{-1}\text{cm}^{-1}$ ),  $N_A$  is Avogadro's constant and  $V_{QD}$  is the volume of the quantum dot. The latter can be calculated from the size  $d$  obtained through TEM analysis or through combining the absorption spectrum with a known sizing curve.

#### 2.3.3.4 Oscillator Strength

When an electromagnetic wave of angular frequency  $\omega$  is incident on a QD, it distorts the negative electron cloud surrounding the positive cores of the atoms in the lattice. As the electrons are bound to these positive cores, they could be considered as springs with natural resonance frequencies. As such,

an electron could be seen as an 'oscillator'. Since a QD is finite in size, these resonance frequencies are different from their bulk counterparts. Only when the frequency of the incident wave matches the natural oscillation frequencies of the electrons, can energy from the electromagnetic wave be dissipated into the electronic system (so-called 'absorption').

To quantify the relative strengths of all these vibrations (so-called 'modes') we associate a 'strength' to each mode, the 'oscillator strength'  $f_{if}$ . Through Fermi's golden rule, quantum mechanics provides us with a very useful expression for this quantity:

$$f_{if} = \frac{2m_e\omega}{3\hbar} |\langle\psi_f|\mathbf{r}|\psi_i\rangle|^2 \quad (2.20)$$

where  $m_e$  is the electron mass,  $\omega$  is the frequency of the oscillation and  $|\langle\psi_f|\mathbf{r}|\psi_i\rangle|$  is the position matrix element. Note that with the above expression, one could theoretically calculate the oscillator strength, *e.g.* through tight-binding. The oscillator strength can also be interpreted as the weighted power a quantum oscillator absorbs compared to the classical oscillator at the same angular frequency.

Experimentally, the oscillator strength is accessible through either the radiative lifetime or the absorbance of an electronic transition. We will elaborate further on this in chapter 3, where we apply this principle to PbS/CdS core/shell QDs.

### 2.3.3.5 Photoluminescence of QDs

When an electron-hole pair is created by absorption of a high energy photon, the electron and hole quickly cool to the band edges where they form an exciton, a quasi-particle formed by the mutual attraction of electron and hole leading to a energy state different than the sum of the individual particle energies. The energy difference is mainly Coulomb attraction, but also exchange interactions could play a role depending on the type of semiconductor (see also section 4.2.1). The excitonic state is of course no equilibrium state for the crystal, meaning the exciton will either dissipate its energy radiatively (through spontaneous photon emission or stimulated emission, *e.g.* in a laser) or non-radiatively. In a regime where no multi-excitons are present, the main non-radiative mechanism is so-called carrier trapping where electrons or holes are 'trapped' in defect states, either on the surface (note that QDs have a large surface to volume ratio) through *e.g.* dangling bonds (unpassivated surface atoms forming mid-gap energy states) or in the bulk of the QD through lattice defects. As such, increasing the emission yield (so-called Quantum Yield (QY)) typically relies on increasing the crystallinity of the QDs and/or passivation of the surface. The

latter is typically done through formation of core/shell QDs where an outer high band gap shell material protects the core states from the surface dangling bonds. For multi-exciton states, non-radiative Auger recombination (see section 2.3.4) is the main exciton loss mechanism.

**Stokes shift** When analyzing the absorption and emission spectra of QDs, one observation immediately jumps to the eye: the band edge exciton emission is red-shifted away from the exciton absorption. This shift is called the Stokes shift in analogy to the same effect observed in molecular systems. Different mechanisms lie at the origin of this shift such as exciton-phonon coupling (*i.e.* the emission of a photon is accompanied by the emission/absorption of a phonon), re-absorption (shorter wavelengths get reabsorbed by the larger particles in an inhomogeneously broadened ensemble), fine structure splitting (e.g. states with no oscillator strength in absorption can become dominant in emission when they are populated through thermal redistribution), ... Other mechanisms such as trap state emission and excited state relaxation will be discussed in chapter 7.

**Linewidth** The linewidth of an optical transition is well known to be inversely proportional to the coherence time (limited by *e.g.* radiative recombination or phonon scattering) of the radiative state. In a solid crystal, with increasing temperature, elastic and inelastic scattering of the exciton by optical or acoustic phonons reduces the exciton lifetime and thus broadens the excitonic line. These contributions are called homogeneous as they apply to every QD in an ensemble in the same way. The (optical) band gap of the QDs is very sensitive to their size (see the Brus formula) due to the quantum confinement effect) and as such, small variations on the size give rise to variations in the emission energy leading to so-called inhomogeneous broadening. One important goal of nanocrystal synthesis is therefore to limit the size dispersion leading to this broadening by making particles as monodisperse as possible, down to the atomic monolayer.

### 2.3.4 Ultrafast Properties

The previous section dealt with the linear optical properties of QDs, *i.e.* the response of QDs to external electromagnetic fields when the QD is in its ground state, meaning no excitations (*e.g.* excitons or single carriers) are present and all system responses are linear in the incident field. In this section, we will consider the fascinating field of ultrafast non-linear QD physics where non-linearities arise from the presence of these excitations.

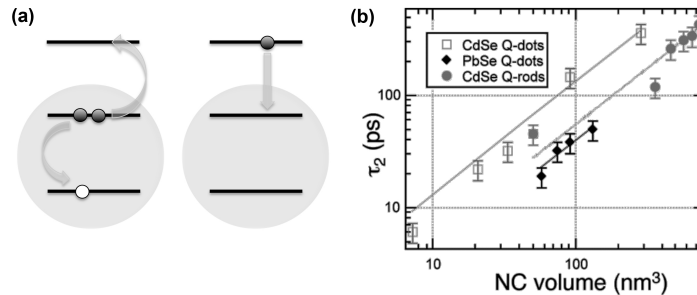


Figure 2.11: Auger Recombination (a) a negative trion (exciton and excess electron) showing Auger recombination where the exciton energy is used to excite the excess electron to a higher energy state through a non-radiative impact ionization process and (b) bi-exciton Auger lifetime as function of QD volume for CdSe (rods and dots) and PbSe dots showing a universal volume scaling law for Auger recombination in type I, core-only nanostructures.

#### 2.3.4.1 Auger Recombination

Auger recombination is a non-radiative recombination mechanism in which carriers transfer both energy and momentum in a collision process<sup>3</sup>. In (bulk) semiconductors, Auger recombination is a three particle event (see Figure 7.16a) where a bound electron-hole pair or 'exciton' collides with a free carrier (either an electron or a hole). Instead of emitting a photon, the exciton transfers its energy to the free carrier which is then promoted to a higher energy state, only to quickly dissipate its excess energy through collision with lattice vibrations (phonons) (so-called 'cooling', see further). As such, the energy of the exciton is lost as heat instead of photon emission, hence the term 'non-radiative'.

As it is a three - particle process, the rate of Auger recombination scales with the cube of the carrier density, making it only relevant in applications of high carrier density for bulk systems (*e.g.* as an efficiency roll-off mechanism in solid-state lasers). In QDs however, carriers are much closer together with much higher interaction strengths. As such, Auger recombination is strongly enhanced leading to bi-exciton (a double exciton) lifetimes  $\tau_{XX}$  in the order of a few hundreds of picoseconds, much faster than the typical single exciton radiative lifetimes (tens of nanoseconds to microseconds). It was shown by Klimov *et al.*<sup>32-34</sup> that the Auger rate ( $\Gamma_A = 1/\tau_A$ ) scales inversely with the volume of the QD ( $V_{QD}$ ), rather independent of

the composition, bulk band structure or shape:  $\Gamma_A = C_A \times V_{QD}^{-1}$ .

Auger is a limiting process in applications that require high carrier densities such as lasers, but can be used to speed up certain processes such as light modulation. As such, manipulation of the process is vital and was perfected during the last decade<sup>35</sup>, largely based on the theoretical work of Efros and Cragg<sup>36</sup>: smoothing of the interfacial potential between core and surrounding (or between core and shell) reduces the Auger rate and breaks the volume scaling law.

The Auger rate is described by Fermi's golden rule:

$$\Gamma_A = \frac{2\pi}{\hbar} |M_{if}|^2 \rho(E_f) \quad (2.21)$$

The matrix element is given by:

$$M_{if} = \langle \Psi_i | V(\mathbf{r}_1 - \mathbf{r}_2) | \Psi_f \rangle \quad (2.22)$$

Considering the case of 2 electrons and 1 hole (a 'negative trion'), the initial state wavefunction  $\Psi_i$  is the product of two electron ground state wavefunctions and the wavefunction  $\Psi_f$  is the product of a ground state hole wavefunction and a high energy electron wavefunction.

The potential energy operator  $V$  is the Coulomb potential between two electrons (at positions  $\mathbf{r}_1$  and  $\mathbf{r}_2$ ):

$$V(\mathbf{r}_1 - \mathbf{r}_2) = \frac{e^2}{4\pi\epsilon_0 |\mathbf{r}_1 - \mathbf{r}_2|} \quad (2.23)$$

#### 2.3.4.2 Statistics of Multi-Excitons

The creation of multi-exciton states through either single or multi-photon absorption can be described using a Poisson ensemble model<sup>33</sup>. This approach is valid in the limit of  $\tau_{pulse} \ll \tau_{Auger}$ , *i.e.* for short excitation pulses. The probability  $P(N)$  to have  $N$  excitations in a nanocrystal (with absorption cross section  $\sigma$ ) that is part of an ensemble subject to a photon fluence  $J_{ph}$  (photons/unit of area) per pulse, is given by a Poissonian distribution around a mean value  $\langle N \rangle = J_{ph} \times \sigma$ :

$$P(N) = \frac{e^{-\langle N \rangle} \times \langle N \rangle^N}{N!} \quad (2.24)$$

Note that the exciton number (or multiplicity)  $N$  is different from the mean exciton number  $\langle N \rangle$ . The scaling of the Auger rate with exciton multiplicity  $N$  depends on the symmetry of the excitons involved<sup>37</sup>. In the case of symmetric 1S-excitons (obtained in highly degenerate QDs, such

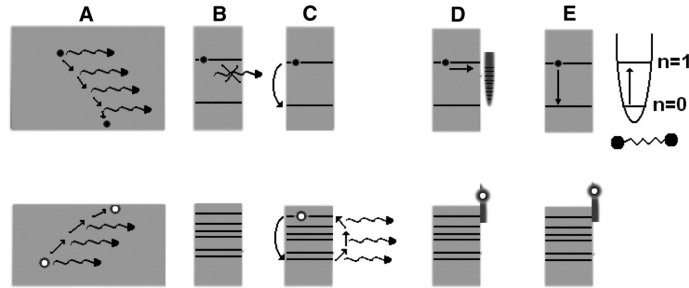


Figure 2.12: Cooling models (a) Sequential phonon emission in bulk (b) Phonon bottleneck due to large energy differences between electronic states in QDs (c) Energy transfer from electron to hole which relaxes through a denser hole state manifold (d) Trap assisted cooling and (e) Energy transfer to surface ligand vibrations. Taken from Pandey et al.<sup>38</sup>

as Pb-chalcogenides ( $g=8$ )) a statistical scaling of the Auger rate  $k_{A,N}$  is found:

$$k_{A,N} \sim N^2(N - 1) \quad (2.25)$$

Deviations from this statistical law are found for semiconductors with low degeneracies and high  $N$ , *e.g.* CdS(e) ( $g=2$ ) where multi-X states are composed of states with different symmetries (S,P).

### 2.3.4.3 Carrier Cooling

When high energy photons are incident on a semiconductor with a small band gap (*e.g.* the lead-chalcogenide based nanocrystals in the near-infrared), a so-called 'hot' electron-hole pair is created. This 'hot' pair has not yet condensed into an exciton with substantial binding energy and can as such be described as an individual excitation (electron or hole) that will dissipate its excess kinetic energy through a variety of processes until it reaches the lowest energy level (LUMO or HOMO, *i.e.* the band edges of the semiconductor). A variety of mechanisms were put forward to explain carrier cooling in nanocrystals, as the situation is slightly different from their bulk semiconductor counterparts. In bulk, carriers with excess kinetic energy bounce around the crystal lattice through frequent collisions with the vibrating (ionic) lattice. Indeed, at room temperature many vibrations are active (so-called phonons, the quantized version of these oscillations) and inelastically scatter (*i.e.* transfer the carrier energy to lattice vibrations which can be seen as a heat reservoir) the carriers until they have dissipated all their kinetic energy.

This requires the coupling of carriers to these phonons, a process called 'electron-phonon coupling'. Coupling to a single phonon might be efficient, but the probability to dissipate energy through multi-phonon collision is very unlikely and is described as a higher order quantum mechanical process of small probability. In bulk, a continuous density of states makes carrier cooling through multi-phonon coupling unnecessary as there are always electron states within one phonon energy available. This is not the case for QDs where, due to the zero-dimensional nature, quantum confinement creates discrete energy levels separated by multiple phonon energies. Typically these spacings are in the range of 100 - 300 meV as opposed to single phonon energies of 10 - 30 meV. The largest energy jump is usually required at the 1P-1S transition, which is deemed the rate-limiting step for hot carriers to reach the band edge. A phonon cooling bottleneck was predicted but was never found experimentally: cooling rates in the order of a few per ps are found, similar to bulk. Many models were put forward to elucidate this apparent paradox (see Figure 2.12), including energy transfer to vibrating ligand molecules on the nearby surface, Auger assisted cooling through a much denser manifold of hole states, etc. ...

Although very relevant for a variety of applications where quick population of the band edge states is required, the relaxation of hot carriers is distinctly different than that of 1P electrons or holes. As we will show in this work, the truly hot excitons relevant for MEG and hot carrier solar cells are at energies where the cooling is still dictated by the underlying bulk cooling mechanism, *i.e.* optical phonon scattering.

#### 2.3.4.4 Multiple Exciton Generation

When a single high energy photon strikes a semiconductor material, it creates by definition a single hot electron-hole pair. Usually, this hot pair dissipates its excess kinetic energy (see previous subsection) very quickly through phonon collisions to reach the band edge where it is at equilibrium. However, the hot carriers carry substantial kinetic energy, allowing them to undergo impact ionization processes very similar to Auger ionization. For example, a hot electron high up in the conduction band can impact a relaxed carrier in the valence band, exciting it over the band gap and thus creating an additional electron-hole pair. The result is a negative trion (electron-hole pair and an extra electron). This process is known as carrier multiplication (indeed, a single hot electron creates more mobile carriers) and is referred to as multiple exciton generation in case of QDs (as the electron-hole pairs condense quickly into excitonic states).

The potential of MEG to enhance the conversion efficiency of solar cells

is obvious: in a regular solar cell, the excess energy of hot excitons created by high energy photons (*e.g.* UV light) is lost as heat (phonons). In a MEG enabled solar cell, part of this excess energy is recovered as an additional exciton is created, leading to an increase in the overall conversion efficiency of the device. Recent reports show that the MEG mechanism can indeed boost the efficiency of solar cells<sup>39</sup> although even the most efficient single junction MEG cell could (in theory) only lead to about 10% increase in overall conversion efficiency compared to the Shockley-Queisser limit<sup>40</sup>.

From an energy conservation point of view, the minimal energy of the exciton to undergo MEG and create a biexciton is  $2E_g$ , where  $E_g$  is the band gap energy of the semiconductor. However, as the energy is distributed over both electron and hole, a more detailed analysis including momentum conservation yields a MEG threshold  $E_{th}$  (for isotropic bands)<sup>40</sup>:

$$E_{th} = \left(2 + \frac{m_e}{m_h}\right)E_g \quad (2.26)$$

Much effort was put into finding QD materials with low MEG thresholds and high efficiency. The former is determined mostly by the band structure, *i.e.* the effective masses of electron and hole. The latter is mainly determined by the competition between MEG and carrier cooling. Indeed, when the MEG rate  $k_{II}$  is slower than carrier cooling  $k_{cool}$  (*e.g.* through phonon emission), no impact ionization will take place reducing the MEG efficiency  $\eta$ :

$$\eta = \frac{k_{II}}{k_{II} + k_{cool}} \quad (2.27)$$

From this, it is quite clear that efficient MEG materials should show high anisotropy in effective masses and slow hot carrier cooling. In this work, we will explore this hot carrier cooling in commonly used lead-chalcogenide PbX (X=S,Se) QDs and encounter a material (HgTe) that shows such high anisotropy in effective mass.

### 2.3.4.5 Intraband Absorption

Intraband absorption, where a photon is absorbed by a conduction band electron (or valence band hole) is not possible in bulk semiconductors without the mediation of a phonon. Indeed, Figure 2.13 shows that momentum conservation requires a phonon to be emitted or absorbed. The process in bulk is called *free carrier absorption* (FCA) and is highly temperature sensitive and quite inefficient as it is a so-called second-order absorption process. Momentum conservation is no longer strictly required in nanoscale

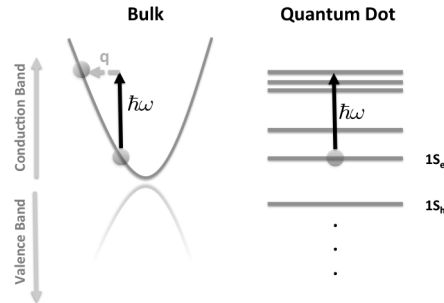


Figure 2.13: Comparison between free carrier absorption in bulk (left) and intraband absorption in QDs (right) of an electron in the conduction band.

systems where the translational symmetry (which lies at the origin of the momentum conservation rule) is broken by reducing the dimensions of the crystal (*e.g.* in 3 dimensions for QDs or 1 dimension for quantum wells). In these specific cases, absorption of a photon by a 'free' carrier (*e.g.* an electron in the quantized conduction band levels) becomes allowed and attains significant oscillator strength (see table 2.1 and Figure 2.15). As such, intraband absorption is a particular example of nanoscale materials outperforming their bulk counterparts.

Focusing on PbSe and PbSe/CdSe QDs, we have shown that intraband absorption<sup>41</sup> takes place with high strength (ca. 10% of the direct interband transitions) and validated the obtained oscillator strengths of the transitions by tight-binding modeling.

### 2.3.5 Colloidal Nanocrystal Lasers

Ever since the demonstration of optical gain with CdSe nanocrystals by Klimov *et al.* in 2000<sup>42</sup>, the idea of using colloidal nanocrystals as a solution processable gain medium has attracted much attention. Indeed, having an inorganic solution processable dye with the benefits of reduced dimensionality (tunability, reduced temperature sensitivity, ...) would greatly reduce the fabrication cost and complexity of current epitaxially built laser diodes and open up new avenues such as diodes built on flexible substrates. In this section, we will discuss the problems of using QDs as gain medium and the routes forward to solving these issues.

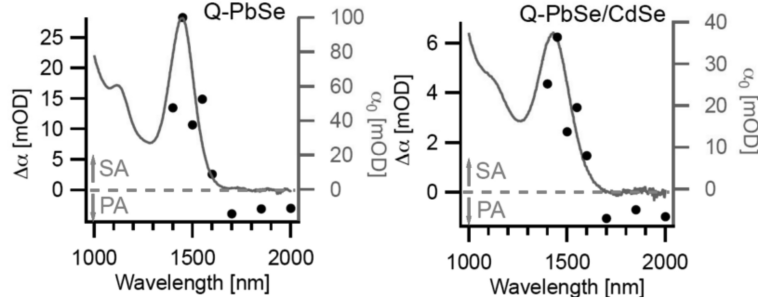


Figure 2.14: Inverted differential absorbance of PbSe and PbSe/CdSe QDs from De Geyter *et al.*<sup>41</sup> plotted together with the linear absorbance spectrum. Note that in this case negative values indicate an increase of absorption upon photo-excitation, so-called photo-induced absorption (PA). We can clearly see this PA extending to energies well below the band gap energy indicating that not spectral shifts, but a new absorption mechanism (intraband absorption) is observed.

PbSe			
$\lambda_{probe}$	$\alpha_{PA,ex}$	$\mu_{PA,ex}$	$\sigma_{PA,ex}$
[nm]	[cm <sup>-1</sup> ]	[cm <sup>-1</sup> ]	[cm <sup>2</sup> ]
1700	$1.54 \cdot 10^{-3}$	187	$9.2 \cdot 10^{-18}$
1850	$1.29 \cdot 10^{-3}$	157	$7.7 \cdot 10^{-18}$
2000	$1.57 \cdot 10^{-3}$	190	$9.7 \cdot 10^{-18}$
PbSe/CdSe			
$\lambda_{probe}$	$\alpha_{PA,ex}$	$\mu_{PA,ex}$	$\sigma_{PA,ex}$
[nm]	[cm <sup>-1</sup> ]	[cm <sup>-1</sup> ]	[cm <sup>2</sup> ]
1700	$8.6 \cdot 10^{-4}$	92	$8.0 \cdot 10^{-18}$
1850	$5.6 \cdot 10^{-4}$	82	$7.1 \cdot 10^{-18}$
2000	$8.6 \cdot 10^{-4}$	92	$8.0 \cdot 10^{-18}$

Table 2.1: Photoinduced absorbance for a population of one exciton in the initial state  $\alpha_{PA,ex}$ , derived from a Poissonian fit, together with the absorption coefficient for PbSe and PbSe/CdSe QDs<sup>41</sup>.

**Problems with QD gain media** The problems with using QD as optical gain medium can be put in 3 categories:

- *Short Gain Lifetime* Optical gain in any medium requires a steady population inversion of the electronic transition involved in order for stimulated emission to dominate over absorption. Due to the large degeneracy ( $g > 2$ ) of the band edge, multiple excitons (X) are required to sustain optical gain. In QDs however, these multi-X states vanish on a 10-100 ps timescale due to ultrafast non-radiative Auger recombination. This becomes especially dramatic for Pb-chalcogenide compounds with an 8-fold degenerate band edge, requiring 4 excitons (per dot) for optical gain. The lifetime of such a quadra-exciton is only in the order of 1-5 ps, a timescale in direct competition with carrier cooling which makes it difficult to reach the 4X population in the first place, let alone sustain it.
- *High Carrier Density* Due to their small size (2-10 nm), even a single excitation represents an enormous carrier density ( $10^{19} - 10^{21} \text{ cm}^{-3}$ ) as compared to bulk standards (which already consider  $10^{18} \text{ cm}^{-3}$  as 'degenerate doping'<sup>3</sup>). This requires high carrier density and combined with the short gain lifetime, high threshold current densities, which may compromise the stability of the QDs. Also, host materials (such as conductive oxides, organics or silicon for integration on SOI) show non-linear and unwanted behaviour (free carrier absorption, thermal degradation, ...) at these high pumping intensities.
- *Loss mechanisms* Apart from the inherent problems (high carrier density and short gain lifetime), quantum dots show also the classical problems faced in any semiconductor: carrier trapping and photo-induced absorption due to free carriers. These loss mechanisms are in direct competition with the band edge inversion condition resulting in higher thresholds for optical gain to compensate the losses.

**Improvement** Electronic wavefunction engineering has led to dramatic increases in performance of colloidal QD gain media over the past 10-15 years. All efforts focus on reducing the influence of Auger recombination on the gain performance, either through suppression of the Auger rate or through modifying the effective band edge degeneracy to enable single-X gain and thus alleviating the associated fast multi-X Auger recombination.

- *Auger Suppression through Interfacial Alloying*  
As was put forward by Cragg and Efros<sup>36</sup>, Auger recombination in zero-dimensional quantum dots arises from the abrupt interface be-

tween inorganic core and the surrounding medium (ligands, solution). Smoothing this interface could in theory lead to giant suppression of the Auger rate. Although easy in theory, this 'interfacial alloying' took some years to perfect and was achieved in core/shell CdSe/CdS nanocrystals grown by a SILAR (Sequential Ion Layer Adsorption Reaction) method where the nanocrystals are grown under high temperature conditions for several tens of hours. A CdSeS alloyed layer is formed, indeed reducing the Auger rate below the volume - law (see Figure 2.15) to the regime of 10-100 ns, comparable to the single exciton radiative lifetime. New approaches developed by Aubert *et al.*<sup>43</sup> at Ghent University allow for much faster synthesis (so-called 'flash' synthesis) of these core/shell structures. It is worthwhile to note that a similar mechanism (combined with a larger volume in general) is found in epitaxial quantum dots where a smooth interface between the dot and the wetting layers is always present<sup>44</sup>.

- *Single Exciton Optical Gain*

Reducing Auger through interfacial alloying is a direct approach to increase the gain lifetime. An indirect approach is found in the work of Klimov *et al.*<sup>45</sup> where the effective degeneracy of the band edge is reduced, *i.e.* the threshold for optical gain to dominate over absorption is reduced to  $\approx 2/3$  instead of  $\approx 1$ . The basic idea is that carrier-carrier repulsion in type II core/shell QDs such as CdS/ZnSe (where similar charges are located in the same spatial region, *e.g.* both electrons in the core and both holes in the shell) can shift the biexciton (XX) absorption away from the single exciton level, making the QDs transparent for photons at the XX-energy, even at a single exciton occupation. Although subtle at first glance, this implies that a regime for  $\langle N \rangle$  exists (between  $2/3$  and  $1$ ) where no short lived multi-X are required to achieve optical gain. This can be observed in the ASE (Amplified Spontaneous Emission) spectra shown in Figure 2.16, where ASE develops at the single X position, rather than at the XX-position, as is the case for type I nanocrystals. The impact of this approach could be even more dramatic for systems with higher degeneracy such as Pb-chalcogenides where the threshold exciton density per QD could be  $8/9$  instead of  $4$ . Although a promising route, no actual lasers have been shown with this technique, in large due to the instability of the QDs due to exposure of the hole to the surface.

Although the routes mentioned above lead to significantly reduced lasing thresholds, the associated carrier densities required are still too high to achieve electrically pumped lasing due to the bi-exciton nature of lasing in this case. Indeed, a back-of-the-envelope calculation teaches us that

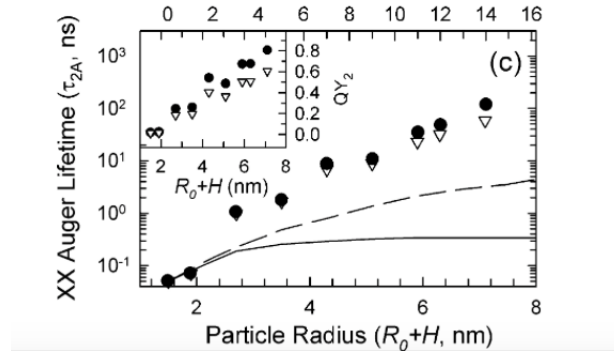


Figure 2.15: Biexciton Auger lifetime of CdSe/CdS core/shell QDs as function of the shell thickness (for a given core size of 3 nm)<sup>35</sup>. The solid line indicates the 'effective' exciton volume scaling (based on the spreading of electrons and holes, instead of the physical volume) and the dashed line corrects for the reduced electron-hole overlap. A deviation is found for increasing shell thickness, indicating a new mechanism (*i.e.* the alloying of the interface) is active.

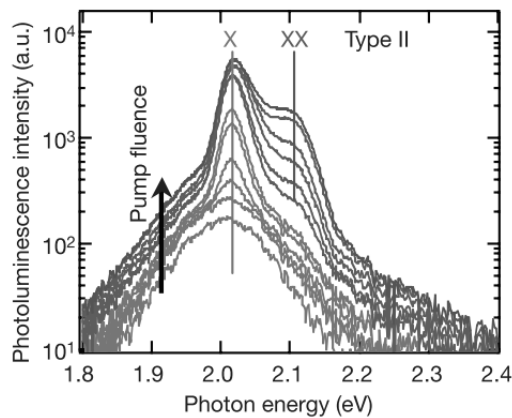


Figure 2.16: Pump-intensity-dependent photoluminescence spectra of a type-II QD sample show the development of a narrow ASE (Amplified Spontaneous Emission) peak near the centre of the single-exciton emission band. The second ASE band, which develops at higher fluences, is located near the XX photoluminescence feature. Taken from Klimov *et al.*<sup>45</sup>

even for a 10 ns bi-exciton Auger lifetime, the required current density to supply to every nanocrystal in a close packed film ( $\approx 10^{12}$  dots per  $\text{cm}^2$ ) these 2 excitons per dot (on average) would still require several  $\text{A}/\text{cm}^2$  to operate. These current levels are at least one order of magnitude too high to sustain in existing electrical schemes (*e.g.* hybrid OLEDs (organic light emitting diode) or inorganic approaches<sup>46</sup>). Moreover, no improvement in near-infrared emitting nanocrystals has been achieved so-far.

In this thesis, we will explore two novel concepts for nanocrystal optical gain: 3 level systems (mediated by an empty mid-gap state) and excited state relaxation. These approaches result in similar gain lifetimes (10-100 ns) as the alloyed approach but require significantly less (up to 3 orders of magnitude) carriers per dot (on average), making electrically pumped lasers feasible for the first time.

## 2.4 Ultrafast Spectroscopy

Many processes in solid state materials happen on timescales beyond our everyday perception. Electrons scattering of lattice defects, absorption and emission of photons, ... all happen on timescales in the order of a few 10 – 100 femtoseconds to several microseconds. To sample these events, a 'probe' is necessary which is temporally shorter than the event to be monitored. For example, non-radiative recombination of electron-hole pairs in nanocrystals happen on a picosecond timescale. To accurately follow the dynamics of this process, a probe is required that is sub-picosecond in duration. A second requirement is that the probe can interact with the material under study. This could be done by monitoring changes in carrier density through a current-voltage measurement, but in order to follow sub-picosecond dynamics electronics falls short and one has to turn to ultrashort optical pulses.

### 2.4.1 White Light Pump-Probe Spectroscopy

At the Technical University of Delft, a white light pump-probe spectroscopy setup is employed offering such ultrashort laser pulses. In practice, samples are pumped using 180 femtosecond pulses at 350 - 1500 nm), created from the 1028 nm fundamental (Pharos SP, 6W, Light Conversion) through non-linear frequency mixing in an OPA (Orpheus, Light Conversion) (see Figures 2.17 and 2.18). Probe pulses were generated in a thin sapphire crystal using 10% of the 1028 nm fundamental of the regenerative amplifier. The pulses were delayed relative to the probe using a delay stage with maximum delay of 2.5 ns (Helios Spectrometer, Ultrafast Systems). The

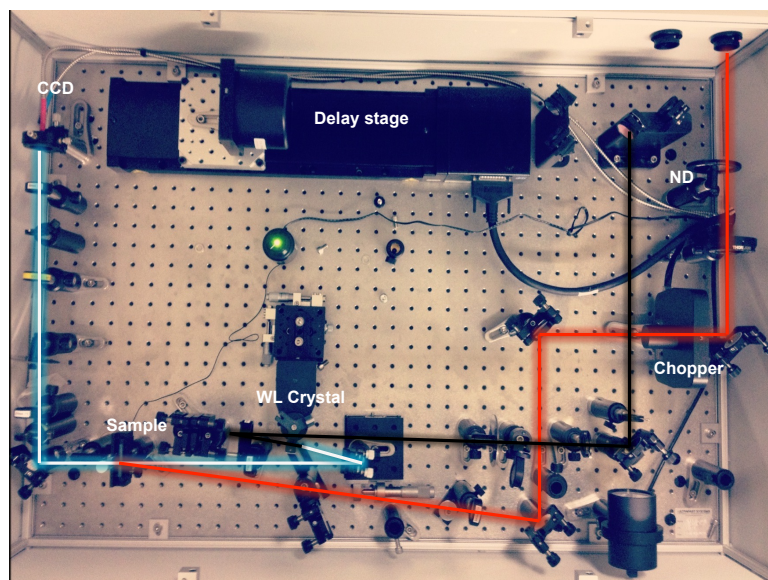


Figure 2.17: Picture of white light transient absorption setup showing the pump beam path (red line) and the white light path (white line). The latter is created by pumping a 1–3 mm sapphire crystal (WL Crystal) with the 1028 nm fundamental of the oscillator (black line) which is sent through a delay stage. The pump and white light probe are crossed at the sample position. After passing through the cuvette, the white light probe is collected with a fiber-to-CCD configuration.

probe spectrum covers the VIS-NIR window from 450 nm up to 1620 nm. Extension to the UV (down to 340 nm) is possible using a thin calcium fluoride crystal instead of the sapphire crystal.

#### 2.4.2 Spectroscopy of Colloidal Quantum Dots

**Basic analysis** QDs are typically dispersed in a transparent solvent (hexane, tetrachloroethylene) to achieve optical densities of ca. 0.1 at the first exciton transition. Samples are sometimes stirred during the measurements to avoid photocharging<sup>47;48</sup>. The average number of absorbed photons (or photo-generated excitons) at time zero  $\langle N \rangle$  was calculated as:  $\langle N \rangle = J_{ph} \sigma_p \times \frac{1 - 10^{-A_{0,p}}}{A_{0,p}}$ . Here  $J_{ph}$  is the photon flux in photons/cm<sup>2</sup> at the pump wavelength,  $\sigma_p$  is the absorption cross-section of the nanocrystals at the pump wavelength and  $A_{0,p}$  is the sample absorbance at that same wavelength. The additional factor corrects for variation of the pump flu-

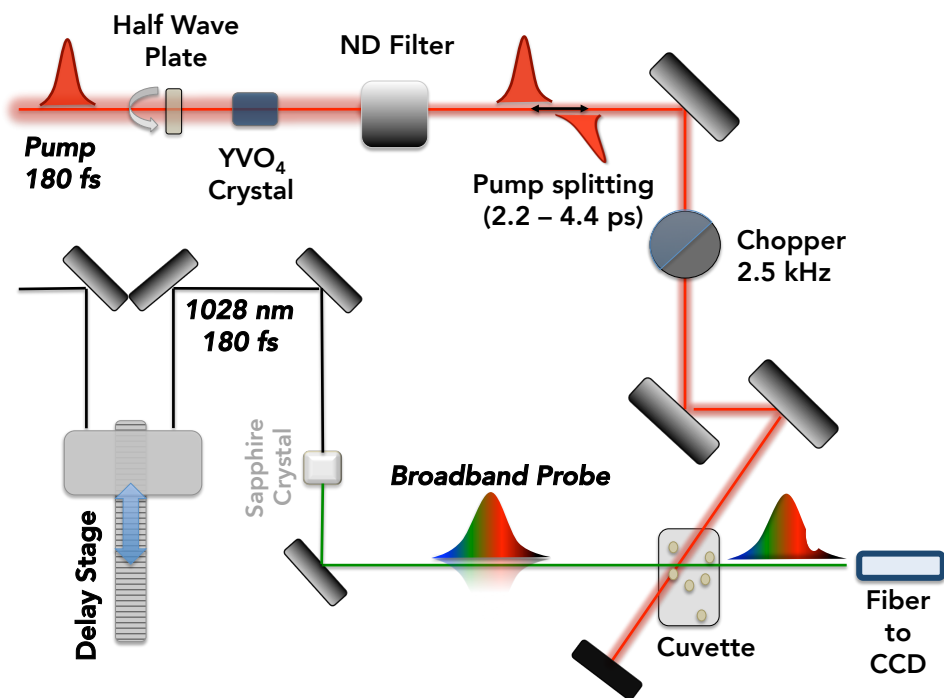


Figure 2.18: Schematic of ultrafast setup shown in Figure 2.17.

ence along the pump beam path length. The cross section  $\sigma_p$  is determined starting from  $\mu_{i,400}$ <sup>2</sup>:

$$\sigma_p = V_{QD} \times \mu_{i,400} \times \frac{A_{0,p}}{A_{0,400}} \quad (2.28)$$

where  $V_{QD}$  is the volume of the quantum dot. The photon flux  $J_{ph}$  is determined by measuring the pulse energy and the pulse pump area using a power meter and a beam profiler, respectively.

**The Differential Absorbance** The absorbance of a QD ensemble will be changed due to the presence of the created excitations by the pump pulse in three distinct ways:

- *Interband Bleach* Carriers occupying discrete energy levels block out optical transitions between those levels, reducing the absorption of the optical transitions between them. Indeed, as only a finite number of carriers is present in the valence band levels and only a finite number of empty states is available in the conduction band, an incident photon can only be absorbed and promote an electron from the valence to the conduction band if these levels are free. As such, electron-hole pairs created by a short pump pulse 'bleach', *i.e.* reduce the absorbance.
- *Intraband Absorption* Absorption of photons can promote electrons from the valence to the conduction band (CB), but in a similar manner promote electrons/holes within the CB/VB to higher quantized levels within that same CB/VB, *e.g.* from 1S to 1P. This process is called intraband absorption, as it occurs within the same band (conduction or valence). Note that it can only occur when a sample is excited, *i.e.* when one or more electron-hole pairs are created. Also unpaired free charges such as single electrons in the conduction band or in surface states (created either through photo-excitation or doping) can give rise to intraband absorption.
- *Spectral Shifts* The presence of (unbalanced) electrical charges in a nanoscale structure implies the presence of electric fields. The latter can shift the linear absorption spectrum (so-called Stark effect) either to higher or lower energy depending on the details of the nanostructure (mostly type of carrier localization, *i.e.* type I or II).

Smaller effects can also play a role, such as changes of oscillator strength of optical transition or changes in reflectance due to a change of refractive index upon photo-excitation (since extinction includes both absorption and

reflection). The non-linear absorbance  $A$  (a sample dependent quantity) is related to the non-linear absorption coefficient  $\alpha$  through the cuvette length  $L$ :  $A = \alpha \times L$ .

Considering the simple case of a  $g$ -fold degenerate valence and conduction band edge and an exciton population below  $g$ , we can write the non-linear absorption coefficient  $\alpha$ <sup>33</sup> as:

$$\alpha(E) = \sum_{N=0}^g P(N) \left\{ \left(1 - \frac{N}{g}\right) \alpha_0(E - (N-1) \times \delta E) - \frac{N/g}{\alpha_0} (E - N \times \delta E) \right\} \quad (2.29)$$

Here  $P(N)$  is the probability to have  $N$  excitons in a nanocrystal ensemble with average occupation  $\langle N \rangle$  according to the poissonian statistic (see previous section). The energy shift  $\delta E$  can be either positive or negative.

We can include intraband absorption (IB) in this expression:

$$\alpha_{IB}(E) = \sum_{N=0}^g N \times P(N) \alpha_{IB}(E) \quad (2.30)$$

Note that the experimentally accesible linear absorbance  $A_0$  and differential absorbance  $\Delta A$  combine (by definition of the latter) to the actual non-linear absorbance:  $A = \Delta A + A_0$ , the absorbance of the sample after photo-excitation. The case where  $A = 0$  is often called 'transparency' (stimulated emission and absorption compensate each other) and when  $A < 0$ , stimulated emission dominates over absorption and a situation of net optical gain is achieved.

### 2.4.3 Pump-Repump Experiments

Due to limitations in the repetition rate of the pump laser and amplifier, the femtosecond pulses are always separated by  $400 \mu s$ , *i.e.* the inverse of the repetition rate (2500 Hz). As such, the response of the QDs to optical pulses is actually an 'isolated' response: the sample is excited for 180 femtoseconds, after which the system is left unaltered for  $400 \mu s$ , a timescale much larger than the typical recombination dynamics of single or multi-excitons. To study how the system refreshes itself after short excitation events, we developed a pump-repump-probe setup, where the initial 180 femtosecond pump pulse is linearly polarized under a desired angle using a half-wave plate and sent through a combination of birefringent yttrium-orthovanadate ( $YVO_4$ ) crystals to create a cascade of 2 pulses separated by the group delay  $\delta t$  imposed through the difference in refractive indices  $|n_o - n_e|$  between ordinary (o) and extra-ordinary (e) waves<sup>1;49</sup>:

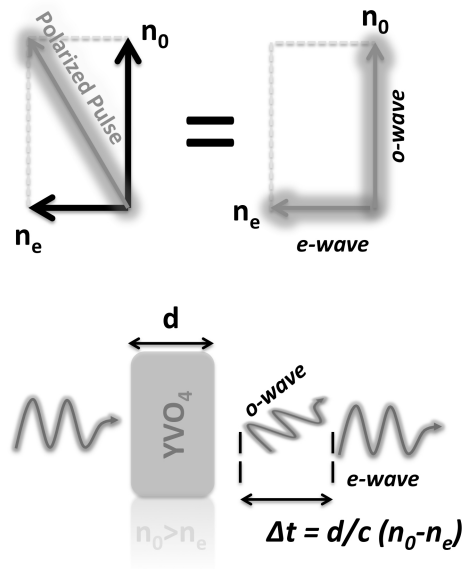


Figure 2.19: Schematic of pulse splitting concept based on the birefringence of an  $YVO_4$  crystal: 2 refractive indices exist for different polarizations of light, so-called ordinary ('o') and extra-ordinary ('e').

$$\delta t = \frac{d}{c} \times |n_o - n_e| \quad (2.31)$$

The pulses are then sent through a depolarizer to avoid any polarization induced effects on the measurement. No substantial pulse broadening is observed after propagation through the crystal sequence. To create 4 pulses an additional rotation through a second half-wave plate is used in combination with a 3rd bi-refracting crystal. This allows us to create 4 pulses separated by 2.2 ps without the need for additional delay stages or optics. The pulses are characterized by looking at the coherent Raman signal at 580 nm induced by the solvent (hexane). Although this type of autocorrelation should be interpreted with caution<sup>1</sup>, no substantial pulse broadening was observed, nor temporally, nor spectrally.

## References

- [1] Saleh, B.; Teich, M. *Fundamentals of Photonics*, 2nd ed.; John Wiley & Sons Ltd., 2007.

- 
- [2] Hens, Z.; Moreels, I. Light Absorption by Colloidal Semiconductor Quantum Dots. *Journal of Materials Chemistry* **2012**, *22*, 10406–10415.
- [3] Kittel, C. *Introduction to Solid State Physics*, 8th ed.; John Wiley & Sons Ltd., 2005.
- [4] Basu, P. *Theory of Optical Processes in Semiconductors: Bulk and Microstructures*; Oxford University Press, 2003.
- [5] Digonnet, M. *Rare-Earth Doped Fiber Lasers and Amplifiers*; Marcel Dekker, inc., 2001.
- [6] Dumon, P. Ph.D. thesis, Ghent University, 2007.
- [7] Bogaerts, W.; De Heyn, P.; Van Vaerenbergh, T.; De Vos, K.; Kumar Selvaraja, S.; Claes, T.; Dumon, P.; Bienstman, P.; Van Thourhout, D.; Baets, R. Silicon microring resonators. *Laser & Photonics Reviews* **2012**, *6*, 47–73.
- [8] Miller, D. Device Requirements for Optical Interconnects to Silicon Chips. *Proceedings of the IEEE* **2009**, *97*, 1166–1185.
- [9] Vlasov, Y. A. Silicon CMOS-Integrated Nano-Photonics for Computer and Data Communications Beyond 100G. *IEEE Communications Magazine* **2012**, 67–72.
- [10] Chen, R.; Tran, T.-t. D.; Ng, K. W.; Ko, W. S.; Chuang, L. C.; Sedgwick, F. G.; Chang-Hasnain, C. Nanolasers grown on silicon. *Nature Photonics* **2011**, *5*, 170–175.
- [11] Justice, J.; Bower, C.; Meitl, M.; Mooney, M. B.; Gubbins, M. A.; Corbett, B. Wafer-scale integration of group III–V lasers on silicon using transfer printing of epitaxial layers **2012**, *6*, 2–6.
- [12] Wang, Z.; Tian, B.; Paladugu, M.; Pantouvaki, M.; Le Thomas, N.; Merckling, C.; Guo, W.; Dekoster, J.; Van Campenhout, J.; Absil, P.; Van Thourhout, D. Polytypic InP nanolaser monolithically integrated on (001) silicon. *Nano letters* **2013**, *13*, 5063–9.
- [13] Chung, I.-S.; Mork, J. Silicon-photonics light source realized by III-V/Si-grating-mirror laser. *Applied Physics Letters* **2010**, *97*, 151113.

- [14] Campenhout, J. V.; Regreny, P.; Seassal, C.; Thourhout, D. V.; Verstuyft, S.; Cioccio, L. D.; Fedeli, J.; Lagahe, C.; Baets, R. Electrically pumped InP-based microdisk lasers integrated with a nanophotonic silicon-on-insulator waveguide circuit. *Optics Express* **2007**, *15*, 6744–6749.
- [15] Jacobsen, R. S.; Andersen, K. N.; Borel, P. I.; Fage-Pedersen, J.; Frandsen, L. H.; Hansen, O.; Kristensen, M.; Lavrinenko, A. V.; Moulin, G.; Ou, H.; Peucheret, C.; Zsigri, B.; Bjarklev, A. Strained silicon as a new electro-optic material. *Nature* **2006**, *441*, 199–202.
- [16] Daldosso, N.; Navarro-Urrios, D.; Pitanti, a.; Gourbilleau, F.; Rizk, R.; Pavesi, L. Erbium and Silicon nanocrystals for light amplification. *LEOS 2007 - IEEE Lasers and Electro-Optics Society Annual Meeting Conference Proceedings* **2007**, *2008*, 933–934.
- [17] Pavesi, L.; Dal Negro, L.; Mazzoleni, C.; Franzò, G.; Priolo, F. Optical gain in silicon nanocrystals. *Nature* **2000**, *408*, 440–4.
- [18] Hoogland, S.; Sukhovatkin, V.; Howard, I.; Cauchi, S.; Levina, L.; Sargent, E. H. A solution-processed 1.53  $\mu\text{m}$  quantum dot laser with temperature-invariant emission wavelength. *Optics express* **2006**, *14*, 3273–81.
- [19] Rong, H.; Jones, R.; Ansheng, L.; Cohen, O.; Hak, D.; Fang, A.; Paniccia, M. A continuous-wave Raman silicon laser. *Nature* **2005**, *433*, 717–9.
- [20] Talapin, D. V.; Lee, J.-S.; Kovalenko, M. V.; Shevchenko, E. V. Prospects of colloidal nanocrystals for electronic and optoelectronic applications. *Chemical reviews* **2010**, *110*, 389–458.
- [21] Ekimov, A.; Efros, A.; Onushchenko, A. Quantum size effect in semiconductor microcrystals. *Solid State Communications* **1982**, *56*, 921–924.
- [22] Efros, A. Interband Absorption of Light in a Semiconductor Sphere. *Sov. Phys. Semicond.* **1982**, *16*, 772–775.
- [23] Rossetti, R.; Nakahara, S.; L.E., B. Quantum Size Effects in the Redox Potentials, Resonance Raman Spectra and Electronic Spectra of Cadmium Sulfide Crystallites in Aqueous Solution. *J. Chem. Phys.* **1983**, *79*, 1086–1088.

- [24] Weller, H.; Koch, U.; Gutierrez, M.; Henglein, A. Absorption and Fluorescence of Extremely Small Zinc Sulfide Particles. *Ber. Bunsen-Ges. Phys. Chem.* **1984**, *88*, 649–656.
- [25] Brus, L. Electron-Electron and Electron-Hole Interactions in Small Semiconductor Crystallites - The Size Dependence of the Lowest Excited Electronic State. *J. Chem. Phys.* **1984**, *80*, 4403–4409.
- [26] Wang, X.; Ren, X.; Kahen, K.; Hahn, M. a.; Rajeswaran, M.; Maccagnano-Zacher, S.; Silcox, J.; Cragg, G. E.; Efros, A. L.; Krauss, T. D. Non-Blinking Semiconductor Nanocrystals. *Nature* **2009**, *459*, 686–9.
- [27] Murray, C.; Norris, J.; Bawendi, M. Synthesis and Characterization of Nearly Monodisperse CdE (E=Sulfur, Selenium, Tellurium) Semiconductor Nanocrystallites. *Journal of the American Chemical Society* **1993**, *115*, 8706–8715.
- [28] Lambert, K.; Dendooven, J.; Detavernier, C.; Hens, Z. Embedding Quantum Dot Monolayers in Alumina Using Atomic Layer Deposition. *Chemistry of Materials* **2010**, *23*, 126 – 128.
- [29] Moreels, I.; Lambert, K.; Smeets, D.; De Muynck, D.; Nollet, T.; Martins, J. C.; Vanhaecke, F.; Vantomme, A.; Delerue, C.; Allan, G.; Hens, Z. Size-dependent optical properties of colloidal PbS quantum dots. *ACS Nano* **2009**, *3*, 3023–30.
- [30] Neeves, A. E.; Birnboim, M. H. Composite structures for the enhancement of nonlinear-optical susceptibility. *J. Opt. Soc. Am. B* **1989**, *6*, 787–796.
- [31] Hooker, S.; Webb, C. *Laser Physics*, 1st ed.; Oxford University Press, 2010.
- [32] Klimov, V. I. Mechanisms for photogeneration and recombination of multiexcitons in semiconductor nanocrystals: implications for lasing and solar energy conversion. *The Journal of Physical Chemistry B* **2006**, *110*, 16827–45.
- [33] *Nanocrystal Quantum Dots*, 2nd ed.; Klimov, V., Ed.; CRC Press, 2010.
- [34] Robel, I.; Gresback, R.; Kortshagen, U.; Schaller, R.; Klimov, V. Universal Size-Dependent Trend in Auger Recombination in Direct-Gap

- and Indirect-Gap Semiconductor Nanocrystals. *Physical Review Letters* **2009**, *102*, 177404.
- [35] García-Santamaría, F.; Brovelli, S.; Viswanatha, R.; Hollingsworth, J. A.; Htoon, H.; Crooker, S. A.; Klimov, V. I. Breakdown of Volume Scaling in Auger Recombination in CdSe / CdS Heteronanocrystals : The Role of the Core-Shell Interface. *Nano Letters* **2011**.
- [36] Cragg, G. E.; Efros, A. L. Suppression of Auger processes in confined structures. *Nano letters* **2010**, *10*, 313–7.
- [37] Klimov, V.; McGuire, J.; Schaller, R.; Rupasov, V. Scaling of multiexciton lifetimes in semiconductor nanocrystals. *Physical Review B* **2008**, *77*, 1–12.
- [38] Pandey, A.; Guyot-Sionnest, P. Slow electron cooling in colloidal quantum dots. *Science (New York, N.Y.)* **2008**, *322*, 929–32.
- [39] Semonin, O. E.; Luther, J. M.; Choi, S.; Chen, H.-Y.; Gao, J.; Nozik, A. J.; Beard, M. C. Peak external photocurrent quantum efficiency exceeding 100% via MEG in a quantum dot solar cell. *Science (New York, N.Y.)* **2011**, *334*, 1530–3.
- [40] Beard, M. C.; Midgett, A. G.; Hanna, M. C.; Luther, J. M.; Hughes, B. K.; Nozik, A. J. Comparing multiple exciton generation in quantum dots to impact ionization in bulk semiconductors: implications for enhancement of solar energy conversion. *Nano letters* **2010**, *10*, 3019–27.
- [41] De Geyter, B.; Houtepen, A. J.; Carrillo, S.; Geiregat, P.; Gao, Y.; Ten Cate, S.; Schins, J. M.; Van Thourhout, D.; Delerue, C.; Siebbeles, L. D.; Hens, Z. Broadband and Picosecond Intraband Absorption in Lead-Based Colloidal Quantum Dots. *ACS Nano* **2012**, *6*, 6067–6074.
- [42] Klimov, V. I.; Mikhailovsky, A.; Xu, S.; Malko, A.; Hollingsworth, J.; Leatherdale, C.; Eisler, H.-J.; Bawendi, M. Optical Gain and Stimulated Emission in Nanocrystal Quantum Dots. *Science* **2000**, *290*, 314–317.
- [43] Cirillo, M.; Aubert, T.; Gomes Pinto Fernandes, R. F.; Van Deun, R.; Emplit, P.; Biermann, A.; Lange, H.; Thomsen, C.; Brainis, E.; Hens, Z. 'Flash' synthesis of CdSe/CdS core–shell quantum dots. *CHEMISTRY OF MATERIALS* **2014**, *26*, 1154–1160.

- 
- [44] Ledentsov, N. N.; Ustinov, V. M.; Shchukin, V. a.; Kopev, P. S.; Alferov, Z. I.; Bimberg, D. Quantum dot heterostructures: Fabrication, properties, lasers (Review). *Semiconductors* **1998**, *32*, 343–365.
- [45] Klimov, V. I.; Ivanov, S. a.; Nanda, J.; Achermann, M.; Bezel, I.; McGuire, J. a.; Piryatinski, A. Single-exciton optical gain in semiconductor nanocrystals. *Nature* **2007**, *447*, 441–6.
- [46] Caruge, J. M.; Halpert, J. E.; Wood, V.; Bulović, V.; Bawendi, M. G. Colloidal quantum-dot light-emitting diodes with metal-oxide charge transport layers. *Nature Photonics* **2008**, *2*, 247–250.
- [47] McGuire, J. a.; Sykora, M.; Robel, I.; Padilha, L. a.; Joo, J.; Pietryga, J. M.; Klimov, V. I. Spectroscopic signatures of photocharging due to hot-carrier transfer in solutions of semiconductor nanocrystals under low-intensity ultraviolet excitation. *ACS nano* **2010**, *4*, 6087–97.
- [48] Midgett, A. G.; Hillhouse, H. W.; Hughes, B. K.; Nozik, A. J.; Beard, M. C. Flowing versus Static Conditions for Measuring Multiple Exciton Generation in PbSe Quantum Dots. *Population (English Edition)* **2010**.
- [49] Zhou, S.; Ouzounov, D.; Li, H.; Bazarov, I.; Dunham, B.; Sinclair, C.; Wise, F. W. Efficient temporal shaping of ultrashort pulses with birefringent crystals. *Applied optics* **2007**, *46*, 8488–92.



# 3

## Advanced Optical Properties of Lead-Chalcogenide Heterostructures

### 3.1 PbS/CdS Core/shell Nanocrystals

#### 3.1.1 Introduction

In the field of colloidal semiconductor nanocrystals or quantum dots, overcoating initial core nanocrystals with an inorganic shell has become a standard procedure to passivate trap states at the nanocrystal surface.<sup>1;2</sup> When the band gap of the shell material contains the bands of the core – so-called type 1 band alignment – this leads to a heterostructure where the electron and hole states are confined in the core, decoupling them from possible trap states at the shell surface.<sup>3;4</sup> Especially the growth of ZnS shells has been widely used in this way to increase the photoluminescence quantum yield of various nanocrystals, including II-VI quantum dots such as CdSe,<sup>5–7</sup> CdTe<sup>8</sup> and ZnSe<sup>9;10</sup> and I-III-VI<sub>2</sub> quantum dots such as CuInS<sub>2</sub><sup>11–13</sup> and CuGaS<sub>2</sub>.<sup>14</sup> Apart from slowing down non-radiative recombination pathways, it was found that shell growth also provides a means to modify the optical properties of the original core quantum dots.<sup>15;16</sup> In particular, the spatial separation of the electron and hole states in a core/shell quantum dot with a staggered band alignment – so-called type 2 – can lead to emission with photon energies lower than the band gap of core and shell, respectively.<sup>15;17–19</sup> Moreover, the electrostatic repulsion between two excitons

in such a core/shell quantum dot made possible light amplification below the threshold of one exciton per quantum dot.<sup>20</sup> In the intermediate case – so-called type 1.5 behavior – either the conduction or valence band of core and shell are aligned, which leads to an enhanced delocalization of the electron or the hole, respectively. In the case of CdSe/CdS heteronanostructures, it was shown that the changed overlap between electron and hole enables a subtle control of the fine structure of the exciton.<sup>21;22</sup>

Opposite from the extensive set of core/shell heteronanostructures emitting in the visible or near infrared (400-1000 nm) – often based on a II-VI core quantum dot – only a limited set of heteronanostructures active at longer infrared wavelengths (1000–3000 nm) are available. Next to HgTe<sup>23</sup>, InAs/GaAs<sup>24</sup> and InAs/InP<sup>25</sup> probably the most widespread combination is that of a IV-VI lead chalcogenide (PbX with X=S,Se,Te) core quantum dot with a II-VI CdX shell. As initially demonstrated for PbSe/CdSe by Pietryga *et al.*<sup>26</sup>, these heteronanostructures can be conveniently made using cationic exchange. Although having a different crystal structure, PbX (rock-salt) and CdX (zinc-blende) share a common selenium sublattice with little mismatch between the respective lattice constants. When using relatively mild cationic exchange conditions, this allows for the formation of heteronanostructures with epitaxial interfaces as demonstrated in particular for the case of PbSe/CdSe and PbTe/CdTe quantum dots.<sup>26;27</sup>

Although this approach to make PbX/CdX heteronanostructures has been picked up by various authors,<sup>28–34</sup> little studies have addressed the optical properties of PbX/CdX core/shell quantum dots. Only for the case of PbSe/CdSe QDs, extinction coefficients and a sizing curve – allowing for the determination of the core diameter from the absorption spectrum are available,<sup>35</sup> while a detailed study by de Geyter *et al.* gave evidence of significant electron delocalization in the shell and an enhanced splitting of the exciton fine structure.<sup>36</sup> In this paper, we extend this analysis to PbS/CdS core/shell quantum dots, made using a similar cationic exchange procedure. Using elemental analysis, we find that the PbS sizing curve can be used for an accurate estimation of the PbS core diameter in PbS/CdS core/shell QDs, while the PbS/CdS absorption coefficient at short wavelengths coincides with the values predicted using the Maxwell-Garnett model in the local field approximation. We show that PbS/CdS core/shell QDs can have a photoluminescence quantum yield (PLQY) of 80% or more and show a single exponential photoluminescence decay with a lifetime in the 1–3  $\mu$ s range. Using an exciton degeneracy  $g$  of 64, we obtain good agreement between the oscillator strength of the first exciton transition as calculated from the photoluminescence lifetime and the expected value for PbS QDs

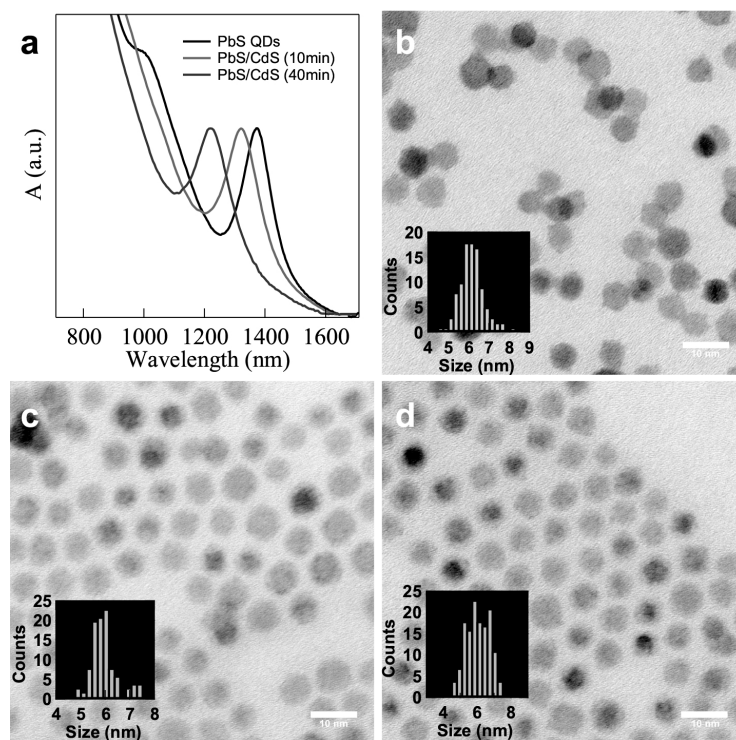


Figure 3.1: (a) Absorption spectra of 5.5 nm PbS QDs and its subsequent PbS/CdS core/shell QDs after 10 and 40 min reaction. (b) TEM overview of the PbS QDs, (c) and (d) TEM overview of the PbS/CdS core/shell QDs after 10 and 40 min reaction respectively. The histograms show that during the cationic exchange the size variations lie well within the uncertainty of the TEM. The TEM scale bars correspond to 10 nm

with the same core diameter. We thus conclude that the electronic structure of PbS and PbS/CdS QDs is highly similar, which is indicative of a type 1 band alignment in PbS/CdS core/shell QDs.

### 3.1.2 Synthesis and Core Size Determination

Exposing a dispersion of PbS QDs to cadmium oleate at temperatures in the range 100–150°C initiates a cationic exchange process where lead cations are replaced by cadmium<sup>26</sup>, thus forming a PbS/CdS core/shell heterostructure. Taking the example of 5.5 nm core PbS QDs exposed to a 20-fold excess of cadmium oleate at 100°C, Figure 3.1a shows that the growth of a

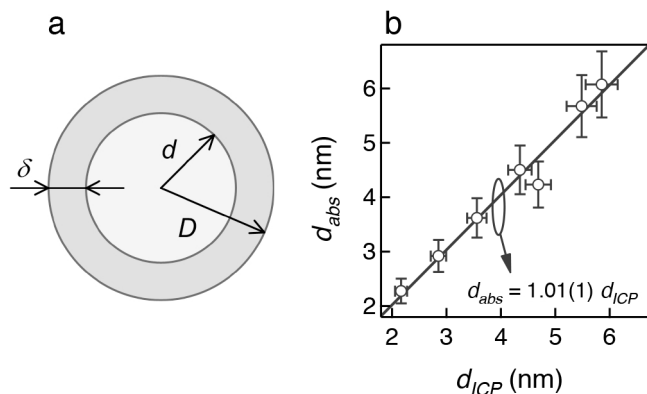


Figure 3.2: (a) Representation of the concentric, spheric core/shell model used in to derive core diameter and shell thickness from the elemental analysis data, with an indication of ( $d$ ) core diameter, ( $D$ ) nanocrystal diameter and ( $\delta$ ) shell thickness. (b) Comparison of ( $d_{abs}$ ) the PbS core diameter as determined from the peak wavelength of the first exciton transition in the UV-Vis spectrum and ( $d_{ICP}$ ) the PbS core diameter as determined using elemental analysis.

CdS shell, and the concomitant reduction of the PbS core, leads to a gradual blue shift of the peak wavelength  $\lambda_{1S-1S}$  of the first exciton transition. Importantly, in line with various literature reports,<sup>27;30</sup> the cationic exchange leaves the overall diameter of the nanocrystals unchanged. According to TEM analysis, the average diameter of the nanocrystals changes from 5.6 to 5.9 nm after a 40 min cationic exchange reaction under the conditions used in Figure 3.1, which is well within the uncertainty on the diameter determination by TEM.

Knowledge of the core diameter and shell thickness is essential to a detailed quantification of the opto-electronic properties of the core/shell QDs.<sup>36;37</sup> As the first exciton transition in PbS/CdS core/shell QDs still shows a well-defined – albeit broadened – absorption peak, we will at first look for a relation between the peak wavelength  $\lambda_{1S-1S}$  and the core diameter. Such a sizing curve is typically used to determine the diameter of core QDs and in the particular case of PbSe/CdSe QDs, it has been shown that the PbSe core diameter can be estimated using the sizing curve of PbSe QDs.<sup>38</sup>

To estimate the average diameter of the PbS core in PbS/CdS core/shell QDs, we determined the amount of Cd and Pb ( $N_{Cd}$  and  $N_{Pb}$ , respectively)

in various samples of PbS/CdS QDs using ICP-MS (Inductively Coupled Plasma Mass Spectrometry). These numbers enable the total volume of CdS ( $V_{\text{CdS}}$ ) and PbS ( $V_{\text{PbS}}$ ) in the sample to be calculated:

$$V_{\text{CdS}} = \frac{a_{\text{CdS}}^3}{4} N_{\text{Cd}} \quad (3.1)$$

$$V_{\text{PbS}} = \frac{a_{\text{PbS}}^3}{8} N_{\text{Pb}} + \frac{a_{\text{PbS}}^3}{8} \frac{N_{\text{Pb}} - 0.2N_{\text{Cd}}}{1.2} \quad (3.2)$$

Here,  $a_{\text{CdS}}$  and  $a_{\text{PbS}}$  denote the lattice constant of CdS and PbS, respectively. To arrive at equations 3.1 and 3.2, we have assumed that the CdS shell is stoichiometric, while the PbS core is not, with a Pb:S ratio of 1.2. Although this ratio varies with size, we take 1.2 as an average value. Having the average volume of CdS and PbS in each core/shell QDs and the core/shell diameter  $D$  and looking at PbS/CdS core/shell QDs as consisting of a spherical PbS core centered within an overall spherical nanocrystal (see Figure 3.2a), the core diameter  $d$  can be calculated as:

$$d = \left( \frac{V_{\text{PbS}}}{V_{\text{CdS}} + V_{\text{PbS}}} \right)^{1/3} D \quad (3.3)$$

An alternative estimation of the core diameter is obtained by applying the PbS sizing curve to the peak wavelength  $\lambda_{1S-1S}$  of the first exciton transition of PbS/CdS core/shell QDs.<sup>39</sup> In Figure 3.2b, we compare the core diameter thus obtained (denoted as  $d_{\text{abs}}$ ) with the core diameter as obtained by applying equation 3.3 (denoted as  $d_{\text{ICP}}$ ). The figure shows that both diameters are directly proportional, with a best fitting line yielding a slope of 1.01(1). We thus conclude that the PbS core diameter of PbS/CdS QDs can be determined from the peak wavelength of the first exciton transition using the PbS sizing curve. This conclusion is in line with a study on PbSe/CdSe QDs,<sup>36</sup> yet it contradicts previous finding on PbS/CdS core/shell QDs.<sup>30</sup>

### 3.1.3 Absorption Coefficient

For core/shell QDs an expression for the intrinsic absorption coefficient has been proposed by Neeves *et al.*<sup>40</sup>, where the indices 'c' and 'sh' refer to

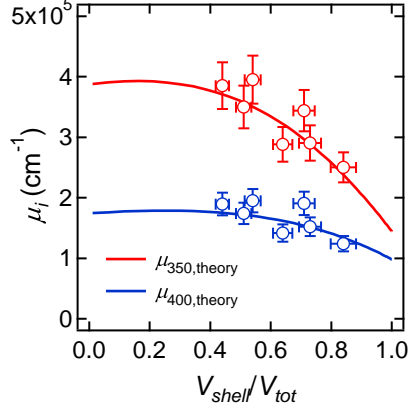


Figure 3.3: Intrinsic absorption coefficient as obtained at (red circles) 350 nm and (blue circles) 400 nm for PbS/CdS core/shell QDs in  $C_2Cl_4$ . The full lines represent theoretical absorption coefficients calculated using the bulk dielectric function of PbS and CdS at the respective wavelengths.

core and shell, respectively:

$$\begin{aligned} \mu_i &= \frac{2\pi}{\lambda n_s} \text{Im}(3\varepsilon_s \beta) \\ \text{with } \beta &= \left( \frac{\varepsilon_{sh}\varepsilon_a - \varepsilon_s\varepsilon_b}{\varepsilon_{sh}\varepsilon_a + 2\varepsilon_s\varepsilon_b} \right) \\ \varepsilon_a &= \varepsilon_c \left( 3 - 2 \frac{V_{sh}}{V_{QD}} \right) + 2\varepsilon_{sh} \frac{V_{sh}}{V_{QD}} \\ \varepsilon_b &= \varepsilon_c \frac{V_{sh}}{V_{QD}} + \varepsilon_{sh} \left( 3 - \frac{V_{sh}}{V_{QD}} \right) \end{aligned} \quad (3.4)$$

This expression shows that in the case of core/shell QDs,  $\mu_i$  depends on  $V_s/V_{tot}$  and on the dielectric functions of core ( $\varepsilon_c$ ), shell ( $\varepsilon_{sh}$ ) and surroundings. In the case of PbSe/CdSe QDs<sup>41</sup>, close agreement was demonstrated between the experimental  $\mu_i$  at short wavelength and a theoretical value calculated using the bulk dielectric function of core and shell in equation 3.4.

For all samples analysed using ICP-OES, we can calculate the volume fraction of PbS/CdS core/shell QDs, assuming an stoichiometric CdS shell and a non-stoichiometric core with a ratio Pb:S 1.2:1. Combining the resulting value with the absorbance of these dispersions, we arrive at experimental values for the intrinsic absorption coefficient. The resulting numbers

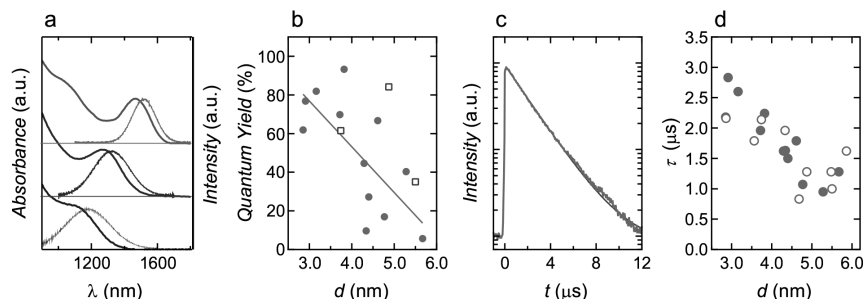


Figure 3.4: (a) Absorption and emission spectra of 5.5 nm PbS QDs (red), PbS/CdS core/shell QDs 0.5 nm shell and 0.8 nm shell. The graph shows the blue shift of the absorption and emission peaks due to the shrinking of the PbS core. (b) Photoluminescence quantum yield as a function of the PbS core for PbS/CdS core/shell QDs (full red dots) and PbS QDs (empty blue squares). (c) Typical decay curve for PbS QDs shown on a logarithmic scale. A single exponential fit is shown. (d) Lifetime as a function of PbS core diameter for PbS QDs (empty red dots) and PbS/CdS core/shell QDs (full red dots).

are represented in Figure 3.3 as a function of the ratio of the shell volume to the total QD volume ( $V_s/V_{tot}$ ) at wavelengths of 400 and 350 nm. Next to the experimental  $\mu_i$ , the full lines in Figure 3.3 represent values obtained through eq 3.4 when using the dielectric function of the bulk PbS and CdS for core and shell, respectively.<sup>42;43</sup> Similar to PbSe/CdSe, a good agreement is obtained between these theoretical values and the experimental data based on ICP-OES analysis. We therefore recommend to use these calculated intrinsic absorption coefficients as a function of  $V_s/V_{tot}$  to calculate the volume fraction and thus the concentration of dispersed PbS/CdS core/shell QDs.

### 3.1.4 Oscillator Strength

Figure 3.4a shows the absorption and emission spectra of 5.5 nm PbS QDs and two samples of PbS/CdS core/shell QDs made from it using cationic exchange at different temperatures and different times. One clearly sees that the photoluminescence follows both the blueshift and the broadening of the first exciton absorption feature. For various PbS/CdS QDs, we determined the photoluminescence quantum yield (PLQY) using an integrating sphere.<sup>44</sup> As indicated in Figure 3.4b, PbS/CdS QDs can have a very high PLQY. Especially for smaller cores, the PLQY typically exceeds 60%, with

a few samples having values above 80 and 90%. As was already reported for the starting core PbS QDs,<sup>45</sup> the QY shows a large sample-to-sample difference, yet it tends to go down with increasing core size. In addition, no marked difference is observed with the PLQY of the original PbS core QDs.

Figure 3.4c shows a typical photoluminescence decay curve for PbS/CdS QDs after excitation with a pulsed dye laser at 480 nm. Opposite from PbSe/CdSe QDs,<sup>36</sup> the decay can be satisfactorily described using a single exponential, yielding luminescent lifetimes  $\tau_{PL}$  in the range 1–3  $\mu$ s. The thus obtained  $\tau_{PL}$  of several samples of PbS and PbS/CdS QDs is plotted as a function of the PbS core diameters in Figure 3.4d. Typical values range between 1 and 3  $\mu$ s, where both for PbS and PbS/CdS QDs, we find that smaller cores yield longer lifetimes, while no clear difference in lifetime emerges between PbS and PbS/CdS QDs. Importantly,  $\tau_{PL}$  as represented in Figure 3.4d is the lifetime obtained by fitting the photoluminescent decay using a single exponential, *i.e.*, without correcting for differences in quantum yield. The dataset shown in Fig 3.4d contains data measured on similar quantum dots with considerably different quantum yields. As a result, calculating the radiative lifetime  $\tau_{rad}$  by dividing the measured lifetime  $\tau_{PL}$  by the quantum yield results in considerable outliers, while  $\tau_{PL}$  itself yields a consistent trend with the PbS core size. We therefore conclude that a mono-exponential fit to the photoluminescent decay directly yields the radiative lifetime, *i.e.*  $\tau_{PL} = \tau_{rad}$ . This could point towards sample heterogeneity, where a fraction of the QDs is dark, while the others emit with a 100% quantum yield, resulting in a PLQY lower than 100% with a PL decay curve still yielding the radiative lifetime.

The radiative lifetime  $\tau_{rad}$  of the first exciton transition is related to the oscillator strength  $f_{1S-1S}$  of this transition. Assuming a  $g$ -fold degenerate first exciton where all the fine structure levels are equally accessible through thermal excitations,  $f_{1S-1S}$  is obtained as:<sup>46</sup>

$$f_{1S-1S} = \frac{2\pi\epsilon_0 c^3 m_e}{e^2} \frac{g}{n_s |f_{LF}|^2 \omega^2 \tau_{rad}^{-1}} \quad (3.5)$$

Here,  $|f_{LF}|^2$  denotes the amplitude squared of the so-called local field factor, which describes the screening of the PbS core by the CdS shell and the solvent.<sup>47</sup> In Figure 3.5, we plot  $f_{1S-1S}$  calculated for PbS/CdS QDs according to equation 3.5 assuming  $g = 64$ . The resulting numbers are compared with figures obtained similarly for PbS QDs and with the oscillator strength of the PbS first exciton transition as calculated using tight

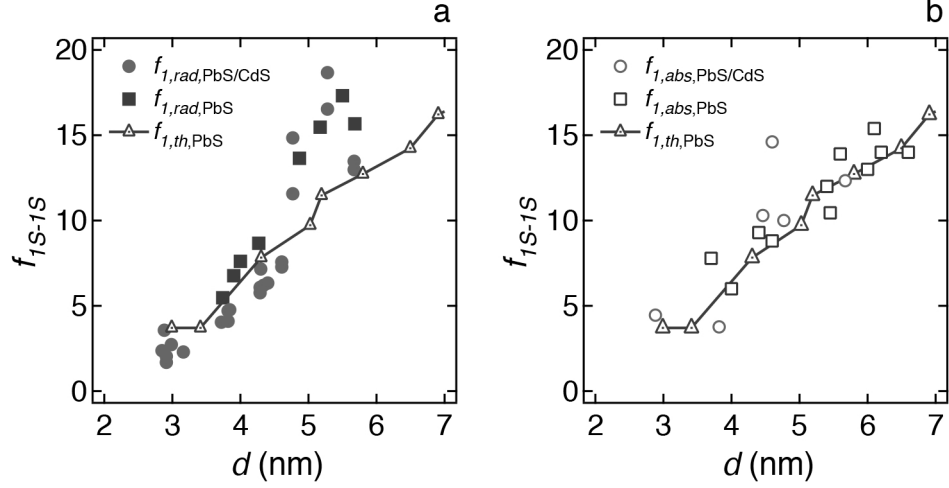


Figure 3.5: Oscillator strength  $f_{1S-1S}$  of the band-edge transition of (blue squares) PbS and (red circles) PbS/CdS QDs as a function of particle size obtained from (a) the radiative lifetime and (b) the spectrum of the intrinsic absorption coefficient. In both cases, the values are compared with theoretical predictions taken from ref. 39 (triangles).

binding methods.<sup>39</sup> Although  $f_{1S-1S}$  as derived from the luminescent lifetime tends to be somewhat smaller for PbS/CdS than for PbS QDs, both agree reasonably well with the predicted value for PbS QDs for core diameters smaller than 5 nm. For larger QDs, the  $f_{1S-1S}$  as obtained from the luminescent lifetime tend to exceed the theoretical oscillator strength. However, these samples tend to have a lower PLQY, which may render the interpretation that  $\tau_{PL}$  equals  $\tau_{rad}$  questionable for larger sizes.

Alternatively,  $f_{1S-1S}$  can be obtained from the intrinsic absorption coefficient spectrum, by integrating  $\mu_i$  over the first exciton peak and including the obtained value ( $\mu_{i,gap}$ ) in the following formula:

$$f_{if,abs} = \frac{2\epsilon_0 c m_e n_s}{e\pi\hbar} \frac{V_{QD}}{|f_{LF}|^2} \mu_{i,gap} \quad (3.6)$$

Due to polydispersity in the samples after cation exchange, the first exciton transition can become difficult to discern from the absorption spectrum, especially for the thicker shells. Moreover, the exact calculation of the integral required to calculate  $f_{if,abs}$  can become doubtful when integrat-

ing over ill-defined transitions. One can imagine that the  $1S - 1S$  band-edge transition gets mixed up with broadened higher order transitions (e.g.  $1P - 1P$ ). We therefore fit the absorbance spectrum to a series of Gaussian spectra superimposed on a polynomial background (see Figure 3.6), including higher order transitions and scattering. The latter is also a means of incorporating the sample polydispersity mentioned above. Subtracting the background from the absorption spectrum gives us a 'net' absorption spectrum used to calculate the value for  $\mu_{i,gap}$ .

For some core/shell samples displayed for  $f_{1,em}$  the dispersity becomes too high for carrying through this background correction. These samples were omitted from the  $f_{1,abs}$  graph. To indicate the need for this background correction, we plot the oscillator strength obtained with and without correction together with the theoretical values for PbS core-only nanocrystals (see 3.7). One can see that for the smaller sizes good coincidence with theory is found only after background correction.

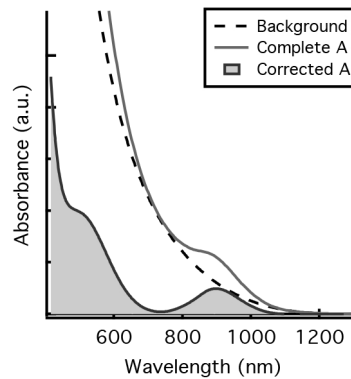


Figure 3.6: Background correction of polydisperse absorption spectra of core/shell samples.

The obtained values are depicted in Figure 3.5b. One can see that PbS/CdS core/shell QDs as well as PbS QDs values follow the trend of the PbS QDs values obtained using tight binding calculations. This result corroborates the argument that PbS/CdS core/shell QDs exhibit a type-I band alignment regime.

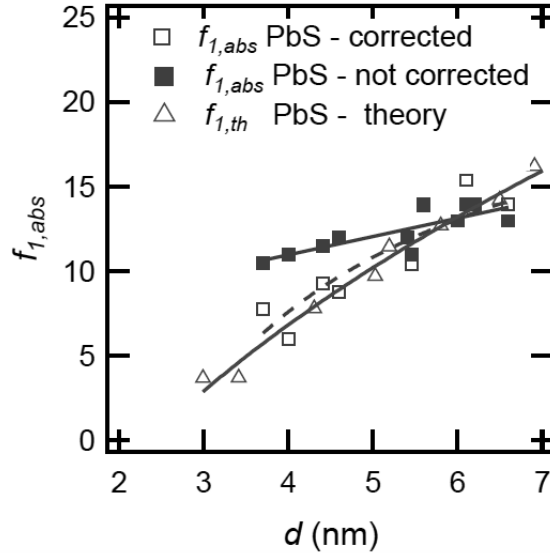


Figure 3.7: Comparison of  $f_{1,abs}$  for PbS core nanocrystals, with and without background correction, to the theoretical predictions<sup>39</sup>.

## 3.2 Optical Properties of Anisotropic Lead-Chalcogenide Nanocrystals

### 3.2.1 Introduction

Building on previous work in the group, lead-chalcogenides and their heterostructures with cadmium chalcogenides (*e.g.* PbS/CdS or PbSe/CdSe) were initially investigated for their potential in near-infrared light emission and amplification. Although great at (spontaneous) light emission with quantum yields up to 80% and tunability from *ca.* 900 nm up to 2100 nm<sup>48</sup>, the lead-salts have their limitations for applications in light amplification due to the high degeneracy of the band edge and strong multi-exciton Auger recombination<sup>49</sup>. Although spherical PbSe/CdSe heterostructures allow some delocalization of the electron<sup>41</sup>, no significant improvement was found in terms of reducing the Auger rates<sup>50</sup>, mostly due to strong Auger processes related to the confined hole states. Formation of anisotropic structures such as rods instead of spherical crystals, offers the advantage of suppressing the Auger rate through the increased volume and reduced X-X interactions<sup>51</sup>. Indeed, the size quantization along the radial direc-

tion of the rod can be sufficient to obtain tunability throughout *e.g.* the near-infrared, while increasing the long axis creates a larger volume for the multi-excitons, reducing their interactions and thus lowering the Auger rate. This was found *e.g.* in CdX rods<sup>51</sup> and is a manifestation of a more general volume scaling of the Auger rate as found by Klimov *et al.*<sup>52</sup>.

### 3.2.2 Synthesis

Standard procedures for synthesizing anisotropic nanostructures rely on the inherent anisotropy in the crystal structure (*e.g.* wurtzite *a* and *c* directions in CdX compounds) to grow a wide variety of complex morphologies ranging from standard rods to even tetrapods<sup>53</sup>. Lead salts have a cubic rock-salt lattice which has no intrinsic anisotropy. As such, synthesizing PbX rods is not possible in a single step procedure. A sequence of cationic exchanges is used instead (see Figure 3.8): The starting material, a CdS rod, is exchanged to Cu<sub>2</sub>S using a copper precursor (tetrakis(acetonitrile)-copper(I)-hexafluorophosphate) mixed with methanol in a Cu:Cd excess of 20:1. The reaction is carried out in a nitrogen-filled glovebox at room temperature. Next, the solution is washed and the Cu<sub>2</sub>S rods are exposed to a mixture of tri-*n*-butylphosphine and lead-acetate. When complete, the solution is again washed and finally the PbS rods are dispersed in toluene.

By means of an additional partial cation exchange with Cd we passivate the surface of the PbS QRs creating a new type of heterostructures in the NIR. These new heterostructures consist of multiple PbS QDs embedded in a CdS quantum rod (see Figure 3.10), a so-called dot-in-rod (DIR). Cationic exchange of Pb by Cd was achieved by adding an excess of Cd oleate to a hot suspension of QRs dissolved in toluene. The degree of exchange can be controlled by changing the reaction time and the temperature (Figure 3.9). It can be seen that longer reaction times and higher temperatures lead to thicker shells with increased PL efficiency.

### 3.2.3 Spontaneous Emission and Morphology

Regarding the morphology, Figure 3.10a shows that CdS QRs are almost single crystalline with few defects. However, after the exchange, PbS QRs exhibit a wavy shape (Figure 3.10b). The rods are formed by multiple segments whose boundaries are caused by different orientations of the rock salt phase. Using high angle annular dark field scanning transmission electron microscopy (HAADF-STEM), we also identified segments of metallic Pb on the surface. Due to these surface defects, photoluminescence quantum yields (PLQY) are low (of a few percent). We demonstrate that this can

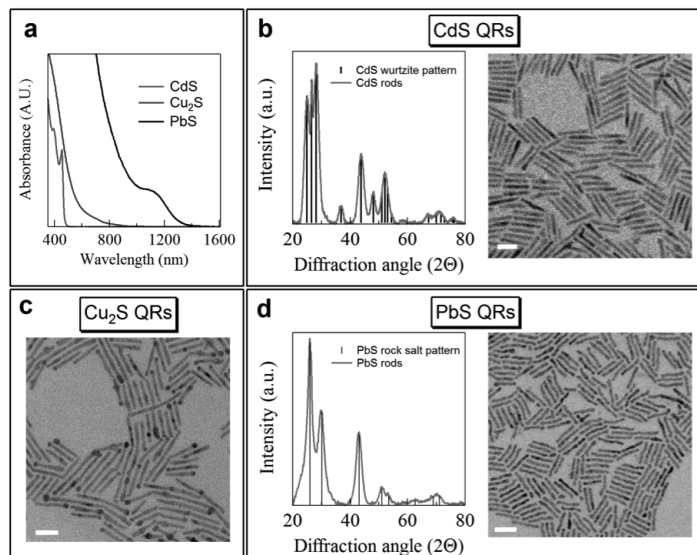


Figure 3.8: (a) Absorption spectra of all the successive cationic exchange steps. (b) XRD diffractogram and TEM overview of the CdS quantum rods (QRs). (c) TEM overview of Cu<sub>2</sub>S QRs. (d) XRD and TEM overview of PbS QRs. All the scale bars are 20 nm.

be overcome by an additional partial cationic exchange step in which Pb is replaced by Cd (see Figure 3.9). The addition of an excess of Cd creates a CdS-shell that isolates the PbS cores from the Pb-particles and defects on the surface that cause the quench in photoluminescence. By controlling the exchange conditions, this results in PbS/CdS DIRs with a PLQY of 45-55%. Moreover, HAADF-STEM makes very clear that the resulting heterostructures are composed of a chain of multiple PbS dots embedded in a CdS rod (see Figure 3.10). The emission wavelength (energy) of the PbS/CdS DIR agrees with that of PbS quantum dots of the same size as the embedded dots which seems to suggest an absence of interdot coupling, reminiscent of the pure type I boundary offset between PbS and CdS (see further).

### 3.2.4 Interdot Coupling

To study the potential electronic coupling between adjacent dots in the rods, we developed a simple effective mass model for the electron and hole states.

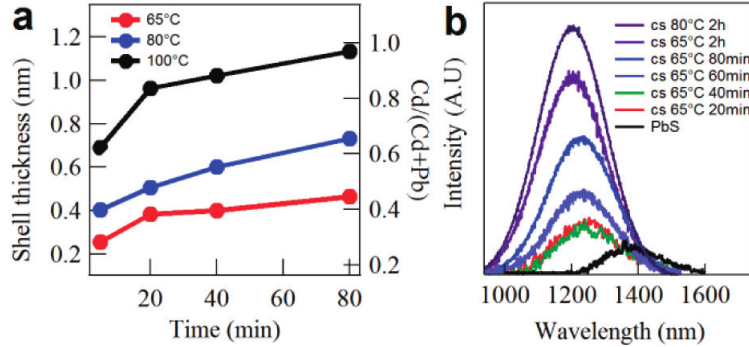


Figure 3.9: Additional cation exchange (a) Evolution of the ratio Cd/(Pb+Cd) and the nominal CdS shell thickness as a function of the reaction time for different reaction temperatures (b) Evolution of the PL spectrum with reaction time for an exchange reaction at 65C, and final PL spectrum for an exchange reaction at 80C.

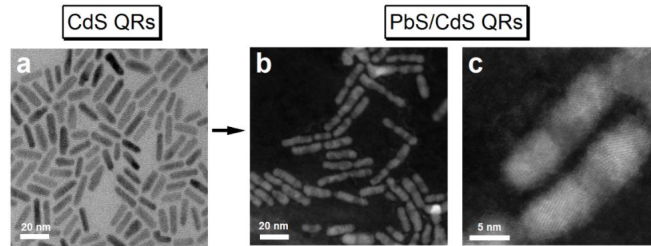


Figure 3.10: High resolution TEM and HAADF images of starting CdS rods (a) and PbS/CdS multiple-dot-in-rods showing the PbS cores (white regions) inside the CdS rod host.

The model solves the stationary Schrödinger equation in three dimensions<sup>1</sup> under the effective mass approximation. In the CdS host, two PbS dots of radius  $R$  are separated by a distance  $L$ . Band offsets of 1.2 eV and 0.9 eV for the valence and conduction band respectively are based on literature values for the PbS/CdS heterojunction. Effective mass parameters are taken from the bulk semiconductors (see table 3.2.4).

<sup>1</sup>Using COMSOL 3.5, a Finite Element Method (FEM) solver

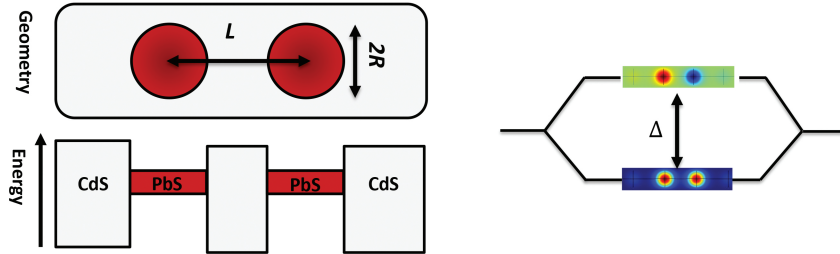


Figure 3.11: FEM simulations: (left) Schematic of simulated geometry: 2 PbS dots of radius  $R$  with an interdistance of  $L$  (note  $L > 2R$ ) and (right) bonding and anti-bonding states separated by energy  $\Delta$ , formed by bringing 2 separate dots closer together.

Material	Electron Mass	Hole Mass
PbS	0.04	0.04
CdS	0.1	0.8

We calculate the energy difference between the bonding and anti-bonding state in a double-dot geometry (as shown in Figure 3.11, right). This splitting would be a direct indication of electronic coupling between the dots and its interpretation is similar to simple molecular binding schemes. We could state that significant coupling requires a splitting of at least  $k_B T$  at room temperature, i.e.  $\approx 25$  meV. Figure 3.13 shows the results: no splitting is observed for the hole states (a) as they do not couple (due to limited leakage outside of the PbS cores, see further) whereas some degree of splitting can be expected for the electron states (b).

The electron and hole wave functions are shown in Figure 3.12 for the case of 4 dots-in-rod (DIR). For the electron in the DIR, 4 states with similar energies are found around 800 meV. Similar values are found for the single dot geometry. A small splitting is observed between the symmetric and anti-symmetric states E1 and E2. This splitting is only a few meV indicating very weak coupling between individual dots. Indeed, the mild conduction band offset (0.9 eV) allows for some electron wavefunction leakage outside of the PbS dot areas, leading to interdot coupling as is observed in Figure ??b. For a radius of 1.85 nm, a separation of  $< 5$  nm would be required to obtain any relevant coupling of the electron states.

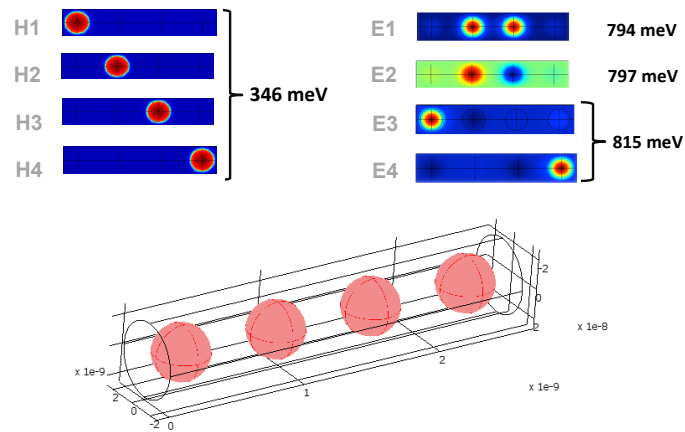


Figure 3.12: Overview of simulation output: (left column) Hole states  $H_i$  showing no interactions and (right column) electron states  $E_i$  showing weak interdot coupling ( $\Delta = 797 - 793 \text{ meV} = 4 \text{ meV}$ , leading to anti-bonding ( $E_2$ ) and bonding states ( $E_1$ )).

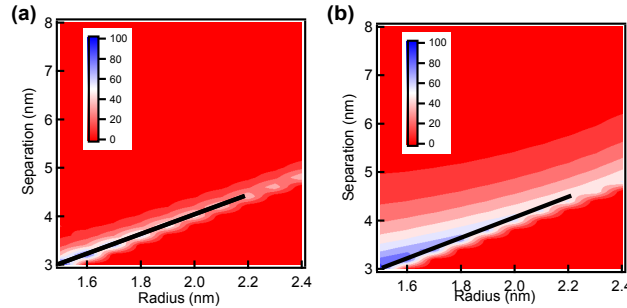


Figure 3.13: Energy difference  $\Delta$  (or binding energy) (in meV, see color scale) between the bonding and anti-bonding states for two dots of radius  $R$  separated by  $L$ . This is shown for the lowest energy hole (a) and electron (b) state. For obvious reasons,  $L > 2R$  as is indicated by the solid black line.

For the hole in the DIR (see Figure ??a), also 4 states with similar energy are found (around 340 meV). Again, similar values are found for the core/shell single dot geometry. The hole states are truly decoupled as there is no sign of wavefunction leakage or energy splitting (not even on a meV scale as for the electron), mostly due to the large valence band offset (1.2 eV) between PbS and CdS.

The radiative lifetime of dot-in-rod samples was comparable to that of dot-only samples. We can understand this from the modeling since the radiative lifetime scales with the overlap of electron and hole wavefunctions (*i.e.* the oscillator strength). From the plots we can see that the average overlap between the electron state and the hole state around the bandgap will be similar for the dot-only and dot-in-rod samples, which confirms the idea of uncoupled dots. Both the core/shell single dot and the dot-in-rod structures show similar energy levels indicating that the dot-in-rod system can be understood as a combination of 4 individual dots without any interactions. This confirms to the experimental observation of similar exciton emission energies of the dot-in-rod and single dot samples.

We can conclude that PbS/CdS dot-in-rod structures show no significant dot-to-dot coupling, as is observed experimentally. Other lead-chalcogenides with smaller core/shell band-offsets might allow for coupling to occur (*e.g.* PbSe/CdSe).

### 3.3 Ultrafast Optical Properties of Lead-Salts for Optical Gain

As colloidal PbS QDs (and their heterostructures with CdS) are excellent near-infrared light emitters, their potential for optical amplification was investigated using ultrafast white light pump-probe spectroscopy.

#### 3.3.1 Spherical PbS Quantum Dots

To study the ultrafast properties of anisotropic PbX heterostructures, we first analyze the basic properties of simple spherical PbS QDs. In Figure 3.14a, the non-linear absorbance spectra for increasing pump fluence (700 nm) are shown after a probe delay of 2.5 ps. Two regions can be distinguished: near the band edge 1S-1S transition, the absorbance is reduced (*i.e.* bleached) due to state filling. However, at longer wavelengths, this bleach gets counteracted by intraband absorption, impeding the absorbance to become negative. The latter hampers the development of net optical gain, *i.e.* a regime where stimulated emission ( $A < 0$ ) dominates over absorption ( $A > 0$ , either through linear or photo-induced events). This observation is quite general and applies to PbSe QDs as well.

The carrier dynamics at higher fluence (see Figure 3.14b) are dominated by multi-exciton Auger recombination. At  $\langle N \rangle = 2.9$ , both bi- and tri-excitons are present in the QDs after carrier cooling is complete ( $> 2.5$  ps). Biexciton lifetimes of 39 ps for a size of 4.3 nm correspond quite well to the literature reports<sup>54</sup>, as does the tri-exciton lifetime of 6.9 ps (assuming cubic scaling of the Auger rate). Under this regime, a quadra-exciton would live only 2.6 ps, a timescale close to the cooling lifetime of 2.5 ps which implies that building up and sustaining anything beyond a 4-exciton (quadra-exciton) state in PbX is very difficult. Note that the latter is the theoretical threshold for optical transparency in the 8-fold degenerate (including spin) PbX system.

From the above, it is clear that using PbX QDs for optical gain is not straightforward:

- Ultrafast Auger recombination of multi-X states reduces the band-edge population on a 10 - 100 ps timescale. To sustain 4 excitons (half the degeneracy of the band edges, a minimum for optical transparency), a new intense pump pulse is required every 2.6 ps which is close to the cooling time needed for hot carriers to relax to the band edge states in the first place.

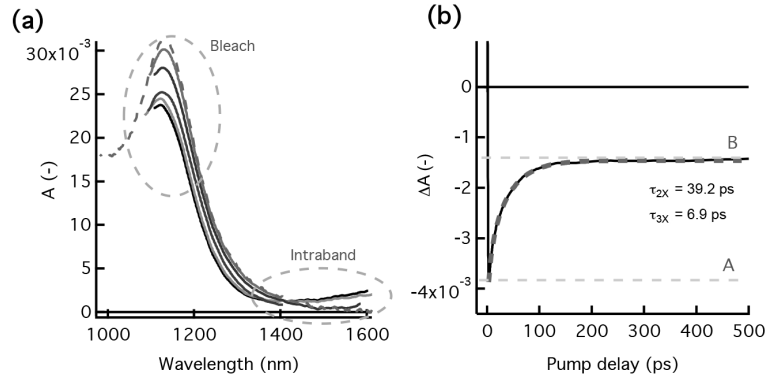


Figure 3.14: Overview of PbS QD (size = 4.3 nm) ultrafast measurements for optical gain: (a) Non-linear absorbance  $A$  after 2.5 ps as function of wavelength for increasing fluence. Two regimes are distinguished: interband bleach and intraband absorption and (b) kinetics at the 1S-1S transition (1138 nm) for a fluence resulting in  $\langle N \rangle = 2.9$ . The levels A/B (see text) are indicated, as is the bi-exponential fit showing a bi- and tri-exciton lifetime of 39.2 and 6.9 ps respectively.

- Intraband absorption at longer wavelengths counteracts the interband bleach required for optical transparency. Since both bleach and intraband scale with the exciton density, net optical gain is difficult, if not impossible, to develop.

As such, we must look for ways to either sustain a multi-X population on longer timescales and/or counteract the photo-induced absorption. The answer could be found in larger volume anisotropic PbX nanocrystals. Indeed, introducing a degree of translational symmetry could counteract the intraband absorption (as momentum conservation typically impedes the latter, see chapter 2) and increasing the volume could reduce the Auger rates<sup>55</sup>.

### 3.3.2 PbS Nanorods

**Absorption cross section** The PbS nanorods discussed before were dispersed in TCE and pumped at 700 nm with increasing fluence to determine the potential for optical gain. To determine the exciton density  $\langle N \rangle$  for pumping with 700 nm, we first calculate the absorption cross section  $\sigma_{400}$ . The latter can be translated to  $\langle N \rangle$  through the photon flux  $J_{ph}$  as:

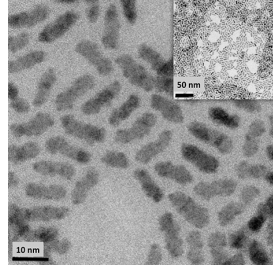


Figure 3.15: TEM image of PbS nanorods with dimensions: 4 nm x 4 nm x 28 nm. Inset shows larger area image.

$$\langle N \rangle = J_{ph} \times \sigma_{400} \times \frac{A_{700}}{A_{400}} \quad (3.7)$$

where  $A_i$  is the sample absorbance at  $\lambda_i$  (see Figure 3.16). Pump absorption along the cuvette length  $L$  (see 2.4.2) is omitted for clarity.

$\sigma_{400}$  can be determined in a similar way to the case of spherical QDs<sup>39</sup> since at high energy (400 nm or 3.1 eV), the absorbance of PbS is bulk-like<sup>46</sup>. The only difference is found in the expression for the local field factor, which includes depolarization effects from the shape anisotropy<sup>56</sup>:

$$\sigma_{400} = V_{rod} \times \frac{\pi \epsilon_{i,400}}{n_s \lambda} (|f_{LF,\perp}|^2 + |f_{LF,\parallel}|^2) \quad (3.8)$$

where  $f_{LF,\perp}$  and  $f_{LF,\parallel}$  are the local field factors parallel and orthogonal to the longitudinal dimension of the rod,  $\epsilon_{i,400}$  is the imaginary part of the bulk PbS dielectric function at 400 nm and  $V_{rod}$  is the volume. For a rod of 4 nm radius and 12 nm length, this results in:  $\sigma_{400} = 4.06 \cdot 10^{-14} \text{cm}^2$ .

**Ultrafast Measurements** Upon photo-excitation at 700 nm, a strong photo-induced absorption (either through intraband absorption or spectral shifts) is observed, followed by rapid carrier cooling (ca. 3 ps). Once the multi-X are cold, they quickly vanish through Auger recombination, sustaining net optical gain only for roughly 5 ps. A bi-exciton lifetime of 73 ps is extracted, which is not dramatically longer than the 39 ps obtained for spherical QDs.

The gain performance of the rods is comparable to the extensive report of optical gain with lead-chalcogenide QDs by Schaller *et al.*<sup>49</sup>: Gain lifetimes for 4.9 nm PbSe QDs in the order of 7 ps for an exciton density ( $\langle N \rangle / V_{QD}$ ) of  $0.32 \text{nm}^{-3}$  compares quite well to our 5 ps and  $0.28 \text{nm}^{-3}$  respectively. An advantage of the rods is the larger absorption cross section

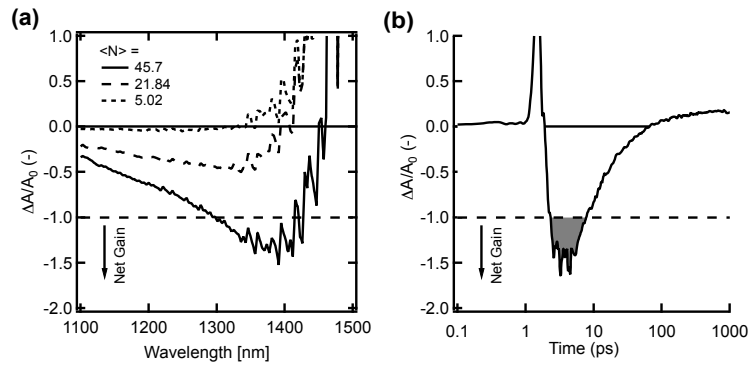


Figure 3.16: Overview of 4 nm x 12 nm rods measurements: (a) Normalized differential absorbance spectrum  $\Delta A/A_0$  for increasing fluence (expressed in  $\langle N \rangle$ ) showing net optical gain for the highest fluence from 1300 to 1430 nm and (b) kinetic of highest fluence measurement at bleach maximum of 1390 nm. Note that net gain is sustained for only  $\sim 5$  ps.

due to the depolarization along the long axis which leads to a factor of 7 increase in absorption cross section. This translates to a factor of 1.4 when corrected for the increased rod volume, *i.e.* a segment of 4 nm PbS in a rod absorbs 1.4 times more light than in a dot.

**Conclusion** PbS QDs and rods were investigated for their potential as colloidal gain media. The high degeneracy of the band edge with the fast Auger recombination of band-edge multi-excitons impedes the development of optical gain. Moreover, the gain is capped by efficient intraband absorption, a feature that we will use to our advantage in chapter 6.

## References

- [1] Kim, M. R.; Chung, J. H.; Lee, M.; Lee, S.; Jang, D.-J. Fabrication, spectroscopy, and dynamics of highly luminescent core-shell InP@ZnSe quantum dots. *Journal of colloid and interface science* **2010**, *350*, 5–9.
- [2] Zhang, Y.; Dai, Q. Q.; Li, X. B.; Cui, Q. Z.; Gu, Z. Y.; Zou, B.; Wang, Y. D.; Yu, W. W. Formation of PbSe/CdSe Core/Shell

- Nanocrystals for Stable Near-Infrared High Photoluminescence Emission. *Nanoscale Research Letters* **2010**, *5*, 1279–1283.
- [3] Dorfs, D.; Franzl, T.; Osovsky, R.; Brumer, M.; Lifshitz, E.; Klar, T. a.; Eychmüller, A. Type-I and type-II nanoscale heterostructures based on CdTe nanocrystals: a comparative study. *Small (Weinheim an der Bergstrasse, Germany)* **2008**, *4*, 1148–52.
- [4] Zhu, Z.; Ouyang, G.; Yang, G. The interface effect on the band offset of semiconductor nanocrystals with type-I core-shell structure. *Physical chemistry chemical physics : PCCP* **2013**, *15*, 5472–6.
- [5] Hines, M. a.; Guyot-Sionnest, P. Synthesis and Characterization of Strongly Luminescing ZnS-Capped CdSe Nanocrystals. *The Journal of Physical Chemistry* **1996**, *100*, 468–471.
- [6] Dabbousi, B. O.; RodriguezViejo, J.; Mikulec, F. V.; Heine, J. R.; Mattoussi, H.; Ober, R.; Jensen, K. F.; Bawendi, M. G. (CdSe)ZnS Core-Shell Quantum Dots: Synthesis and Characterization of a Size Series of Highly Luminescent Nanocrystallites. *J. Phys. Chem. B* **1997**, *101*, 9463–9475.
- [7] Dethlefsen, J. R.; Dø sving, A. Preparation of a ZnS shell on CdSe quantum dots using a single-molecular ZnS precursor. *Nano letters* **2011**, *11*, 1964–9.
- [8] Tsay, J. M.; Pflughoefft, M.; Bentolila, L. a.; Weiss, S. Hybrid approach to the synthesis of highly luminescent CdTe/ZnS and Cd-HgTe/ZnS nanocrystals. *Journal of the American Chemical Society* **2004**, *126*, 1926–7.
- [9] Wu, Y.; Arai, K.; Yao, T. Temperature dependence of the photoluminescence of ZnSe/ZnS quantum-dot structures. *Physical review. B, Condensed matter* **1996**, *53*, R10485–R10488.
- [10] Nikesh, V. V.; Mahamuni, S. Highly photoluminescent ZnSe / ZnS. *Semiconductor Science and Technology* **2001**, *16*, 687–690.
- [11] Trizio, L. D.; Prato, M.; Genovese, A.; Casu, A.; Povia, M.; Simonutti, R.; Alcocer, M. J. P.; Andrea, C. D.; Tassone, F.; Manna, L. Strongly Fluorescent Quaternary Cu In Zn S Nanocrystals Prepared from Cu<sub>1-x</sub>InS<sub>2</sub> Nanocrystals by Partial Cation Exchange. *Chem. Mater.* **2012**, *24*, 2400–2406.

- [12] Song, W.-S.; Yang, H. Efficient White-Light-Emitting Diodes Fabricated from Highly Fluorescent Copper Indium Sulfide Core/Shell Quantum Dots. *Chemistry of Materials* **2012**, *24*, 1961–1967.
- [13] Jang, E.-P.; Song, W.-S.; Lee, K.-H.; Yang, H. Preparation of a photo-degradation-resistant quantum dot-polymer composite plate for use in the fabrication of a high-stability white-light-emitting diode. *Nanotechnology* **2013**, *24*, 045607.
- [14] Song, W.-S.; Kim, J.-H.; Lee, J.-H.; Lee, H.-S.; Do, Y. R.; Yang, H. Synthesis of color-tunable CuInGaS solid solution quantum dots with high quantum yields for application to white light-emitting diodes. *Journal of Materials Chemistry* **2012**, *22*, 21901.
- [15] Kim, S.; Fisher, B.; Eisler, H.-J.; Bawendi, M. Type-II quantum dots: CdTe/CdSe(core/shell) and CdSe/ZnTe(core/shell) heterostructures. *Journal of the American Chemical Society* **2003**, *125*, 11466–7.
- [16] Balet, L. P.; Ivanov, S. a.; Piryatinski, a.; Achermann, M.; Klimov, V. I. Inverted Core/Shell Nanocrystals Continuously Tunable between Type-I and Type-II Localization Regimes. *Nano Letters* **2004**, *4*, 1485–1488.
- [17] Zeng, Q. H.; Kong, X. G.; Sun, Y. J.; Zhang, Y. L.; Tu, L. P.; Zhao, J. L.; Zhang, H. Synthesis and Optical Properties of Type II CdTe/CdS Core/Shell Quantum Dots in Aqueous Solution Via Successive Ion Layer Adsorption and Reaction. *J. Phys. Chem. C* **2008**, *112*, 8587–8593.
- [18] Dennis, A. M.; Mangum, B. D.; Piryatinski, A.; Park, Y.-S.; Hannah, D. C.; Casson, J. L.; Williams, D. J.; Schaller, R. D.; Htoon, H.; Hollingsworth, J. a. Suppressed blinking and Auger recombination in near-infrared type-II InP/CdS nanocrystal quantum dots. *Nano letters* **2012**, *12*, 5545–51.
- [19] Nemchinov, A.; Kirsanova, M.; Hewa-Kasakarage, N. N.; Zamkov, M. Synthesis and Characterization of Type II ZnSe/CdS Core/Shell Nanocrystals. *Journal of Physical Chemistry C* **2008**, *112*, 9301–9307.
- [20] Klimov, V. I.; Ivanov, S. a.; Nanda, J.; Achermann, M.; Bezel, I.; McGuire, J. a.; Piryatinski, A. Single-exciton optical gain in semiconductor nanocrystals. *Nature* **2007**, *447*, 441–6.

- [21] Rainò, G.; Stöferle, T.; Moreels, I.; Gomes, R.; Hens, Z.; Mahrt, R. F. Controlling the exciton fine structure splitting in CdSe/CdS dot-in-rod nanojunctions. *ACS nano* **2012**, *6*, 1979–87.
- [22] Shabaev, a.; Rodina, a. V.; Efros, A. L. Fine structure of the band-edge excitons and trions in CdSe/CdS core/shell nanocrystals. *Physical Review B* **2012**, *86*, 205311.
- [23] Keuleyan, S.; Lhuillier, E.; Guyot-Sionnest, P. Synthesis of colloidal HgTe quantum dots for narrow mid-IR emission and detection. *Journal of the American Chemical Society* **2011**, *133*, 16422–4.
- [24] Harris, L.; Mowbray, D. J.; Skolnick, M. S.; Hopkinson, M.; Hill, G. Emission spectra and mode structure of InAs/GaAs self-organized quantum dot lasers. *Applied Physics Letters* **1998**, *73*, 969.
- [25] Cao, Y.-w.; Banin, U. Synthesis and Characterization of InAs / InP and. *Angewandte Chemie (International ed. in English)* **1999**, *38*, 3692–3694.
- [26] Pietryga, J. M.; Werder, D. J.; Williams, D. J.; Casson, J. L.; Schaller, R. D.; Klimov, V. I.; Hollingsworth, J. A. Utilizing the lability of lead selenide to produce heterostructured nanocrystals with bright, stable infrared emission. *Journal of the American Chemical Society* **2008**, *130*, 4879–4885.
- [27] Lambert, K.; De Geyter, B.; Moreels, I.; Hens, Z. PbTe/CdTe Core/Shell Particles by Cation Exchange, a HR-TEM study. *Chemistry of Materials* **2009**, *21*, 778–780.
- [28] Neo, M. S.; Venkatram, N.; Li, G. S.; Chin, W. S.; Ji, W. Synthesis of PbS / CdS Core-Shell QDs and their Nonlinear Optical Properties. *Society* **2010**, 18037–18044.
- [29] Wheeler, D. a.; Fitzmorris, B. C.; Zhao, H.; Ma, D.; Zhang, J. Ultrafast exciton relaxation dynamics of PbS and core/shell PbS/CdS quantum dots. *Science China Chemistry* **2011**, *54*, 2009–2015.
- [30] Zhao, H.; Chaker, M.; Wu, N.; Ma, D. Towards controlled synthesis and better understanding of highly luminescent PbS/CdS core/shell quantum dots. *J. Mater. Chem.* **2011**, —.
- [31] Zhang, Y.; Dai, Q. Q.; Li, X. B.; Cui, Q. Z.; Gu, Z. Y.; Zou, B.; Wang, Y. D.; Yu, W. W. Formation of PbSe/CdSe Core/Shell

- Nanocrystals for Stable Near-Infrared High Photoluminescence Emission. *Nanoscale Research Letters* **2010**, *5*, 1279–1283.
- [32] Abel, K. a.; Qiao, H.; Young, J. F.; van Veggel, F. C. J. M. Four-Fold Enhancement of the Activation Energy for Nonradiative Decay of Excitons in PbSe/CdSe Core/Shell versus PbSe Colloidal Quantum Dots. *The Journal of Physical Chemistry Letters* **2010**, *1*, 2334–2338.
- [33] Xu, T.; Wu, H.; Si, J.; McCann, P. Optical transitions in PbTeCdTe quantum dots. *Physical Review B* **2007**, *76*, 155328.
- [34] Groiss, H.; Kaufmann, E.; Springholz, G.; Schwarzl, T.; Hesser, G.; Schaffler, F.; Heiss, W.; Koike, K.; Itakura, T.; Hotei, T.; Yano, M.; Wojtowicz, T. Size control and midinfrared emission of epitaxial PbTeCdTe quantum dot precipitates grown by molecular beam epitaxy. *Applied Physics Letters* **2007**, *91*, 222106.
- [35] Geyter, B. D.; Hens, Z. The absorption coefficient of PbSe / CdSe core / shell colloidal quantum dots The absorption coefficient of PbSe / CdSe core / shell colloidal quantum dots. *Applied Physics Letters* **2012**, *161908*, 2010–2013.
- [36] De Geyter, B.; Justo, Y.; Moreels, I.; Lambert, K.; Smet, P. F.; Van Thourhout, D.; Houtepen, A. J.; Grodzinska, D.; de Mello Donega, C.; Meijerink, A.; Vanmaekelbergh, D.; Hens, Z. The different nature of band edge absorption and emission in colloidal PbSe/CdSe core/shell quantum dots. *ACS nano* **2011**, *5*, 58–66.
- [37] Nguyen, T.; Habinshuti, J.; Justo, Y.; Gomes, R.; Mahieu, G.; Godey, S.; Nys, J.; Carrillo, S.; Hens, Z.; Robbe, O.; Turrell, S.; Grandidier, B. Charge carrier identification in tunneling spectroscopy of core-shell nanocrystals. *Physical Review B* **2011**, *84*, 1–8.
- [38] Moreels, I.; Lambert, K.; De Muynck, D.; Vanhaecke, F.; Poelman, D.; Martins, J. C. J. C.; Allan, G.; Hens, Z. Composition and Size-Dependent Extinction Coefficient of Colloidal PbSe Quantum Dots. *Chem. Mater.* **2007**, *19*, 6101–6106.
- [39] Moreels, I.; Lambert, K.; Smeets, D.; De Muynck, D.; Nollet, T.; Martins, J. C. J. C.; Vanhaecke, F.; Vantomme, A. A.; Delerue, C.; Allan, G.; Hens, Z. Size-Dependent Optical Properties of Colloidal PbS Quantum Dots. *ACS Nano* **2009**, *3*, 3023–3030.

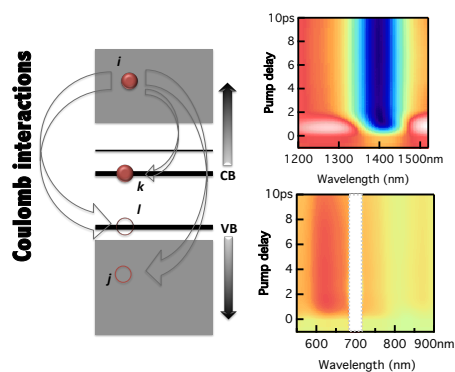
- [40] Neeves, A. E.; Birnboim, M. H. Composite structures for the enhancement of nonlinear-optical susceptibility. *J. Opt. Soc. Am. B* **1989**, *6*, 787–796.
- [41] De Geyter, B.; Hens, Z. The absorption coefficient of PbSe/CdSe core/shell colloidal quantum dots. *Applied Physics Letters* **2010**, *97*, 161908.
- [42] Suzuki, N.; Sawai, K.; Adachi, S. Optical Properties of PbSe. *J. Appl. Phys.* **1995**, *77*, 1249–1255.
- [43] Ninomiya, S.; Adachi, S. Optical Properties of Cubic and Hexagonal Cdse. *J. Appl. Phys.* **1995**, *78*, 4681–4689.
- [44] Porrès, L.; Holland, A.; På lsson, L.-O.; Monkman, A. P.; Kemp, C.; Beeby, A. Absolute measurements of photoluminescence quantum yields of solutions using an integrating sphere. *Journal of fluorescence* **2006**, *16*, 267–72.
- [45] Moreels, I.; Justo, Y.; De Geyter, B.; Haustraete, K.; Martins, J. C.; Hens, Z. Size-Tunable, Bright, and Stable PbS Quantum Dots: A Surface Chemistry Study. *ACS Nano* **2011**, *5*, 2004–2012.
- [46] Hens, Z.; Moreels, I. Light absorption by colloidal semiconductor quantum dots. *Journal of Materials Chemistry* **2012**, *22*, 10406.
- [47] Neeves, A.; Birnboim, M. Composite Structures for the Enhancement of Nonlinear-Optical Susceptibility. *J. Opt. Soc. Am. B* **1989**, *6*, 787–796.
- [48] Moreels, I.; Justo, Y.; De Geyter, B.; Haustraete, K.; Martins, J. C.; Hens, Z. Size-tunable, Bright, and Stable PbS Quantum Dots: A Surface Chemistry Study. *ACS Nano* **2012**, *5*, 2004–2012.
- [49] Schaller, R. D.; Petruska, M. a.; Klimov, V. I. Tunable Near-Infrared Optical Gain and Amplified Spontaneous Emission Using PbSe Nanocrystals. *The Journal of Physical Chemistry B* **2003**, *107*, 13765–13768.
- [50] Cirloganu, C. M.; Padilha, L. a.; Lin, Q.; Makarov, N. S.; Velizhanin, K. a.; Luo, H.; Robel, I.; Pietryga, J. M.; Klimov, V. I. Enhanced carrier multiplication in engineered quasi-type-II quantum dots. *Nature communications* **2014**, *5*, 4148.

- 
- [51] Htoon, H.; Hollingsworth, J.; Dickerson, R.; Klimov, V. Effect of Zero- to One-Dimensional Transformation on Multiparticle Auger Recombination in Semiconductor Quantum Rods. *Physical Review Letters* **2003**, *91*, 1–4.
- [52] Robel, I.; Gresback, R.; Kortshagen, U.; Schaller, R.; Klimov, V. Universal Size-Dependent Trend in Auger Recombination in Direct-Gap and Indirect-Gap Semiconductor Nanocrystals. *Physical Review Letters* **2009**, *102*, 177404.
- [53] Yin, Y.; Alivisatos, P. Colloidal nanocrystal synthesis and the organic-inorganic interface. *Nature* **2005**, *437*, 664–70.
- [54] Stewart, J. T.; Padilha, L. a.; Qazilbash, M. M.; Pietryga, J. M.; Midgett, A. G.; Luther, J. M.; Beard, M. C.; Nozik, A. J.; Klimov, V. I. Comparison of carrier multiplication yields in PbS and PbSe nanocrystals: the role of competing energy-loss processes. *Nano letters* **2012**, *12*, 622–8.
- [55] Padilha, L. a.; Stewart, J. T.; Sandberg, R. L.; Bae, W. K.; Koh, W.-K.; Pietryga, J. M.; Klimov, V. I. Aspect Ratio Dependence of Auger Recombination and Carrier Multiplication in PbSe Nanorods. *Nano letters* **2013**, *13*, 1092–9.
- [56] Kamal, J. S.; Gomes, R.; Hens, Z.; Karvar, M.; Neyts, K.; Compernelle, S.; Vanhaecke, F. Direct determination of absorption anisotropy in colloidal quantum rods. *Physical Review B* **2012**, *85*, 035126.



# 4

## Coulomb Shifts upon Exciton Addition to Photoexcited PbS Quantum Dots



Using ultrafast hyperspectral transient absorption (TA) spectroscopy, we determine the biexciton addition energies in PbS quantum dots (QDs) with different sizes when either a cold or a hot exciton is added to a QD already containing a cooled exciton. The observed dependence of this so-called biexciton addition energy on the QD diameter and the exciton energy can be rationalized by interpreting the addition energies as the result of an imbalance in the Coulomb interactions between the newly created carriers

and the carriers already present in a QD. The obtained results are therefore relevant from both a fundamental and practical point of view. They provide experimental data on Coulomb interaction between charge carriers in confined semiconductors that can be compared with theoretical estimates and understanding in particular the way hot-cold biexciton addition energies influence the transient absorption spectrum adds a new element to the transient absorption toolbox for the opto-electronic properties of colloidal QDs.

## 4.1 Introduction

An ubiquitous property of excited QDs in this respect is the shift of their absorbance spectrum relative to that of unexcited QDs. These spectral shifts are typically attributed to an imbalance in the mutual electron-electron, electron-hole and hole-hole Coulomb interactions upon addition of an exciton to an already excited QD. In the case of core/shell heteronanostructures with a staggered band alignment for example, repulsive biexciton interactions were used to achieve single exciton gain<sup>1</sup>, which is otherwise unattainable when using the QD band gap transition for stimulated emission. From a more practical point of view, spectral shifts complicate the interpretation of transient absorption spectra. When present, variations of the absorbance of a QD ensemble at a given wavelength after pulsed photo-excitation do not simply reflect state-filling or photo-induced absorption and a detailed analysis of the full transient absorption spectrum is needed<sup>2;3</sup>.

In spite of the importance of spectral shifts upon exciton addition for the interpretation of transient absorption spectra and the possibility to use them for tweaking QD properties, few studies have systematically addressed the properties of these shifts. Especially the effect of Coulomb interactions on high energy transitions remains an unexplored field, although the high energy transient absorption of near-infrared quantum dots for example is extremely important for studying the dynamical properties of hot carriers relevant for multiple-exciton generation<sup>4;5</sup> or carrier extraction in photovoltaic cells or photodetectors<sup>6</sup>. A possible complication in this respect is the fact that a proper evaluation of spectral shifts requires the recording of the transient spectrum over a sufficiently broad wavelength range with high spectral resolution. Initial attempts by Trinh *et al.*<sup>2</sup> were conducted on PbSe QDs but it is only recently that full broadband transient absorption studies have been reported for near-infrared absorbing QDs<sup>3;7;8</sup>. These however focus mostly on near-infrared probing for multiple exciton generation and as such, do not give a detailed account of exciton addition energies.

Here, we report on a comprehensive study of spectral shifts  $\Delta$  upon (multiple) exciton addition to photoexcited PbS quantum dots using transient absorption spectroscopy with white light probing. We focus first on the addition of an exciton resonant with the bandgap transition, *i.e.*, a so-called *cold* exciton, where the spectral shift  $\Delta_{cc}$  between two cold excitons is obtained by fitting the transient absorbance to a model function containing  $\Delta_{cc}$  as an adjustable parameter. The ensuing biexciton addition energy is negative, with a magnitude that goes down with increasing quantum dot diameter. Next, we show that upon creation of a high energy exciton, *i.e.*, a so-called *hot* exciton, the interaction with cold excitons already present also results in a spectral redshift. The corresponding hot-cold biexciton addition energy  $\Delta_{hc}$  is largely independent of the excitation energy and scales proportionally to the number of cold excitons present. The magnitude of  $\Delta_{hc}$  decreases with increasing quantum dot diameter and systematically exceeds the magnitude of  $\Delta_{cc}$ . On the other hand, no significant spectral shifts are measured upon addition of a hot exciton to quantum dots already containing hot excitons. Hence, we determine that biexciton shifts increase as:  $\Delta_{hc} > \Delta_{cc} \gg \Delta_{hh}$ . We discuss these exciton addition energies and their relative magnitude in terms of an imbalance of the electron-electron, hole-hole and electron-hole Coulomb interactions between the newly added charge carriers and the carriers already present in the quantum dot.

## 4.2 Concepts

### 4.2.1 Exciton Addition Energies and Coulomb Shifts

In a single electron picture, photon absorption can transfer an electron from an initial state  $i$  to a final state  $j$  of a quantum dot, where the photon energy matches the energy difference  $\Delta\epsilon_{0,ij}$  given by:

$$\Delta\epsilon_{0,ij} = \epsilon_{e,j} + \epsilon_{h,i} - J_{eh,ji} \quad (4.1)$$

Here, the subscript 0 indicates that the photon is absorbed by an unexcited QD, while  $\epsilon_{e,j}$  and  $\epsilon_{h,i}$  denote the electron and hole energy level, respectively – counted as positive numbers starting from the uppermost valence-band level – and  $J_{eh,ji}$  is the absolute value of the Coulomb interaction energy between an electron in state  $j$  and a hole in state  $i$  (see Figure 4.1a). In writing eq 4.1, we have neglected possible contributions from configuration interaction or exchange interaction<sup>9;10</sup>. If the QD already contains  $N$  excitons, the transition between the same single electron states will occur at an energy difference  $\Delta\epsilon_{N,ij}$  that may differ from  $\Delta\epsilon_{0,ij}$  due to Coulomb interactions between the newly created electron-hole pair and the electrons

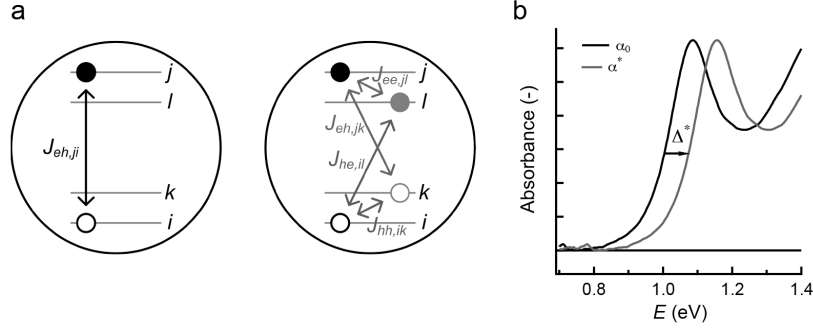


Figure 4.1: (a) Scheme depicting (left) electron-hole Coulomb interaction upon creation of an electron-hole pair  $(j, i)$  in an unexcited quantum dots and (right) additional Coulomb interaction terms upon creation of the same electron-hole pair  $(j, i)$  in a quantum dot already containing an electron-hole pair  $(l, k)$ . (b) Representation of an absorption spectrum  $\alpha_0$  and its counterpart  $\alpha^*$ , shifted by an energy difference  $\Delta^*$ .

and holes already present in the quantum dots. Using the different Coulomb terms as shown in Figure 4.1a,  $\Delta\epsilon_{N,ij}$  can be written as:

$$\Delta\epsilon_{N,ij} = \Delta\epsilon_{0,ij} - \sum_k (J_{eh,jk} - J_{hh,ik}) - \sum_l (J_{he,il} - J_{ee,jl}) \quad (4.2)$$

Here, the indices  $k$  and  $l$  label the states of all electrons and holes already present in the QD.

The concept of a spectral shift refers to the fact that the same electronic transition is observed at a different photon energy. The spectral shift  $\Delta_{N,ij}$  for exciton addition to a QD already containing  $N$  excitons can therefore be defined as:

$$\Delta_{N,ij} = \Delta\epsilon_{N,ij} - \Delta\epsilon_{0,ij} \quad (4.3)$$

Using eqs 4.1 and 4.2,  $\Delta_{N,ij}$  can be written as:

$$\Delta_{N,ij} = - \sum_k (J_{eh,jk} - J_{hh,ik}) - \sum_l (J_{he,il} - J_{ee,jl}) \quad (4.4)$$

In principle,  $\Delta_{N,ij}$  depends on the electron and hole states occupied by the newly formed exciton and by the excitons already present. When analyzed using transient absorption spectroscopy,  $\Delta_{N,ij}$  can therefore depend on the pump and probe photon energy and the pump-probe time delay. Assuming however that all Coulomb interaction terms are independent of the particular states occupied by the electrons and the holes already present, labeled

in general as 0, eq 4.4 becomes:

$$\Delta_{N,ij} = -N (J_{eh,j0} + J_{he,i0} - J_{hh,i0} - J_{ee,j0}) = N\Delta \quad (4.5)$$

One sees that in this case a spectral shift is obtained proportional to the number of excitons present and determined by the net difference of  $e-h$  Coulomb attraction and  $e-e$  and  $h-h$  repulsion between the newly formed electron-hole pair and the electrons and holes already present.

### 4.2.2 Determination of Spectral Shifts

In general, the absorption spectrum  $\alpha^*$  of an ensemble of quantum dots after photoexcitation is the weighted average of the spectra of quantum dots containing 0, 1, 2, *etc.* excitons. Denoting the fraction of quantum dots containing  $N$  excitons by  $x_N$ , we have<sup>2</sup>:

$$\alpha^*(\epsilon, t) = \sum_N x_N(t) \alpha_N(\epsilon, t) \quad (4.6)$$

With  $t$  denoting the time delay after the pump pulse, eq 4.6 explicitly takes the time dependence of the fractions  $x_i$  and the absorption spectra  $\alpha_i$  into account, where the former can change due to exciton recombination while, *e.g.*, exciton cooling can affect the latter. Spectral shifts are one of the parameters that determine the difference between  $\alpha_N$  and  $\alpha_0$ , and they can be determined by fitting the spectrum  $\alpha^*$  to eq 4.6 while using parameterized expressions for each spectrum  $\alpha_N$ .

A more direct determination of spectral shifts is possible when the only difference between  $\alpha^*$  and the spectrum  $\alpha_0(\epsilon)$  before excitation is a spectral shift by an energy  $\Delta^*$ . In that case, one has (see Figure 4.1b):

$$\alpha^*(\epsilon) = \alpha_0(\epsilon - \Delta^*)$$

For sufficiently small spectral shifts,  $\Delta^*$  can thus be calculated as:

$$\Delta^*(\epsilon) = \frac{\alpha_0(\epsilon) - \alpha^*(\epsilon)}{(d\alpha_0(\epsilon)/d\epsilon)} \quad (4.7)$$

Using eq 4.6 and writing the spectral shift between the absorption spectrum  $\alpha_N$  and  $\alpha_0$  as  $\Delta_N$ , the spectrum  $\alpha^*$  can be expressed as:

$$\alpha^*(\epsilon) = \sum_N \left( \alpha_0(\epsilon) - \frac{d\alpha_0}{d\epsilon} \Delta_N \right) x_N$$

Entering this expression in eq 4.7, it thus follows that the overall spectral shift  $\Delta$  is obtained as the weighted average of the shifts  $\Delta_N$ :

$$\Delta^* = \sum_i \Delta_N x_N \quad (4.8)$$

When  $\Delta_N$  is proportional to  $N$  (see eq 4.5), we obtain the result that  $\Delta^*$  is proportional to the average number of excitons per QD  $\langle N \rangle$ :

$$\Delta^* = \langle N \rangle \Delta \quad (4.9)$$

### 4.3 Experimental Section

Oleylamine (OLA) capped PbS QDs were synthesized using the procedure described by Cademartiri *et al.*<sup>11</sup> and modified by Moreels *et al.*<sup>12</sup>. After synthesis, the OLA ligand shell is substituted by oleic acid (OA). An exchange to OA is typically performed by adding OA to a toluene suspension of PbS QDs in a ratio of 1.5:10 OA/toluene. After precipitation with ethanol and centrifugation, the QDs are resuspended in toluene and the exchange is repeated.

Samples were excited using 180 femtosecond pump pulses at 700 nm, created from the 1028 nm fundamental (Pharos SP, 6W, Light Conversion) through non-linear frequency mixing in an OPA (Orpheus, Light Conversion). Probe pulses were generated in a sapphire crystal using the 1028 nm fundamental. The pulses were delayed relative to the pump using a delay stage with maximum delay of 2.5 ns (Helios Spectrometer, Ultrafast Systems). The probe spectrum in our experiments covers the VIS-NIR window from 550 nm up to 1600 nm. PbS quantum dots were dispersed in an optically transparent solvent (tetrachloroethylene) to achieve optical densities of 0.1 at the first exciton transition and samples were stirred during all measurements. The average number of absorbed photons (or equivalently created excitons)  $\langle N \rangle$  can be calculated from the photon flux  $J_{ph}$ , the cuvette length  $L$  and the nanocrystal absorption cross section at the pump wavelength  $\sigma_{700}$ :  $\langle N \rangle = J_{ph} \times \sigma_{700} \times \frac{1 - 10^{-\alpha_{0,700} L}}{\alpha_{0,700} L}$ . Assuming Poissonian statistics<sup>13</sup>, one can write the probability to have  $N$  excitons in a nanocrystal as:  $P(N) = \frac{e^{-\langle N \rangle} \langle N \rangle^N}{N!}$ .

## 4.4 Results and Discussion

### 4.4.1 Near - Band Gap Probing

Figure 4.2a shows the linear absorbance spectrum  $A_0$  of a dispersion of 5.2 nm PbS QDs, together with the 2D transient absorbance (TA) image  $\Delta A$  in the wavelength range 1200–1520 nm (1.03–0.81 eV), recorded following a 180 fs optical pump pulse that creates on average 0.1 excitons per QD. At wavelengths around the band gap transition of 1400 nm (0.88 eV), a reduced absorption is observed due to the filling of the highest valence-band and lowest conduction-band states by the cooled exciton. Apart from a slight reduction in intensity, the transient absorption shows little variation in the time range 2.5–500 ps (see Figure 4.2b), which is much shorter than the single exciton lifetime<sup>14</sup>. In Figure 4.2c, the non-linear absorbance  $A^* = A_0 + \Delta A$  recorded 500 ps after the pump pulse is plotted for different pump fluences as characterized by the average number of excitons  $\langle N \rangle$ .  $A^*$  decreases with increasing  $\langle N \rangle$  due to more extensive state filling and its maximum shows a progressive redshift relative to the maximum of  $A_0$  when the pump fluence is raised.

After a time delay of 500 ps, all multiexcitons initially present after the pump pulse have decayed by Auger recombination and only unexcited and singly excited quantum dots remain. Figure 4.2c therefore indicates that the addition energy of a cold exciton, *i.e.*, resonant with the bandgap, to a quantum dot already containing a cold exciton is negative. To quantify this so-called cold-cold biexciton addition energy  $\Delta_{cc}$ , we write the non-linear absorbance  $A^*$  according to eq 4.6 as function of the average exciton number at time zero  $\langle N \rangle$ :

$$A^* = x_0 A_0 + x_1 A_1 = e^{-\langle N \rangle} A_0(\epsilon) + \left[ 1 - e^{-\langle N \rangle} \right] \left[ \frac{3}{4} A_0(\epsilon - \Delta_{cc}) + A_{IB} \right] \quad (4.10)$$

Here, we have used the fact that the presence of a cold exciton will reduce the absorption cross section of the bandgap transition by 1/4 since PbS quantum dots have 8-fold degenerate band edge states. Moreover, the  $A_1$  spectrum is shifted in energy by an amount  $\Delta_{cc}$  and we have introduced an energy independent term  $A_{IB}$  to describe photoinduced absorption in excited quantum dots due to intraband transitions<sup>15</sup>. For PbS quantum dots with three different sizes, we have fitted the above model to the transient absorption spectra recorded using the 3 different average fluences shown in Figure 4.2c, using  $\Delta_{cc}$  and  $A_{IB}$  as the only adjustable parameters for each trace. This allows us to obtain both a value for  $\Delta_{cc}$  and an estimate of the uncertainty on this number. As shown in Figure 4.2d, the resulting spectral

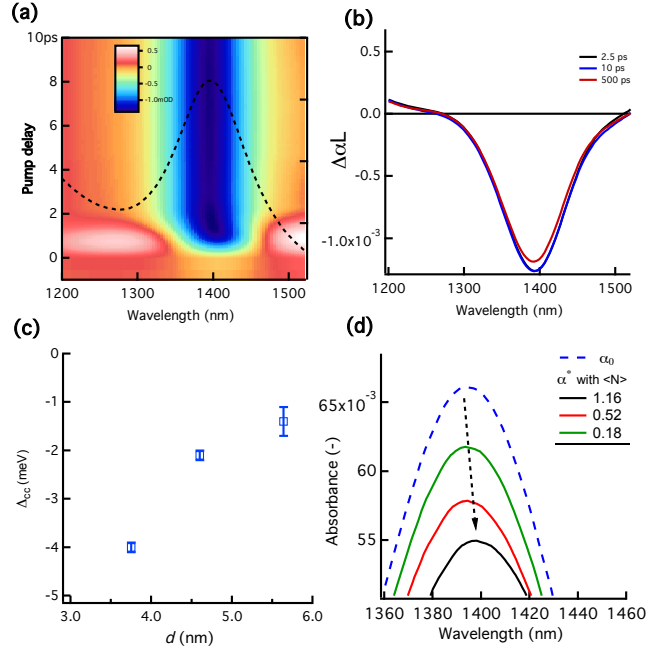


Figure 4.2: Low energy (*i.e.* resonant) probing overview (a) 2D time-wavelength map upon 700 nm, 180 fs photo-excitation (creating  $\langle N \rangle = 0.1$ ) of 5.2 nm PbS QDs, plotted together with the linear absorption spectrum  $A_0$  (solid red line) (b) Spectral cuts at 2.5 ps, 10 ps and 500 ps. (c) The cold-cold shift  $\Delta_{cc}$  as function of particle size and (d) non-linear absorbance  $A^*(= \Delta A + A_0)$  for different fluences  $\langle N \rangle$ .

shifts  $\Delta_{cc}$  hardly depend on the pump fluence and ranges from -4.0 to -1.4 meV for 3.75 to 5.6 nm PbS quantum dots.

In principle, it should be possible to derive the addition energy of a cold exciton to a quantum dot containing a hot exciton from the transient absorbance spectrum in the first picoseconds after photoexcitation, *i.e.*, before exciton cooling. However, this cold-hot biexciton addition energy  $\Delta_{ch}$  is difficult to evaluate reliably since hot excitons impose multiple effects on the band edge transition apart from regular energy shifts due to Coulomb type interactions. As was pointed out by different authors, a hot electron-hole pair has not yet condensed into an exciton<sup>16;17</sup>. It has been argued that this transient charge state induces a transient dipole moment, thus breaking symmetry of the spherical quantum dots and allowing symmetry-forbidden dipole transition (such as S-P) to gain oscillator

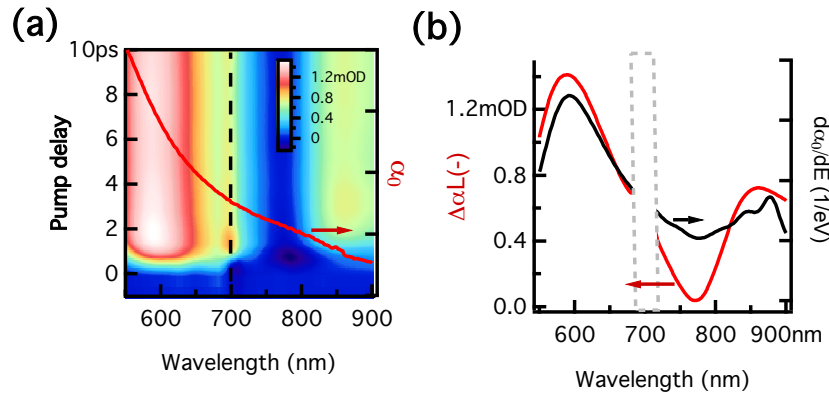


Figure 4.3: High energy probing overview (a) 2D time-wavelength map upon 700 nm, 180 fs photo-excitation (dashed vertical line) (creating  $\langle N \rangle = 0.1$ ) of 3.75 nm PbS QDs, plotted together with the linear absorption spectrum  $\alpha_0$ . (b) Spectral cut at 2.5 ps from (a) plotted together with  $d\alpha_0/dE$  in the wavelength range of 550 nm – 900 nm.

strength or broaden up. Other reports<sup>15</sup> pointed out that hot carriers showed increased intraband absorption, giving an additional transient component to  $\Delta A$  at early times which is dependent on energy. Since this makes that no reliable parametrization of any  $A_N$  can be put forward, we refrain from determining  $\Delta_{ch}$  using a fitting procedure.

#### 4.4.2 Above Band Gap Probing

Figure 4.3a shows the linear absorbance spectrum of a dispersion of 3.75 nm PbS QDs, together with the transient absorbance spectrum in the wavelength range 550 – 900 nm (2.25 – 1.38 eV), recorded following a 180 fs optical pump pulse that creates on average 0.1 excitons per QD. Clearly the differential absorbance is positive. This implies that excited quantum dots absorb light more strongly than unexcited quantum dots at photon energies corresponding to 1.6–2.4 times the bandgap transition energy. This photoinduced absorption clearly depends on the probe-photon wavelength but shows only little change, if any, as a function of the pump-probe delay.

Figure 4.3b depicts a spectral cut of the TA spectrum taken at 2.5 ps, together with the derivative  $d\alpha_0/dE$ . It follows that at photon energies at around 2.1 eV (600 nm), where the photoinduced absorption is largest, also  $d\alpha_0/dE$  peaks, whereas at wavelengths around 1.6 eV (750 nm), both the

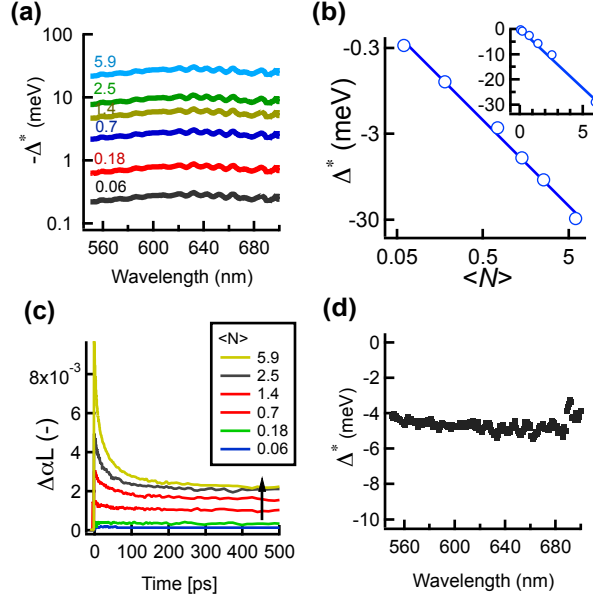


Figure 4.4: Analysis of 3.75 nm PbS (a) Spectrum of the energy shift  $\Delta^*$  after 2.5 ps calculated from equation 4.7 for different average occupations  $\langle N \rangle$ . (b) Same energy shift at 580 nm, showing a linear dependence on  $\langle N \rangle$ . (c) Time dependence of TA signal at 580 nm for different fluences. (d) Shift calculated from  $\Delta\alpha$  at 500 ps under high fluence  $\langle N \rangle = 5.9$  such that  $P(N \geq 1) = 1$ .

photoinduced absorption and  $d\alpha_0/d\epsilon$  attain a minimum value. Referring to eq 4.7, this suggests that the photoinduced absorption at these high photon energies results from a wavelength independent spectral shift. Using this equation to calculate this presumed spectral shift  $\Delta^*$  from the experimental TA spectrum after 2.5 ps, *i.e.*, after the excitons created by the pump pulse have cooled to the band edges, we indeed find a largely constant, negative shift between photon energies of 550 and 700 nm (see Figure 4.4a). Moreover, by increasing the pump fluence, it follows that the shift  $\Delta^*$  thus calculated changes proportionally to the average number of excitons  $\langle N \rangle$  per QD (see Figure 4.4b). In this respect,  $\Delta^*$  has all the properties expected for a true spectral shift according to the simple model expressed by eq 4.9. We therefore tentatively link the slope of the  $\Delta^*$  vs  $\langle N \rangle$  curve – which amounts to  $-4.7 \pm 0.2$  meV – to the net biexciton Coulomb interaction  $\Delta$  as introduced in eq 4.5 between the hot exciton created by the probe pulse and a

cold exciton resulting from the pump pulse. We will refer to this number as  $\Delta_{hc}$ , *i.e.*, the hot-cold exciton addition energy, where the observation that  $\Delta_{hc} < 0$  points towards biexciton attraction.

Further confirmation of the interpretation of the photo-induced absorption as a spectral shift resulting from a non-zero exciton addition energy follows from the time dependence of  $\Delta^*$ . As can be seen in Figure 4.4c, the photoinduced absorption decreases within the first 100 ps after photoexcitation to a steady background value once  $\langle N \rangle$  is equal to or higher than 0.7. This is the typical lifetime of multi-excitons that recombine *via* non-radiative Auger processes, which indicates that time-dependence of  $\Delta^*$  follows that of  $\langle N \rangle$ . Moreover, when the pump fluence is increased such that  $\langle N \rangle \approx 6$  right after the pump pulse,  $\Delta^*$  attains a value of  $-4.6$  meV after 500 ps (see Figure 4.4d), a number agreeing with the spectral shift  $\Delta$  attributed before to the hot-cold biexciton addition. Since almost all QDs contain a single exciton for this combination of pump intensity and pump-probe delay, this result confirms the consistency of the interpretation put forward.

In Figure 4.5, we represent the spectral shift  $\Delta^*$  for a sample of 3.75 nm PbS QDs after a 700 nm pump pulse that creates on average 0.18 excitons per QD. It follows that  $\Delta^*$  levels off at a value of  $-0.78$  meV within 2 ps after the pump pulse. In line with Figure 4.3, this value corresponds to  $\approx 0.17\Delta_{hc}$ , such that it can indeed be attributed to the hot-cold biexciton interaction. On the other hand, within the first ps after the pump pulse, the absolute value of  $\Delta^*$  gradually increases from naught to this final value. At these early stages, the exciton created by the pump pulse has not yet relaxed to the band edges, a conclusion confirmed by the gradual increase of the bleach of the band gap transition within the same time span (see Figure 4.5, blue trace). This means that the time evolution of  $\Delta^*$  reflects the evolution of the biexciton addition energy from a hot-hot to a hot-cold combination. As such, we could estimate an upper limit to the hot-hot interaction from a deconvolution with the 180 fs pump pulse creating the hot excitation. An example is shown in Figure 4.5 (dotted line), yielding a  $\Delta_{hh}$  of 0.2 meV as upper limit which is 4 times smaller than the corresponding hot-cold shift. We therefore conclude that the hot-hot biexciton interaction  $\Delta_{hh}$  is small as compared to  $\Delta_{hc}$ .

Figure 4.6 summarizes  $\Delta_{hc}$  as determined for PbS quantum dots of different sizes. One sees that especially for the smallest QDs studied, *i.e.*, 3.75–5.65 nm,  $\Delta_{hc}$  decreases quickly with increasing diameter. For the larger QDs, it drops to values in the range  $-1.5$  to  $-1$  meV. As compared to  $\Delta_{hc}$ , the exciton addition energies  $\Delta_{cc}$  as determined previously are smaller by 15 to 35%.

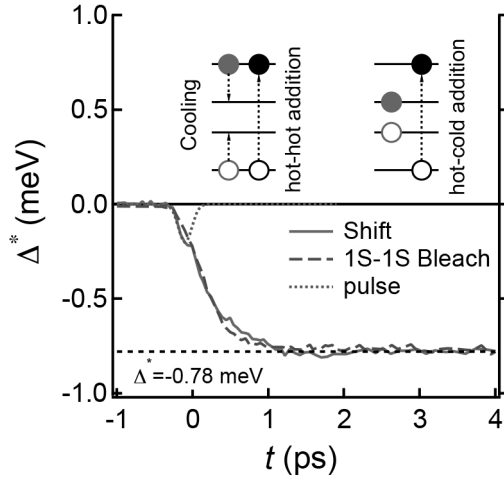


Figure 4.5: Representation of (solid line) spectral shift at 580 nm during carrier cooling upon 700 nm photoexcitation and (dashed line) the (rescaled) bleach at the 1S-1S band gap transition of 3.75 nm PbS QDs. The fluence was chosen as to create 0.18 excitons on average, which is sufficiently low to avoid any influence of multi-excitons. As indicated by the dotted line, the spectral shift reaches a value of  $-0.78$  meV within  $\approx 2$  ps after photoexcitation. The dotted grey line depicts the 180 fs pump pulse.

## 4.5 Discussion

We have shown that after photoexcitation of a quantum dot ensemble using a femtosecond pump pulse, the absorbance of the sample at photon energies well above the bandgap transition increases. The change in absorbance is consistent with a spectral redshift constant in energy, which we attribute to non-zero bi- or multiexciton addition energies. It follows that the hot-cold addition energy corresponds to the product of the biexciton addition energy  $\Delta_{hc}$  and the number of cold excitons present in the quantum dot. This biexciton addition energy is a negative number – leading to the observed spectral redshifts – with a magnitude of a few meV. It is largely independent of the actual state of the hot exciton and its magnitude decreases with increasing quantum dot diameter. Since the initial dynamics of the spectral redshift is identical to that of exciton cooling – raising from naught to a steady value within 1-2 ps – we conclude that the hot-hot biexciton addition energy  $\Delta_{hh}$  appears to be negligible as compared to  $\Delta_{hc}$ . This set of biexciton addition energies is complemented by the analysis of the spectral

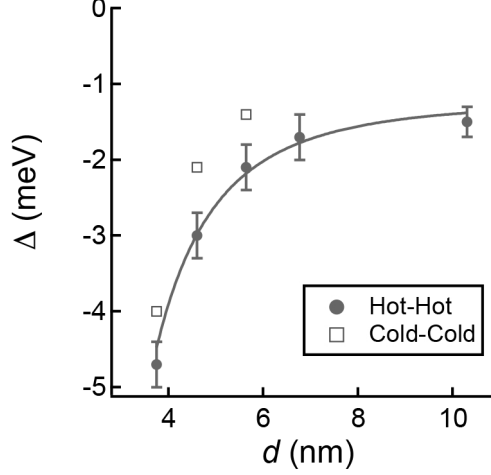


Figure 4.6: Different interaction energies for varying PbS diameter  $d$ : The hot-cold biexciton interaction energy  $\Delta_{hc}$  and the cold-cold  $\Delta_{cc}$ . A  $1/d^3$  dependence is fit to  $\Delta_{hc}$ , indicative of an expected Coulomb type size dependence.

bleach around the band gap transition, where the cold-cold biexciton addition energy could be derived from a fit of the nonlinear absorbance to a model function that takes into account state filling, spectral shifts and photoinduced absorption due to intraband transitions. As compared to  $\Delta_{hc}$ ,  $\Delta_{cc}$  is smaller by about 15-35%, while showing a similar dependence on the quantum dot diameter.

Apart from providing an interpretation of the photoinduced absorption at high photon energies, this study thus yields numbers for the hot-hot, hot-cold and cold-cold biexciton addition energy that can be compared to the expected, either based on qualitative arguments or on more detailed numerical calculations. As argued before, non-zero biexciton addition energies are typically attributed to imbalances in Coulomb attraction and repulsion between the four charge carriers constituting the biexciton. Using the notation introduced previously, the Coulomb interaction  $J_{eh,jk}$  between an electron in state  $j$  and a hole in state  $k$  can be expressed in terms of the respective single particle eigenfunctions  $\psi_{c,j}$  and  $\psi_{v,k}$  as<sup>10</sup>:

$$J_{eh,jk} = \int \int \frac{|\psi_{c,j}(\mathbf{r}_1)|^2 |\psi_{v,k}(\mathbf{r}_2)|^2}{\varepsilon(\mathbf{r}_1, \mathbf{r}_2) |\mathbf{r}_1 - \mathbf{r}_2|} d\mathbf{r}_1 d\mathbf{r}_2 \quad (4.11)$$

Here,  $\mathbf{r}_1$  and  $\mathbf{r}_2$  are the position vector of the electron and the hole, respectively, whereas  $\varepsilon(\mathbf{r}_1, \mathbf{r}_2)$  is the microscopic dielectric function. Based on

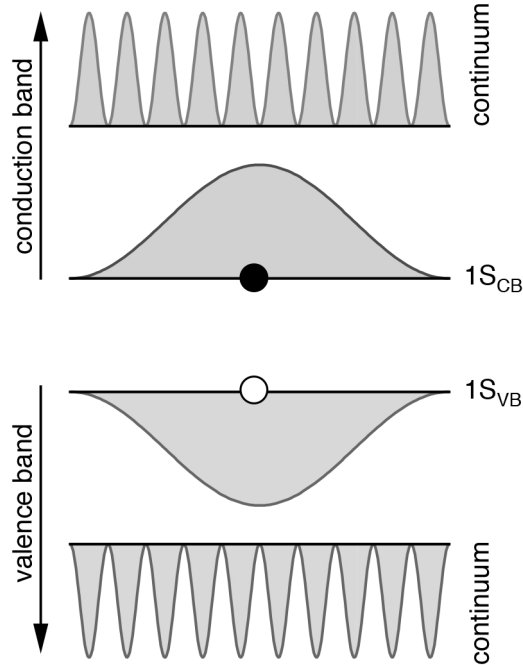


Figure 4.7: Schematic representation of the square of the envelope wavefunction of electron and hole states at the band edges and in the high energy continuum of conduction and valence band states, respectively.

eq 4.11, one sees from eq 4.4 that the biexciton addition energy will indeed get smaller with increasing quantum dot diameter, a trend in line with our observations. Moreover, exciton addition energies will reduce to zero when the wavefunction amplitude of all electron and hole states involved is spread identically over a quantum dot. In the same way, eq 4.5 indicates that with one cold electron-hole pair present, biexciton addition energies will be independent of the state of the second exciton when the electron wavefunction amplitudes and the hole wavefunction amplitudes of different electron-hole pairs again have a similar distribution over the quantum dot.

Using these rules of thumb, the experimental findings on the different biexciton addition energies, *i.e.*,  $\Delta_{cc}$ ,  $\Delta_{hc}$  and  $\Delta_{hh}$  can be rationalized by looking at the envelope wavefunction of electrons or holes at the band edges and at higher conduction or valence band states. The former are composed of small wavenumber components with an amplitude that is maximal in the center of the dot (see Figure 4.7). On the other hand, the latter are

made up of high wavenumber components with an amplitude more equally distributed over the entire quantum dot, a distribution that will be similar for different high energy states. As a result, one expects that hot-hot biexciton addition energies should be small since all electron and hole states involved have a similar distribution of their wavefunction amplitude over the quantum dot. Hot-cold biexciton addition energies on the other hand can be considerably larger, yet given the similar spreading of high energy electron and high energy hole states over the quantum dot, they will show little dependence on the particular state the hot exciton is in. Finally, since the wavefunction amplitude of band-edge electrons and holes will be more alike than that of band-edge electrons and high energy electrons or band edge holes and high energy holes, the cold-cold biexciton addition energy will tend to be smaller than the hot-cold addition energy.

The observation that the hot-cold addition energy scales as the product of the biexciton addition energy and the average number of excitons is also useful for practical purposes. Since the transient absorption spectrum of PbS quantum dots after exciton cooling is only determined by these spectral shifts in the wavelength range between 550 and 700 nm, knowledge of  $\Delta_{hc}$  enables a direct determination of  $\langle N \rangle$  from the differential absorbance at a single wavelength. Since  $\langle N \rangle$  is a central quantity in the study of processes such as multi-exciton generation, the results shown here suggest that these may be studied more directly by looking at spectral shifts in the visible part of the transient absorption spectrum rather than analyzing absorption changes around the bandgap transition.

## 4.6 Conclusion

We have presented an experimental study on the biexciton addition energy in colloidal PbS quantum dots for the cases where a cold exciton is added to a quantum dot already containing a cold exciton ( $\Delta_{cc}$ ) and a hot exciton is added to a quantum dot already containing a cold exciton ( $\Delta_{hc}$ ) or a hot exciton ( $\Delta_{hh}$ ). These exciton addition energies are derived from the transient absorption spectrum, either around the bandgap transition for cold exciton addition or at photon energies well above the bandgap for hot exciton addition. Since the transient absorbance is determined by a combination of state filling, spectral shifts and intraband absorption in the former case, we fit the differential absorbance to a model function to derive  $\Delta_{cc}$ . For hot exciton addition on the other hand, we find that the transient absorbance in the wavelength range studied is only determined by a spectral shift. As a result, a more direct determination of  $\Delta_{hc}$  and  $\Delta_{hh}$  from the transient absorbance is possible. Interestingly, we find that  $\Delta_{hc}$  is largely independent of the ac-

tual hot electron state and decreases strongly with increasing quantum-dot diameter. As compared to  $\Delta_{hc}$ ,  $\Delta_{hh}$  is negligible whereas  $\Delta_{cc}$  is smaller by 15-35% in the diameter range studied. These qualitative features of the different biexciton addition energies can be understood by interpreting the biexciton addition energy in terms of an imbalance of the Coulomb interactions between the newly created charge carriers and the charge carriers already present in the quantum dots.

## References

- [1] Klimov, V. I.; Ivanov, S. A.; Nanda, J.; Achermann, M.; Bezel, I.; McGuire, J. A.; Piryatinski, A. Single-exciton optical gain in semiconductor nanocrystals. *Nature* **2007**, *447*, 441–6.
- [2] Trinh, M. T.; Houtepen, A. J.; Schins, J. M.; Piris, J.; Siebbeles, L. D. A. Nature of the second optical transition in PbSe nanocrystals. *Nano Lett.* **2008**, *8*, 2112–7.
- [3] Gesuele, F.; Sfeir, M. Y.; Koh, W.-K.; Murray, C. B.; Heinz, T. F.; Wong, C. W. Ultrafast supercontinuum spectroscopy of carrier multiplication and biexcitonic effects in excited states of PbS quantum dots. *Nano Lett.* **2012**, *12*, 2658–64.
- [4] Beard, M. C.; Luther, J. M.; Semonin, O. E.; Nozik, A. J. Third Generation Photovoltaics based on Multiple Exciton Generation in Quantum Confined Semiconductors. *Accounts Chem. Res.* **2013**, *46*, 1252–1260.
- [5] Witzel, W.; Shabaev, A.; Hellberg, C.; Jacobs, V.; Efros, A. Quantum Simulation of Multiple-Exciton Generation in a Nanocrystal by a Single Photon. *Phys. Rev. Lett.* **2010**, *105*, 1–4.
- [6] Tisdale, W. A.; Williams, K. J.; Timp, B. a.; Norris, D. J.; Aydil, E. S.; Zhu, X.-Y. Hot-Electron Transfer from Semiconductor Nanocrystals. *Science* **2010**, *328*, 1543–1547.
- [7] Gdor, I.; Sachs, H.; Roitblat, A.; Strasfeld, D. B.; Bawendi, M. G.; Ruhman, S. Exploring Exciton Relaxation and Multiexciton Generation in PbSe Nanocrystals Using Hyperspectral Near-IR Probing. *ACS Nano* **2012**, *6*, 3269–3277.
- [8] Gdor, I.; Yang, C.; Yanover, D.; Sachs, H.; Lifshitz, E.; Ruhman, S. Novel Spectral Decay Dynamics of Hot Excitons in PbSe Nanocrystals.

- tals: A Tunable Femtosecond PumpHyperspectral Probe Study. *J. Phys. Chem. C* **2013**, *117*, 26342–26350.
- [9] Franceschetti, A.; Zunger, A. Addition energies and quasiparticle gap of CdSe nanocrystals. *Appl. Phys. Lett.* **2000**, *76*, 1731.
- [10] An, J. M.; Franceschetti, A.; Zunger, A. The Excitonic Exchange Splitting and Radiative Lifetime in PbSe Quantum Dots. *Nano Lett.* **2007**, *7*, 2129–2135.
- [11] Cademartiri, L.; Montanari, E.; Calestani, G.; Migliori, A.; Guagliardi, A.; Ozin, G. A. Size-dependent extinction coefficients of PbS quantum dots. *J. Am. Chem. Soc.* **2006**, *128*, 10337–46.
- [12] Moreels, I.; Justo, Y.; De Geyter, B.; Haustraete, K.; Martins, J. C.; Hens, Z. Size-tunable, Bright, and Stable PbS Quantum Dots: A Surface Chemistry Study. *ACS Nano* **2012**, *5*, 2004–2012.
- [13] Klimov, V. I. Quantization of Multiparticle Auger Rates in Semiconductor Quantum Dots. *Science* **2000**, *287*, 1011–1013.
- [14] Justo, Y.; Geiregat, P.; Hoecke, K. V.; Vanhaecke, F.; Donega, C. D. M.; Hens, Z. Optical Properties of PbS/CdS Core/Shell Quantum Dots. *J. Phys. Chem. C* **2013**, *117*, 20171–20177.
- [15] De Geyter, B.; Houtepen, A. J.; Carrillo, S.; Geiregat, P.; Gao, Y.; Ten Cate, S.; Schins, J. M.; Van Thourhout, D.; Delerue, C.; Siebbeles, L. D. A.; Hens, Z. Broadband and Picosecond Intraband Absorption in Lead-Based Colloidal Quantum Dots. *ACS Nano* **2012**, *6*, 6067–6074.
- [16] Cho, B.; Peters, W. K.; Hill, R. J.; Courtney, T. L.; Jonas, D. M. Bulklike hot carrier dynamics in lead sulfide quantum dots. *Nano Lett.* **2010**, *10*, 2498–505.
- [17] Trinh, M. T.; Sfeir, M. Y.; Choi, J. J.; Owen, J. S.; Zhu, X. A hot electron-hole pair breaks the symmetry of a semiconductor quantum dot. *Nano Lett.* **2013**, *13*, 6091–7.



# 5

## Hot Carrier Phonon Bottleneck in Lead-Chalcogenide Nanocrystals

We present a detailed hyperspectral analysis of the ultrafast dynamics of hot charge carriers in colloidal lead-chalcogenide nanocrystals. Carrier accumulation at high energy critical points in the Brillouin zone is demonstrated and explained theoretically in terms of a hot carrier cooling bottleneck related to the lead-chalcogenide band structure. These hot carriers are essential for a variety of applications such as fast material modulation, lasers, hot carrier charge transfer in photovoltaic cells and multiple-exciton generation. We suggest using the bulk band structure as a first indication to predict hot carrier cooling dynamics.

### 5.1 Introduction

Absorption of photons by a semiconductor with an energy exceeding the band gap transition results in the formation of hot electron-hole pairs that quickly dissipate their excess free energy, resulting in (quasi) thermalized conduction band electrons and valence band holes. For photovoltaic solar energy conversion, this cooling of the hot electron-hole pair is a major loss channel that restricts the maximum conversion efficiency of a single junction solar cell to the Shockley-Queisser limit<sup>1</sup>. Harvesting this excess free energy by competing processes such as hot charge carrier transfer has

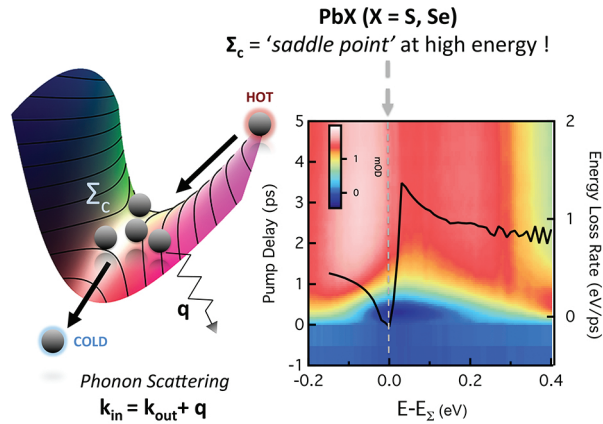


Figure 5.1: Overview of phonon bottleneck results.

proven challenging due to the high cooling rate, which can reach  $1 \text{ ps}^{-1}$  or more due to electron-phonon and/or carrier-carrier interactions.<sup>2</sup> On the other hand, good use can be made of the high cooling rate for all-optical light modulation, where response times of a few ps have been demonstrated using, *e.g.*, hot carriers generated by light absorption in graphene<sup>3</sup> or injected in ITO through a plasmonic nanoparticle as a sensitizer.<sup>4</sup> Similar approaches of hot electron transfer following the optical excitation of surface plasmons have recently been applied in catalysis<sup>5</sup>, photovoltaics, photodetection<sup>6</sup> and nanoscopic imaging<sup>7</sup>.

In the field of semiconductor nanocrystals or quantum dots (QDs), electron-hole pair cooling has attracted wide interest especially since a slowing down of electron and hole cooling due to a phonon bottleneck was predicted.<sup>8</sup> The discrete energy levels in QDs may be separated by several LO phonon energies hence requiring multi-phonon emission for cooling, a process which is very unlikely. Whereas for specially designed QDs, a slowing of the cooling of the conduction band electron from its 1P to its 1S state could be confirmed,<sup>9</sup> carrier cooling appeared to remain fast in most QDs with rates still close to  $1 \text{ ps}^{-1}$ , a result often attributed to additional cooling pathways involving Auger processes or energy transfer to surface ligands<sup>9</sup>. Nevertheless, it proved possible to harvest the excess energy of hot excitons either by hot carrier transfer<sup>10</sup> or the generation of multiple excitons.<sup>11–13</sup> Both processes involve hot electron-hole pairs with a substantial excess energy – at least the QD band gap in the case of multiple exciton generation – and their efficiency therefore depends on competition with cooling of electrons and holes occupying energy levels far from the

band edges. Most studies of carrier cooling however focus on the changing occupation of states close to the band edge. Since filling of band-edge states is the end point of the cooling process, this only gives a view on the rate determining step of the entire cooling cascade, which very often corresponds to the 1P-1S transition. Being the final stage of the cooling cascade, this makes that the cooling rates thus obtained are not the most relevant for multiple exciton generation or hot carrier transfer.

## 5.2 Experiments

Here, we analyze electron-hole pair cooling in PbS and PbSe colloidal QDs after excitation with high energy photons where, by means of white light transient absorption spectroscopy, energy levels throughout the entire Brillouin zone are probed. PbS and PbSe are probably the most widely studied QDs for photovoltaics and photodetection, showing effective multiple exciton generation at thresholds close to the theoretical limits<sup>11;12;14</sup> and yielding the most efficient QD-based solar cells.<sup>15</sup> In bulk, both have a direct band gap at the 4-fold degenerate  $L$  point of the Brillouin zone. At higher energy, there are a number of critical points, most notably along the  $\Sigma$  and  $\Delta$  direction in the Brillouin zone, which result in specific, size-dependent features in the QD absorption spectrum as well.<sup>16–18</sup> Most notably, we observe a transient accumulation of charge carriers at the critical point along the  $\Sigma$  direction – labeled as  $\Sigma_c$  – when the pump-photon energy exceeds the energy difference at  $\Sigma_c$ . We link this cooling bottleneck, which slows down carrier cooling to the net rate of  $\approx 1 \text{ ps}^{-1}$  that is typically observed when monitoring band-edge states, to the energy level structure around  $\Sigma_c$  and we show that cooling *via*  $\Sigma_c$  is the dominant pathway for high energy charge carriers. Moreover, the buildup rate of the carrier population at  $\Sigma_c$  gives a direct way to probe cooling rates of high energy charge carriers, cooling rates that are most relevant for competing processes such as multiple exciton generation or hot carrier transfer.

We start with results obtained on PbS nanocrystal dispersions synthesized according to a procedure described by Moreels *et al.*<sup>21</sup>, with average diameters  $d_{NC}$  that we determined from the peak wavelength of the first exciton transition as indicated in Figure 5.2a.<sup>19</sup> As shown in Figure 5.2b, various transitions between valence and conduction band states can be traced back by means of the second derivative of the absorbance, where next to the well-known 1S-1S and 1P-1P transitions a third transition at visible wavelengths stands out. In the case of PbSe QDs, a similar feature was attributed to electron transitions close to the critical point in the band structure along the  $\Sigma$  direction,<sup>18</sup> *i.e.*, the point we indicate as  $\Sigma_c$  (see Figure 5.2c). Fig-

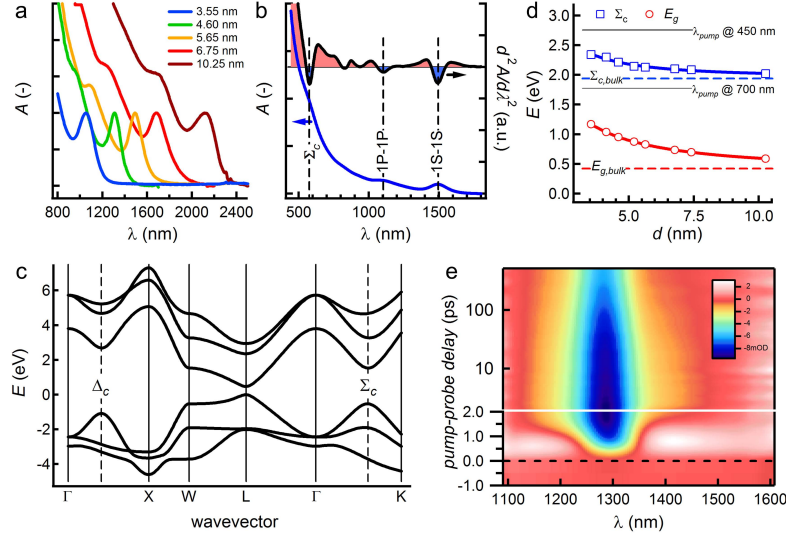


Figure 5.2: (a) Overview of absorption spectra of PbS QDs of different sizes, including (blue, orange, dark red) the three samples used in this study. For each spectrum, the legend indicates the average diameter as determined from the maximum of the first exciton absorption.<sup>19</sup> (b) Absorption spectrum and second derivative spectrum of 5.65 nm PbS QDs with an assignment of the most relevant absorption features as the 1S-1S, 1P-1P and  $\Sigma_c$  transition. (c) Representation of the PbS bulk band structure with an indication of the critical points  $\Sigma_c$  and  $\Delta_c$  along  $\Sigma$  and  $\Delta$ . (d) Size-dependence of the 1S-1S and the  $\Sigma_c$  transition energy, together with an indication (dashed lines) of the corresponding bulk values<sup>20</sup> and the photon energies corresponding to the pump wavelengths used in this study. (e) Time-wavelength map of the differential absorbance near the bandgap transition for 4.6 nm PbS nanocrystals.

Figure 5.2d demonstrates that the feature appearing at visible wavelengths in the second derivative spectra of PbS QDs shows weaker confinement than the bandgap transition and extrapolates with increasing  $d_{NC}$  to the  $\Sigma_c$  energy difference of 1.94 eV as reported for bulk PbS.<sup>20</sup> As this behaviour is highly similar to that of the  $\Sigma_c$  transition in PbSe QDs, we also attribute this visible feature in PbS QDs to the electronic transitions around  $\Sigma_c$  as already suggested by Cadmeratiri *et al.*<sup>17</sup>.

Figure 5.2e shows the change of the absorption spectrum of 4.6 nm PbS QDs around their bandgap transition following a 180 fs laser pulse at

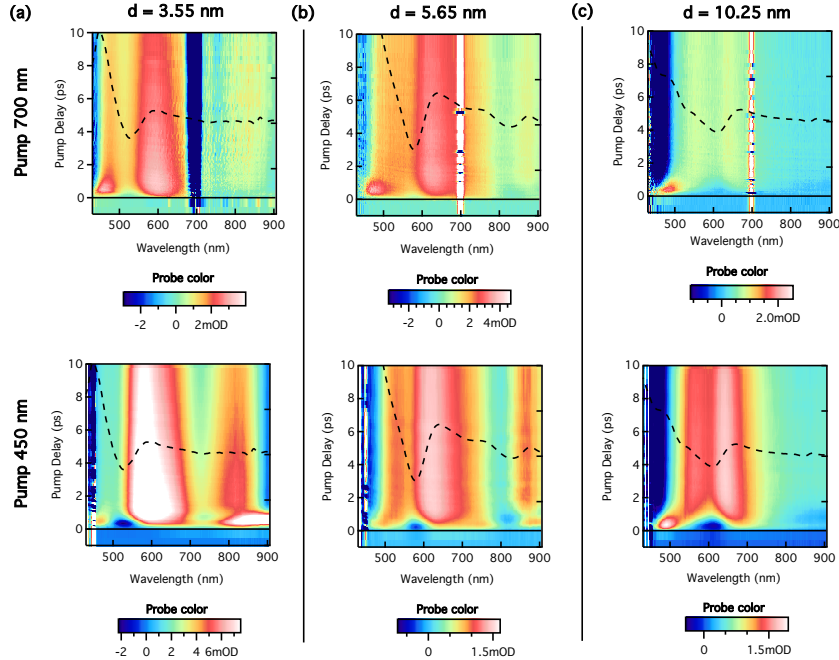


Figure 5.3: Contour maps of  $\Delta A$  illustrating the carrier dynamics of the high energy transition (*i.e.* in the visible spectrum) for 3 different sizes of PbS nanocrystals: (a) 3.55 nm, (b) 5.65 nm and (c) 10.25 nm. Samples were pumped at 700 nm (top row) and 450 nm (bottom row). Color scale goes from negative (blue) to positive (red). The black dotted line is the second derivative of the corresponding linear absorption spectrum. Minimum corresponds to the onset of the absorption of the  $\Sigma$ -point transitions.

700 nm that creates on average 0.3 excitons per QD. The change in absorption, defined as the difference in absorbance  $\Delta A = A^* - A_0$  of the dispersion after and before photoexcitation, respectively, is represented by a color code as a function of probe wavelength and time delay after the excitation pulse. The figure shows the typical reduction of the bandgap absorption due to the occupation of the band-edge states by photogenerated electrons and holes.<sup>22</sup> The buildup of the bleach signal around the bandgap transition within the first 1 – 2 ps after the pump pulse reflects the final step of the cooling of the photogenerated charge carriers to the band-edge states, a process accompanied by a strong reduction of the sub-bandgap photoinduced absorption related to intraband transitions.<sup>23</sup>

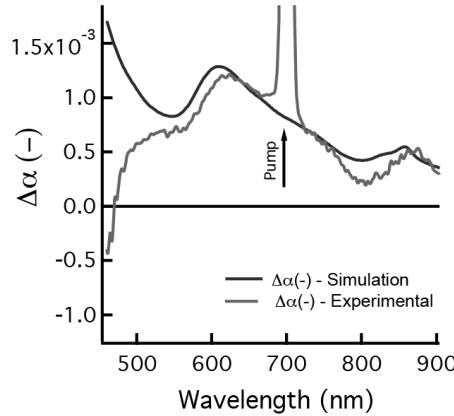


Figure 5.4: Representation of the measured  $\Delta A$  spectrum for 5.65 nm PbS excited at 700 nm and the  $\Delta A$  spectrum calculated assuming a wavelength-independent spectral shift of -1.3 meV.

Being the result of a cascade of cooling steps *via* phonon emission, the rate of band-edge state filling may not give an accurate view on the initial cooling dynamics of the high energy electron and hole created by the pump pulse, which is the most relevant in view of competing processes such as hot carrier extraction or carrier multiplication<sup>14</sup>. Therefore, we probed the transient absorption at photon energies well above the QD bandgap. As shown in Figure 5.3a-c, such above bandgap transient absorption maps are dominated by photo-induced absorption ( $\Delta A > 0$ ) for all PbS QDs studied when using a pump wavelength of 700 nm ( $\hbar\omega = 1.77$  eV). As is shown in Figure 5.4 this photo-induced absorption results from a spectral redshift that is largely independent of the probe wavelength. Following the argumentation developed in chapter 4 and the paper by Geiregat et al.<sup>24</sup>, we attribute this spectral shift to the net Coulomb interaction between the exciton(s) resulting from the pump-pulse and the exciton newly created by the probe pulse.

When changing the excitation wavelength to 450 nm, *i.e.*, to photon energy well above the  $\Sigma_c$  transition, the most notable difference in the transient absorption maps is the appearance of a short lived negative  $\Delta A$  at around 500–600 nm. The occurrence of this bleach feature in the first 1–2 ps after photoexcitation, *i.e.*, the typical cooling time, points to the temporal blocking of electronic transitions due to the accumulation of cooling charge carriers in particular electronic states. The dashed line added to each transient absorption map in Figure 5.3 represents the second derivative of the respective absorption spectra, where the dip corresponds to the position of

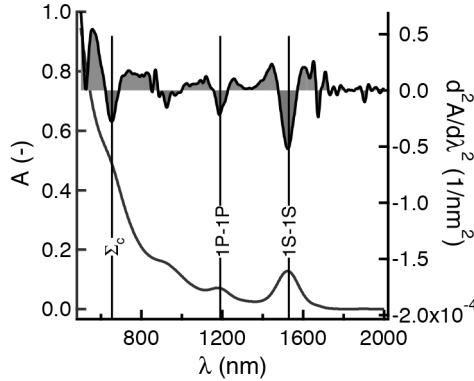


Figure 5.5: Linear absorption spectrum of 4.8 nm PbSe nanocrystals, showing the 1S-1S and 1P-1P transitions at lower energy and the  $\Sigma_c$ -transition at higher energies.

the  $\Sigma_c$  transition (see Figure 5.2b). It can be clearly seen that for each QD sample analysed the wavelength range of the transient bleach corresponds to that of the  $\Sigma_c$  transition. We thus conclude that the cooling of charge carriers can be shortly delayed in the electronic states around the critical point along the  $\Sigma$  direction in the Brillouin zone.

**PbSe Analysis** To show the general character of the observed effect in PbS, we also measured on 4.8 nm PbSe nanocrystals. The PbSe nanocrystals were synthesised using a method described by Steckel *et al.*<sup>25</sup>. The linear absorption spectrum is shown in Figure 5.5 and shows similar features as the spectra obtained for PbS QDs: 1S-1S and 1P-1P transitions are clearly discerned, as is the  $\Sigma_c$  ensemble at higher energies (shorter wavelengths). Similar 2D maps are obtained after 350 nm and 1500 nm photoexcitation, *i.e.* above and below the  $\Sigma_c$  transition respectively (see Figure 5.6).

### 5.3 Kinetic Analysis: a 3 Level Model

Taking vertical cuts through the 2D maps of Figure 5.3 at the maximum of this transient bleach feature, we obtain the kinetic traces displayed in Figure 5.7a for the 5.65 nm PbS nanocrystals. We clearly observe that excitation above the  $\Sigma_c$ -transition (at 450 nm pump) leads to a trace distinctly different from excitation below  $\Sigma_c$  (at 700 nm). While pumping at 700 nm only leads to the rapid buildup of a photo-induced absorption, a bleach

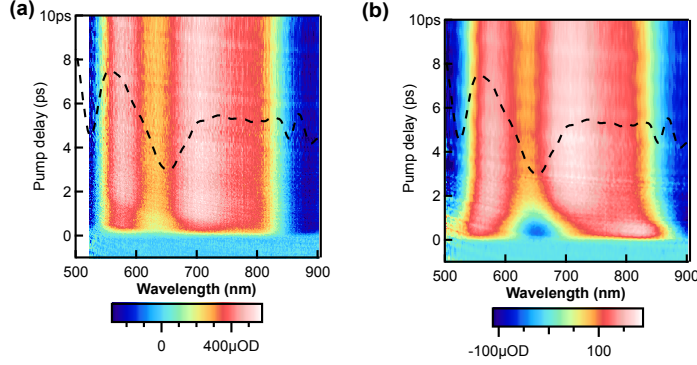


Figure 5.6: Contour maps of  $\Delta A$  illustrating the carrier dynamics of the high energy transition (*i.e.* in the visible part of the spectrum) for 4.8 nm PbSe QDs. Color scale goes from negative (blue) to positive (red). The black dotted line is the second derivative of the corresponding linear absorption spectrum where the minimum corresponds to the onset of the absorption of the  $\Sigma_c$ -point transitions: (a) excitation at 1300 nm and (b) at 350 nm.

feature develops and vanishes for the sample pumped at 450 nm on a sub-picosecond timescale. If we interpret the transient absorption at 450 nm as composed of a bleach feature due to charge carrier accumulation and photo-induced absorption due to exciton-exciton interaction, the trace recorded with a 700 nm pump can be seen as a measure for the photo-induced absorption background. The resulting net bleach, obtained by subtracting the (properly rescaled) 700 nm from the 450 nm pump trace has been added to Figure 5.7a.

We tentatively model this net bleach by considering 3 different states, representing hot carriers, carriers occupying states around  $\Sigma_c$  and cold carriers, where hot carriers occupy the states around  $\Sigma_c$  at a rate  $k_{in}$  and these cool down further at a rate  $k_{out}$  (see Figure 5.7b). As a result, the transient exciton population  $\langle N \rangle_{\Sigma}(t)$  around  $\Sigma_c$  can be described as:

$$\langle N \rangle_{\Sigma}(t) = \frac{k_{in}}{k_{out} - k_{in}} f \langle N \rangle \left( e^{-k_{in}t} - e^{-k_{out}t} \right) \quad (5.1)$$

Here,  $\langle N \rangle$  represents the average number of excitons created per QD by the pump pulse and  $f$  is the fraction of excitons cooling *via*  $\Sigma_c$ . A fit of the net bleach to Eq 5.1 is shown in Figure 5.7c, where the bleach signal has been rescaled to represent the occupation probability  $\sigma(t)$  of the states

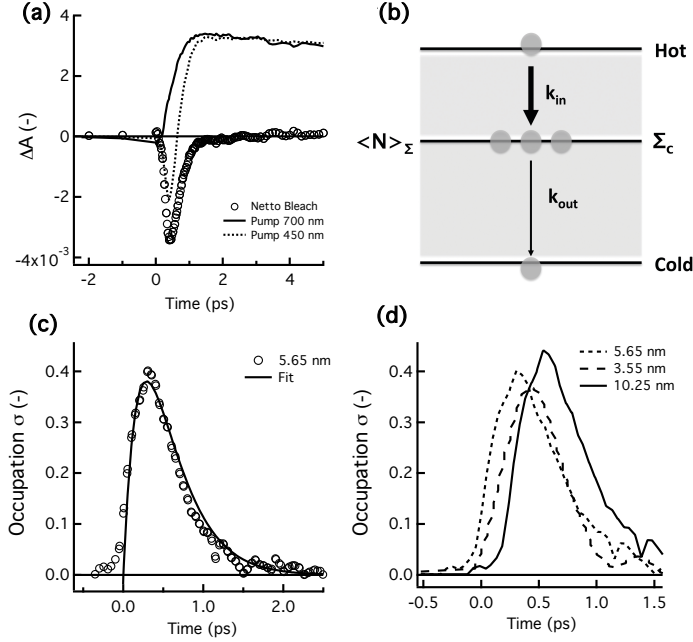


Figure 5.7: Kinetic analysis of  $\Delta A$  of 5.65 nm QDs (a) Carrier dynamics at  $\Sigma_c$  for excitation below (700 nm) and above (450 nm) the  $\Sigma_c$ -transition. Empty markers indicate the netto bleach. (b) Schematic depicting simple 3-level approach to model the observed netto bleach at  $\Sigma_c$ : inflow from carriers from higher energy (hot) and outflow to lower energy (cold) levels. (c) Probability  $\sigma(t)$  to have 1 exciton in the ensemble of  $\Sigma$ -states as a function of time (see text) for the 5.65 nm size PbS QDs. A fit to Eq 5.1 of the experimental data (empty circles) is shown (solid red line). (d) Probability  $\sigma(t)$  for the 3 sizes studied.

around  $\Sigma_c$  ( $\sigma(t) = \langle N \rangle_{\Sigma} / f \langle N \rangle$ ). The corresponding rates  $k_{in}$  and  $k_{out}$  have been summarized in Table 1 for the different PbS QDs studied. One sees that, regardless of the QD size, the rate of cooling towards and away from  $\Sigma_c$  amounts to  $\approx 3.8$  and  $2.8 \text{ ps}^{-1}$ , which implies that  $\sigma(t)$  reaches a maximum value of  $\approx 0.4$ .

We see that passage via the  $\Sigma$  direction critical point delays the cooling of charge carriers. By means of  $k_{in}$ , the 3-level model analysis provides a way to estimate the initial cooling rate of hot charge carriers and not the final cooling rates which are typically measured when looking at state filling of the band-edge states. Clearly, this initial cooling rate is what matters for

QD	$d_{NC}$ (nm)	$k_{in}$ (ps <sup>-1</sup> )	$k_{out}$ (ps <sup>-1</sup> )
PbS	3.55	3.8	2.8
PbS	5.65	3.9	2.9
PbS	10.2	4.1	3.1
PbSe	4.80	1.85	2.7

Table 5.1: Summary of the rates of cooling towards ( $k_{in}$ ) and away from ( $k_{out}$ )  $\Sigma_c$  as obtained by fitting the experimental traces to Eq 5.1.

QD	$d_{NC}$ (nm)	$w_{E,in}$ (eV ps <sup>-1</sup> )	$w_{ph,in}$ (ps <sup>-1</sup> )
PbS	3.55	0.76	29
PbS	5.65	1.2	45
PbS	10.2	1.5	58
PbSe	4.80	0.37	44

Table 5.2: Summary of the energy loss rates  $w_{E,in}$  and phonon emission rates  $w_{ph,in}$ .  $w_{E,in}$  (see text) is obtained from the product of  $k_{in}$  and the energy per charge carrier to be dissipated for cooling towards  $\Sigma_c$ .

most processes aiming at harvesting the hot exciton energy. Moreover, this rate will also set a limit to applications such as light modulation that could make use of the rapid change of opto-electronic properties that come with cooling. It should be noted that the figure of  $\approx 4$  ps<sup>-1</sup> reported here most likely underestimates the cooling rate since it approaches the reciprocal of the temporal width of the pump pulse.

## 5.4 Spectral Analysis: the Relevance of the Bottleneck

A key quantity in Eq 5.1 is the fraction  $f$  of the excited electron-hole pairs that cool *via*  $\Sigma_c$ . When  $f \approx 1$ , most charge carriers experience a temporal slowing down of their cooling, which increases the probability for competing processes to harvest the excess free energy of the electron-hole pair. On the other hand, when  $f \ll 1$ , the observation of a slowdown of the cooling rate merely serves as a way to estimate the initial hot carrier cooling rate yet has little influence on the overall carrier cooling rate. Considering again the valence and conduction band states around  $\Sigma_c$  as single levels with re-

spective degeneracies  $g_V$  and  $g_C$  provides us with a way to estimate  $f$  from the maximum bleach of the absorbance. Within this picture, the integrated absorption coefficient (related to the experimentally accessible absorbance  $A$  through  $A = \alpha L / \ln 10$ , with  $L$  the cuvette length) of the  $\Sigma_c$  transition can be written as:

$$\alpha_{int,\Sigma_c} = g_V g_C \alpha_{0,\Sigma_c} \quad (5.2)$$

Here,  $\alpha_{0,\Sigma_c}$  represents the average integrated absorption coefficient of an individual transition between valence and conduction band contributing to the  $\Sigma_c$  absorbance. If an exciton is present in these levels, the absorption coefficient changes due to state filling and the possibility for stimulated emission. The resulting non-linear absorption coefficient reads:

$$\alpha_{int,\Sigma_c}^* = (g_V - 1)(g_C - 1)\alpha_{0,\Sigma_c} - \alpha_{0,\Sigma_c} \quad (5.3)$$

As a result, we can write the normalized change in transmission (bleach) for an average occupation  $\langle N \rangle$  as:

$$\frac{\Delta\alpha}{\alpha_{int,\Sigma_c}} = \frac{\alpha_{int,\Sigma_c}^* - \alpha_{int,\Sigma_c}}{\alpha_{int,\Sigma_c}} = \frac{g_V + g_C}{g_V g_C} \langle N \rangle_{\Sigma_c} \quad (5.4)$$

Hence, the maximum normalized bleach after integration becomes:

$$\frac{\Delta\alpha}{\alpha_{int,\Sigma_c}} = \frac{g_V + g_C}{g_V g_C} f \sigma_{max} \langle N \rangle \quad (5.5)$$

To determine the fraction  $f$  of hot carriers cooling via  $\Sigma_c$  from the experimental transient absorption data, the degeneracies  $g_V$  and  $g_C$  must be known. Since there are 12 equivalent  $\Sigma$  directions, the degeneracies  $g_V$  and  $g_C$  should be 24 at least (including spin). On the other hand,  $g_V$  and  $g_C$  will be capped by the product of the density of states around  $\Sigma_c$  for bulk PbS and the spectral width of the  $\Sigma_c$  bleach. In Figure 5.8, we plot the density of states needed according to Eq 5.5 to have  $f = 1$  or  $f = 0.1$  together with the above mentioned lower and upper limits to the degeneracy, where we used a density of states of 0.5 eV/PbS unit cell for bulk PbS around  $\Sigma_c$ .<sup>26</sup> One sees that for all QD sizes studied, the degeneracy needed to have  $f = 1$  closely agrees with that calculated from the bulk density of states while for the smallest QDs,  $f = 0.1$  corresponds to degeneracies that are physically impossible. We thus conclude that a sizeable fraction of the excitons, if not all excitons, cool via  $\Sigma_c$  and thus experience a transient slow-down of the cooling rate.

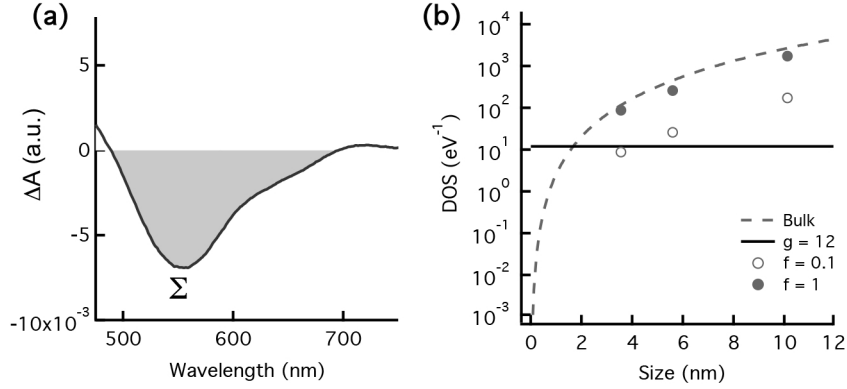


Figure 5.8: Estimation of fraction  $f$  of hot carriers cooling *via*  $\Sigma_c$  (a) Netto bleach spectrum used to calculate integrated absorption spectrum  $\delta\alpha$  (b) Bulk prediction and lower limit for number of states involved in the  $\Sigma_c$  transition. Markers indicate the experimentally obtained values for  $f = 0.1$  (empty markers) and  $f = 1$  (filled markers). The coincidence of the  $f = 1$ -markers with the bulk number of states indicates that  $f$  is of the order of unity, indicating that also the fraction of the hot carriers cooling *via*  $\Sigma_c$  is of the order of unity.

## 5.5 Relaxation Modeling

To gain a better understanding of the observed reduction of the cooling rate, we return to the band structure of bulk PbS, which we calculated within the tight-binding approximation. As shown in Figure 5.2c, the lowest conduction band minima and the highest valence band maxima are located at the eightfold degenerate L points of the Brillouin zone. Other critical points can be found, for example, along the  $\Sigma$  ([110]) and  $\Delta$  ([100]) direction, where in particular around  $\Sigma_c$ , our results point towards a slowing down of charge carrier cooling. Importantly, both  $\Sigma_c$  and  $\Delta_c$  are saddle points, meaning that the first derivatives of the energy  $E_{\mathbf{k}}$  with respect to the three components of  $\mathbf{k}$  vanishes – giving rise to a high density of states and a marked feature in the optical absorption spectrum – whereas the band curvature is either positive or negative depending on the direction in the Brillouin zone. For example, near  $\mathbf{k}_{\Sigma_c} = \frac{\pi}{a}[1, 1, 0]$ , the conduction band can be approximated as:

$$E_{c,\mathbf{k}} \approx E_{c,\Sigma_c} + \frac{\hbar^2}{2} \left( \frac{\delta k_{110}^2}{m_{110}} + \frac{\delta k_{1\bar{1}0}^2}{m_{1\bar{1}0}} - \frac{\delta k_{001}^2}{m_{001}} \right) \quad (5.6)$$

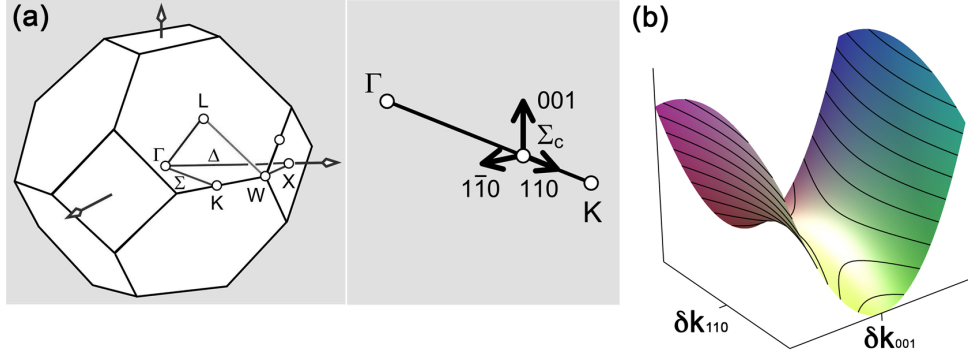


Figure 5.9: (a) Representation of (left) the Brillouin zone of the fcc lattice with an indication of the most prominent symmetry points and directions and (right) the local coordinate system introduced to analyse the dispersion relation around  $\Sigma_c$ . (b) 2D plot of the energy dispersion as a function of  $\delta k_{110}$  and  $\delta k_{001}$  showing pronounced positive curvature (light effective mass) along  $(110)$  and a relatively small negative curvature (heavy effective mass) along  $(001)$ .

Here,  $\delta \mathbf{k} = (\delta k_{110}, \delta k_{1\bar{1}0}, \delta k_{001})$  is defined as the difference between the wavevector  $\mathbf{k}$  of the actual electron state and  $\mathbf{k}_{\Sigma_c}$ , projected on the directions indicated by the subscript (see Figure 5.9a) and  $m_{110}$  ( $0.20 m_0$ ),  $m_{1\bar{1}0}$  ( $0.17 m_0$ ) and  $m_{001}$  ( $0.80 m_0$ ) are the corresponding effective masses. As shown in Figure 5.9b, the energy dispersion is positive along the  $[110]$  ( $\Sigma_c \rightarrow K$ ) and  $[1\bar{1}0]$  ( $\Sigma_c \rightarrow X$ ) direction yet it is negative along  $[001]$  ( $\Sigma_c \rightarrow L$ ) (these directions have been indicated in Figure 5.9a). Moreover, the effective mass is much larger, *i.e.*, the energy surface is far less curved, along  $[001]$  than along the two others directions, which feature similar curvature.

## 5.6 Tight Binding Calculations

### 5.6.1 PbS Band Structure around Critical Points

The conduction band near  $\Sigma_c(\mathbf{k} = \mathbf{k}_0)$  approximately behaves as:

$$E_{c,\mathbf{k}} \approx E_{c,\Sigma_c} + \frac{\hbar^2}{2} \left( \frac{\delta k_{110}^2}{m_{110}} + \frac{\delta k_{1\bar{1}0}^2}{m_{1\bar{1}0}} - \frac{\delta k_{001}^2}{m_{001}} \right) \quad (5.7)$$

In which the energy and the  $\mathbf{k}$ -vector are defined with respect to the  $\Sigma_c$ -point taken as reference  $\epsilon(\mathbf{k}) = E(\mathbf{k}) - E(\mathbf{k}_0)$ .  $m_{110} = 0.19 m_0$ ,  $m_{1\bar{1}0} = 0.14 m_0$  and  $m_{001} = 0.65 m_0$  are the effective masses along  $[110]$ ,  $[1\bar{1}0]$  and  $[001]$  directions, respectively. The energy dispersion is positive along  $[110]$  ( $\Sigma - K$ ) and  $[1\bar{1}0]$  ( $\Sigma - X$ ) directions but is negative along the  $[001]$  direction ( $\Sigma - L$  in Figure 5.10). The effective mass along  $[001]$  is much heavier than the two others which have similar values. As shown by Delerue et al.<sup>27</sup>, this behavior can be understood using an effective tight-binding model of  $p$  orbitals ( $p_x, p_y, p_z$ ) on Pb and S (Se) atoms in which only nearest-neighbor  $pp\sigma$  hopping matrix elements ( $V_{pp\sigma}$ ) are considered. Due to the rock-salt structure of PbS (PbSe),  $p_x$  orbitals only couple to  $p_x$  ones (idem for  $p_y$  and  $p_z$ ), and we are left with a simple problem of independent chains of  $p_x, p_y$ , and  $p_z$  orbitals along  $x, y, z$  axes, respectively. The  $p_x$  bands in this model are given by:

$$E_x(\bar{k}) = \left( \frac{E_p^{Pb} + E_p^S}{2} \right) \pm \sqrt{\frac{E_p^{Pb} + E_p^S}{2} + 4V_{pp\sigma}^2 \cos^2\left(\frac{k_x a}{2}\right)} \quad (5.8)$$

where  $E_p^{Pb}$  and  $E_p^S$  are the on-site  $p$  energies for Pb and S, respectively ( $E_p^{Pb} > E_p^S$ ). Formally, similar expressions hold for  $p_y$  and  $p_z$  bands. Positive and negative signs describe conduction and valence bands, respectively.  $p_x$  and  $p_y$  conduction bands present a minimum at  $\mathbf{k}_0$  where they are degenerate ( $k_x = k_y = \pi/a$ ).  $E_x(k)$  and  $E_y(k)$  do not depend on  $k_z$ , the two bands are totally flat along  $z$  (*i.e.* along  $\Sigma - L$ ). Beyond this simple model, when the spin-orbit interaction and other (smaller) hopping terms are introduced in the effective Hamiltonian, the coupling between  $p_x$  and  $p_y$  bands leads to the formation of two separate bands and the lowest conduction band acquires negative dispersion along  $\Sigma - L$  due to the repulsion between the two bands, giving a minimum at  $L$ . The effective masses along  $[110]$  and  $[1\bar{1}0]$  directions are small because of the strong  $pp\sigma$  interaction.  $m_{001}$  is heavier because the band dispersion along  $[001]$  is only induced by smaller couplings, in particular by the spin-orbit interaction.

The situation is formally symmetric in the valence band. Equation 9 is still valid if  $\epsilon(\mathbf{k}) = E(\mathbf{k}) - E(\mathbf{k}_0)$  is taken as the energy of the hole. The effective masses are  $m_{110} = 0.22 m_0$ ,  $m_{1\bar{1}0} = 0.17 m_0$ , and  $m_{001} = 3.1 m_0$ . The mass along  $[001]$  is very heavy because the valence bands are more localized on sulfur atoms than on lead atoms, and the spin-orbit coupling is almost negligible on a light element such as sulfur. Figure 5.10 shows that the highest valence band is quite flat along the  $\Sigma - L$  direction.

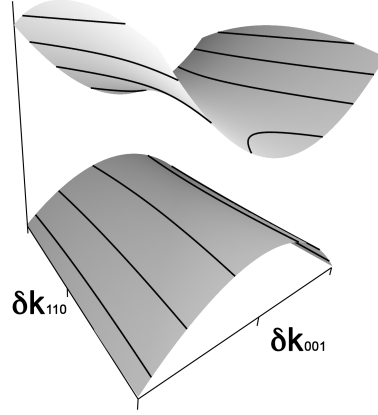


Figure 5.10: Schematic showing the energy dispersion along  $\delta\mathbf{k}_{110}$  and  $\delta\mathbf{k}_{001}$  for both conduction (top surface) and valence band (lower surface).

### 5.6.2 Carrier Cooling in Polar Semiconductors

The cooling of hot carriers in polar materials like PbS and PbSe is mainly due to scattering by longitudinal optical (LO) phonons,<sup>28</sup> where the matrix element describing the coupling between electrons and LO phonons has been derived by Fröhlich<sup>29;30</sup>. Assuming dispersionless LO phonons of energy  $\hbar\omega_{LO}$  (26 meV in PbS<sup>31</sup>, 17 meV in PbSe<sup>32</sup>), we accordingly define the rate of energy loss  $w_E$  as  $\pm\hbar\omega_{LO}$  multiplied by the scattering rate  $w$  (in 1/s) for emission (+) or absorption (−) of a phonon. Using the Fermi golden rule, the energy loss rate for a carrier in a state  $|\mathbf{k}\rangle$  can then be determined by summing over all possible phonon wavevectors  $\mathbf{q}$ :<sup>29</sup>

$$w_E(\mathbf{k}) = \frac{(2\pi e\hbar\omega_{LO})^2}{\hbar V} \left( \frac{1}{\varepsilon(\infty)} - \frac{1}{\varepsilon(0)} \right) \sum_{\mathbf{q}} \frac{|\langle \mathbf{k} - \mathbf{q} | e^{-i\mathbf{q}\cdot\mathbf{r}} | \mathbf{k} \rangle|^2}{q^2} \times \dots$$

$$\{ (N + 1)\delta(E_{\mathbf{k}-\mathbf{q}} - E_{\mathbf{k}} + \hbar\omega_{LO}) - N\delta(E_{\mathbf{k}-\mathbf{q}} - E_{\mathbf{k}} - \hbar\omega_{LO}) \}$$
(5.9)

Here,  $N = 1/[\exp(\hbar\omega_{LO}/kT) - 1]$  is the average number of phonons at temperature  $T$  in a given mode,  $\varepsilon_0$  and  $\varepsilon_\infty$  are the static and high frequency dielectric constant and  $V$  is the crystal volume. The first term in the second line of Eq 5.9 describes the emission of phonons, the second the absorption.

We used Equation 5.9 to calculate the energy loss rate for hot charge carriers using the bulk PbS electron states calculated in tight-binding (see Methods section), considering  $10^9$  different  $\mathbf{q}$  vectors in the Brillouin zone.

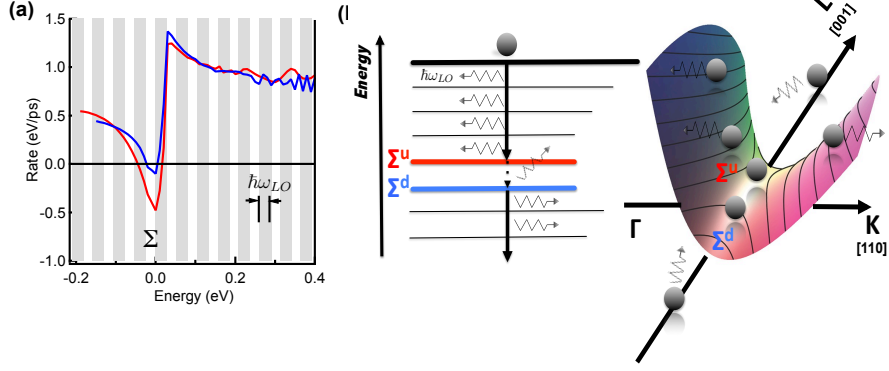


Figure 5.11: (a) Energy loss rate at 300K calculated for an electron (light line) or hole (dark line) placed in the lowest (highest) conduction (valence) band near the  $\Sigma_c$  ( $\mathbf{k}_0 = \frac{\pi}{a}[110]$ ) point where the zero of energy corresponds to the energy of  $\Sigma_c$ . The  $\bar{k}$ -vector of the initial electron state is oriented along [110] with respect to  $\mathbf{k}_0$  for  $E > 0$  and along [001] for  $E < 0$  (b) A depiction of a hot carrier cooling through a process of fast phonon emission (with quantized energy  $\hbar\omega_L$ ) until a bottleneck transition is reached, denoted as  $\Sigma_c^u \rightarrow \Sigma_c^d$ .

Figure 5.11 represents the resulting rate at 300 K for electrons and holes near  $\Sigma_c$ . For electrons with a relatively high excess energy relative to  $E_{\Sigma_c}$  ( $E - E_{\Sigma_c} \gg \hbar\omega_L$ ) the rate is more or less constant, in the  $\text{eV ps}^{-1}$  range. This is a typical result for hot carrier relaxation in polar materials<sup>28</sup> and its order of magnitude agrees with the rate  $w_{E,in}$  derived here for carrier cooling towards  $\Sigma_c$  (see Table 5.1). However, when the carrier energy is progressively reduced, the rate first slightly increases but then suddenly drops to reach very small values. Decreasing the energy below  $E_{\Sigma_c}$  results again in a saturation of the cooling rate, yet at a smaller value than at high energy. The behavior for holes near  $\Sigma_c$  is similar, but even more pronounced. Negative rates are predicted in an energy window of about 70 meV at 300 K, which means that the hole has a higher probability to move up, *i.e.* absorb a photon, than down. This is a direct consequence of the almost flat valence-band energy surface in the [001] direction, which implies a very high hole effective mass in that direction.

Our findings can be understood more qualitatively by returning to Equation 5.9, which shows that two elements favor high loss rates. First, non-

zero contributions to the loss rate are only obtained for those phonons where the phonon energy and momentum matches the energy difference between the initial and a final electron state. Hence for a given phonon dispersion relation, the larger the electron density of states, the higher the cooling rate. Second, having  $q^2 = |\mathbf{q}|^2$  in the numerator implies that high loss rates result from electron scattering by phonons that meet energy and momentum conservation with small magnitude phonon or scattering wavevectors  $\mathbf{q}$ , *i.e.*, when the gradient  $\nabla_{\mathbf{k}}E$  is large (see next section). Returning to the dispersion relation around  $\Sigma_c$ , it follows that both elements favor rapid cooling towards  $\Sigma_c$  yet hamper cooling away from  $\Sigma_c$ . While there are two directions of positive curvature with low effective masses, there is only one of negative curvature with a high effective mass. This results in a higher density of states and steeper energy gradients above than below  $\Sigma_c$ , which makes that the change of direction of the scattering wavevector necessary to pass  $\Sigma_c$  constitutes a significant bottleneck for cooling of electrons and holes towards the band edges.

## 5.7 Phonon Scattering

Equation 5.9 shows that a scattering process is allowed when  $E(\mathbf{k} - \mathbf{q}) - E(\mathbf{k}) + \hbar\omega_L = 0$ , and its intensity is the highest for long wavelength phonons, for large values of  $1/q^2$  (with  $q = |\mathbf{q}|$ ). In Figure 5.12, we have considered an electron above the  $\Sigma$  point with  $k$  along  $[110]$  and the emission of phonon with energy  $\hbar\omega_L \approx 26\text{meV}$  and momentum  $\mathbf{q} = q(\cos(\theta)\sin(\phi), \sin(\theta)\sin(\phi), \cos(\phi))$  defined with respect to the principal axes  $[110]$ ,  $[1\bar{1}0]$  and  $[001]$ . At given  $\theta$  and  $\phi$ ,  $q$  is entirely fixed by the energy conservation rule. When the carrier energy is high (0.2 eV in Figure 5.12a), the most likely scattering event is for  $\theta = 0$  and  $\phi = \pi/2$  *i.e.*  $\bar{q}$  parallel to  $\bar{k}$ , found for the hot carrier relaxation in usual bands.

However, for a carrier just at 5 meV above the saddle point ( $E(\mathbf{k}) - E(\mathbf{k}_0) < \hbar\omega_L$ ), this kind of process is no longer possible since a non zero component  $\mathbf{q}$  along  $[001]$  is required to reach energy states below the  $\Sigma_c$  point. Figure 5.12b shows the highest probability of scattering is obtained for  $\phi = 0$ , *i.e.*  $\mathbf{q}$  orthogonal to  $\mathbf{k}$ . In addition, the corresponding values of  $1/q^2$  are small because  $m_{001}$  is heavy and therefore high  $q$  is required to fulfill the energy conservation. Another important point which explains the slow cooling near the saddle point is that the parameter space corresponding to energies below the  $\Sigma_c$  point is quite narrow since it is mainly determined by a single component of  $\mathbf{k}$ ,  $k_{001}$ . Figure 5.13 demonstrates that the behavior for holes near the  $\Sigma_c$  point is the same as for electrons.

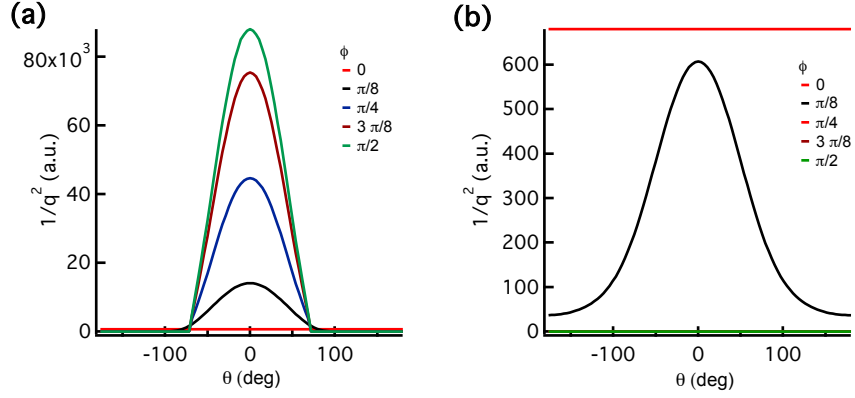


Figure 5.12: Inverse squared modulus of the phonon wavevector  $q$  emitted when an electron is scattered from a state of energy  $E(\mathbf{k})$  to a state of energy  $E(\mathbf{k} - \mathbf{q})$ .  $\mathbf{k} - \mathbf{k}_0$  is along the  $[110]$  direction such that  $E(\mathbf{k}) - E(\mathbf{k}_0) = 200$  meV (a) or 5 meV (b).  $\mathbf{q}$  is written as  $\mathbf{q} = q(\cos(\theta) \sin(\phi), \sin(\theta) \sin(\phi), \cos(\phi))$  along the principal axes  $[110]$ ,  $[1\bar{1}0]$  and  $[001]$ . The quantity  $1/q^2$  is plotted versus  $\theta$  for different values of  $\phi$ . Zero values of  $1/q^2$  mean that the transition is energetically forbidden. The vertical scale is arbitrary but can be compared between figures.

### 5.7.1 Cascade Model

Importantly, Figure 5.8 shows that the energy range of slow cooling around  $\Sigma_c$  is one to two phonon energies wide. This results in a picture of high energy carriers that (1) cool towards  $\Sigma_c$  by the rapid, successive emission of LO phonons, (2) slow down around  $\Sigma_c$  due to the reorientation of the scattering wavevector, which involves one or two slow phonon emission steps and (3) continue cooling towards the band edge states by rapid, successive phonon emission. This leads to a more precise interpretation of the rates  $k_{in}$  and  $k_{out}$  in the phenomenological 3-level model we introduced to describe the transient bleach around  $\Sigma_c$ . The incoming rate  $k_{in}$  is the effective rate of the first part of the cooling process. As such, it is equal to the ratio between the energy loss rate  $w_E$  (see table 5.2) and the energy the electron and the hole dissipate before reaching  $\Sigma_c$  or – phrased differently – to the product of the phonon emission rate  $w_{ph,in}$  and the number of phonons to be emitted before reaching  $\Sigma_c$ . Both  $w_{E,in}$  and  $w_{ph,in}$  thus calculated have been added to Table 5.1. Importantly, since the measured

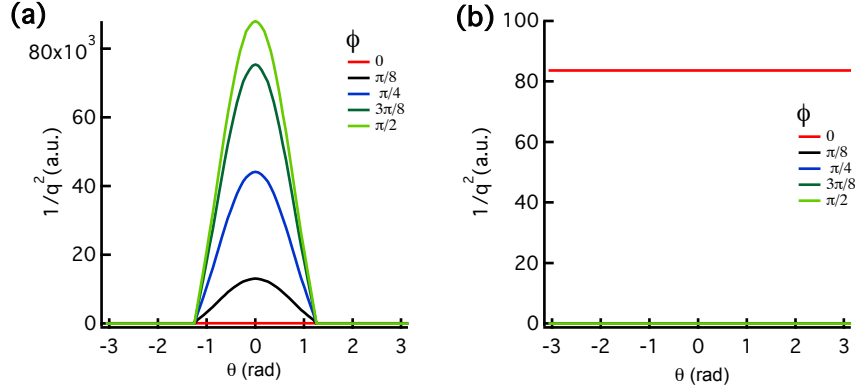


Figure 5.13: Similar to Figure 4 but for holes in the highest valence band.

cooling rate  $k_{in}$  is close to the width of the pump pulse, the highest rates calculated should be seen as lower limits to the true energy loss and phonon emission rate. The outgoing rate  $k_{out}$  on the other hand corresponds to the slow emission of one or two phonons around  $\Sigma_c$ . Especially the comparison of the phonon emission rate for cooling towards ( $w_{ph,in} > 50 \text{ ps}^{-1}$ ) and around  $\Sigma_c$  ( $w_{ph,out} \approx 2.5 - 5 \text{ ps}^{-1}$ ) makes clear how considerable a bottleneck  $\Sigma_c$  is for carrier cooling.

### 5.7.2 Four Level Approximation

The fast phonon emission (step 1 in the cascade model discussed above) can be modeled as a continuous process. Indeed, if we presume a staircase of  $Z + 1$  energy levels, each separated by the LO phonon energy, where  $k$  is the rate of cooling from a given level to the next, lower level (upward

transitions are neglected), we can write the following rate equations:

$$\begin{aligned}\frac{dN_1}{dt} &= -kN_1 \\ \frac{dN_2}{dt} &= kN_1 - kN_2 \\ \frac{dN_3}{dt} &= kN_2 - kN_3 \\ &\dots \\ \frac{dN_Z}{dt} &= kN_{Z-1} - kN_Z \\ \frac{dN_{Z+1}}{dt} &= kN_Z\end{aligned}$$

These equations can all be solved progressively, using the boundary condition that  $N_1$  is initially equal to  $N_0$ , while all other  $N_i$  are zero at  $t = 0$ . The time evolution of  $N_{Z+1}$  is obtained from the requirement that  $\sum_i N_i = N_0$ .

**Solution** From the first of the equations and the initial condition, the time dependence of  $N_1$  is immediately obtained as:

$$N_1(t) = N_0 e^{-kt} \quad (5.10)$$

In the same way,  $N_2$  is obtained as ( $dN_2/dt|_{t=0} = kN_0$ ):

$$N_2(t) = N_0 (kt) e^{-kt} \quad (5.11)$$

In general,  $N_i$  can be obtained as ( $d^{i-1}N_i/dt^{i-1}|_{t=0} = k^{i-1}N_0$ ):

$$N_i(t) = N_0 \frac{(kt)^{i-1}}{(i-1)!} e^{-kt} \quad (5.12)$$

As a result,  $N_{Z+1}$  can be written as:

$$N_{Z+1} = N_0 \times \left\{ 1 - \left( 1 + kt + \dots + \frac{(kt)^{Z-1}}{(Z-1)!} \right) e^{-kt} \right\} \quad (5.13)$$

**Discussion** The solution for  $N_{Z+1}$  is a function that starts from zero and increases to reach  $N_0$  when  $t \rightarrow \infty$ . To get an idea for the characteristic time of this increase, we look for the point where the slope  $dN_{Z+1}/dt$  is maximal. Hence, we look for the time where:

$$\frac{d^2N_Z}{dt^2} = 0 \quad (5.14)$$

Using the differential equations and there solutions, this condition can be rewritten as:

$$N_{Z-1} - N_Z = \frac{(kt)^{Z-2}}{(Z-2)!} - \frac{(kt)^{Z-1}}{(Z-1)!} = 0 \quad (5.15)$$

We thus have:

$$t = \frac{Z-1}{k} \quad (5.16)$$

We thus find that the characteristic buildup time of the last level scales proportionally to ratio between the number of steps ( $Z$ ) and the rate per step ( $1/k$ ). This is similar to the travel time being the ratio between the distance travelled and the speed. It thus makes sense to see measured cooling times as the ratio between the number of cooling steps and the cooling rate of a single step or, alternatively, as the ratio between the energy to be dissipated and the cooling rate per energy range. Hence:

$$\tau_{cool} = \frac{\Delta E[\text{eV}]}{k[\text{eV/ps}]} \quad (5.17)$$

As a result, the cooling rate can be obtained as:

$$k = \frac{\Delta E}{\tau_{cool}} = \Delta E \times k_{cool} \quad (5.18)$$

**4 level model** Under the assumptions above, we can describe carrier cooling from the excited state to the 'upper' level at  $\Sigma_c$  (eu) and from the 'down' state at  $\Sigma_c$  to the ground state (g) as continuous processes. As such we can write a set of differential equations describing the occupation probabilities of each level (excited,upper,down and ground).

$$\frac{\partial P_e}{\partial t} = -\frac{P_e}{\tau_{eu}} \quad (5.19)$$

$$\frac{\partial P_u}{\partial t} = \frac{P_e}{\tau_{eu}} - \frac{P_u}{\tau_{ud}} \quad (5.20)$$

$$\frac{\partial P_d}{\partial t} = \frac{P_u}{\tau_{ud}} - \frac{P_d}{\tau_{dg}} \quad (5.21)$$

Using the appropriate boundary conditions ( $\sum_i P_i = 1$ ,  $P_e(0) = 1$ ,  $P_{u,d}(0) = 0$ ), we find:

$$P_e(t) = e^{-\frac{t}{\tau_{eu}}} \quad (5.22)$$

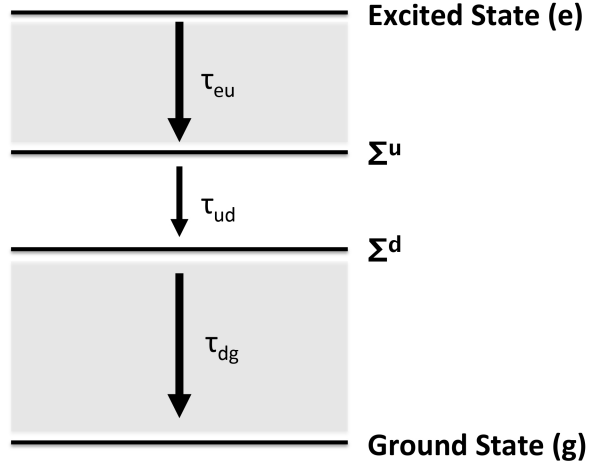


Figure 5.14: Schematic depicting the 4 levels considered in the modeling of carrier accumulation: an excited state, a ground state and an ensemble of  $\Sigma_c$ -states [u(pper),d(down)].

$$P_u(t) = \frac{\tau_{ud}}{\tau_{ud} - \tau_{eu}} \times (e^{-\frac{t}{\tau_{ud}}} - e^{-\frac{t}{\tau_{dg}}}) \quad (5.23)$$

$$P_d(t) = \frac{1}{\tau_{ud} - \tau_{eu}} \left\{ \frac{\tau_{dg}\tau_{ud}}{\tau_{ud} - \tau_{dg}} \times (e^{-\frac{t}{\tau_{ud}}} - e^{-\frac{t}{\tau_{eu}}}) - \frac{\tau_{dg} - \tau_{eu}}{\tau_{eu} - \tau_{dg}} \times (e^{-\frac{t}{\tau_{eu}}} - e^{-\frac{t}{\tau_{dg}}}) \right\} \quad (5.24)$$

$$P_g(t) = 1 - P_e - P_u - P_d \quad (5.25)$$

Assuming  $\tau_{ud} \gg \tau_{eu,dg}$ , which is validated by the tight binding calculation of the limiting cooling step (rate drops to roughly 1/40 of the rate above  $\Sigma_c$ , see Figure 5.11), we can simplify the occupancy of the  $\Sigma_c$ -ensemble (*i.e.*  $P_u + P_d$  to  $P_u$ ):

$$P_u(t) = \frac{\tau_{ud}}{\tau_{ud} - \tau_{eu}} \times (e^{-\frac{t}{\tau_{ud}}} - e^{-\frac{t}{\tau_{dg}}}) \quad (5.26)$$

where the interpretation of the in- and outflow rates ( $k_{in,out}$ ) used before refer to the transition "excited-upper" and "upper-down" respectively.

## 5.8 From Bulk to Nanocrystals

Electron states in nanocrystals can be seen as linear combinations of bulk states, which essentially results in a quantization of the electron wavevectors  $\mathbf{k}$ . Taking the case of cubic nanocrystals with an edge length  $L$  for example, the energies  $E$  of the quantized states around  $\Sigma_c$  read:

$$E = E_{c,\Sigma_c} + \frac{\hbar^2}{2m_{110}} \left( \frac{n_{110}\pi}{L} \right)^2 + \frac{\hbar^2}{2m_{1\bar{1}0}} \left( \frac{n_{1\bar{1}0}\pi}{L} \right)^2 - \frac{\hbar^2}{2m_{001}} \left( \frac{n_{001}\pi}{L} \right)^2 \quad (5.27)$$

Here,  $n_{110}$ ,  $n_{1\bar{1}0}$  and  $n_{001}$  are non-zero, positive integers that quantize the incremental wavevector  $\delta\mathbf{k}$  in the directions indicated by the subscript. The experiments presented here show that at energies well above  $\Sigma_c$ , the cooling of hot carriers remains as efficient as in bulk, with very similar characteristic energy loss rates in the eV ps<sup>-1</sup> range. We thus conclude that size quantization does not really limit the cooling of carriers in these energy ranges. Since the energy splitting between states is in practice never exactly equal to a LO phonon energy, multi-phonon processes are required. The stronger coupling to acoustic phonons in nanocrystals compared to bulk certainly contributes to compensate the energy mismatch.<sup>27;33</sup> However, the driving force for the relaxation remains the coupling to LO phonons which follows the same rules as in the bulk but taking into account quantized components.

In particular, it appears that all the conclusions about the dimensionality of the parameter space for the final state and the directionality of  $\mathbf{q}$  with respect to  $\mathbf{k}$  remain valid. In bulk, the threshold for the change in energy loss rate, linked to the necessary change in the direction of the scattering wavevector is near the energy gap  $\Delta E_{\Sigma_c}$  at  $\Sigma_c$ . Given the difference in effective masses for the directions of positive and negative curvature, the threshold will be close to  $\Delta E_{\Sigma_c} + \hbar^2\pi^2/L^2 \left( \frac{1}{m_{110}} + \frac{1}{m_{1\bar{1}0}} \right)$  in nanocrystals. Further cooling requires an increase of the quantum number  $n_{001}$ , *i.e.*, the quantized equivalent of a change in direction of the scattering wavevector. Hence, we indeed expect the slow down of carrier cooling to shift to higher energy for smaller nanocrystals and follow, as observed, the quantization of energy levels around  $\Sigma_c$ . Eq 5.27 is only an approximation due to its dependence on a parabolic band structure and a particular nanocrystal geometry. More elaborate calculations show that the eigenstates are somewhat spread in  $\mathbf{k}$  space. In addition, since there are twelve  $\Sigma_c$  points, inter-valley couplings mix all the states. Including the spin degree of freedom, this leads to

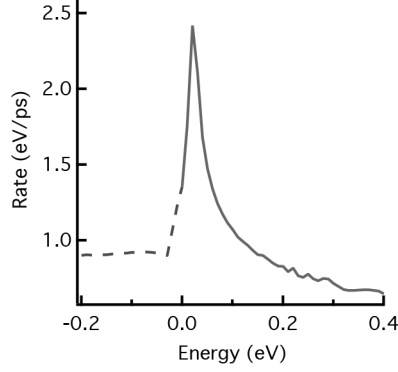


Figure 5.15: Energy loss rate at 300K calculated for an electron placed in the lowest conduction band near the  $\Delta$  point at  $0.82\frac{\pi}{a}[100]$ . The zero of energy corresponds to the  $\Delta_c$  point ( $E(\mathbf{k}_0) = 2.69$  eV). The  $\mathbf{k}$  vector of the initial electron state is oriented along  $[100]$  (red solid line) or  $[010]$  (blue dashed line) directions. Results for the  $[001]$  direction (not shown) are the same as for  $[010]$ .

a high density of states in the vicinity of  $\Sigma_c$ . These effects should contribute to broaden the energy range where the carrier accumulation occurs. However, the experimental results show that the underlying effects originating from the saddle points of the bulk remain efficient.

## 5.9 The Role of Saddle Points

The band structure of bulk PbS (PbSe) is characterized by other saddle points where a similar analysis could be applied to assess their influence on the cooling rate. Most notably, a saddle point  $\Delta_c$  is present along the  $\Delta$  direction ( $\Gamma \rightarrow X$ ), whose energy gap of  $\approx 3$  eV falls outside of the range of the TA setup used here. Calling this direction the parallel one, the band dispersion around  $\mathbf{k}_{\Delta_c} \approx 0.82\frac{\pi}{a}(1, 0, 0)$  can be approximated as:

$$E_{c,\mathbf{k}} \approx E_{c,\Delta_c} + \frac{\hbar^2}{2} \left( \frac{\delta k_{\parallel}^2}{m_{\parallel}} - \frac{\delta k_{\perp}^2}{m_{\perp}} \right) \quad (5.28)$$

Here, we introduce the effective masses  $m_{\parallel}$  ( $\approx 0.16m_0$ ) along  $\Delta$  and  $m_{\perp}$  ( $\approx 0.51m_0$ ) for the two directions perpendicular to  $\Delta$ . In contrast to  $\Sigma_c$ , we calculate a strong enhancement of the cooling rate near  $\Delta_c$ .

This can be readily understood from the band dispersion where now two directions instead of one have a negative dispersion instead of one.

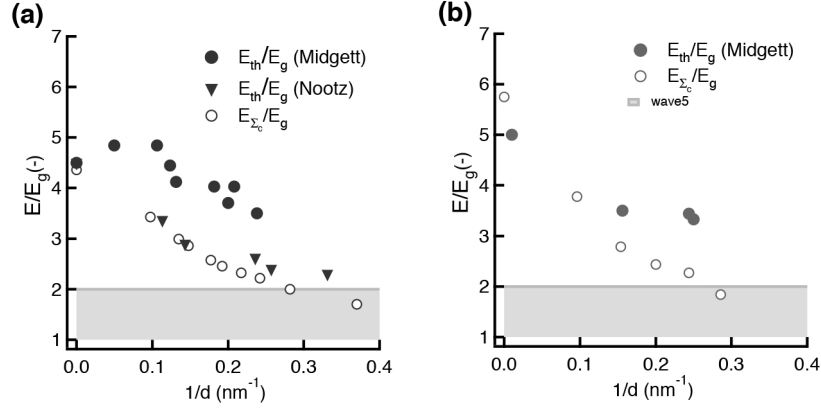


Figure 5.16: Comparison of  $\Sigma_c$  and threshold energy for MEG (normalized to the band gap energy  $E_g$ ) for (a) PbS from Beard<sup>37</sup> and Nootz<sup>38</sup> (b) PbSe<sup>39</sup> as function of the inverse particle size  $1/d$ . Note that the bulk limit<sup>40</sup> corresponds to  $1/d = 0$ .

Therefore, when the carrier is close to the saddle point, the parameter space for the final state is determined by one additional degree of freedom that considerably increases the density of allowed processes and thus the cooling rate. We thus predict that, opposite from  $\Sigma_c$ ,  $\Delta_c$  does not constitute a bottleneck for electron cooling.

Apart from polar semiconductors, many other materials exhibit saddle points in their energy dispersion giving rise to interesting new phenomena such as graphene where the M-point is a saddle point at high energy giving rise to peculiar excitonic Fano resonances<sup>34</sup> and electron-phonon coupling<sup>35</sup>. Recent reports on silicon nanocrystals indicate the potential of harvesting delayed hot excitons for short-lived luminescence<sup>36</sup>.

## 5.10 Relevance of Bottleneck for Multiple Exciton Generation

The relaxation rate of hot electron-hole pairs is of particular importance for QD-based photovoltaic cells that exploit multiple-exciton generation (MEG), where a single hot electron-hole pair creates multiple electron-hole pairs with lower energy<sup>13;41</sup>. Several authors have considered the efficiency of MEG to be the result of the competition between the generation of multiple excitons via impact ionization and hot carrier relaxation<sup>14;41–43</sup>. There-

fore the characterization of hot carrier relaxation is of great importance for understanding the efficiency of MEG. The relevant rate in this context is the cooling rate of carriers at high excess energy, above the energy threshold for MEG  $E_{th}$ . An intriguing question arising from the results shown here is whether the cooling bottleneck around  $\Sigma_c$  is responsible for the efficient MEG that is observed in PbS and PbSe QDs. If so, one would expect the MEG threshold, *i.e.*, the energy where the yield of excitons starts to exceed 100%, to be related to  $E_{\Sigma_c}$ . Figure 5.16 therefore represents both  $E_{\Sigma_c}$  and the few available data on the MEG threshold for PbS<sup>37;38</sup> and PbSe<sup>37</sup> QDs<sup>37;39;40</sup> as a function of the reciprocal QD diameter  $1/d_{NC}$ , where the bulk values are also included at  $1/d_{NC} = 0$ .<sup>40</sup>

In the case of bulk PbS and PbSe,  $E_{\Sigma_c}/E_g$  amounts to 4.36 and 5.75, respectively. Interestingly, both numbers correspond closely to the experimental bulk MEG thresholds<sup>40</sup>. As a result of the higher effective masses at  $\Sigma_c$  compared to the band edge effective masses,  $E_{\Sigma_c}/E_g$  decreases with decreasing diameter. For both PbS and PbSe QDs, the MEG threshold follows the same trend, yet the available sets of data show considerable discrepancies. Whereas the MEG threshold as determined by Nootz *et al.* closely follows  $\Sigma_c$ ,<sup>38</sup> Midgett *et al.* report MEG thresholds that exceed  $E_{\Sigma_c}/E_g$  by more than the QD bandgap for 4 nm PbS and PbSe QDs. Figure 5.16 also indicates that for PbS and PbSe QDs smaller than  $\approx 3.5$  nm,  $E_{\Sigma_c}/E_g$  drops below 2. This is below the energy conservation threshold, which implies that the slow cooling around  $\Sigma_c$  is irrelevant for MEG observed in these QDs.

Since MEG is a process that competes with charge carrier cooling, the MEG efficiency in PbS and PbSe QDs is closely related to the cooling rate, where higher MEG efficiencies imply slower cooling<sup>42;43</sup> MEG can be considered an impact ionization process and the efficiencies can be calculated in that framework. As such, for bulk PbS and PbS QDs we computed the number of generated excitons when impact ionization competes with phonon cooling. As shown by Allan *et al.*<sup>42</sup>, the impact ionization rates can be calculated using an atomistic tight-binding approach, but this is only possible for small QDs (diameter  $< 3$  nm) and for bulk PbS. In order to extend the simulations to larger QDs, we have used the simplified method described and justified by Delerue *et al.*<sup>44</sup>. In brief, the impact ionization rates are numerically interpolated between the results for small QDs and bulk. The dynamics of the carriers is simulated on an energy grid with discrete levels spaced by 5 meV. For the cooling, the lifetime  $\tau_{phonon}$  (40 fs and 500 fs) for the decay by emission of one phonon ( $\hbar\omega_{LO} = 25$  meV) is considered as a parameter independent of the carrier energy.

Focusing on PbS QDs, we theoretically retrieve MEG efficiencies that

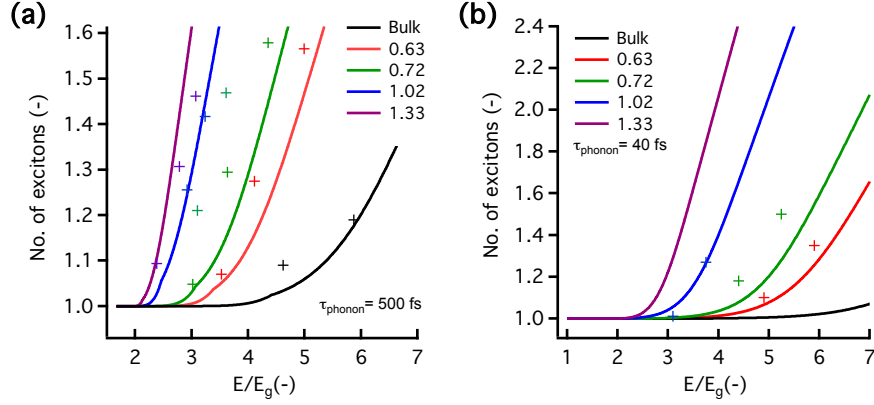


Figure 5.17: MEG quantum yield (expressed in number of created excitons per photon) for PbS QDs versus normalized photon energy for (a) phonon lifetime of 500 fs (with experimental data (markers) from Nootz *et al.*<sup>38</sup> and (b) 40 fs (with experimental data (markers) from Midgett *et al.*<sup>37</sup>).

closely follow  $E_{\Sigma_c}/E_g$  – as reported by Nootz *et al.* – for phonon emission rates of  $\approx 2 \text{ ps}^{-1}$  (see Figure 5.17a). On the other hand, we obtain the lower efficiencies found by Midgett *et al.* if the phonon emission rate is raised to  $\approx 25 \text{ ps}^{-1}$  (see Figure 5.17b). Based on the figures provided in Table 5.1, it follows that both possibilities seem consistent with our experimental data. If the MEG threshold effectively follows  $E_{\Sigma_c}/E_g$ , it requires a slowing down of the cooling to a rate that corresponds to what we find around  $\Sigma_c$ . On the other hand, if MEG is only effective for excitations well above  $\Sigma_c$ , it competes with a much faster cooling where again, the rate we measure can reasonably account for the experimental thresholds. It thus appears that the understanding of the mechanism behind MEG (impact ionization or other (*e.g.* Auger assisted energy transfer similar to P-S cooling CdSe<sup>9</sup>)), and the possible role of the slow cooling around  $\Sigma_c$  would strongly benefit from a more precise determination of the MEG threshold as a function of QD size.

## 5.11 Conclusion

We have shown that PbS quantum dots exhibit a transient absorption bleach at photon energies corresponding to the  $\Sigma_c$  transition. This is interpreted in terms of a temporal accumulation of charge carriers due to a slowing down of charge carrier cooling. This temporal accumulation of cooling carri-

ers enables us to quantify the energy loss rate of hot electron-hole pairs and to estimate that the fraction of hot carriers cooling *via* this  $\Sigma_c$  bottleneck is of the order of 1. Importantly, we demonstrate that this cooling bottleneck is intrinsically linked to the properties of the band structure of bulk PbS around the critical point  $\Sigma_c$ . In this way, the occurrence or absence of cooling bottlenecks and their influence on the effective cooling rate can be predicted for nanocrystal materials other than PbS. Ultimately, this will contribute to a more optimal choice of materials that either harvest or dissipate more effectively the excess energy of hot electron-hole pairs in nanocrystals.

## References

- [1] Ross, R.; Nozik, A. Efficiency of Hot-Carrier Solar Energy Converters. *J. App. Phys.* **1982**, *53*, 3813.
- [2] Kambhampati, P. Hot Exciton Relaxation Dynamics in Semiconductor Quantum Dots : Radiationless Transitions on the Nanoscale. *J. Phys. Chem. C* **2011**, *115*, 22089–22109.
- [3] Li, W.; Chen, B.; Meng, C.; Fang, W.; Xiao, Y.; Li, X.; Hu, Z.; Xu, Y.; Tong, L.; Wang, H.; Liu, W.; Bao, J.; Shen, Y. R. Ultrafast All-Optical Graphene Modulator. *Nano Lett.* **2014**.
- [4] Abb, M.; Albella, P.; Aizpurua, J.; Muskens, O. L. All-Optical Control of a Single Plasmonic Nanoantenna-ITO Hybrid. *Nano Lett.* **2011**, *11*, 2457–2463.
- [5] Mukherjee, S.; Libisch, F.; Large, N.; Neumann, O.; Brown, L. V.; Cheng, J.; Lassiter, J. B.; Carter, E. A.; Nordlander, P.; Halas, N. J. Hot Electrons Do the Impossible: Plasmon-Induced Dissociation of H<sub>2</sub> on Au. *Nano Lett.* **2013**, *13*, 240–247.
- [6] Clavero, C. Plasmon-induced Hot-Electron Generation at Nanoparticle/Metal-oxide Interfaces for Photovoltaic and Photocatalytic Devices. *Nat. Photonics* **2014**, *8*, 95–103.
- [7] Giugni, a.; Torre, B.; Toma, a.; Francardi, M.; Malerba, M.; Alabastri, a.; Proietti Zaccaria, R.; Stockman, M. I.; Di Fabrizio, E. Hot-Electron Nanoscopy using Adiabatic Compression of Surface Plasmons. *Nat. Nanotechnol.* **2013**, *8*, 845–52.

- [8] Nozik, A. Spectroscopy and Hot Electron Relaxation Dynamics in Semiconductor Quantum wells and Quantum dots. *Ann. Rev. Phys. Chem.* **2001**, *52*, 193–231.
- [9] Pandey, A.; Guyot-Sionnest, P. Slow Electron Cooling in Colloidal Quantum Dots. *Science* **2008**, *322*, 929–32.
- [10] Tisdale, W. a.; Williams, K. J.; Timp, B. a.; Norris, D. J.; Aydil, E. S.; Zhu, X.-Y. Hot-Electron Transfer from Semiconductor Nanocrystals. *Science* **2010**, *328*, 1543–1547.
- [11] Sandeep, C. S. S.; Cate, S. T.; Schins, J. M.; Savenije, T. J.; Liu, Y.; Law, M.; Kinge, S.; Houtepen, A. J.; Siebbeles, L. D. a. High charge-carrier mobility Enables Exploitation of Carrier Multiplication in Quantum-Dot Films. *Nat. Comm.* **2013**, *4*, 1–6.
- [12] Aerts, M.; Suchand Sandeep, C. S.; Gao, Y.; Savenije, T. J.; Schins, J. M.; Houtepen, A. J.; Kinge, S. S.; Siebbeles, L. D. a. Free Charges Produced by Carrier Multiplication in Strongly-Coupled PbSe Quantum Dot Films. *Nano Lett.* **2011**, *11*, 4485–4489.
- [13] Semonin, O. E.; Luther, J. M.; Choi, S.; Chen, H.-Y.; Gao, J.; Nozik, A. J.; Beard, M. C. Peak External Photocurrent Quantum Efficiency Exceeding 100% via MEG in a Quantum Dot Solar Cell. *Science* **2011**, *334*, 1530–3.
- [14] Klimov, V. I.; Stewart, J. T.; Padilha, L. a.; Qazilbash, M.; Pietryga, J. M.; Midgett, A. G.; Luther, J.; Beard, M. C.; Nozik, A. Comparison of Carrier Multiplication Yields in PbS and PbSe Nanocrystals: The Role of Competing Energy-Loss Processes. *Nano Lett.* **2011**, 111212123654001.
- [15] Lee, J.-W.; Son, D.-Y.; Ahn, T. K.; Shin, H.-W.; Kim, I. Y.; Hwang, S.-J.; Ko, M. J.; Sul, S.; Han, H.; Park, N.-G. Quantum-Dot-Sensitized Solar Cell with Unprecedentedly High Photocurrent. *Scientific Reports* **2013**, *3*, 1050.
- [16] Hens, Z.; Vanmaekelbergh, D.; Kooij, E.; Wormeester, H.; Allan, G.; Delerue, C. Effect of Quantum Confinement on the Dielectric Function of PbSe. *Phys. Rev. Lett.* **2004**, *92*, 026808.
- [17] Cademartiri, L.; Montanari, E.; Calestani, G.; Migliori, A.; Guagliardi, A.; Ozin, G. a. Size-Dependent Extinction Coefficients of PbS Quantum Dots. *J. Am. Chem. Soc.* **2006**, *128*, 10337–46.

- [18] Koole, R.; Allan, G.; Delerue, C.; Meijerink, A.; Vanmaekelbergh, D.; Houtepen, A. J. Optical Investigation of Quantum Confinement in PbSe Nanocrystals at Different Points in the Brillouin Zone. *Small* **2008**, *4*, 127–33.
- [19] Moreels, I.; Lambert, K.; Smeets, D.; De Muynck, D.; Nollet, T.; Martins, J. C.; Vanhaecke, F.; Vantomme, A.; Delerue, C.; Allan, G.; Hens, Z. Size-Dependent Optical Properties of Colloidal PbS Quantum Dots. *ACS Nano* **2009**, *3*, 3023–30.
- [20] Kanazawa, H.; Adachi, S. Optical Properties of PbS. *J. Appl. Phys.* **1998**, *83*, year.
- [21] Moreels, I.; Justo, Y.; De Geyter, B.; Haustraete, K.; Martins, J. C.; Hens, Z. Size-tunable, Bright, and Stable PbS Quantum Dots: A Surface Chemistry Study. *ACS Nano* **2011**, *5*, 2004–2012.
- [22] Klimov, V. Optical Nonlinearities and Ultrafast Carrier Dynamics in Semiconductor Nanocrystals. *J. Phys. Chem. B* **2000**, *104*, 6112–6123.
- [23] De Geyter, B.; Houtepen, A. J.; Carrillo, S.; Geiregat, P.; Gao, Y.; Ten Cate, S.; Schins, J. M.; Van Thourhout, D.; Delerue, C.; Siebbelles, L. D.; Hens, Z. Broadband and Picosecond Intraband Absorption in Lead-Based Colloidal Quantum Dots. *ACS Nano* **2012**, *6*, 6067–6074.
- [24] Geiregat, P.; Houtepen, A.; Justo, Y.; Grozema, F. C.; Van Thourhout, D.; Hens, Z. Coulomb Shifts upon Exciton Addition to Photoexcited PbS Colloidal Quantum Dots. *The Journal of Physical Chemistry C* **2014**, *118*, 22284–22290.
- [25] Steckel, J. S.; Yen, B. K. H.; Oertel, D. C.; Bawendi, M. G. On the mechanism of lead chalcogenide nanocrystal formation. *Journal of the American Chemical Society* **2006**, *128*, 13032–3.
- [26] Kohn, S.; Yu, P.; Petroff, Y.; Shen, Y.; Tsang, Y.; Cohen, M. Electronic Band Structure and Optical Properties of PbTe, PbSe and PbS. *Physical Review B* **1973**, *8*, 1477–1488.
- [27] Kohn, W.; Luttinger, J. Motion of Electrons and Holes in Perturbed Periodic Fields. *Physical Review* **1955**, *97*, 869–883.
- [28] Conwell, E. *High Field Transport in Semiconductors*; Academic Press, 1967.

- [29] Fröhlich, H.; Pelzer, H.; Zienau, S. Properties of Slow Electrons in Polar Materials. *Phil. Mag.* **41** **1950**, *41*, year.
- [30] Frhlich, H. Theory of Electrical Breakdown in Ionic Crystals. *Proceedings of the Royal Society of London. Series A, Mathematical and Physical Sciences* **1937**, *160*, pp. 230–241.
- [31] Dalven, R. Electron-Optical-Polaron Coupling Constant in PbS, PbSe and PbTe. *Physical Review B* **1971**, *3*, 1953–1954.
- [32] Habinshuti, J.; Kilian, O.; Cristini-Robbe, O.; Sashchiuk, a.; Ad-dad, a.; Turrell, S.; Lifshitz, E.; Grandidier, B.; Wirtz, L. Anomalous Quantum Confinement of the Longitudinal Optical Phonon Mode in PbSe Quantum Dots. *Phys. Rev. B* **2013**, *88*, 115313.
- [33] Takagahara, T. Electron-Phonon Interactions and Excitonic Dephas-ing in Semiconductor Nanocrystals. *Phys. Rev. Lett.* **1993**, *71*, 3577–3580.
- [34] Chae, D.-H.; Utikal, T.; Weisenburger, S.; Giessen, H.; Klitz-ing, K. V.; Lippitz, M.; Smet, J. Excitonic Fano Resonance in Free-Standing Graphene. *Nano Lett.* **2011**, *11*, 1379–82.
- [35] Jorio, A.; Kasperczyk, M.; Clark, N.; Neu, E.; Maletinsky, P.; Vijayaraghavan, A.; Novotny, L. Optical-Phonon Resonances with Saddle-Point Excitons in Twisted-Bilayer Graphene. *Nano Lett.* **2014**.
- [36] de Boer, W. D. a. M.; Timmerman, D.; Dohnalová, K.; Yassievich, I. N.; Zhang, H.; Buma, W. J.; Gregorkiewicz, T. Red Spectral Shift and Enhanced Quantum Efficiency in Phonon-Free Photoluminescence from Silicon Nanocrystals. *Nat. Nanotechnol.* **2010**, *5*, 878–84.
- [37] Midgett, A. G.; Luther, J. M.; Stewart, J. T.; Smith, D. K.; Padilha, L. A.; Klimov, V. I.; Nozik, A. J.; Beard, M. C. Size and Composition Dependent Multiple Exciton Generation Efficiency in PbS, PbSe, and PbS. *Nano Lett.* **2013**, *13*, 30783085.
- [38] Nootz, G.; Padilha, L.; Levina, L.; Sukhovatkin, V.; Webster, S.; Brzo-zowski, L.; Sargent, E.; Hagan, D.; Van Stryland, E. Size Dependence of Carrier Dynamics and Carrier Multiplication in PbS Quantum Dots. *Phys. Rev. B* **2011**, *83*, 1–7.

- [39] Midgett, A. G.; Hillhouse, H. W.; Hughes, B. K.; Nozik, A. J.; Beard, M. C. Flowing versus Static Conditions for Measuring Multiple Exciton Generation in PbSe Quantum Dots. *J. Phys. Chem. C* **2010**, *114*, 17486–17500.
- [40] Pijpers, J. J. H.; Ulbricht, R.; Tielrooij, K. J.; Osherov, a.; Golan, Y.; Delerue, C.; Allan, G.; Bonn, M. Assessment of Carrier-Multiplication Efficiency in Bulk PbSe and PbS. *Nature Physics* **2009**, *5*, 811–814.
- [41] Beard, M. C.; Luther, J. M.; Semonin, O. E.; Nozik, A. J. Third Generation Photovoltaics based on Multiple Exciton Generation in Quantum Confined Semiconductors. *Accounts Chem. Res.* **2013**, *46*, 1252–1260.
- [42] Allan, G.; Delerue, C. Role of Impact Ionization in Multiple Exciton Generation in PbSe Nanocrystals. *Physical Review B* **2006**, *73*, 205423.
- [43] Allan, G.; Delerue, C. Influence of electronic structure and multiexciton spectral density on multiple-exciton generation in semiconductor nanocrystals: Tight-binding calculations. *Phys. Rev. B* **2008**, *77*, 125340.
- [44] Delerue, C.; Allan, G.; Pijpers, J. J. H.; Bonn, M. Carrier Multiplication in Bulk and Nanocrystalline Semiconductors: Mechanism, Efficiency, and Interest for Solar Cells. *Phys. Rev. B* **2010**, *81*, 125306.

# 6

## All-Optical Wavelength Conversion using PbS Nanocrystals

Owing to their widely tuneable optical properties and strong light-matter interaction, colloidal nanocrystals (or quantum dots, QDs) are considered for next-generation photonic devices such as solution processable lasers, solar cells, light-emitting diodes and photo-detectors integrated on-chip. More advanced photonic devices, such as all-optical wavelength converters would equally benefit from a solution processable material offering ultrafast conversion with high extinction ratio and low insertion loss. All-optical wavelength conversion is considered more energy and cost effective than the classical approaches where electrical and optical domains are switched to transfer information. However, the lack of cost-effective materials with sufficiently adequate properties hampers the development of this application. Here we show that tuning the interplay between two well documented material properties of QDs, intraband absorption (previously considered an adverse material property as it hampers optical gain) and interband bleach can lead to a very strong and ultrafast modulation of light. This demonstrates that QDs could be used as the sought-after cost-effective medium for all-optical wavelength conversion. Using this approach, we can convert wavelengths at rates up to 3 orders of magnitude faster than existing approaches relying on NCs and match the state-of-the-art in converters speed in speed, yet with significantly cheaper materials and with stronger light-matter interaction leading to devices with much smaller footprints and

switching energies. The demonstrated effect opens up a new field of QDs as enabling medium for low-power integrated photonics and sheds a new light on intraband absorption as a useful material property of colloidal nanocrystals.

## 6.1 Introduction

All-optical signal processing is widely seen as a key enabler of high bitrate, low power and cost-efficient data communication<sup>1,2</sup>. One of the basic functions involves the conversion of a data stream from a first (pump) to a second (probe) wavelength channel. This so-called wavelength conversion requires materials that show a strong and fast response of their optical constants at the probe wavelength to changes in light intensity at the pump wavelength. Published examples make use of phase modulation through  $\chi_3$  non-linearities<sup>3</sup> or direct amplitude modulation<sup>4</sup>. The phase modulation effects are typically weak and require either long interaction lengths or complex interferometric configurations (*e.g.* Mach-Zehnders) with the need for high input powers. Amplitude modulation requires epitaxially grown III-V semiconductors<sup>5</sup>, which are expensive and not directly compatible with, *e.g.* the commercially interesting silicon-on-insulator (SOI) platform. To overcome these drawbacks, novel opto-electronic materials such as colloidal quantum dots (QDs) and graphene have seen an increasing interest for applications in all-optical signal processing in general and wavelength conversion in particular. Li *et al.*<sup>6</sup> for example showed that carrier cooling in graphene leads to a picosecond, broadband modulation of the absorption coefficient, yet the relatively weak interaction of graphene with light makes that high input powers are needed to achieve rather modest modulation depths of  $\approx 0.3$ . Pacifici *et al.*<sup>7</sup> demonstrated a similar wavelength conversion scheme using the absorption of the probe light by intraband transitions in QDs photoexcited by the pump light. As compared to graphene, QDs have larger absorption coefficients, possibly yielding a larger modulation depth and a smaller device footprint. However, the modulation rate will be limited by the single exciton recombination rates of  $10^8 \text{ s}^{-1}$  in II-VI QDs such as CdSe and CdTe<sup>8</sup> and  $10^6 \text{ s}^{-1}$  in IV-VI QDs such as PbS<sup>9</sup> and PbSe<sup>10</sup>. These limitations can be overcome when multi-exciton states are addressed, which show a much faster recombination rate of  $10^{11} \text{ s}^{-1}$  due to Auger recombination.<sup>11</sup> Using the different stimulated emission rate of different multiexciton states for example, all optical modulation with a 3 dB bandwidth close to 1 THz was achieved using CdSe/ZnS QDs<sup>12</sup>. On the other hand, photoinduced changes linked to the formation of multi-exciton states in QDs are highly nonlinear and thus strongly

power dependent and require high power signals or, equivalently, a large energy per pulse. Moreover, the material response will still contain more slowly varying contributions due to the recombination of single excitons. Here, we show that the trade-off between speed and non-linearity when using colloidal QDs for all-optical signal processing is not inevitable. Using PbS QDs, we demonstrate that a specific probe wavelength range exists where the effects of photobleaching, photoinduced absorption<sup>13</sup> and spectral shifts<sup>14</sup> cancel, apart from the first picosecond following photoexcitation by the pump pulse. This results in an intense, linear and ultrafast optical response that maintains its characteristics under excitation using 450 and 225 Gb/s pulse trains. We argue that this makes colloidal QDs an ideal material for low power, picosecond wavelength conversion that can be used in small footprint, integrated photonic devices. In addition, it sheds a new light on intraband absorption as a useful material property of colloidal QDs.

## 6.2 Light Absorption by Photo-Excited Quantum dots

We make use of 4.6 nm PbS QDs synthesized by injecting sulphur dissolved in oleylamine in a mixture of lead chloride and oleylamine according to established literature procedures<sup>15;16</sup>. Their absorption spectrum (see Figure 6.1, solid red line) features the typical characteristic of optical transitions between size-quantized levels in the valence and the conduction band, labelled as 1S-1S and 1P-1P. In addition, Figure 6.1 shows the differential absorbance  $\Delta A$  for the same QDs following a 180 fs, 700 nm pump pulse that creates on average 0.93 excitons per QD as a time-wavelength intensity map around the 1S-1S transition. Focusing first on the differential absorbance at delay times longer than  $\approx 1$  ps, one notices a strong reduction of the absorption (bleach, ( $\Delta A < 0$ )) at around 1300 nm, which reflects the occupation of the band-edge states (state - filling) by electrons and holes. The decay observed between 1 and 100 ps is typically attributed to Auger recombination of multiexcitons<sup>17;18</sup>, where a detailed analysis yields a time constant of 43 ps in our case.

At wavelengths longer than 1500 nm on the other hand, a relatively weak photoinduced absorption ( $\Delta A > 0$ ) is observed. This shows the same decay dynamics as the bandgap bleach and has been attributed before to intraband transitions involving the cooled electron and hole that occupy the band-edge states. A markedly different differential absorbance spectrum appears within the first picosecond after photoexcitation. Here, the photoinduced absorption is considerably stronger and extends over a much wider range of wavelengths. These initial dynamics has been attributed to exciton cooling by De Geyter *et al.*, where it was concluded that a hot exci-

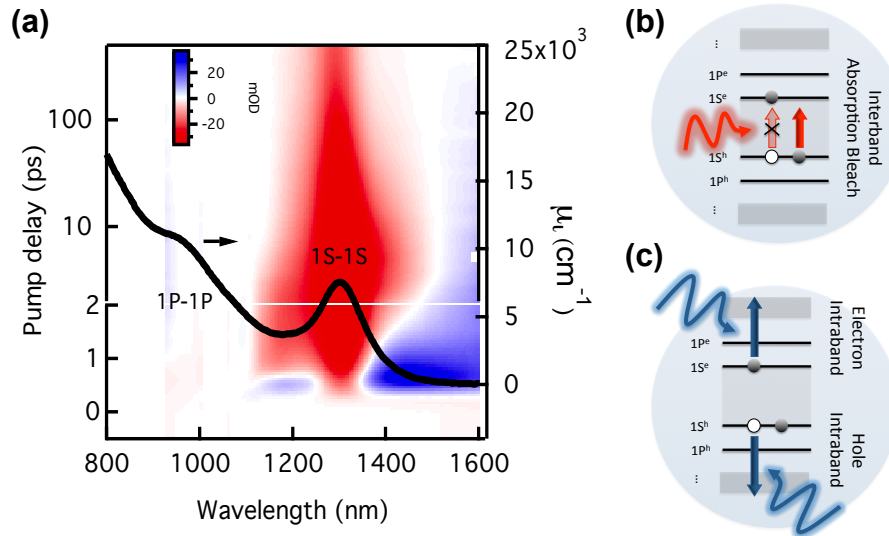


Figure 6.1: Overview (a) 2D time-wavelength map of band edge differential absorbance spectrum  $\Delta A$  after 700 nm photo-excitation creating on average 0.93 excitons per QD ( $\langle N \rangle = 0.93$ ). Also, the intrinsic absorption spectrum  $\mu_i$  of 4.6 nm PbS quantum dots (QDs) dispersed in hexane is shown (solid black line). The lowest energy exciton transitions are labeled 1P-1P and 1S-1S. (b-c) Schematic depicting the two relevant ultrafast processes discussed in this work: interband (b) and intraband (c) absorption for a singly excited nanocrystal in the 1S-1S manifold (here 2-fold degenerate for simplicity).

ton shows considerably stronger intraband absorption than a cold exciton<sup>13</sup>.

**Contribution of spectral shifts** In addition, also the decrease of the biexciton addition energy upon exciton cooling and the concomitantly reduced redshift of the absorption spectrum<sup>14</sup> will add to the rapid drop of the photo-induced absorption close to the band gap transition. Although these spectral shifts are important, it can be shown (see Figure 6.2) that the main contribution to the photo-induced absorption at longer wavelengths is due

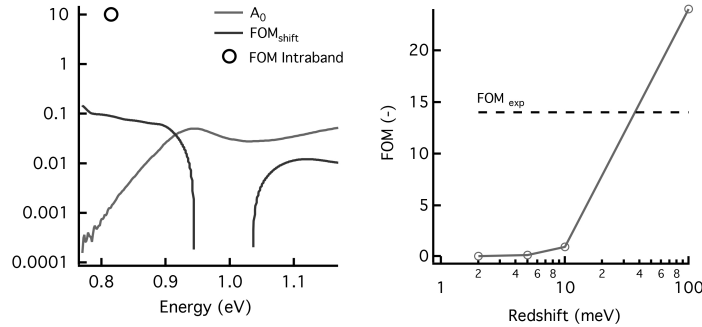


Figure 6.2: Estimation of contribution of spectral shifts compared to intraband absorption: (left) linear absorption spectrum of used sample with FOM (see further,  $FOM = \Delta A/A_0$ ) for a spectral redshift of 2 meV (corresponding to  $\langle N \rangle = 1$ ). The experimental FOM (for  $\langle N \rangle = 1$ ) at the matching wavelength (indicated by empty marker at 0.81 eV) is 2 orders of magnitude larger, indicating the dominance of hot carrier intraband absorption over spectral shifts. (right) FOM for an increasing redshift (in meV) at the matching wavelength. A shift of around 50 - 100 meV would be needed to explain the experimental FOM. Note that actual measured shifts are in the range of 1 - 10 meV per created exciton<sup>14</sup>

to intraband absorption.

### 6.3 Matching State Filling and Intraband Transitions

The interplay between hot carrier intraband absorption and band-gap bleach during exciton cooling can be analysed in more detail using spectral cuts of the transient absorbance taken at fixed delay times as represented in Figure 6.3a. At early times (0.3-0.4 ps), photoinduced absorption by hot excitons is pronounced and the band-gap bleach is limited since exciton cooling is far from complete. As a result, the differential absorbance is strong and positive apart from a small region around the bandgap transition. After exciton cooling (2-2.5 ps), the photoinduced absorption is reduced and the band-gap bleach has become more distinct. As a result, a net photoinduced absorption is only attained at wavelengths well beyond the bandgap transition. In a later stage (2.5 - 100 ps), multiexciton recombination further reduces the differential absorbance without however inducing significant spectral changes.

A remarkable point made clear by the spectral cuts shown in Figure 6.3a concerns the wavelength at which the opposing effects of photoinduced absorption (by intraband transition) and photobleaching (by state filling) yield a zero net differential absorption. Since both change during exciton cooling, this matching wavelength  $\lambda_m$  obviously shifts during the first 1-2 ps after photoexcitation. More importantly however is that this matching wavelength stays constant at  $\lambda_m = 1520$  nm for longer pump-probe delay times, without being affected by multiexciton recombination. Knowing the origin of the opposing effects (the presence of excitons opening up intraband transitions and blocking interband transitions) this can be readily explained: indeed, as all effects scale proportionally to  $\langle N \rangle$  after exciton cooling,  $\lambda_m$  should be independent of  $\langle N \rangle$ .

The significance of the matching wavelength being independent of  $\langle N \rangle$  can be appreciated better by looking at vertical cuts of Figure 6.1b taken at different wavelengths (see Figure 6.3b). At wavelengths shorter than  $\lambda_m$ , intraband transitions by hot carriers induce a strong initial photoinduced absorption that quickly decays with the cooling rate to reach a negative value, the subsequent time evolution of which reflects the decay of multiexcitons and, eventually, single excitons. Opposite from this, a residual photoinduced absorption remains after exciton cooling at wavelengths longer than  $\lambda_m$  on which the exciton recombination dynamics is imprinted as well. However, at the matching wavelength, the initial differential absorption drops to zero within 1-2 ps to remain zero, irrespective of further exciton recombination. At this wavelength, unexcited and excited QDs containing cold excitons have the same absorption coefficient and therefore, exciton recombination has no effect on the absorption coefficient. Given this interpretation for the transient  $\Delta A_{\lambda_m}(t)$  at the matching wavelength, its time evolution should hardly depend on the pump wavelength (as long as this is short enough to create hot excitons) and on the pump fluence. In Figure 6.4a we show a normalized  $\Delta A_{\lambda_m}$  transient while increasing the pump wavelength from the originally used 700 nm to 1100 nm in steps of 100 nm. Clearly, apart from quasi-resonant excitation at 1100 nm, all  $\Delta A(\lambda_m)$  are indeed largely identical in shape. The  $\Delta A_{\lambda_m}$  transient can be fitted to a double exponential decay, containing a faster component with a time constant of 0.65 ps and a slower component with a time constant of 1.05 ps (see Figure 6.4b). We attribute this two-component decay to the successive cooling of the hot carriers from the higher energy continuum of electron or hole states to the size quantized P states, followed by further cooling from these P state to the S states at the bottom of the conduction band or the top of the valence band due to phonon or Auger assisted relaxation<sup>19</sup>. The P-S cooling can indeed be expected to limit the decay rate since it requires the

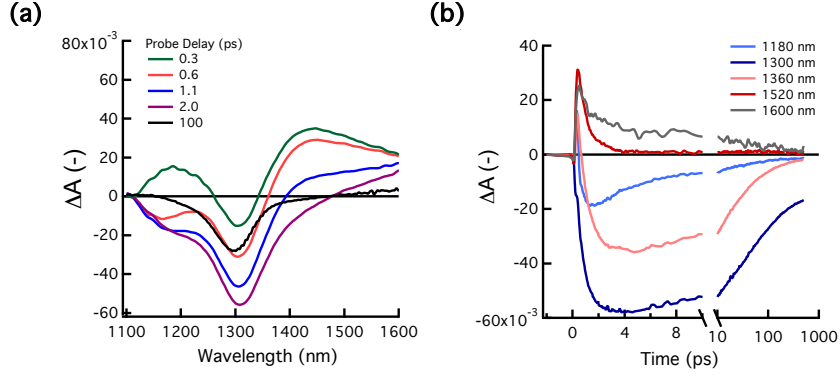


Figure 6.3: Kinetics and spectra (a) Differential absorbance  $\Delta A$  spectra at different probe delays obtained from horizontal cuts of Figure 6.1 and (b) kinetic traces at different wavelengths (vertical cuts of Figure 6.1).

largest energy change. Other reports attribute this double dynamic to fine structure reorganization of the highly degenerate band edge state ensemble<sup>20</sup>. Figure 6.4c represent the  $\Delta A_{\lambda_m}$  transient normalized relative to the absorbance  $A_0$  of unexcited QDs at 1520 nm as recorded for different pump fluences, each characterized by  $\langle N \rangle$ . The maximum ratio  $\frac{\Delta A}{A_0}$  – which we will use as a figure of merit (FOM) – determines the light intensity of a probe signal at  $\lambda_m$  that is additionally absorbed in the presence of a pump pulse:

$$\frac{\Delta A}{A_0} = \frac{\log(I_{t,0}) - \log(I_{t,p})}{\log(I_0) - \log(I_{t,0})} \quad (6.1)$$

Here,  $I_0$  is the incident light intensity while  $I_{t,p}$  and  $I_{t,0}$  are the transmitted intensity in the absence and presence of the pump pulse, respectively. Figure 6.4c shows that the FOM for a given pump pulse scales proportionally to  $\langle N \rangle$ , reaching a value of 23 for  $\langle N \rangle = 1.39$ . Moreover, since the FOM decay rate is largely independent of  $\langle N \rangle$ , we conclude that the  $\frac{\Delta A}{A_0}$  transient is a linear function of the pump intensity that provides an ultra-fast and intense increase of the extinction of a probe beam at the matching wavelength in the presence of a pump beam.

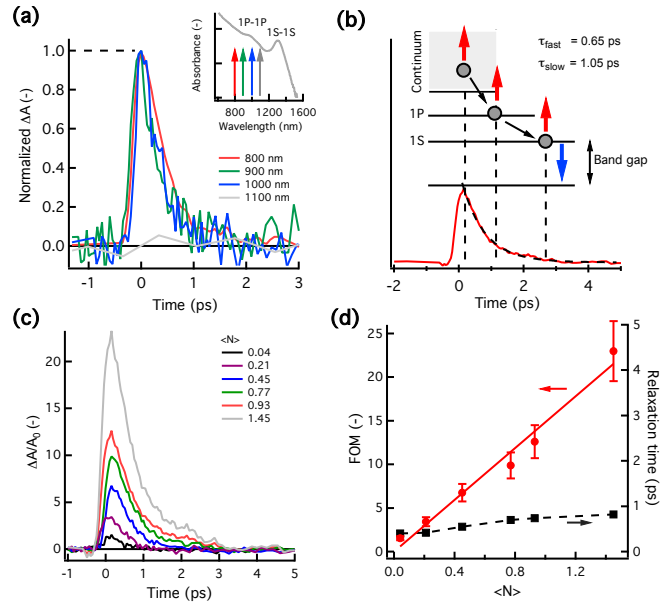


Figure 6.4: Pump wavelength and power dependence (a) Normalized QD response at matching wavelength as function of pump wavelength. Inset shows the wavelengths used compared to the linear QD absorption spectrum. No difference in dynamics is observed up until the  $1P_h-1P_e$  energy level is reached (at *ca.* 1100 nm). (b) Schematic of proposed mechanism of 1P-1S limited hot carrier cooling in relation the observed response at the matching wavelength. A bi-exponential fit yields a fast and slow relaxation rate of 0.65 ps and 1.05 ps respectively. (c) FOM for increasing pump fluence as expressed by increasing average exciton population  $\langle N \rangle$  (d) FOM (red circles) for increasing fluence plotted with time constant (black squares, overall decay). A linear fit (FOM =  $C \times \langle N \rangle$ ) to the data is shown (solid red line).

## 6.4 Strength and Dynamics

### 6.4.1 Refresh Timescale

The intensity and speed of the  $\Delta A_{\lambda_m}$  transient could make QDs ideal to convert a high bit rate optical signal carried by the pump beam to a probe beam at  $\lambda_m$  without photo-induced insertion loss. This however requires that the fast, intense and linear QD response is maintained when reducing the time delay between the pump pulses to a few picoseconds only, which

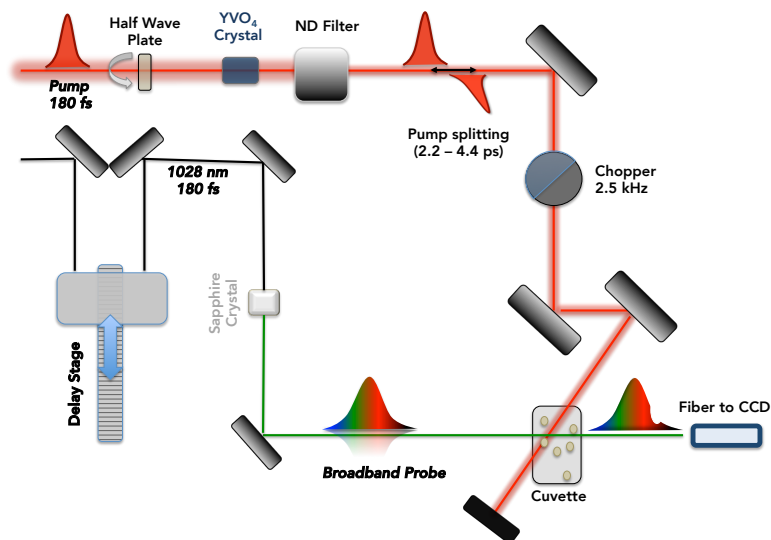


Figure 6.5: Schematic of setup used for pump-repump-probe experiments where multiple pump pulses are created using a series of birefringent  $YVO_4$  crystals.

would correspond to refresh rates in the range 0.1-1 terahertz. To investigate this, we have pumped the samples with trains of 2 or 4 pulses, in which each pulse is separated by only 2.2 or 4.4 ps (denoted as short and long delay). The pulse 'trains' are created by a method described in chapter 2. The initial 180 femtosecond pulse is linearly polarized under a desired angle using a half-wave plate and sent through a combination of birefringent  $YVO_4$  crystals to create a cascade of 2 pulses separated by the group delay imposed through the difference in refractive index between ordinary and extra-ordinary waves. The pulses are then sent through a depolarizer to avoid any polarization induced effects. No substantial pulse broadening is observed after propagation through the crystal sequence. To create 4 pulses an additional rotation through a second half-wave plate is used in combination with a 3rd bi-refringent crystal. This allows us to create 4 pulses separated by 2.2 ps without the need for additional delay stages or optics. The pulses are characterized by looking at the coherent Raman signal at 580 nm induced by the solvent (hexane). Although this type of autocorrelation should be interpreted with caution, no substantial pulse broadening was observed, nor temporally, nor spectrally.

The transient absorption map for a long delay, 2-pulse excitation in Fig-

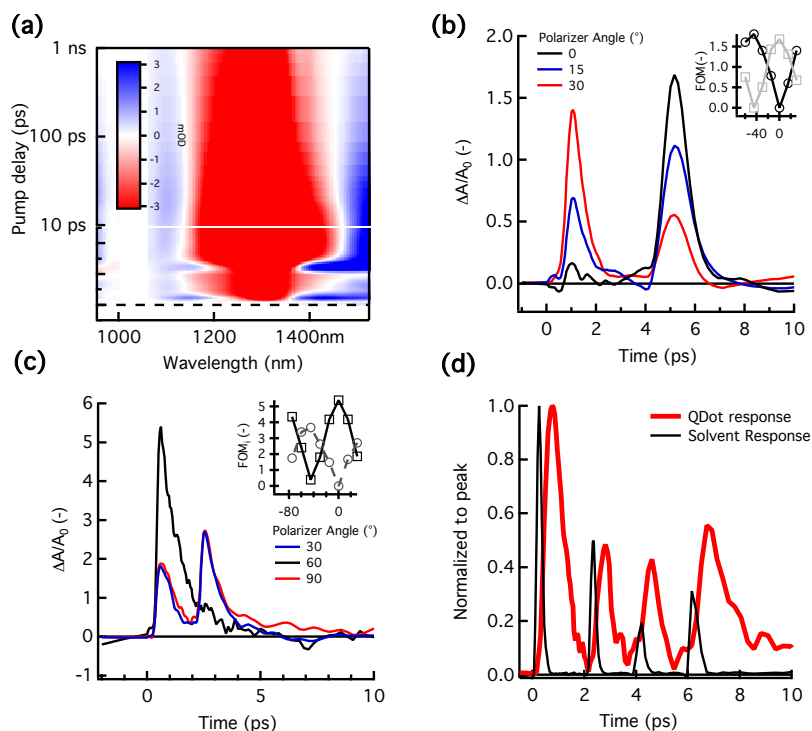


Figure 6.6: Ultrashort refresh times (a) 2D time-wavelength map of pump-repump-probe experiment with 4.4 ps separation between pump and re-pump. (b-c) Kinetics at matching wavelength for different input combinations showing the ability of the system to refresh after 4.4 ps (b) and 2.2 ps (c) respectively. (d) 4 pulse experiment showing the ability to process multiple pulses at a rate of ca. 250 Gb/s. Also plotted is the response of the solvent (n-hexane) as a measure of the pulse arrival time.

Figure 6.6a clearly shows that the second pump pulse results in a strong and broadband photoinduced absorption due to intraband transitions linked to the newly created hot excitons. As a result, the  $\Delta A_{\lambda_m}$  transients shown in Figures 6.6b-c are composed of a sequence of two clearly distinguishable absorption bursts even if the pulse separation is only 2.2 ps. Moreover, the linear dependence between the absorption amplitude and the signal intensity is maintained (see insets of Figures 6.6b-c) and also a 4-pulse excitation with 2.2 ps delay is converted into 4 absorption bursts at the matching wavelength (Figure 6.6d).

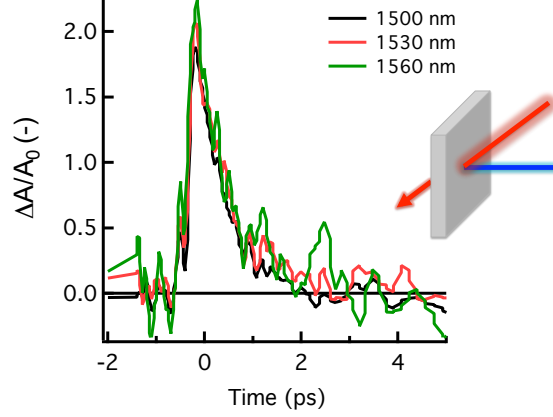


Figure 6.7: Demonstration of wavelength conversion in thin (75 nm) spincoated film of PbS QDs on a glass substrate.

#### 6.4.2 Interaction Lengths

Figure 6.7 represents a  $\Delta A_{\lambda_m}$  - transient recorded on a thin film of PbS QDs, a configuration more relevant for applications. Thin films are fabricated using spincoating from a dilute solution at 2000 rpm on silica glass substrates. Film thickness is obtained from AFM analysis and optical measurements. A similar behaviour is found as with dispersed QDs, where the opposing effects of photobleaching and photoinduced absorption match over an even broader wavelength range. The film thickness needed to achieve an appreciable modulation of the probe beam can be estimated by rescaling  $\Delta A_{\lambda_m}$  into an absorption coefficient transient. Since  $\Delta A_{\lambda_m}$  scales proportionally to  $\langle N \rangle$ , this is readily achieved within the framework of the intrinsic absorption coefficient  $\mu_i$ , a quantity that expresses the absorption coefficient for a fictitious material of quantum dot volume fraction  $f = 1$ . Accordingly the transient intrinsic absorption coefficient  $\Delta \mu_{i,\lambda_m}$  at the matching wavelength can be defined as:

$$\Delta \mu_{i,\lambda_m} = \frac{FOM}{\langle N \rangle} \mu_{i,\lambda_m} \quad (6.2)$$

Knowing  $\mu_{i,\lambda_m}$  (see Figure 6.1a) and using the relation between the FOM and  $\langle N \rangle$  (see Figure 6.4d), we find that the  $\Delta \mu_{i,\lambda_m}$  transient attains a maximum of  $5200 \text{ cm}^{-1}$ . Assuming a QD volume fraction  $f$  of 0.2 in a QD thin film, this implies that an approximately  $10 \mu\text{m}$  thick QD film would be needed to achieve a  $1/e$  modulation of the probe beam in the presence of the pump pulse at a time scale of 1 picosecond and a FOM of 11 dB. These

dimensions are compatible with, for example, integration on the end of a fibre tip or very compact integrated photonic devices.

## 6.5 Technological Relevance

### 6.5.1 Competitive Technologies for Wavelength Conversion

All-optical wavelength conversion is considered for future optical networks<sup>1</sup> as it provides a way around the electrical-optical-electrical (EOE) hurdle faced by fiber-to-the home networks these days. Switching the signals from the electrical domain to the optical domain (and back) are energy consuming and add to system complexity and operating costs. If optical signals could be processed (*i.e.* modulation and conversion of optical datastreams) entirely in the optical domain, both fabrication and operating costs could be reduced significantly. Currently, all-optical wavelength conversion relies on either phase modulation through  $\chi_3$  non-linearities (e.g. Kerr effect, four-wave mixing) or direct amplitude modulation (cross-amplitude modulation in SOA's). The phase modulation effects are typically weak requiring either long interaction lengths or complex interferometric configurations (e.g. Mach-Zehnders) with the need for high input powers. Amplitude modulation requires epitaxy of III-V semiconductors which are expensive and not directly compatible with *e.g.* the commercially interesting silicon-on-insulator (SOI) platform.

The use of novel materials such as QDs and graphene has seen increasing interest in recent years. Nanocrystals for all-optical wavelength conversion and logic was suggested by several groups: their approaches rely respectively either on pure intraband absorption, more complex hybrid surface functionalized films with limited extinction ratio<sup>21</sup> and complex multi-X behaviour requiring high pump fluences for operation<sup>12</sup>. For example, using classical intraband absorption<sup>13</sup>, the maximum FOM attainable is 8 (*i.e.* the X degeneracy of the 1S-1S ensemble) under multi-X fluences with a maximum speed of roughly 5–50 ps (multi-X Auger lifetime). We obtain higher FOMs at faster speed with sub-X fluences. Our approach does not require the use of multi-X, is readily applicable to standard surface functionalized nanocrystals and offers much higher FOMs (up to 12 for sub-X fluences) in a wide spectral range.

Another possible candidate could be found in graphene, as was recently demonstrated by Li et al.<sup>6</sup>. However, owing to the 2D character, the FOM demonstrated is small ( $\text{FOM} \ll 1$ ) requiring long interaction lengths. Moreover, the interaction of graphene with light is weak requiring high input powers to achieve conversion.

All-optical wavelength conversion requires a number of specific material properties: Transparency to bit-rates and formats, fast setup times of output, conversion to both shorter and longer wavelengths, moderate input power, idle conversion (ability to leave signal unaltered), polarization insensitivity, large extinction ratios and simple implementation. The nanocrystal platform proposed in this work meets all but one requirement (conversion to shorter wavelengths) under the zero-insertion loss condition. One issue remaining is the density of input and target wavelengths. Since the initial carrier has to be hot (*i.e.* carry excess energy), we cannot realize conversion between two closely spaced wavelengths (energies). As such, we should envisage applications where classic telecom signals (1260 nm - 1675 nm) are converted between the outer wavelength bands (*e.g.* O to L) in the existing OESCL band or to new wavelength bands such as the widely researched long wave infrared spectral around 2 micrometer<sup>22;23</sup>. This new spectral region would provide a solution to the increasing bandwidth issue and provides in addition reduced latency and dispersion, allowing denser wavelength spacing for *e.g.* WDM (Wavelength Division Multiplexing) applications.

### 6.5.2 Integration on SOI

To further increase the nonlinear interaction between the pump and probe beams in the QD thin film the latter could be integrated with an optical waveguide. It was recently shown that a QD film coated on a silicon waveguide interacts with the guided mode, thereby changing, *e.g.* its extinction coefficient<sup>24;25</sup>. Hence, when injecting a strong pump pulse in such a QD coated waveguide, a guided mode at the matching wavelength will undergo a fast absorption burst. Such a wavelength convertor could in particular be relevant for the increasingly popular silicon and silicon nitride based integrated waveguide platforms<sup>3;26;27</sup>. These are very attractive because their fabrication can rely on mature CMOS processing techniques and they allow for very compact devices due to the high index contrast. In addition they offer the possibility for monolithic electronic-photonic interfaces, which could lead to important savings in cost and power consumption. However the refractive index of silicon and silicon nitride exhibits only weak dependence on the light intensity precluding the realization of efficient all-optical switches and wavelength convertors. The combination with a QD thin film, which does exhibit strong and ultrafast non-linearities could resolve this issue.

**Modeling** To assess the potential of such a wavelength convertor, we modelled the FOM and extinction ratio for some generic waveguide configurations, characterised by an active area  $S$ , a modal confinement factor  $\Gamma$  denoting the power confined in the QD layer, a waveguide length  $L$  and an input pulse energy  $E_p$ . To evaluate the energy required to convert a pump pulse with energy  $E_{pulse,c}$  (at  $\lambda_c$ , e.g. at 1000 nm) to a target wave at  $\lambda_t$  (e.g. 1520 nm), we consider a waveguide (either integrated or fiber) configuration where the nanocrystals (QDs) are confined in an area  $S$  with (transverse) modal field confinement  $\Gamma$ , *i.e.* the fraction of the total optical mode that actually propagates in the area where the QDs are present (see Figure 6.8) The actual scaling for the intrinsic absorption coefficients should also include the volume fraction  $f$  of the QD film.

For simplicity, we only consider losses from the QD film, not from scattering or in and outcoupling to the waveguide itself. The intrinsic modulation scales with the average exciton density  $\langle N \rangle$  (see Figure 6.4c), created by absorption of photons at  $\lambda_c$ . Due to absorption of the carrier wave, the initial pulse energy will diminish upon propagation through the device with length  $L$ , such that in general  $\langle N \rangle$  will be a function of position  $x$ :

$$\langle N \rangle(x) = J_{ph,c}(x) \times \sigma_c \quad (6.3)$$

where  $J_{ph,c}$  is the photon flux at the carrier wavelength (photons/cm<sup>2</sup>) and  $\sigma_c$  is the absorption cross section of the QDs at that same wavelength. We can write  $J_{ph,c}$  as follows:

$$J_{ph,c}(x) = \frac{E_{pulse,c}}{\hbar\omega_c} \times e^{(-\Gamma f \mu_{i,c} x)} \times \frac{\Gamma}{S} \quad (6.4)$$

where indices  $(c, t)$  refer to (carrier, target) respectively.

By definition (see further), the change in absorption scales with the average exciton density  $\langle N \rangle$  through the intrinsic modulation coefficient  $\Delta\mu_{t,i}$ :

$$\Delta\mu_t(x) = \langle N \rangle(x) \times f \Delta\mu_{i,t} \quad (6.5)$$

where  $\Delta\mu_{i,t} = 5200 \text{ cm}^{-1}$ . As such, we can write the following for the beam intensity  $I$  at the target wavelength:

$$\frac{dI(x)}{dx} = -\Gamma(\mu_t + \Delta\mu_t(x)) \times I(x) \quad (6.6)$$

where  $\Gamma\mu_t$  is the regular linear absorption loss at the target wavelength  $\lambda_t$  without the carrier wave present. Solving this with the appropriate boundary conditions, gives us the extinction of the target wave after propagating

through a length  $L$  in the presence of a carrier wave with energy  $E_{pulse,c}$ .

$$\ln\left(\frac{I(L)}{I_0}\right) = -\left\{\Gamma f \mu_{i,t} L + \Delta \mu_{i,t} \times \frac{E_{pulse,c}}{\hbar \omega_c} \times \frac{\sigma_c \Gamma}{S \times \mu_{i,c} L} \times (1 - e^{-\Gamma \mu_{i,c} f L})\right\} \quad (6.7)$$

Note that the attenuation of the target wave in absence of the pump pulse, is given by:

$$\ln\left(\frac{I(L)}{I_0}\right) = -\Gamma f \mu_{i,t} L \quad (6.8)$$

Remembering the expression for the FOM (see Equation 6.1), we can rewrite the FOM based on the previous expression:

$$FOM = \frac{\Delta \mu_{i,t}}{\mu_{i,t}} \times \frac{E_{pulse,c} \sigma_c}{S \hbar \omega_c} \times \frac{1 - e^{-\Gamma f \mu_{i,c} L}}{f \mu_{i,c} L} \quad (6.9)$$

To evaluate the energy required to switch with a given FOM, we can write this as:

$$E_{pulse,c} = FOM \times \frac{\mu_{i,t}}{\Delta \mu_{i,t}} \times \frac{\hbar \omega_c S}{\sigma_c} \times \frac{f \mu_{i,c} L}{1 - e^{-\Gamma f \mu_{i,c} L}} \quad (6.10)$$

**Results** The main characteristics are shown in Figure 6.9, where the energy per bit required for reaching a FOM of 5 is plotted as a function of the interaction length for a fixed active area and different confinement factors. More detailed calculations, in line with the possible implementation of the convertor as a PbS films sandwiched between two Si waveguides or a QD-coated optical fibre<sup>6;22;28</sup> (see Figure 6.8) are shown in Figure 6.10.

### 6.5.3 Conversion Bandwidth

Although the wavelength where interband absorption and interband bleach match is quite special, a rather large range of wavelengths exist where they 'almost' match. Figure 6.11a shows a  $\Delta A$  transient at 1560 nm, at the lower energy side of the matching wavelength of 1520 nm for this sample. The transient does not drop back to zero because residual intraband absorption ( $\Delta A > 0$ ) remains uncanceled by interband bleach ( $\Delta A < 0$ ). We can define a background absorption  $A_{bg}$  corresponding to this residual absorption, which differs from the linear absorption  $A_0$ . It is clear that  $A_{bg} = 0$  for the matching wavelength. This description leads to a modified figure of merit (FOM):

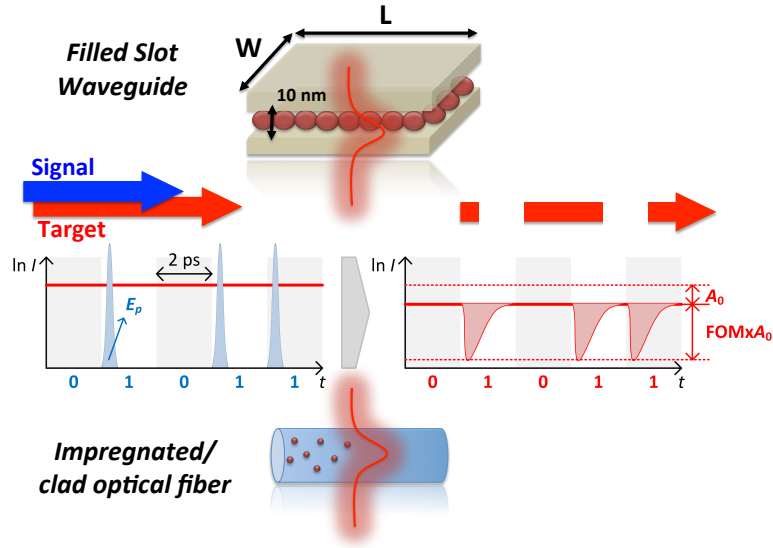


Figure 6.8: Integration considerations: Wavelength conversion scheme with incident pump (solid red)/probe (blue) sequence and corresponding output, using either a typical integrated SOI design with slot waveguide containing nanocrystals or a impregnated glass fiber.

$$\text{FOM}_{bg} = \frac{\Delta A_{max}}{A_{bg} + A_0} \quad (6.11)$$

Note that the regular FOM is indeed retrieved for  $A_{bg} = 0$  at the matching wavelength  $\lambda_m$ .

In Figure 6.11b,  $\text{FOM}_{bg}$  is shown for different conversion rates (1 and 2 ps, *i.e.* 1 THz and 500 GHz respectively). We can see that conversion up to 1600 nm is still possible, even at 1 THz, albeit with a reduced FOM. Note that a FOM of 1 for an exciton density of  $\approx 1$  corresponds closely to the case of pure intraband modulation without compensation (see chapter 2).

#### 6.5.4 Other Materials

The concept of matching interband and intraband transitions is quite general and applies to other materials beyond PbS as well. For example, HgTe QDs, studied for gain purposes in chapter 7, show similar properties as PbS though slightly different: the achievable FOM is much larger, yet the achievable speed is roughly 3 times slower. We attribute the larger FOM

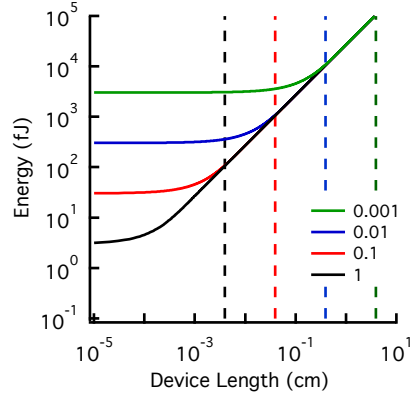


Figure 6.9: Switching energy (in femtojoule) per bit as function of device length  $L$  (in cm) to obtain a FOM of 5 in a  $1 \mu\text{m} \times 10 \text{ nm}$  area for different mode confinements  $\Gamma$  (0.001 – 1). Also shown are the 3dB - lengths (vertical dashed lines) for linear propagation in absence of the pump pulse.

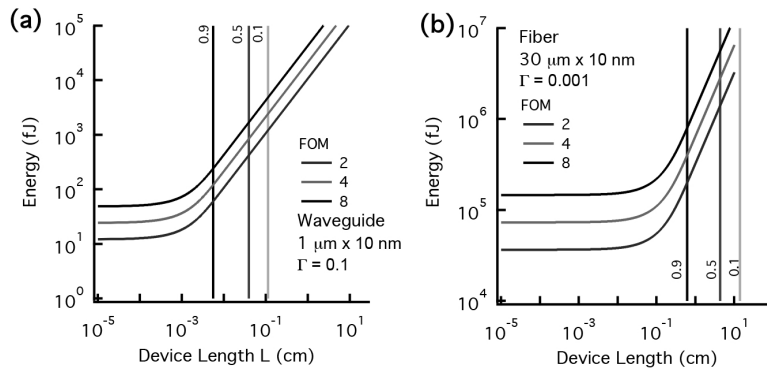


Figure 6.10: Evaluation of switching energy per bit (in fJ/bit) for a FOM of 1/2 (red) and 2 (blue) as function of device length (in cm). The cases of a slot waveguide and an optical fiber are considered. The vertical lines correspond to linear extinctions in absence of the pump pulse of 0.9, 0.5 and 0.1.

to the contribution of trap-states to the bleach spectrum, effectively red-shifting  $\Delta A$  compared to  $A_0$ , leading to a larger (if not 'infinite') FOM. The conversion speed is slower (roughly 3 times) because of slower carrier cooling in HgTe (see Figure 6.12).

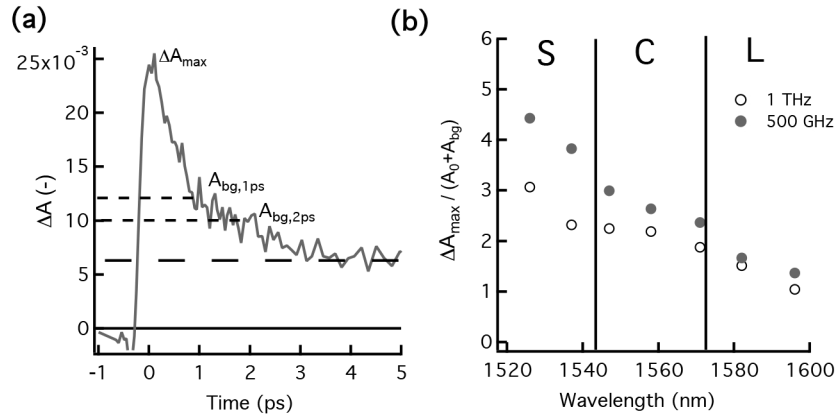


Figure 6.11: Conversion bandwidth (a)  $\Delta A$  transient at the lower energy (longer wavelength) side of the matching wavelength (1560 nm), indicating the  $A_{bg}$  for both 1 (1 THz) and 2 ps (500 GHz). The exciton density  $\langle N \rangle = 0.93$ . (b) Modified figure-of-merit  $FOM_{bg}$  for various wavelengths and conversion rates. The telecommunication bands S/C/L are also indicated.

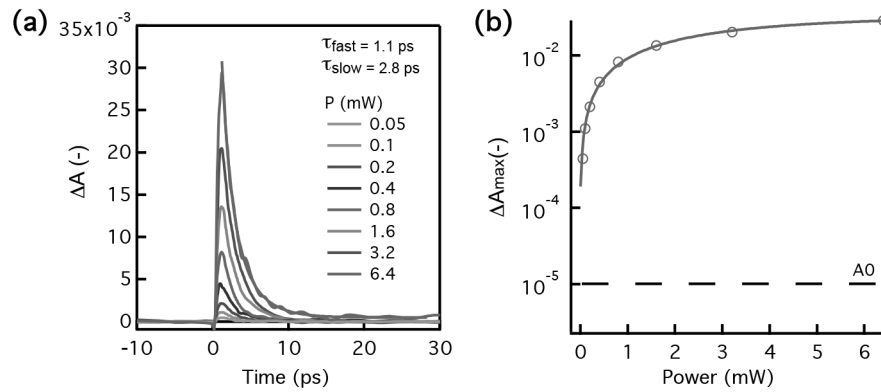


Figure 6.12: Wavelength conversion with 3.5 nm HgTe QDs (a)  $\Delta A$  at the matching wavelength of 1400 nm for increasing pump fluence and (b) Estimation of FOM showing the maximum  $\Delta A$  and the linear absorption  $A_0$  at the matching wavelength.

## 6.6 Conclusion

Using ultrafast broadband pump-probe spectroscopy, we show that colloidal PbS nanocrystals can be used for all-optical wavelength conversion with near-zero insertion loss, high extinction ratio and high speed. We estimate the energy required to switch under these conditions between a carrier and a target wave as 1–10 fJ/bit for two realistic photonic devices functionalized with QDs: an SOI slot waveguide and a photonic crystal fiber. Comparing QDs to other (novel) materials for AO wavelength conversion shows its great potential owing to material stability, solution processability, speed and improved light-matter interaction (compared to e.g. graphene).

## References

- [1] Alduino, A.; Paniccia, M. Wiring electronics with light. *Nature Photonics* **2007**, *1*, 153–155.
- [2] Yoo, S. Wavelength Conversion Technologies for WDM Network Applications. *Journal of Lightwave Technology* **1996**, *14*, 955–966.
- [3] Leuthold, J.; Koos, C.; Freude, W. Nonlinear silicon photonics. *Nature Photonics* **2010**, *4*, 535–544.
- [4] Durhuus, T.; Mikkelsen, B.; Joergensen, C. All-Optical Wavelength Conversion by Semiconductor Optical Amplifiers. *Journal of Lightwave technology* **1996**, *14*, 942–954.
- [5] Leuthold, J.; Moller, L.; Jaques, J. 160 Gbit/s All-Optical Wavelength Converter and Assessment of Its Regenerative Properties. *Electronics Letters* **2004**, *40*, 554–555.
- [6] Li, W.; Chen, B.; Meng, C.; Fang, W.; Xiao, Y.; Li, X.; Hu, Z.; Xu, Y.; Tong, L.; Wang, H.; Liu, W.; Bao, J.; Shen, Y. R. Ultrafast All-Optical Graphene Modulator. *Nano letters* **2014**, *14*, 955–959.
- [7] Pacifici, D.; Lezec, H. J.; Atwater, H. a. All-optical modulation by plasmonic excitation of CdSe quantum dots. *Nature Photonics* **2007**, *1*, 402–406.
- [8] Gong, K.; Zeng, Y.; Kelley, D. F. Extinction Coefficients, Oscillator Strengths, and Radiative Lifetimes of CdSe, CdTe, and CdTe/CdSe Nanocrystals. *The Journal of Physical Chemistry C* **2013**, *117*, 20268–20279.

- [9] Justo, Y.; Geiregat, P.; Hoecke, K. V.; Vanhaecke, F.; Donega, C. D. M.; Hens, Z. Optical Properties of PbS / CdS Core / Shell Quantum Dots. *Journal of Physical Chemistry C* **2013**, *117*, 20171–20177.
- [10] De Geyter, B.; Justo, Y.; Moreels, I.; Lambert, K.; Smet, P. F.; Van Thourhout, D.; Houtepen, A. J.; Grodzinska, D.; de Mello Donega, C.; Meijerink, A.; Vanmaekelbergh, D.; Hens, Z. The Different Nature of Band Edge Absorption and Emission in Colloidal PbSe/CdSe Core/Shell Quantum Dots. *ACS nano* **2011**, *5*, 58–66.
- [11] Klimov, V. I. Quantization of Multiparticle Auger Rates in Semiconductor Quantum Dots. *Science* **2000**, *287*, 1011–1013.
- [12] Saari, J. I.; Krause, M. M.; Walsh, B. R.; Kambhampati, P. Terahertz Bandwidth All-Optical Modulation and Logic Using Multiexcitons in Semiconductor Nanocrystals. *Nano letters* **2013**.
- [13] De Geyter, B.; Houtepen, A. J.; Carrillo, S.; Geiregat, P.; Gao, Y.; Ten Cate, S.; Schins, J. M.; Van Thourhout, D.; Delerue, C.; Siebbeles, L. D.; Hens, Z. Broadband and Picosecond Intraband Absorption in Lead-Based Colloidal Quantum Dots. *ACS Nano* **2012**, *6*, 6067–6074.
- [14] Geiregat, P.; Houtepen, A.; Justo, Y.; Grozema, F. C.; Van Thourhout, D.; Hens, Z. Coulomb Shifts upon Exciton Addition to Photoexcited PbS Colloidal Quantum Dots. *The Journal of Physical Chemistry C* **2014**, *118*, 22284–22290.
- [15] Moreels, I.; Justo, Y.; De Geyter, B.; Haustraete, K.; Martins, J. C.; Hens, Z. Size-tunable, Bright, and Stable PbS Quantum Dots: A Surface Chemistry Study. *ACS Nano* **2012**, *5*, 2004–2012.
- [16] Cademartiri, L.; Montanari, E.; Calestani, G.; Migliori, A.; Guagliardi, A.; Ozin, G. a. Size-dependent extinction coefficients of PbS quantum dots. *Journal of the American Chemical Society* **2006**, *128*, 10337–46.
- [17] Schaller, R. D.; Petruska, M. a.; Klimov, V. I. Tunable Near-Infrared Optical Gain and Amplified Spontaneous Emission Using PbSe Nanocrystals. *The Journal of Physical Chemistry B* **2003**, *107*, 13765–13768.
- [18] Stewart, J. T.; Padilha, L. a.; Qazilbash, M. M.; Pietryga, J. M.; Midgett, A. G.; Luther, J. M.; Beard, M. C.; Nozik, A. J.;

- Klimov, V. I. Comparison of carrier multiplication yields in PbS and PbSe nanocrystals: the role of competing energy-loss processes. *Nano letters* **2012**, *12*, 622–8.
- [19] Pandey, A.; Guyot-Sionnest, P. Slow electron cooling in colloidal quantum dots. *Science (New York, N.Y.)* **2008**, *322*, 929–32.
- [20] Johnson, J. C.; Gerth, K. A.; Song, Q.; Murphy, J. E.; Nozik, A. J.; Scholes, G. D. Ultrafast Exciton Fine Structure Relaxation Dynamics in Chalcogenide Nanocrystals. *Nano Letters* **2008**, *8*, 1374–1381.
- [21] Gao, Y.; Suchand Sandeep, C. S.; Schins, J. M.; Houtepen, A. J.; Siebbeles, L. D. a. Disorder strongly enhances Auger recombination in conductive quantum-dot solids. *Nature communications* **2013**, *4*, 2329.
- [22] Lyngsø, J. K.; Mangan, B. J.; Jakobsen, C.; Roberts, P. J. 7-cell core hollow-core photonic crystal fibers with low loss in the spectral region around 2  $\mu\text{m}$ . *Optics Express* **2009**, *17*, 23468–23473.
- [23] Li, Z.; Heidt, A. M.; Daniel, J. M. O.; Jung, Y.; Alam, S. U.; Richardson, D. J. Thulium-doped fiber amplifier for optical communications at 2  $\mu\text{m}$ . *Optics Express* **2013**, *21*, 9289–9297.
- [24] Omari, A.; Geiregat, P.; Van Thourhout, D.; Hens, Z. Light absorption in hybrid silicon-on-insulator/quantum dot waveguides. *Optics Express* **2013**, *21*, 23272.
- [25] Omari, A.; Xie, W.; Geiregat, P.; Van Thourhout, D.; Hens, Z. Modeling the Optical Properties of Low-cost Colloidal Quantum Dot Functionalized Strip SOI Waveguides. *IEEE Journal of Selected Topics in Quantum Electronics* **2014**, 1–1.
- [26] Rickman, A. The commercialization of silicon photonics. *Nature Photonics* **2014**, *8*, 579–582.
- [27] Simply silicon. *Nature Photonics* **2010**, *4*, 491–491.
- [28] Wu, H.; Zhang, Y.; Yan, L.; Jiang, Y.; Zhang, T.; Feng, Y.; Chu, H.; Wang, Y.; Zhao, J.; Yu, W. W. Temperature effect on colloidal PbSe quantum dot-filled liquid-core optical fiber. *Optical Materials Express* **2014**, *4*, 1856.



# 7

## Thresholdless Optical Gain using HgTe Quantum Dots

The use of colloidal quantum dots (QDs) as tunable and solution-processable gain media for optical amplifiers or lasers is still elusive in spite of 15 years of intense research. Gain thresholds remain too high and gain lifetimes too short for practical purposes. These properties are intrinsically linked to the QDs being effective 2-level systems, where the emitting transition is countered by absorption. Here, we show that HgTe QDs exhibit size-tunable stimulated emission throughout the infrared telecom window at a threshold 2 orders of magnitude lower than ever reported for QDs. We demonstrate that stimulated emission involves a high oscillator strength transition to a gap state, making HgTe QDs a nearly thresholdless effective 3-level system. The combination of gain coefficient, threshold and lifetime of HgTe QDs meets the requirements for DC electrical pumping.

### 7.1 Introduction

Several material systems were investigated over the past 30 years of QDs research<sup>1</sup>, most of them for applications in the visible part of the spectrum. However, the recent decade saw increased interest in particles that absorb and emit light in the near-infrared (NIR, 900 - 2000 nm)<sup>2:3</sup> and mid-infrared (MIR, beyond 2000 nm)<sup>4</sup> for applications in integrated photonics

(sensing and telecommunication), photodetection<sup>5</sup> and photovoltaics (*e.g.* for solution processable solar cells exploiting multiple-exciton generation (MEG)<sup>6</sup>, ...). Especially the near-infrared is a wavelength range of great technological relevance as it would allow the extension of fiber and silicon based photonics with potentially cheaper and more efficient light sources based on QDs.

Efforts in this direction are dominated by PbX (lead-chalcogenide) compounds (where X = S, Se, Te) which can be size tuned to emit roughly from 800 nm to 2400 nm, covering the entire near-infrared band with high quantum yield and excellent size uniformity<sup>2</sup>. In terms of light absorption, MEG was observed for all of these materials<sup>6</sup>, boosting the interest in their use as light absorbers in solar cells. Size variation (tuning the band gap) and deliberately modified surface chemistry (tuning the energy offset) allows the creation of single junction and/or stacked pn-junction photovoltaic cells operating at high efficiency (record: 8,85% under AMG 1.5) with solution processability and ambient stability for months. Even in terms of light emission, these PbX QDs behave superbly well, emitting light with quantum efficiencies over 50% and after some surface treatment (cation exchange) or encapsulation even great ambient stability<sup>2,7-9</sup>.

However, in terms of non-linear optical properties, PbX compounds should be considered only in a few cases. As was elaborated in chapter 6, the ultrafast hot carrier cooling and Auger recombination can be used to modulate light on picosecond timescales. However, the same properties that benefit light modulation, hamper light amplification. Indeed, maintaining a steady population inversion in lead-chalcogenides requires at least 4 excitations per dot (due to the 8-fold degeneracy of the conduction and valence band) which requires 1 photon per dot roughly every 1 – 10 ps since multi-excitons (MX) vanish on that timescale due to the fast Auger recombination<sup>10</sup>.

HgTe (or more general HgX where X=S,Se,Te) is considered as an alternative for the PbX compounds<sup>11</sup>. HgTe is a unique member of the zincblende semiconductor family as it is a semi-metal with a direct negative bulk band gap, which is unique for compound materials. Alloying HgTe with CdTe allows for band gap tunability in bulk. Owing to the negative band gap in bulk, the band gap can also be tuned from the long-wave infrared (LWIR) down to the near-infrared (NIR) by means of quantum confinement effects. Indeed, by shrinking the size of a HgTe crystal down to the nanoscale, the band gap becomes size dependent and confinement energies up to 1 eV are possible for 3 to 4 nm particles.

Although nanocrystalline HgTe (and bulk HgCdTe alloys) are widely recognized as excellent materials for near to mid-infrared photodetection<sup>4,12,13</sup>,

their viability as emitters in these wavelength ranges have not been heavily investigated<sup>14</sup>. As our interest lies in the near-infrared, the synthesis is tuned to obtain narrow and size-tunable photoluminescence throughout the entire near-infrared spectrum (from 1100 nm to 1600 nm).

As was mentioned by Lhuillier *et al.*<sup>4</sup>, the lower degeneracy of the band edge and reduced density of states should facilitate population inversion and reduce Auger rates. A possible disadvantage is the possible occurrence of surface states due to the inverted band structure<sup>13</sup>, but it will turn out these work greatly to our advantage !

## 7.2 Synthesis and Linear Optical Properties

### 7.2.1 Synthesis

Colloidal HgTe QDs were synthesized (see Figure 7.1) by modifying the procedure of Keuleyan *et al.*<sup>15</sup> and Sungwoo *et al.*<sup>16</sup> As such, 270 mg (1 mmol) of mercury chloride, 1.6 mL (6 mmol) of dodecanethiol (DDT) and 8 mL of oleylamine (OLA) were mixed in a 25 mL flask and degassed under vacuum at 100°C for one hour, after which the reaction mixture was placed under nitrogen while keeping the temperature at 60°C. Next, 1 mL of a 1 M solution of tellurium in tri-octylphosphine was rapidly injected and a black-colored reaction mixture was obtained within a few seconds. The reaction mixture was kept at the injection temperature to allow for QD growth for 1 minute (1220 nm emission) to 3 minutes (1300 nm emission), after which the reaction was quenched by injecting 10 mL of toluene and cooling with a water bath. As obtained HgTe QDs were purified 2 times using toluene and methanol. Polystyrene (100.000 g/mol) was added to as obtained solutions to avoid clustering on TEM grids.

A modified procedure yielding increased size mono-dispersity was developed recently<sup>13</sup>. In this procedure, 54mg (0.2 mmol) of HgCl<sub>2</sub> and 11.6 ml of OLA were mixed in a 25 ml flask and flushed under nitrogen at 120°C for one hour and then the reaction mixture was placed under nitrogen while keeping the injecting temperature at 55°C. Next, 0.1ml of TOP-Te (trioctylphosphine telluride, 2 mmol) diluted with 5ml of OLA was rapidly injected and QDs are allowed to grow at temperatures from 50°C to 100°C. The reaction was quenched by injecting 2 ml of dodecanethiol, 0.2 ml of TOP and 6 ml of toluene with a water bath. As obtained HgTe QDs were purified 2 times using toluene and methanol. Typical growth time for the 50°C synthesis is 30 seconds for particles with a first exciton peak at 1084 nm and 60 seconds for 1152 nm.

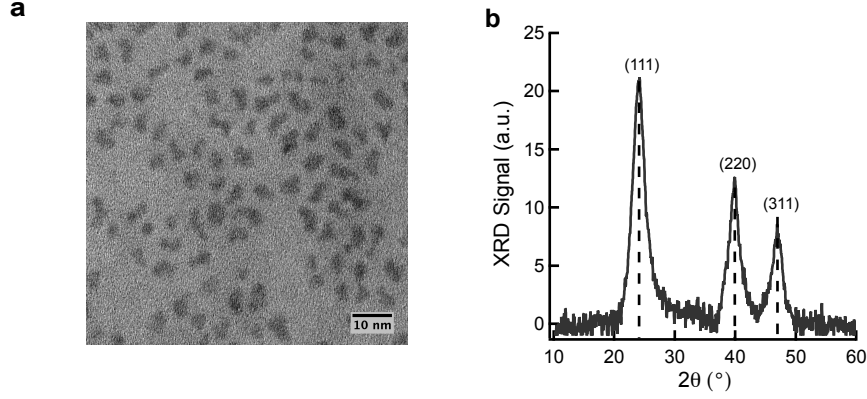


Figure 7.1: Structural Properties of HgTe QDs (a) HR-TEM (High Resolution Transmission Electron Microscope) image of  $3.5 \pm 0.3$  nm dodecane-thiol capped HgTe nanocrystals (b) XRD (X-Ray Diffraction) confirms zinc-blende crystallinity. Dashed lines indicate positions of the bulk HgTe diffraction pattern.

## 7.2.2 Absorbance

By varying the temperature (from  $50^\circ\text{C}$  to  $100^\circ\text{C}$ ), the size of the crystals formed is varied from roughly 4 nm to 7 nm. Larger sizes can be obtained by increasing synthesis temperature and/or applying re-growth techniques<sup>13</sup>. We should note that the band gap of bulk HgTe is actually negative<sup>17</sup> (so-called *inverted* band structure or semi-metallic behaviour) meaning that the band gap energies of roughly 1 eV obtained for the smallest sizes actually represent quite large confinement energies.

To estimate concentrations and evaluate intrinsic optical parameters (*e.g.* intrinsic gain), the intrinsic absorption coefficient at 400 nm is determined from the bulk optical constants of HgTe<sup>18</sup>:

$$\mu_i = \frac{2\pi}{\lambda n_s} |f_{LF}|^2 \epsilon_i \quad (7.1)$$

$$\mu_{i,400nm} = 4.84 \cdot 10^5 \text{ cm}^{-1} \quad (7.2)$$

where the local field factor for spherical nanocrystals is defined as (see Chapter 2):

$$f_{LF} = \frac{3\epsilon_h}{\epsilon_d + 2\epsilon_h} \quad (7.3)$$

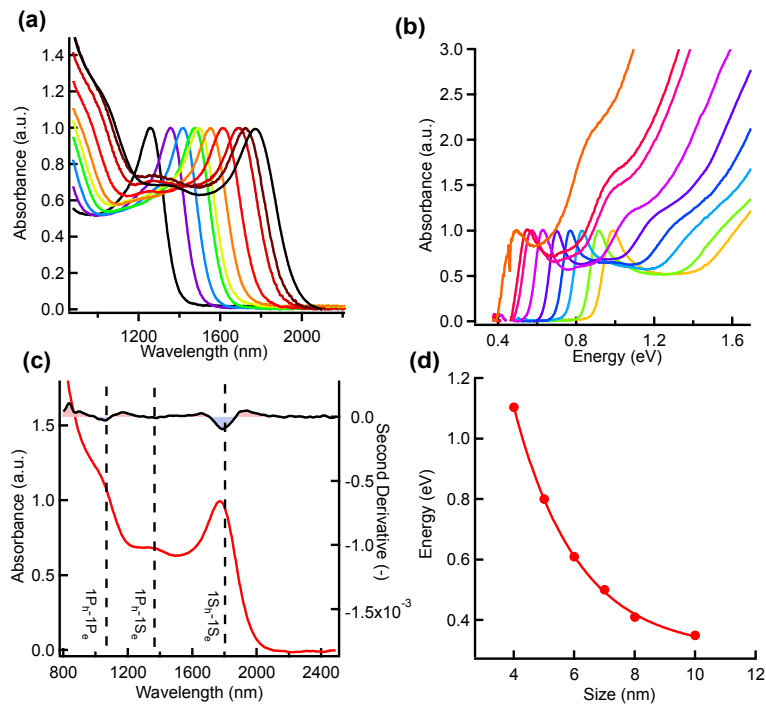


Figure 7.2: (a) Absorption spectra of HgTe QDs showing the extreme size tunability offered by HgTe over the near-infrared window with excellent size dispersity, (b) Combination of absorption spectra of 60°C and 100°C syntheses showing narrow absorption features into the mid-infrared. (c) Identification of different transitions through second derivative analysis and (d) a sizing curve (both from Keuleyan *et al.*<sup>13</sup>), relating the energy of the first excitonic feature to the particle size.

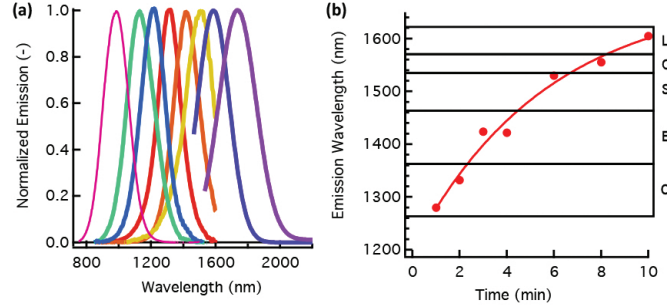


Figure 7.3: Size tunability of photoluminescence (a) Peak emission wavelength of 60°C synthesis for aliquots taken at different times (up to 10 minutes). (b) The entire telecommunication (OESCL) band is covered as is indicated with the solid lines.

Concentrations and absorption cross sections (*e.g.* to determine  $\langle N \rangle$  in the ultrafast experiments, see further) can be derived from the sizing curve (see Figure 7.2c) in combination with  $\mu_{i,400nm}$ <sup>19</sup>:  $\sigma_{abs,400} = V_{QD} \times \mu_{i,400nm}$ , with  $V_{QD}$  the volume of the quantum dot.

Recent reports by Lhuillier *et al.*<sup>14</sup> also report on the intrinsic absorption coefficient (obtained through elemental analysis), yielding values close to our theoretical estimate:

$$\frac{\sigma_{Lhuillier}}{\sigma_{theory}} \simeq 0.87 \quad (7.4)$$

### 7.2.3 Photoluminescence

The photoluminescence (PL) of HgTe QDs was addressed by a number of recent studies<sup>14;15;20</sup> and similar values for quantum yield (QY) (7-15%) and PL lifetime  $\tau$  (in the order of 20 – 40 ns, see Figure 7.5) were found. Tight binding calculations yield a lifetime  $\tau_{rad}$  of ca. 300 ns. Combining lifetime and QY seems to be consistent:  $\tau \simeq \tau_{rad} \times QY$ , indicating homogeneity of the sample.

Figure 7.4 shows a fluorescence line-narrowing experiment on monodisperse HgTe QDs, showing that the linewidths measured at room temperature are mostly limited by homogeneous (*e.g.* phonon coupling, decoherence) mechanisms rather than inhomogeneous effects (*e.g.* size distribution). Figure 7.3 shows the tunability of HgTe PL over the entire OESCL band, making the material very relevant for applications in silicon photonics and fiber based telecommunication.

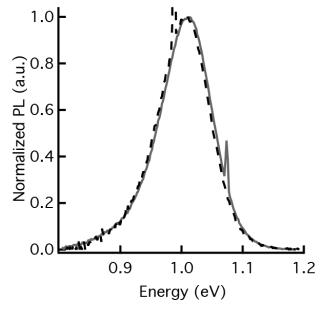


Figure 7.4: Excitation spectroscopy on HgTe QDs showing PL spectra for excitation at 1150 (solid black) and 1250 nm (dashed red).

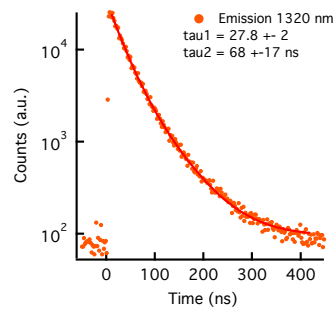


Figure 7.5: Photoluminescence lifetime measurement on 1320 nm emitting HgTe QDs with bi-exponential fit.

### 7.2.4 Low Temperature

Samples are deposited by dropcasting from toluene solutions on quartz substrates and loaded into a contact cryostat (Helium contact type) where the temperature is varied from 4.2 to 250 K. Upon photo-excitation with 400 nm (3.1 eV) the photoluminescence of the dropcast film is collected as a function of temperature (see Figure 7.6a). Even at room temperature, the emission can be decomposed in 3 components: two interband terms (labeled as X2 and X1) and a 'subgap' state, labeled 'gap'. This gap emission will be used later on to explain the peculiar ultrafast dynamics of HgTe, particularly the observed low threshold amplification. The energy of the different components is plotted as function of temperature in Figure 7.6c where a clear redshift (decreasing energy) with decreasing temperature is observed for all components. The energy difference  $E_{X2} - E_{X1}$  is constant over the studied temperature range at 30 meV. The gap-state intensity amounts to 30–40% of the total emission (see Figure 7.7).

## 7.3 Theoretical Description of Energy Level Structure of HgTe Quantum Dots

In this section, the optical properties and energy level structure of HgTe QDs is discussed as calculated within a tight binding framework by Delerue *et al.*<sup>17</sup>.

### 7.3.1 Methods

In a first step, the single-electron states are computed using a tight-binding model of HgTe. In a second step, the excitonic states  $\Psi_{exc,i}$  are obtained using a Configuration Interaction (CI) method, *i.e.* they are expanded in a basis of Slater determinants built using the single-particle states obtained in tight-binding. The optical cross section of a single nanocrystal of dielectric constant  $\epsilon_{in}$  embedded in a solvent of dielectric constant  $\epsilon_{out}$  is given by:

$$\sigma(\hbar\omega) = \frac{4\pi^2 e^2 |f_{LF}|^2}{cn} \times \sum_i \omega_i |V_i|^2 L(\hbar\omega - \hbar\omega_i) \quad (7.5)$$

Here  $\hbar\omega$  is the photon energy,  $\hbar\omega_i$  is the energy of the excitonic state  $\Psi_{exc,i}$ ,  $n = \sqrt{\epsilon_{out}}$ ,  $f_{LF} = \frac{3\epsilon_h}{\epsilon_d + 2\epsilon_h}$  is the local-field factor. The dipolar matrix element matrix element  $V_i$  is given by:

$$V_i = \sum_n \langle 0 | e \cdot \mathbf{r}_n | \Psi_{exc,i} \rangle \quad (7.6)$$

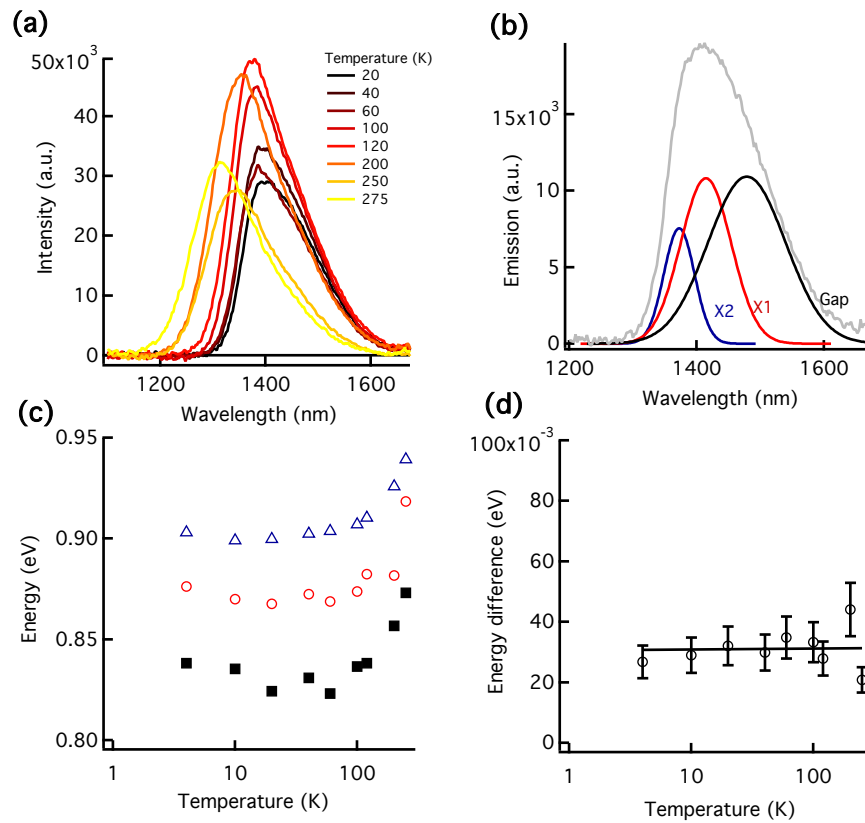


Figure 7.6: Overview of low temperature measurements: (a) Photoluminescence of dropcasted film after 400 nm photo-excitation as function of temperature, (b) decomposition in 3 components, (c) energy position of different components (gap (black squares), X1 (red circles) and X2 (blue triangles)) and (d) energy difference between the two interband components.

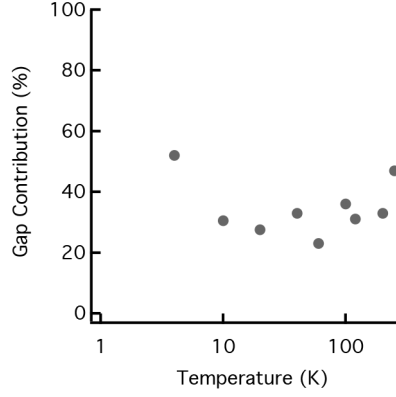


Figure 7.7: Contribution of gap states (in %) to total emission as function of temperature.

where  $r_n$  is the position of the electron  $n$  and  $\mathbf{e}$  is the polarization vector. The function  $L$  is a Gaussian which describes the homogeneous/inhomogeneous broadening (here 35 meV) of the optical transitions. The radiative lifetime  $\tau$  is calculated using:

$$\frac{1}{\tau} = \frac{4e^2 |f_{LF}|^2 n}{3c^3 \hbar} \times \sum_i p_i \omega_i^3 |V_n|^2 \quad (7.7)$$

Here,  $p_i$  is the thermal population of the excitonic state  $\Psi_{exc,i}$  at 300 K. The effective dielectric constant is calculated in tight-binding as described in earlier work by Delerue *et al.*<sup>21</sup>. Basically, the screened electrostatic potential in a nanocrystal is calculated on which we apply a uniform (static) electric field. By fitting this potential using the expression derived from classical electrostatic theory, we deduce a value of  $\epsilon_{in} = 6.8$  for a spherical nanocrystal of diameter 3.5 nm. We assume that the resulting local-field factor is the same in tetrahedral nanocrystals as in spherical nanocrystals with the same volume.

### 7.3.2 Band Structure and Absorption Spectra

Figure 7.8 represents the upper valence band (low energy side) and lower conduction band (high energy side) electronic states of spherical, 3.5 nm HgTe QDs calculated using the semi-empirical tight binding approach described before. Whereas the lowest conduction band level (CB1) is a 2-fold degenerate state well separated from higher levels, two closely spaced, 4-fold degenerate levels (VB1 and VB2) are found at the top of the valence

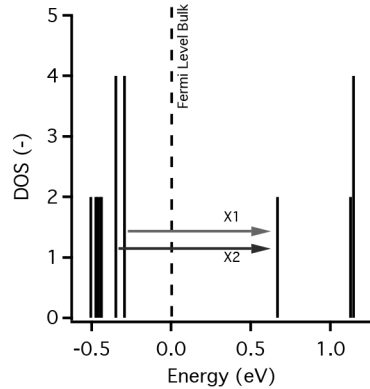


Figure 7.8: Density of States in the valence and conduction band calculated by tight binding.

band. Combining these single particle states into exciton states yields the possible optical transitions observed in our experiments.

Figure 7.9 shows the thus calculated absorption spectrum for both neutral (no holes or electrons) and singly charged (1 electron or 1 hole) QDs. In the charged cases, additional intraband absorption occurs at longer wavelengths, especially involving intraband transitions of holes. The 2- and 4-fold degeneracy of the CB1 and VB1 states lead to an 8-fold degenerate lowest energy exciton denoted by X1. The combination of CB1 and VB2 states lead to a second exciton, X2, with a similar 8-fold degeneracy, separated from X1 by 54 meV in this calculation. This energy difference strongly exceeds the typical phonon energies in HgTe (17 meV)<sup>14</sup>, possibly slowing down relaxation between these states. Importantly, the X2 transition has an oscillator strength about 10 times larger than X1 (see Figure 7.9), making that X2 dominates the absorption spectrum. Qualitatively similar results are obtained for tetrahedral nanocrystals, which indicates that this basic picture of the level structure can be used to interpret experimental results on an ensemble of differently shaped HgTe QDs.

## 7.4 Nearly Thresholdless Optical Gain

### 7.4.1 Methods

Samples were pumped using 180 femtosecond pulses at 700 nm, created from the 1028 nm fundamental (Pharos SP, 6W, Light Conversion) through non-linear frequency mixing in an OPA (Orpheus, Light Conversion). Probe

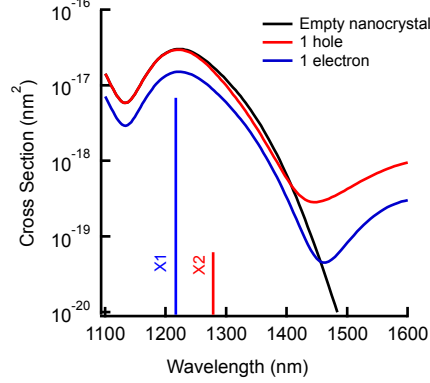


Figure 7.9: Absorption cross section of an empty, singly charged (electron/hole) spherical HgTe QD calculated with tight binding.

pulses were generated in a sapphire crystal using the 1028 nm fundamental. The pulses were delayed relative to the probe using a delay stage with maximum delay of 2.5 ns (Helios Spectrometer, Ultrafast Systems). The probe spectrum covers the NIR window from 1100 nm up to 1620 nm. HgTe QDs were dispersed in a transparent solvent (tetrachloroethylene) to achieve optical densities of  $\sim 0.1$  at the first exciton transition. No air-free sample handling was required as HgTe is, under our conditions, insensitive to oxidation. The average number of absorbed photons (or photo-generated excitons) at time zero  $\langle N \rangle$  was calculated as:

$$\langle N \rangle = J_{ph} \times \sigma_{700} \frac{1 - 10^{-A_{0,700}}}{A_{0,700}} \quad (7.8)$$

Here  $J_{ph}$  is the photon flux per pulse in photons/cm<sup>2</sup> at 700 nm,  $\sigma_{700}$  is the absorption cross section of the nanocrystals at the pump wavelength of 700 nm and  $A_{0,700}$  is the sample absorbance at 700 nm. The additional factor corrects for variation of the pump fluence along the pump beam path length. The cross section  $\sigma_{700}$  is determined starting from  $\mu_{i,400}$  (see 7.2.2) as<sup>22</sup>:

$$\sigma_{700} = V_{QD} \times \mu_{i,400} \times \frac{A_{0,700}}{A_{0,400}} \quad (7.9)$$

Here,  $V_{QD}$  is the volume of the quantum dot. Note that the (relative) error on  $V_{QD}$  is 32% due to the size distribution obtained through TEM-analysis. This allows us to determine the scaling factor between pump fluence (mW) and absorbed photons as  $0.31 \pm 0.1$  X/mW. This translates into an error of 32% on all mentioned  $\langle N \rangle$  values.

### 7.4.2 Band Edge Dynamics

Figure 7.10a shows a 2D image of the differential absorbance, obtained after a 700 nm pump pulse that leads to an average number of absorbed photons per QD  $\langle N \rangle$  of 0.1. The bleach of the first exciton transition, clearly visible around 1200 nm, narrows down and loses intensity in the first nanosecond after the pump pulse. In addition, the change in absorbance extends up to 1500 nm, a wavelength well beyond the first exciton transition. At these longer wavelengths, little dynamics is observed within the timeframe of the TA measurement. By comparing the difference  $\delta A = \Delta A(2500\text{ps}) - \Delta A(5\text{ps})$  between spectral cuts at 5 ps (when carrier cooling is complete, see also Figure 7.16a) and 2.5 ns, it follows that especially the bleach at the blue side of the first exciton transition is reduced (see Figure 7.10b). In view of the tight binding calculations, we attribute this change to the depletion of the high energy X2 manifold with large oscillator strength in favour of the lower energy X1, which has much lower oscillator strength. A detailed decomposition of the spectra shows that the X1-X2 splitting is 76 meV, similar to the 54 meV splitting predicted by tight binding calculations. The X2-X1 relaxation happens on a 700 ps time-scale, a decay component also found in the time resolved photoluminescence traces (see Figure 7.11). We thus conclude that the bleach of the first exciton transition reflects a relaxation of the holes between the VB2 and VB1 states.

### 7.4.3 Fluence Dependence of Gain Threshold

A more striking observation is the extension of the bleach spectrum up to 1500 nm. Figure 7.12a compares the corresponding bleach measured at a 2.5 ns delay for different pump fluences (increasing  $\langle N \rangle$  from 0.006 to 0.3) with the linear absorption and photoluminescence spectrum. It follows that at the long wavelength side a situation where  $|\Delta A| > |A_0|$  is reached, *i.e.* the sample amplifies the probe light, even for very low pump fluences. To make this observation more clear, Figure 7.12b plots the spectrum of the nonlinear absorbance  $A = \Delta A + A_0$ , again measured for a 2.5 ns delay, for different pump fluences. Note that this delay strongly exceeds the lifetime of multi-X (which decay on a 50 ps timescale), such that QDs contain a single exciton at the most. At low fluence ( $\langle N \rangle < 0.006$ ), absorption dominates and  $A > 0$  at all wavelengths. However, when increasing the fluence,  $A$  becomes negative in a small spectral region. Increasing the fluence further, yet remaining well below  $\langle N \rangle = 1$ , broadens this gain region from 1290 nm to 1510 nm, covering 3 technologically relevant transparency windows of commercial glass fibre (O,E and S-band, 1260 to 1530 nm, see also Figure 7.3b). From Figure 7.12b, we can derive the threshold for stim-

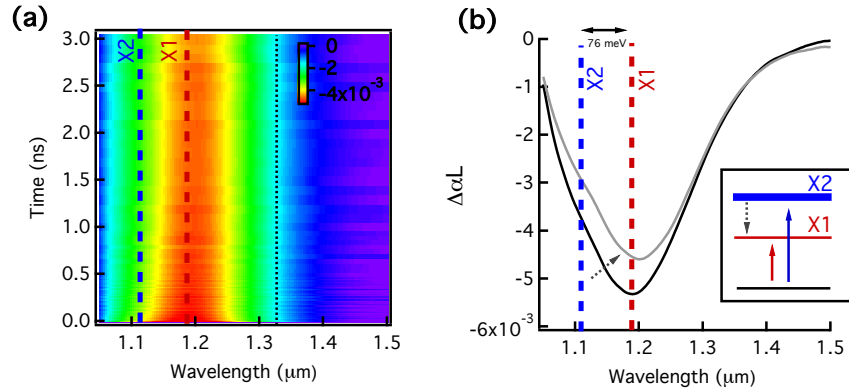


Figure 7.10: Two dimensional plot of  $\Delta A$ , both as function of wavelength and time (a) Broadband image showing the broad bleach ( $\Delta A < 0$ ) obtained after 700 nm photo-excitation at  $t = 0$  with average number of absorbed photons per nanocrystal  $\langle N \rangle = 0.1$ . The band edge features X1 and X2 as predicted by the tight binding calculations (see Figure 7.9) are added for comparison. (b) Taking spectral cuts at 5 ps (solid black line) and 2500 ps (solid grey line) shows the fine structure relaxation within the HgTe band edge, *i.e.* holes spread from VB2 to VB1 with a 700 ps time constant.

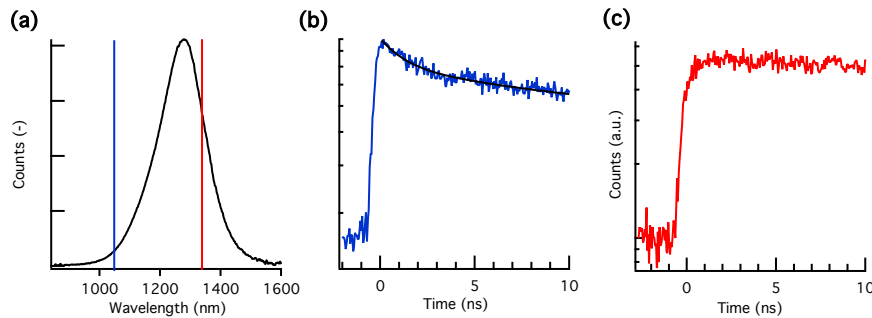


Figure 7.11: Zoom of photoluminescence decay at blue and red side of emission spectrum (a) Steady state photoluminescence (PL) under 700 nm excitation. (b) PL decay at 1030 nm (blue line in (a)) and (c) 1370 nm (red line in (a)) for 700 nm excitation (excitation pulse width = 0.1 ns). A bi-exponential fit in (b) yields a fast component lifetime of 1.1 ns, similar to the 0.7 ns component observed in the TA experiments.

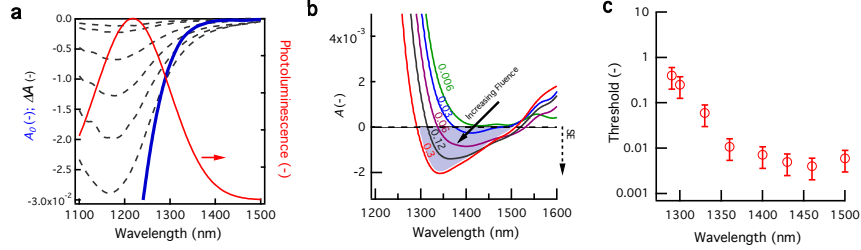


Figure 7.12: Analysis of fluence dependence for 1220 nm emitting HgTe QDs (a) Fluence dependent difference spectra  $\Delta A$  (grey dashed line), taken 2.5 ns after photo-excitation at 700 nm, plotted together with the linear absorption  $A_0$  (solid blue line) and steady-state emission (solid red line). (b) Non-linear absorption spectra  $A$ , again taken 2.5 ns after photo-excitation. Stimulated emission (SE) corresponds to  $A < 0$ . The maximum gain bandwidth extends from 1310 to 1500 nm at sub-X fluence ( $\langle N \rangle = 0.3$ ). (c) The wavelength dependence of the gain threshold.

ulated emission as a function of wavelength. This is displayed in Figure 7.12c, which clearly shows that the threshold for optical gain is far below the single exciton occupation ( $\langle N \rangle = 1$ ), dropping to 0.005 at 1500 nm. Note that this is, to the best of our knowledge, the lowest gain threshold ever reported for colloidal QDs, both in the visible and near-infrared part of the spectrum. Similar observations are made for particles emitting at 1300 nm (see Figure 7.13) where only the spectrum is redshifted compared to the 1220 nm emitting particles of Figure 7.12.

The condition for stimulated emission  $A < 0$  is mathematically equivalent to  $\frac{|\Delta A|}{A_0} > 1$ , an expression called the normalized bleach. The latter is often used in systems with small spectral shifts where it can be directly related to a state-filling expression<sup>23</sup>. Indeed, neglecting spectral shifts and intraband absorption, we can write in a simple  $g$ -fold degenerate 2-level system:

$$\frac{|\Delta A|}{|A_0|}(E) = \sum_{N=1}^g P(N) \left(1 - \frac{2N}{g}\right) \quad (7.10)$$

In systems without strong spectral shifts, the normalized bleach is limited to a value of 2. It is clear that for a system with strong spectral shifts, this no longer holds as the absorption cross section for excited dots is at substantially different energies than for unexcited dots. This will evidence itself as values for the normalized bleach much larger than 2, as is seen in

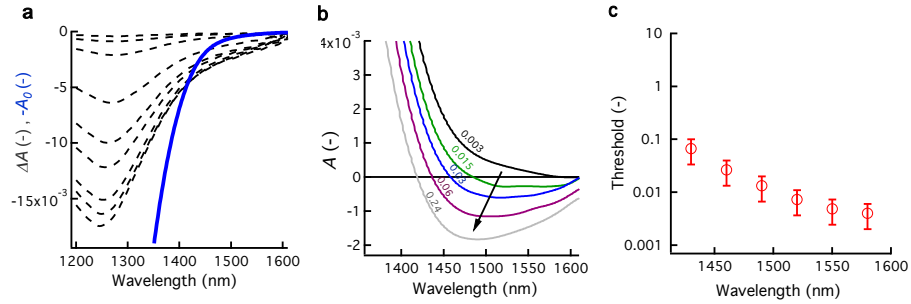


Figure 7.13: Analysis of fluence dependence for 1300 nm emitting HgTe QDs (a) Fluence dependent difference spectra  $\Delta A$  (grey dashed line), taken 2.5 ns after photo-excitation at 700 nm, plotted together with the linear absorption  $A_0$  (solid blue line). (b) Non-linear absorption spectra  $A$ , again taken 2.5 ns after photo-excitation. Stimulated emission (SE) corresponds to  $A < 0$ . The maximum gain bandwidth extends from 1400 nm to beyond 1600 nm at sub-X fluences ( $\langle N \rangle = 0.3$ ). (c) The wavelength dependence of the gain threshold as obtained from figure (b) (see text).

the case of HgTe (see Figure 7.14).

#### 7.4.4 Exciton Dynamics and Gain Lifetime

To confirm the single exciton character of the observed optical gain, we analyze the decay of the bleach signal, *i.e.*, the gain lifetime. If the gain effectively occurs in the single exciton regime, the decay should be on the order of the luminescent lifetime, *i.e.* 30-40 ns. Representative kinetic traces (at 1340 nm) are shown in Figure 7.15. As we know from the previous analysis, increasing the fluence renders  $A$  negative at populations far below  $\langle N \rangle = 1$ . More importantly however, the stimulated emission appears to be constant and persists longer than the measurable time window of the TA setup (2.5 ns). A fit to the apparently constant (in reality very slow) decay yields a lifetime of 34 ns, close to the measured 40 ns lifetime of single X. These findings confirm that the stimulated emission we observe is indeed due to singly excited QDs.

As can be seen in Figure 7.15, faster decay components show up at higher pump fluence where multi-X states can be formed by multi-photon absorption. These multi-X decay on a 50 picosecond time-scale (see Figure 7.16b), which is typical for biexciton Auger recombination<sup>24;25</sup>, quickly leaving behind a single excitation in the dots. Although ultrafast dynamics

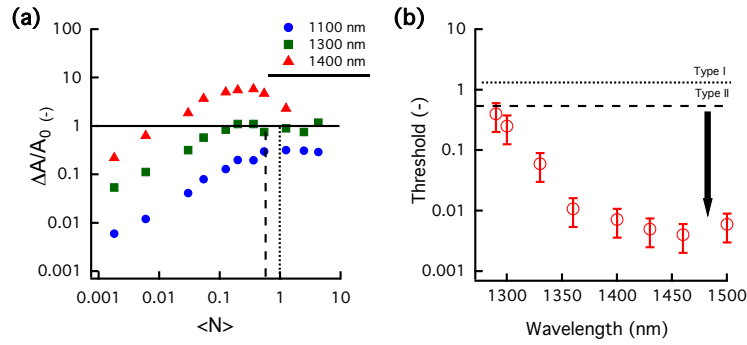


Figure 7.14: Analysis of 1220 nm emitting HgTe QDs (a) Normalized bleach for 3 different wavelengths throughout the broad bleach band. (b) Threshold comparison to best efforts in the visible part of the spectrum.

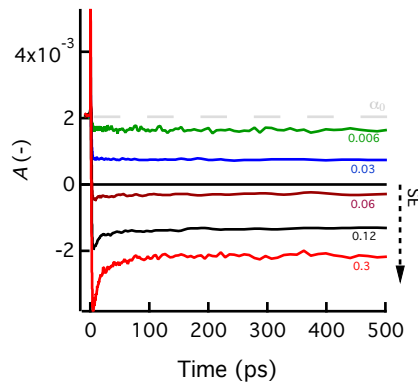


Figure 7.15: Kinetics of  $A$  at 1340 nm (gain maximum) for increasing fluence. Note that  $A < 0$  (reached at  $\langle N \rangle \ll 1$ ) corresponds to net optical gain, *i.e.* where stimulated emission dominates over absorption.

due to multi-X are present at higher pump fluence, we stress that the transient absorption does not drop below the gain threshold after the decay of the multi-X, confirming once more that multi-X are not required for optical gain. At higher fluences, an even faster 10-20 ps component is imposed on the kinetics which will be discussed further.

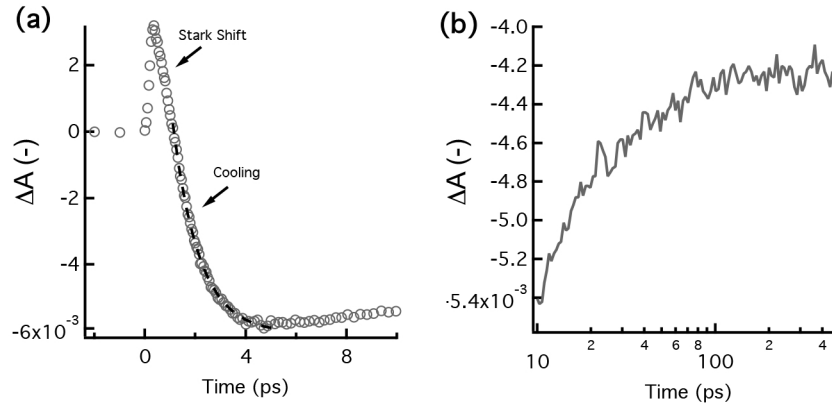


Figure 7.16: Zoom of carrier dynamics (a) carrier cooling and (b) bi-exciton Auger-recombination on a 50 ps timescale.

#### 7.4.5 High Fluence Regime

A very fast component (10 ps) is also superimposed on the multi-X decay (see Figure 7.15), a feature that was also observed in studies on multiple-exciton generation<sup>25</sup>. In line with that work, we attribute this component to fast non-radiative recombination in charged QDs that are formed at higher pump fluences. A clear indication of this is found in the low fluence traces, where no ultrafast (10 ps) components are present. Moreover, refreshing the pumped volume through stirring reduces the relative weight of the ultrafast component, indicating that the recombination is not intrinsic but due to formation of charged species in the volume under study (see Figure 7.17). A more in-depth explanation of this fast component is given further on when a model is developed to explain the complete picture of exciton dynamics in HgTe QDs.

With a degeneracy of 2 and 4 of the CB1 and VB1 states, population inversion at the bandgap transition will be reached at  $\langle N \rangle = 4/3$  in the absence of size dispersion. When increasing the pump fluence up to these levels, an additional gain feature indeed appears at early time delays (10 ps, Figure 7.18a). This new gain band lies at the blue side of the low fluence gain. Opposite from the low fluence gain (2.5 ns, Figure 7.18a), it is lost at long delay times, with a detailed fitting yielding a lifetime of 93 ps at pumping levels of  $\langle N \rangle = 1.2$ . Moreover, its threshold  $\langle N \rangle$  exceeds 1 at the shortest wavelengths where it occurs (Figure 7.18b). Based on this short lifetime and the threshold fluence, we attribute this additional gain band to multi-exciton gain across the X1 transition.

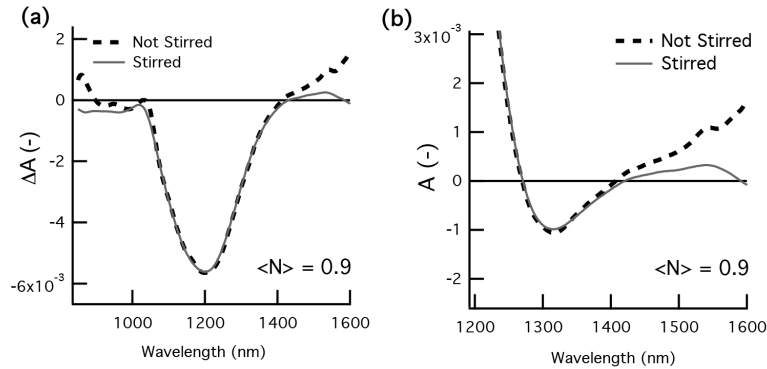


Figure 7.17: Influence of stirring the photo-excited solution at high fluence ( $\langle N \rangle = 0.9$ ) on the differential absorbance  $\Delta A$  (a) and the non-linear absorbance  $A$ . Note that at low fluence, stirring has no effect (not shown).

Figure 7.18a shows that increasing the fluence beyond the single exciton level ( $\langle N \rangle = 1$ ) also introduces a rising absorptive background at the low energy side of the bleach spectrum. This reduces the stimulated emission and eventually leads to net absorption. We attribute the rising background to the presence of charged QDs that can result from, *e.g.* Auger ionization of multi-excitons formed at higher pump fluences. As indicated by tight binding calculations (see Figure 7.9), residual holes will in particular give rise to a sizable additional absorption due to intraband transitions. This excess amount of holes could also be correlated to the occurrence of the fast 10 ps component observed in the kinetic traces. Indeed, charged species will give rise to higher order recombination, *e.g.* due to unbalanced excitons such as trions (single hole and exciton).

## 7.5 Theoretical Models for Thresholdless Optical Gain

A variety of models can be put forward to explain the remarkable thresholdless gain. The essence is that in order to observe thresholdless behaviour, the transition involved in the stimulated emission at energy  $E$  should have no counterpart in absorption at that same energy  $E$ . This excludes simple 2-level models or 3-level models with a dopant. However, two other routes remain plausible: an electronic model with a mid gap trap state and a structural model with excited state relaxation. In this section, we will discuss in more detail these two models, concluding that for HgTe the trap state model is most adequate in explaining the wealth of observations brought forward

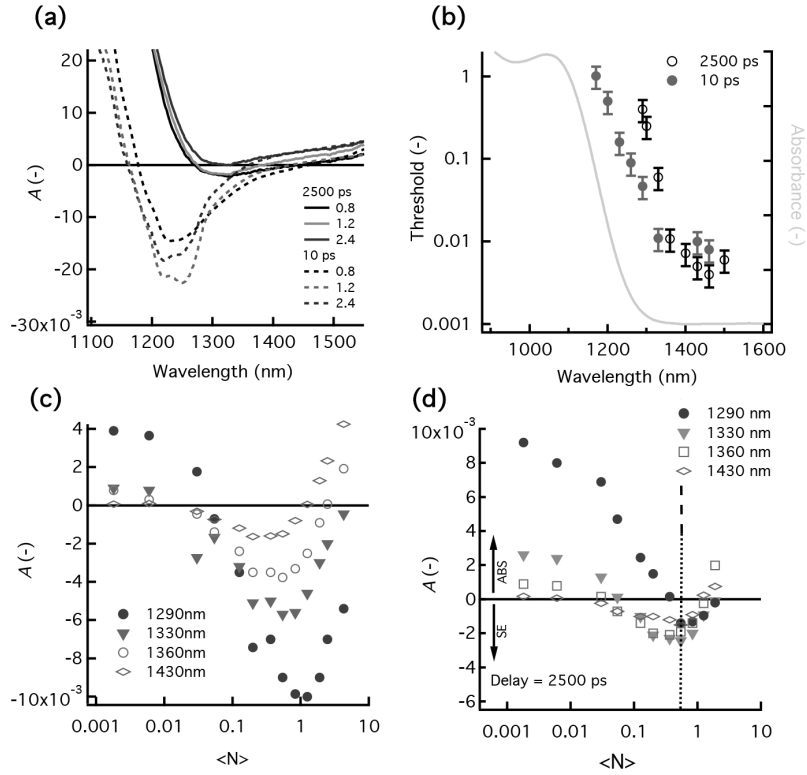


Figure 7.18: High fluence regime (a) Early time (10ps, dashed lines) and late-time (2500 ps, solid lines) non-linear absorbance spectra  $A$  for higher fluence (expressed as  $\langle N \rangle$ ) (b) Wavelength dependence of gain threshold after 10 ps (red solid markers) and after 2500 ps (black empty markers), plotted together with linear absorbance (grey solid line)  $A_0$  (c) Fluence dependence of non-linear absorbance  $A$  after 10 ps for different probe wavelengths throughout the gain bandwidth. Note that optical gain corresponds to  $A < 0$ , *i.e.* stimulated emission (SE) dominates over absorption (ABS). We observe a loss of stimulated emission at higher pump fluence which we attribute to increased hole intraband absorption due to increased nanocrystal charging under high excitation rates. (d) Similar as (c), but after 2500 ps.

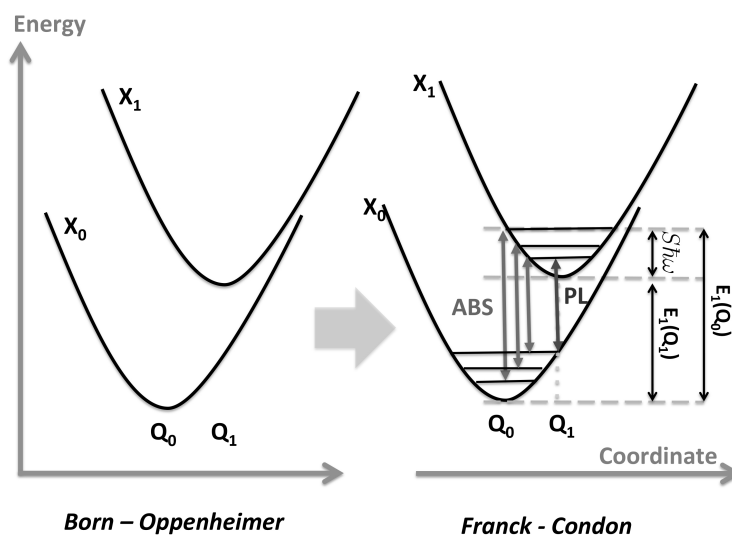


Figure 7.19: Transition from Born-Oppenheimer (BO) approach (calculation of electronic energy levels on a fixed nuclear background) to the Franck-Condon approximation (using the electronic energy levels from BO as starting point, harmonic oscillators for each level are introduced representing vibrationally excited states). Vertical transitions for absorption (ABS) and emission (PL) are indicated.

in the previous experimental section.

### 7.5.1 Excited State Relaxation

The description of molecular excited and ground states relies on the Born-Oppenheimer approximation (BO)<sup>26</sup>. In its simplest form, BO boils down to describing the total molecular system as two roughly independent entities: nuclei, whose position is expressed through a general 'configuration coordinate'  $Q$ , and the electron density. The mathematical translation of this idea is writing the total wavefunction of the system as a product of two new wavefunctions: a nuclear part and an electronic part. Since the mass of the nuclei is much larger than that of the electrons, we can neglect (in first approximation) the kinetic energy (operator) of the nuclei. This results in a static nuclear background to solve the electronic problem, a much more manageable problem.

Having calculated the electronic energy levels (both for ground and ex-

cited states) for varying nuclear positions ( $Q_i$ ) (see Figure 7.19), we can apply the concept of Franck-Condon to the optical transition between them: transitions between electronic levels are always vertical, *i.e.* they happen for a fixed nuclear configuration. The motivation here is that electron dynamics are much faster than the motion of the atoms due to their lighter mass. This allows us to describe any electronic excitation (*e.g.* due to photon absorption or emission) as instantaneous. When this transition is complete, the molecular structure (the position of the atoms) can still change to accommodate the excited electron(s) which is typically observed as relaxation: the excited electronic state is not necessarily relaxed in energy when built upon the ground state atomic configuration. Such relaxation typically involves the emission of phonons to relax the structure to the structural ground state for that given electronic configuration.

A typical picture that will be used in the following section is given in Figure 7.20 where three electronic states X0 (ground state), X1 and X2 are considered: When molecules are photo-excited, they undergo a transition from an electronic ground state to an excited electronic state. Initially, this excited electronic state is built upon the same atomic (or ionic) background (vertical transition at  $Q_0$ ) but after phonon emission (or absorption) the molecule relaxes (typically on a picosecond timescale) to a new configuration  $Q_1$ . After some time the molecule relaxes again to the ground state electronic configuration through photon emission, either spontaneous or stimulated. The relaxation is characterized by the Franck-Condon shift  $S\hbar\omega$ , where  $\hbar\omega$  is the phonon energy.

The cross section for photon absorption of a nanocrystal in its ground state is:

$$\sigma^{A,0}(h\nu) = \frac{\sigma_0}{\sqrt{4\pi kT S\hbar\omega}} \exp\left(-\frac{(h\nu - E_X)^2}{4kT S\hbar\omega}\right) \quad (7.11)$$

The cross section for stimulated emission from the first excited state (relaxed) is given by<sup>27</sup>:

$$\sigma^{SE}(h\nu) = -\frac{\alpha^{SE}\sigma_0}{\sqrt{4\pi kT S\hbar\omega}} \exp\left(-\frac{(h\nu - E_X + 2S\hbar\omega)^2}{4kT S\hbar\omega}\right) \quad (7.12)$$

which is centered on the vertical transition SE. Note that  $\alpha^{SE} < 1$

**Configuration Coordinate Diagram** The energy in the ground state can be written in the form of the potential energy of a harmonic oscillator with a general 'configuration coordinate'  $Q$ :

$$E_0(Q) = \frac{1}{2}KQ^2 \quad (7.13)$$

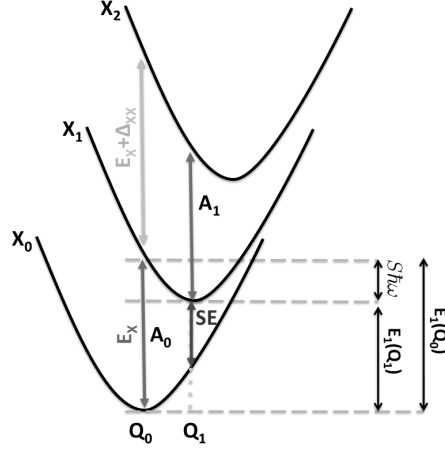


Figure 7.20: Overview of excited state relaxation model with relevant electronic energy levels ( $X_i$ ) at different configuration coordinates ( $Q_i$ ) with energies and Franck-Condon shift  $S\hbar\omega$ .

In the first excited state, we can write:

$$E_1(Q) = E_X - fQ + \frac{1}{2}KQ^2 \quad (7.14)$$

where  $f$  represents the force induced by the creation of one exciton and  $E_X$  is the single exciton energy. The minimum of  $E_1$  is at  $Q_1 = \frac{f}{K}$ , which amounts by definition to:

$$E_1(Q_1) = E_X - S\hbar\omega \quad (7.15)$$

As such,  $\frac{f^2}{2K} = S\hbar\omega$ . The vertical transition energy SE is given by:

$$E_1(Q_1) - E_0(Q_1) = E_X - 2S\hbar\omega \quad (7.16)$$

The energy in the second excited state is given by:

$$E_2(Q) = 2E_X + \Delta_{XX} - 2fQ + \frac{1}{2}KQ^2 \quad (7.17)$$

where  $\Delta_{XX}$  describes the exciton-exciton interaction effects on the transition energy (see chapter 4). We used the approximation that the addition of a second exciton induces a double force  $2f$ . The vertical transition energy A1 is given by:

$$E_2(Q_1) - E_1(Q_1) = E_X + \Delta_{XX} - 2S\hbar\omega \quad (7.18)$$

Already an important conclusion can be drawn: if  $\Delta_{XX} = 0$ , the absorption in the excited state takes place at the same energy as the stimulated emission irrespective of the interaction strength ( $S\hbar\omega$ ).

Therefore, the cross section for the absorption in the excited state is given by:

$$\sigma^{A,1}(h\nu) = \frac{\alpha^{A1}\sigma_0}{\sqrt{4\pi kTS\hbar\omega}} \exp\left(-\frac{(h\nu - E_X + 2S\hbar\omega)^2}{4kTS\hbar\omega}\right) \quad (7.19)$$

where  $\alpha^{A1} < 1$ .

**The  $\alpha$  coefficients** The coefficients  $\alpha^{A1}$  and  $\alpha^{SE}$  are used to incorporate Pauli exclusion, degeneracies, etc. ...

Consider a simple 2-fold generate HOMO and LUMO, with relative occupation  $n_{0,1}$  (note:  $n_0 + n_1 = 1$ ). Inhomogeneous broadening is taken into account through a simple gaussian distribution:

$$g(E_X) = \frac{1}{\sqrt{\pi}\Gamma} \exp\left(-\frac{(E_X - E_X^0)^2}{\Gamma^2}\right) \quad (7.20)$$

$$\alpha(h\nu) = n_{NC} \int (1 - n_1)\sigma^{A,0}(h\nu) + n_1(\sigma^{SE}(h\nu) + \sigma^{A1}(h\nu))g(E_X)dE_X \quad (7.21)$$

Using  $\gamma = \sqrt{4kTS\hbar\omega}$ , the homogeneous broadening, we can now calculate the integrals for ground state absorption  $A_0$ , excited state absorption  $A_1$  and stimulated emission  $A_{SE}$ .

$$A_0 = \int \sigma^{A,0}(h\nu)g(E_X)dE_X \quad (7.22)$$

which results in:

$$A_0 = \frac{\sigma_0}{\sqrt{\pi}\sqrt{\gamma^2 + \Gamma^2}} \exp\left(-\frac{(h\nu - E_X^0)^2}{\gamma^2 + \Gamma^2}\right) \quad (7.23)$$

Similarly, we obtain:

$$A_1 = \frac{\alpha^{A,1}\sigma_0}{\sqrt{\pi}\sqrt{\gamma^2 + \Gamma^2}} \exp\left(-\frac{(h\nu - E_X^0 - \Delta_{XX} + 2S\hbar\omega)^2}{\gamma^2 + \Gamma^2}\right) \quad (7.24)$$

$$A_{SE} = -\frac{\alpha^{SE}\sigma_0}{\sqrt{\pi}\sqrt{\gamma^2 + \Gamma^2}} \exp\left(-\frac{(h\nu - E_X^0 + 2S\hbar\omega)^2}{\gamma^2 + \Gamma^2}\right) \quad (7.25)$$

**Thresholds** The threshold for optical gain is defined as:  $\alpha(h\nu) = 0$  or equivalently:  $(1 - n_1^{th})A_0 + n_1^{th}(A_{SE} + A_1) = 0$ , which leads to:

$$n_1^{th} = \frac{A_0}{A_0 - A_{SE} - A_1} \quad (7.26)$$

If  $A_{SE} + A_1 = 0$ , for example when  $\Delta_{XX} = 0$  and  $\alpha^{SE} = \alpha^{A1} = 1/2$ , the threshold for transparency becomes unity ( $n_1^{th} = 1$ ).

**No Lattice Relaxation** In absence of any lattice relaxation,  $S = 0$  leads to  $A_{SE} = -\alpha^{SE}A_0$ . In an energy range where  $A_1 \ll A_0$  (e.g. for strong X-X interactions when  $\Delta_{XX}$  is large), we get:

$$n_1^{th} \approx \frac{A_0}{A_0(1 + \alpha^{SE})} = \frac{1}{1 + \alpha^{SE}} \quad (7.27)$$

This amounts to  $2/3$  if  $\alpha^{SE} = 1/2$ . This regime is obtained in the case of type II nanocrystals<sup>28</sup> where indeed thresholds close to  $2/3$  are observed. Important to note is that for the case of a simple 2-fold degenerate HOMO-LUMO system with no lattice relaxation, the threshold is always between  $2/3$  and  $1$  !

**Strong Lattice Relaxation** In the case of strong coupling (or lattice relaxation), we obtain  $S\hbar\omega \gg \sqrt{\gamma^2 + \Gamma^2}$ , which leads indeed to a large Stokes shift between absorption and emission. For energies above the absorption energy  $E_X$ , we can write:

$$n_1^{th} \approx \frac{A_0}{-A_{SE} - A_1} \quad (7.28)$$

which may be well below unity. This situation is commonly observed in dyes used for commercial dye lasers (e.g. rhodamine, ...) <sup>29</sup>.

**Numerical Examples and the Case of HgTe** The quantities derived in the previous paragraph can be combined to calculate the absorption under different conditions: probability of photoexcited dots  $n_1$ , lattice relaxation strength  $S\hbar\omega$  and the biexciton (XX) shift  $\Delta_{XX}$ . We assume  $\sqrt{\gamma^2 + \Gamma^2} = 60$  meV,  $\alpha^{SE} = \alpha^{A1} = 0.5$  and  $E_0 = 1.08$  eV. As we can see from Figure 7.21, the simultaneous presence of lattice relaxation and XX shift is required to obtain stimulated emission at  $n_1 \ll 1$ . This is a manifestation of excited state absorption: indeed, if an excitation is present in the QD in the electronic state X1, it will give both bleach of the emitting state (as the X0-X1 is bleached), but induce absorption at the

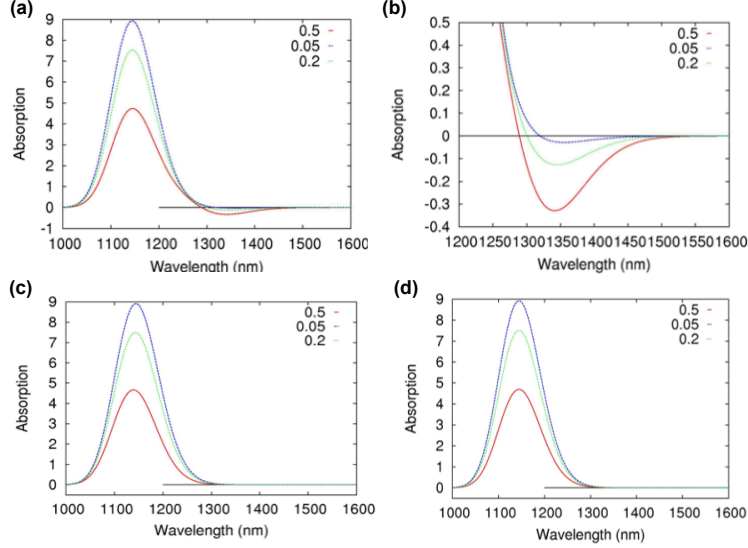


Figure 7.21: Overview of calculated absorption spectra for different conditions and  $n_1$  from 0.05 to 0.5 (red, green, blue): (a) Lattice relaxation  $S\hbar\omega = 60\text{meV}$  with small XX shift ( $\Delta_{XX} = 10\text{meV}$ ), (b) Zoom of the gain region of (a), (c) No lattice relaxation ( $S\hbar\omega = 0$ ) and small XX shift ( $\Delta_{XX} = 10\text{meV}$ ) and (d) Lattice relaxation ( $S\hbar\omega = 60\text{meV}$ ) without shift  $\Delta_{XX} = 0\text{meV}$ .

same energy (in this case from X1 to X2, not from X0 to X1). This concept is known in dye lasers where multi-body effects induce an additional excited state shift (similar to the  $\Delta_{XX}$  in QDs)<sup>30;31</sup>. However, no theoretical evidence was found until now to support the idea of strong lattice relaxation in HgTe QDs: lattice relaxations of only a few meV are obtained considering acoustical phonons (through the deformation potential  $a_g = VdE_g/dV \sim 3.7\text{ eV}$ ) and no evidence for strong coupling to optical phonons (*e.g.* through asymmetry in electron and hole charge densities) are found. As such, we cannot invoke the excited state-relaxation (ESR) mechanism to explain the low gain thresholds observed in HgTe QDs. The concept of ESR is of course very useful in terms of design paradigm for efficient QD laser dyes: starting from theory, we can look for materials with strong electron-phonon coupling or materials that are easily deformed (*e.g.* very small QDs approaching the molecular regime)<sup>32</sup>.

### 7.5.2 Four Level System

HgTe QDs exhibit optical gain below the one-exciton-per-QD limit as evidenced by their low fluence threshold for stimulated emission and the long gain lifetime. Moreover, the gain thresholds measured (see Figure 7.12) appear to be limited only by residual loss channels such as intraband absorption at longer wavelengths<sup>?</sup>. This remarkable observation of nearly thresholdless gain in HgTe QDs implies that an emitting transition is involved that has no counterpart in absorption at that specific wavelength, as is the case in specific 3-level and all 4-level systems. With QDs, this requirement is not met by the bandgap transition. As a result, this transition only yields gain in the multi-X regime, unless more advanced core/shell nanocrystals exhibiting repulsive multi-X interactions are used. These can bring the threshold slightly below the  $\langle N \rangle = 1$  level, yet the almost thresholdless gain observed here remains out of reach also for these QDs. Thresholdless gain in QDs can be possible on the other hand if the gain transition involves states within the bandgap. Indeed, transitions of a conduction-band electron to a gap state that is empty in unexcited QDs or of a valence-band hole to an occupied gap state that have no counterpart in absorption would make QDs nearly thresholdless effective 3-level systems. Although it is well-known that localized gap states can be deliberately introduced in QDs by doping<sup>33;34</sup>, or may result from incomplete surface passivation<sup>35</sup>, optical gain via such states has never been reported.

In the case of HgTe QDs, the assumption that nearly thresholdless gain is related to a transition of a conduction-band electron to a shallow, empty gap state (see Figure 7.22a) leads to a concise picture in line with the experimental data. After non-resonant photo-excitation and the initial cooling, the two 4-fold degenerate hole states (VB1/VB2) and 2-fold degenerate electron states (CB) are occupied. Further cooling of the hole states imposes a slow decay on the interband transition, where the bandgap bleach loses the contribution of the X2 transition. At high fluence, short lived multi-X gain is observed across the interband transition. The presence of a shallow, empty gap state just above the VB1 state leads to the apparent extension of the bandgap bleach to longer, sub-bandgap wavelengths. As it has no counterpart in the absorption spectrum of unexcited QDs, this transition can lead to the observed optical gain at fluences as low as 0.005 excitations per QD. The attribution of the sub-bandgap gain to a transition between CB1 and an empty gap state agrees with the observation that the dynamics of the VB2/VB1 hole relaxation is not observed in the gain dynamics (see Figure 7.22b). Within this model, the conduction-band electron has two parallel decay pathways. The gain coefficient of the gap-state transition

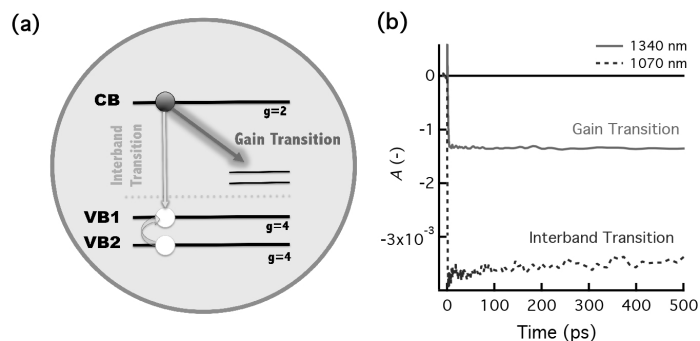


Figure 7.22: Thresholdless optical gain (a) Proposed model for thresholdless stimulated emission involving unoccupied shallow trap states close to the valence band. (b) Influence of hole X2-X1 dynamics on gain transition (1340 nm) and interband transition (1070 nm).

(see section 7.6.3) appears to be substantially lower than the absorption coefficient of the bandgap transition. However, it is sufficiently large to add power to the probe pulse by stimulated emission without competing linear absorption, leading to nearly thresholdless optical gain.

**Gain Cross Section after Washing** To corroborate the link between optical gain and a gap-state related transition, we analysed the gain cross section of a given batch of HgTe QDs as a function of the number of sample purification cycles. Purification of colloidal QDs by addition of a non-solvent is typically used to separate the nanocrystals from residual reaction products (excess ligands, unreacted precursors, side products, ...). It is however well known that repetitive washing reduces the photoluminescence efficiency by introducing surface states, a consequence of stripping passivating ligands from the nanocrystal surface<sup>36</sup>. As shown in Figure 7.23, we find that the relative gain cross section here determined as the ratio of the nonlinear absorption at 1340 nm of the sample analysed relative to a singly washed sample with equal concentration of QDs increases with the number of washing steps. This is a strong indication that gain is indeed related to a transition involving a gap state at the QD surface, *e.g.*, created by an incomplete ligand coverage, rather than a transition intrinsic to HgTe QDs. Unless mentioned otherwise, the measurements presented here have been performed on doubly washed HgTe QDs. An important remark is that although the cross section for gain is larger in more washed samples, the carrier density  $\langle N \rangle$  that can be sustained before photo-induced absorption

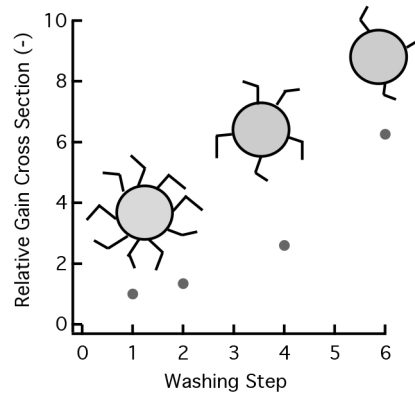


Figure 7.23: Increase of gain cross section (at 1340 nm) with subsequent washing steps, indicating that the shallow trap responsible for the thresholdless optical gain, is related to a surface defect (e.g. by insufficient surface passivation).

takes over the stimulated emission is smaller making the overall achievable absolute gain smaller in more washed samples.

**Trap-Related Emission at Room Temperature** A question rises whether we can observe the gap state transition at room-temperature, e.g. through analysis of the photoluminescence spectrum. Figure 7.24 shows the photoluminescence (PL) spectrum of monodisperse HgTe QDs after excitation at 700 nm at room temperature. We can clearly distinguish the gap related emission (from CB1 to the gap state) and the interband emission (from CB1 to VB1). The difference spectrum between interband and gap PL clearly shows a narrow region at longer wavelengths where gap emission is the only contributor to the PL signal.

An interesting route to follow would be the control of the gap state population through electrochemistry<sup>37</sup>. Not only would this provide conclusive evidence for the gain mechanism, it would also allow to deplete the gap state completely, potentially increasing the gain cross section.

**Fast Decay Component** We attribute the fast (10–20 ps) decay component to unbalanced exciton recombination due to hole charging of the nanocrystals under high fluence excitation rates. This is based on 3 observations:

- Electron charging can only increase the gain cross section since it is

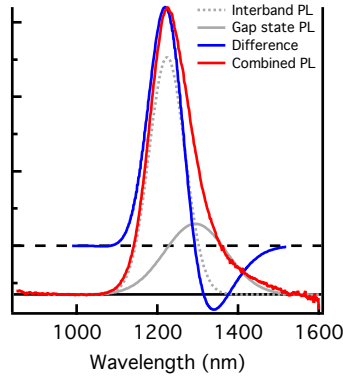


Figure 7.24: Room temperature photoluminescence after 700 nm photo-excitation showing the decomposition in an interband transition and a gap state emission. The difference spectrum ( $PL_{IB} - PL_{GS}$ ) shows that there is a spectral region where GS emission is the sole contributor to the sample PL.

the only carrier involved in the gain transition. Charging with holes will not increase the gain cross section, but leads instead to an increase of PA and a loss of gain. This is evidenced in the high fluence stirred/non-stirred comparison (see Figure 7.17) where stirring reduces the influence of hole charging by refreshing the excited volume.

- Hole intraband absorption is spectrally closer to the interband bleach and is much stronger (up to 1 order of magnitude) than electron intraband absorption (see section on tight binding calculations).
- The weight of the fast decay component is smaller at the low energy side of the spectrum, involving only electron mediated transitions.

As such, holes are not involved in the gain transition but limit it by charging the crystals under high excitation rates, leading to a dominance of hole induced intraband absorption over stimulated emission. Electrons give rise to both interband bleach and trap-assisted stimulated emission. To alleviate the gain quenching at high excitation rate, a hole sink (e.g. by introducing charge transfer layers aimed at hole extraction) could be introduced.

## 7.6 HgTe for Integrated Photonics

### 7.6.1 Thin Film Formation

The ultrafast properties of HgTe obtained in the previous sections were obtained on solutions of HgTe QDs dispersed in apolar solvents. To translate these exciting properties (low threshold, long gain lifetime and large gain magnitude) to an actual integrated amplifier or laser, we should process the QDs into thin films. A crucial parameter to evaluate is the degree of clustering in the solution phase. Indeed, all solution-to-film transfer techniques, such as spincoating or Langmuir-Blodgett, depend on the colloidal stability and quality of the starting solution. The HgTe QDs are capped with thiol-based ligands (dodecane-thiol as standard). These ligands are known to show clustering and their metal-complexes (*e.g.* mercury-thiolates) are known to show long range ordering. The latter can be present in the synthesis solution through reaction of thiols with the mercury chloride. In the first synthesis route, thiols are added from the beginning, together with the mercury chloride. In the second route, thiols are only added during workup, but still unreacted mercury chloride can be present.

It was suggested by Kershaw *et al.*<sup>38</sup> that these mercury-thiolates form a gel-like network clustering together a few QDs in a 10–20 nm cluster. We observed similar cluster sizes using DLS (Dynamic Light Scattering) (see Figure 7.26). They attribute photo-charging of the QDs to the presence of these clusters (*e.g.* trapping of carriers in the interconnected and rather ionic network). As such, breaking them apart could improve the performance of HgTe as we attributed the gain reduction at high fluence to this photocharging.

Breaking these clusters apart can be done using sonication or addition of a spacer polymer (such as poly-methyl methacrylate (PMMA) or polystyrene (PS)). Addition of PS was used to obtain preliminary TEM images as the 10–20 nm clusters do not allow for decent imaging of the small (3–4 nm) QDs. An alternative could be the use of an element sensitive HAADF-STEM (High Angular Annular Dark Field) probe which would be insensitive to the lighter carbon making up the ligand/polymer surroundings of the heavier QDs (Hg and Te are much heavier than carbon).

The optical properties of HgTe QDs in thin film are very similar to those measured in solution: similar spectral widths for absorption and emission are found with similar PL decay times. A small ( $\sim 40$  meV) redshift is observed in the thin films compared to solution which could be attributed to a reduction of dielectric screening in the thin films. Other reports have suggested continued growth (and concomitant redshift of the excitonic features) of HgSe and HgTe QDs, even in thin film phase.

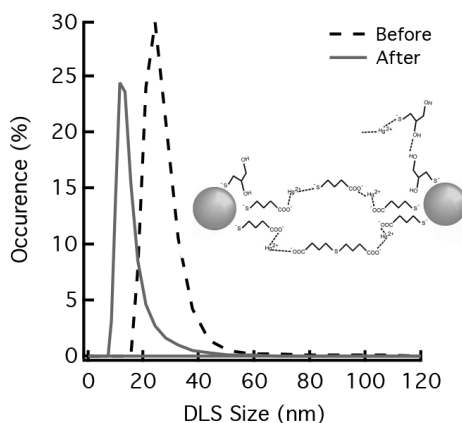


Figure 7.25: DLS (Dynamic Light Scattering) spectra (before and after sonication) of HgTe QDs in tetrachloro-ethylene showing the effect of sonication on the average cluster size.

**Transient absorption measurements** Dropcasted thin films of HgTe were investigated under similar conditions as the solutions: optical gain was found under similar sub-X fluences, albeit strongly redshifted and with much shorter gain lifetimes (see Figure 7.27). As we can see in Figure 7.27b, a large part of the bleach vanishes on a  $\sim 10$  ps timescale, similar to the observed fast decay component in the solution measurements. The longer 100 ps timeconstant could be attributed to Auger recombination, albeit it twice slower than the solution case.

We attribute this decreased performance to strong photo-charging in the films due to increased clustering. Indeed, it was found that films of HgTe are not stable and show degradation (redshift of spontaneous emission, no significant broadening) over time at room temperature. No effects are observed when storing samples in the fridge. Further studies should elucidate this issue: possible routes are dispersion in polymers, measurements at lower temperature and already resolving the clustering issue in solution phase.

### 7.6.2 Performance

Colloidal quantum dots (QDs) combine size-tuneable electronic energy levels with a suitability for solution-based processing, which makes them ideal for numerous optoelectronic applications<sup>39</sup>. QD photodetectors<sup>12</sup>, solar cells<sup>40</sup>, white LEDs and displays<sup>41</sup> all make use of the broad QD absorp-

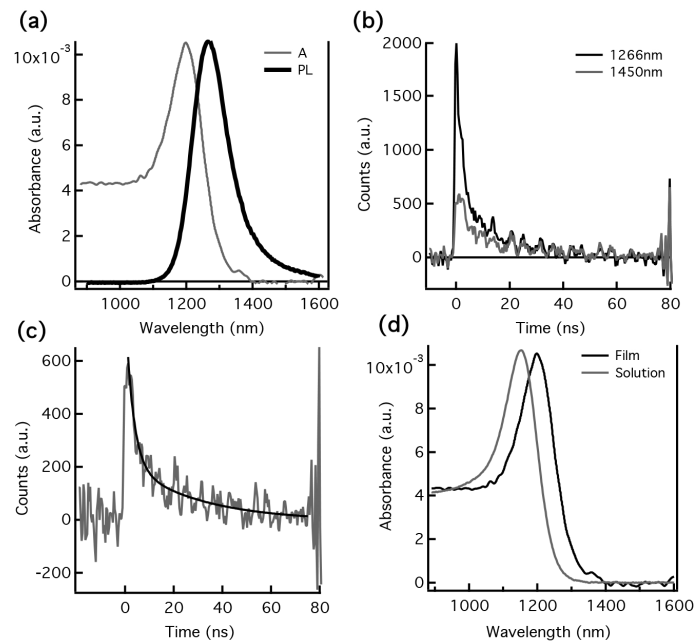


Figure 7.26: Overview of thin film (100 nm, spincoated) properties: (a) Absorbance and photoluminescence (PL), (b) PL decay measured at the interband peak (1260 nm) and at the subgap emission (1450 nm), (c) bi-exponential fit to PL decay of the sub-gap emission showing 3.6 (70%) and 31 ns (30%) components and (d) comparison of solution and thin film absorption spectrum showing a redshift of 41 meV of the 1S-1S transition.

A similar shift is observed in the photoluminescence spectra.

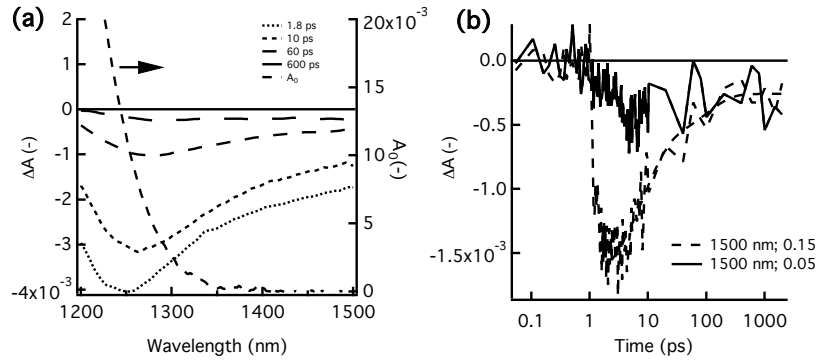


Figure 7.27: Overview of HgTe thin film measurements: (a) Bleach spectra for different probe delays at  $\langle N \rangle = 0.5$  and (b) Bleach kinetics at 1500 nm for 2 different fluences (0.05 and 0.15). The dashed black line is a biexponential fit yielding a 8 and 100 ps lifetime.

tion spectrum with its size-dependent onset corresponding to the lowest energy exciton (X) or bandgap transition and/or the tunable, narrow emission spectrum resulting from exciton recombination. Application development is further driven by unique characteristics such as multi-X generation<sup>42</sup> or room-temperature single photon emission and the possibility to fine-tune opto-electronic properties by heterostructure formation<sup>9</sup>, doping or alloying<sup>43</sup>.

Tunable, low cost and solution processable gain media could have an equal impact on devices relying on optical gain, such as lasers or amplifiers. Taking the example of the telecom wavelengths around 1.3 and 1.55  $\mu\text{m}$ , lasers are now mostly fabricated through expensive epitaxial growth of III-V semiconductors. In the case of the popular silicon photonics platform, whereby densely packed photonic integrated circuits are fabricated starting from silicon-on-insulator (SOI) for applications in classical datacommunication but also for signal processing and sensing<sup>44;45</sup>, this implies that no native optical gain medium is even available. Solutions relying on bonding of III-V dies, direct epitaxial growth of III-V on silicon<sup>46</sup>, erbium doping and strained Ge are heavily investigated but suffer from cost, upscaling and efficiency issues or limited gain bandwidth.

Although stimulated emission involving the bandgap transition has been demonstrated for different QDs<sup>10;47;48</sup>, their use as gain media has been limited. This is largely due to the QDs being effective two-level systems, where stimulated emission and absorption involve transitions between the

same discrete band edge states. Since these are degenerate, QDs must contain more than one exciton on average to achieve population inversion<sup>47</sup>. Next to this intrinsic drawback of two-level gain media, multi-X rapidly recombine through non-radiative Auger processes<sup>49</sup>, limiting the gain lifetime to a few tens of picoseconds. Although the resulting high thresholds can be reached by optical pumping using pulsed lasers<sup>46</sup>, it makes electrical pumping of QD-based gain media infeasible.

Two strategies have been proposed to circumvent the limitations imposed by multi-X gain. It proved possible to slow down Auger recombination through interfacial alloying in core/shell QDs and/or using large volume QDs<sup>50</sup>. Alternatively, single-X gain<sup>51</sup> has been demonstrated using so-called type II core/shell QDs, where the spatial separation of electron and hole leads to repulsive X-X interactions, lifting the effective level degeneracy. Unfortunately, both strategies are restricted to a few materials typically involving Cd-based QDs emitting in the visible and gain still relies on a two level scheme.

The reported optical gain in dispersions of HgTe QDs is achieved at average exciton numbers per nanocrystal  $\langle N \rangle$  as low as 0.005. Intrinsic gain coefficients of about  $500 \text{ cm}^{-1}$  are demonstrated and the extrapolated gain lifetime corresponds to the single exciton lifetime. We attribute this almost thresholdless gain to stimulated emission between the lowest conduction band level and shallow, empty surface states near the first valence band level, thus creating a nearly thresholdless, effective 3-level system. Since the gain characteristics meet the requirements for DC electrical pumping<sup>52</sup>, this result shows that the use of effective 3-level systems is the way forward for developing performing QD-based gain media.

### 7.6.3 Intrinsic Material Gain

The gain thresholds reported here for HgTe QDs are the lowest ever for optical amplification using colloidal materials (outperforming by 2 orders of magnitude the best Cd-based structures available in the visible range of the spectrum) and the gain lifetime exceeds that of multi-exciton gain by 3 orders of magnitude. Still, the question remains whether an effective 3-level system like HgTe QDs, where gain involves a transition to a gap state, can provide the modal threshold gain needed to achieve lasing when embedding the QDs in a photonic feedback structure. To answer this question, Figure 7.30 shows the intrinsic gain coefficient  $g_i$  of 2 different batches of HgTe QDs, emitting at 1220 nm and 1300 nm.

We calculate the intrinsic gain  $g_i$  plugging in the volume fraction  $f$  and the measured non-linear absorption  $A$  (note that  $A < 0$  in case of stimulated

emission):

$$g_i = -\frac{\ln(10)A}{fL} \quad (7.29)$$

Where  $f$  can be calculated from:

$$f = \frac{\ln(10)A_{0,400}}{\mu_{i,400}} \quad (7.30)$$

Although the intrinsic values seem low compared to typical band edge values ( $10^4 \text{ cm}^{-1}$ ), we can still link this to the 40

Actual gain coefficients are obtained by multiplying  $g_i$  with the QD volume fraction  $f$ , which amounts to 0.2–0.3 in a close packed film of dodecanethiol capped HgTe QDs (Figure 7.28, dashed lines). One sees that gain coefficients of  $100 \text{ cm}^{-1}$  are achieved across the entire telecommunication window (indicated with the standard pass bands O/E/S/C/L). These values lie between the gain obtained in erbium-doped fiber amplifiers<sup>53</sup> (EDFA) used in C-band telecommunication ( $10^{-2} - 10^{-3} \text{ cm}^{-1}$ ) and that of common epitaxially grown semiconductors<sup>54</sup> ( $10^3 \text{ cm}^{-1}$ ) used in integrated photonics, making HgTe a suitable material for both fiber based and integrated amplifiers. Moreover, the combination of gain threshold, gain lifetime and gain coefficients of  $100 \text{ cm}^{-1}$  make HgTe QDs a very promising gain material for integrated photonics, where in particular electrically pumped devices become feasible. Indeed, as mentioned by Wood et al. gain lifetimes of *ca.* 100 ns are required at sub-1 exciton population to achieve DC electrical pumping<sup>52</sup>, specifications that are largely met by the colloidal HgTe QDs used in this work.

The intrinsic gain is the gain provided by a fictitious material of 100% HgTe with the equivalent oscillator strength of a HgTe nanocrystal at that wavelength. Since in close packed films the actual volume occupied by HgTe nanocrystals is smaller, we have to correct with the appropriate volume fraction ( $f = 0.2\text{--}0.3$ ), resulting in modal gains of 100/cm.

#### 7.6.4 Benchmarking HgTe for Optical Interconnects

HgTe QDs exhibit an intrinsic gain of  $500 \text{ cm}^{-1}$ , which implies a modal gain of  $100 \text{ cm}^{-1}$  in a close packed film of QDs which is considerably higher (see Figure 7.30) than what can be reached in rare earth doped amplifiers currently used in telecom networks (*e.g.* EDFAs). Compared to III-V semiconductor devices, HgTe QDs exhibit lower gain, but they allow for much easier and cheaper processing and the peak gain wavelength can be (see Figure 7.29) set freely over a much wider range (by controlling their size). They can be applied as a close packed film, *e.g.*, as an overlay

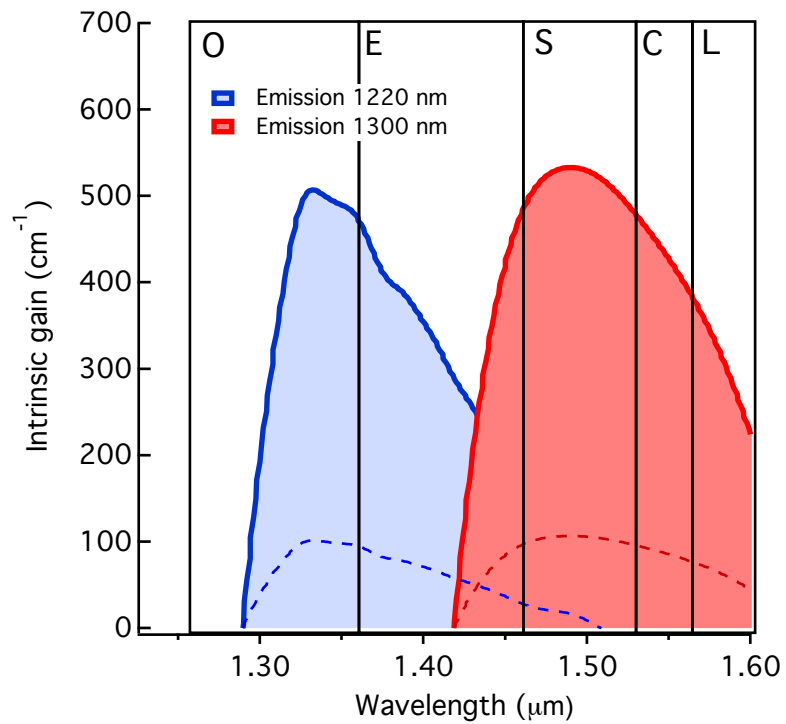


Figure 7.28: HgTe intrinsic material gain for two different samples emitting at 1220 nm (blue) and 1300 nm (red). The color-matching dashed lines indicate the volume-fraction corrected material gain. Note that the material gain provided by only 2 different sizes of HgTe covers the entire OESCL band with typical values over  $100 \text{ cm}^{-1}$ .

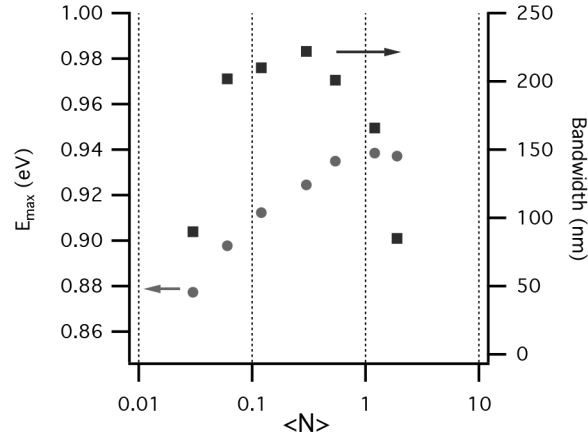


Figure 7.29: Energy (in eV) of stimulated emission maximum and bandwidth (in nm) for increasing fluence with 1220 nm emitting HgTe QDs.

on high index contrast integrated waveguides or they can be dispersed in a polymer matrix, allowing to integrate them, *e.g.* in single or multi-mode polymer waveguides embedded in printed circuit boards (PCBs).

## 7.7 Conclusion

We observed nearly thresholdless optical amplification in HgTe QDs. This is attributed to a gap-state related transition that makes HgTe QDs an effective 3-level system, for which population inversion can be reached at pump fluences substantially below the one-exciton-per-QD level. Although in this case, the gap states are related to the synthesis and processing methods used, these results change the current paradigm for light amplification using colloidal QDs. Rather than engineering the electronic properties (see chapter 2: type II structures, Auger suppression), one should focus on obtaining effective 3 level systems. When providing a sufficiently high gain coefficient, they can easily outperform the inherent 2 level systems obtained through the widely used electronic wavefunction engineering thanks to their low gain threshold and long gain lifetime. Further research must therefore address methods for the controlled formation of optimized gap states, either by surface engineering or impurity doping, a search that would profit from the support of theoretical calculations of level energies and transition oscillator strengths. A possible alternative is found in the mechanism of excited

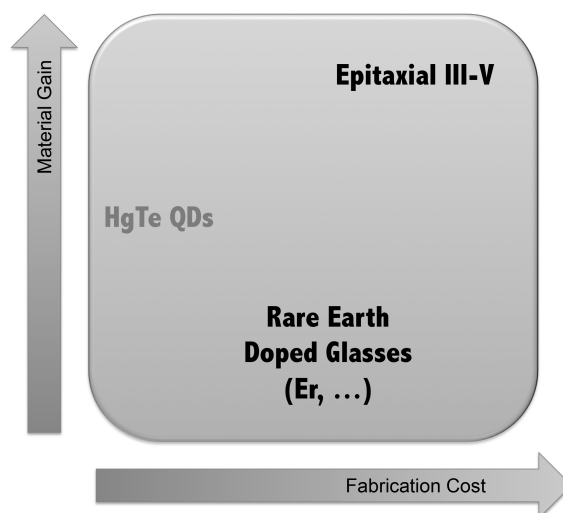


Figure 7.30: Benchmark of HgTe material gain and fabrication cost against other commercial solutions.

state relaxation. Although not applicable to the case of HgTe, other materials with strong electron-phonon coupling could enable this mechanism to provide similar low gain thresholds as observed in the case of HgTe.

## References

- [1] Talapin, D. V.; Lee, J.-S.; Kovalenko, M. V.; Shevchenko, E. V. Prospects of Colloidal Nanocrystals for Electronic and Optoelectronic Applications. *Chemical reviews* **2010**, *110*, 389–458.
- [2] Moreels, I.; Justo, Y.; De Geyter, B.; Haustraete, K.; Martins, J. C.; Hens, Z. Size-tunable, Bright, and Stable PbS Quantum Dots: A Surface Chemistry Study. *ACS Nano* **2012**, *5*, 2004–2012.
- [3] Moreels, I.; Lambert, K.; Smeets, D.; De Muynck, D.; Nollet, T.; Martins, J. C.; Vanhaecke, F.; Vantomme, A.; Delerue, C.; Allan, G.; Hens, Z. Size-dependent optical properties of colloidal PbS quantum dots. *ACS Nano* **2009**, *3*, 3023–30.
- [4] Lhuillier, E.; Keuleyan, S.; Liu, H.; Guyot-Sionnest, P. Mid-IR Colloidal Nanocrystals. *Chemistry of Materials* **2013**, *25*, 1272–1282.

- [5] McDonald, S. a.; Konstantatos, G.; Zhang, S.; Cyr, P. W.; Klem, E. J. D.; Levina, L.; Sargent, E. H. Solution-processed PbS quantum dot infrared photodetectors and photovoltaics. *Nature Materials* **2005**, *4*, 138–42.
- [6] Beard, M. C.; Luther, J. M.; Semonin, O. E.; Nozik, A. J. Third Generation Photovoltaics based on Multiple Exciton Generation in Quantum Confined Semiconductors. *Accounts Chem. Res.* **2013**, *46*, 1252–1260.
- [7] Justo, Y.; Geiregat, P.; Hoecke, K. V.; Vanhaecke, F.; Donega, C. D. M.; Hens, Z. Optical Properties of PbS / CdS Core / Shell Quantum Dots. *Journal of Physical Chemistry C* **2013**, *117*, 20171–20177.
- [8] Justo, Y.; Goris, B.; Kamal, J. S.; Geiregat, P.; Bals, S.; Hens, Z. Multiple dot-in-rod PbS/CdS heterostructures with high photoluminescence quantum yield in the near infrared. *Journal of the American Chemical Society* **2012**, *134*, 5484–5487.
- [9] De Geyter, B.; Justo, Y.; Moreels, I.; Lambert, K.; Smet, P. F.; Van Thourhout, D.; Houtepen, A. J.; Grodzinska, D.; de Mello Donega, C.; Meijerink, A.; Vanmaekelbergh, D.; Hens, Z. The Different Nature of Band Edge Absorption and Emission in Colloidal PbSe/CdSe Core/Shell Quantum Dots. *ACS nano* **2011**, *5*, 58–66.
- [10] Schaller, R. D.; Petruska, M. a.; Klimov, V. I. Tunable Near-Infrared Optical Gain and Amplified Spontaneous Emission Using PbSe Nanocrystals. *The Journal of Physical Chemistry B* **2003**, *107*, 13765–13768.
- [11] Lhuillier, E.; Keuleyan, S.; Zolotavin, P.; Guyot-Sionnest, P. Mid-infrared HgTe/As<sub>2</sub>S<sub>3</sub> field effect transistors and photodetectors. *Advanced materials (Deerfield Beach, Fla.)* **2013**, *25*, 137–41.
- [12] Keuleyan, S.; Lhuillier, E.; Brajuskovic, V.; Guyot-Sionnest, P. Mid-infrared HgTe colloidal quantum dot photodetectors. *Nature Photonics* **2011**, *5*, 489–493.
- [13] Keuleyan, S. E.; Guyot-sionnest, P.; Delerue, C.; Allan, G. Mercury Telluride Colloidal Quantum Dots : Electronic Structure , Photocurrent Detection up to 12  $\mu\text{m}$ . *ACS Nano* **2014**, *8*, 8676–82.
- [14] Lhuillier, E.; Keuleyan, S.; Guyot-Sionnest, P. Optical properties of HgTe colloidal quantum dots. *Nanotechnology* **2012**, *23*, 175705.

- [15] Keuleyan, S.; Lhuillier, E.; Guyot-Sionnest, P. Synthesis of colloidal HgTe quantum dots for narrow mid-IR emission and detection. *Journal of the American Chemical Society* **2011**, *133*, 16422–4.
- [16] Kim, S.; Kim, T.; Im, S. H.; Seok, S. I.; Kim, K. W.; Kim, S.; Kim, S.-W. Bandgap engineered monodisperse and stable mercury telluride quantum dots and their application for near-infrared photodetection. *J. Mater. Chem.* **2011**, *21*, 15232–15236.
- [17] Allan, G.; Delerue, C. Tight-binding calculations of the optical properties of HgTe nanocrystals. *Physical Review B* **2012**, *86*, 1–6.
- [18] Adachi, S. *Optical Constants of Crystalline and Amorphous Semiconductors*; Kluwer Academic, 1999.
- [19] Hens, Z.; Moreels, I. Light Absorption by Colloidal Semiconductor Quantum Dots. *Journal of Materials Chemistry* **2012**, *22*, 10406–10415.
- [20] Keuleyan, S.; Kohler, J.; Guyot-Sionnest, P. Photoluminescence of Mid-Infrared HgTe Colloidal Quantum Dots. *The Journal of Physical Chemistry C* **2014**, *118*, 2749–2753.
- [21] Delerue, C.; Lannoo, M.; Allan, G. Concept of dielectric constant for nanosized systems. *Physical Review B* **2003**, *68*, 115411.
- [22] Hens, Z.; Moreels, I. Light Absorption by Colloidal Semiconductor Quantum Dots. *Journal of Materials Chemistry* **2012**, *22*, 10406–10415.
- [23] *Nanocrystal Quantum Dots*, 2nd ed.; Klimov, V., Ed.; CRC Press, 2010.
- [24] Robel, I.; Gresback, R.; Kortshagen, U.; Schaller, R.; Klimov, V. Universal Size-Dependent Trend in Auger Recombination in Direct-Gap and Indirect-Gap Semiconductor Nanocrystals. *Physical Review Letters* **2009**, *102*, 177404.
- [25] Al-Otaify, A.; Kershaw, S. V.; Gupta, S.; Rogach, A. L.; Allan, G.; Delerue, C.; Binks, D. J. Multiple exciton generation and ultrafast exciton dynamics in HgTe colloidal quantum dots. *Physical Chemistry Chemical Physics* **2013**, *15*, 16864–16873.
- [26] Bransden, B.; Joachain, C. *Quantum Mechanics*; Pearson Education Limited, 2000.

- [27] Delerue, C.; Lannoo, M. *Nanostructures: Theory and Modeling*; Springer, 2004.
- [28] Klimov, V. I.; Ivanov, S. a.; Nanda, J.; Achermann, M.; Bezel, I.; McGuire, J. a.; Piryatinski, A. Single-exciton optical gain in semiconductor nanocrystals. *Nature* **2007**, *447*, 441–6.
- [29] Hooker, S.; Webb, C. *Laser Physics*, 1st ed.; Oxford University Press, 2010.
- [30] Dasgupta, K.; Nair, L. Effect of Excited-State Absorption at Signal Wavelength in Pulsed-Dye-Laser Amplifiers. *IEEE Journal of Selected Topics in Quantum Electronics* **1990**, *26*, 189–192.
- [31] Denton, R. T. et al. Excited Singlet-State Absorption in Dyes and Their Effect on Dye Lasers. *IEEE Journal of Selected Topics in Quantum Electronics* **1977**, *13*, 962–967.
- [32] Martin, E.; Delerue, C.; Allan, G.; Lannoo, M. Theory of Excitonic Exchange Splitting and Optical Stokes Shift in Silicon Nanocrystals: Applications to Porous Silicon. *Physical Review B* **1994**, *50*, 18258.
- [33] Viswanatha, R.; Brovelli, S.; Pandey, A.; Crooker, S. a.; Klimov, V. I. Copper-doped inverted core/shell nanocrystals with "permanent" optically active holes. *Nano letters* **2011**, *11*, 4753–4758.
- [34] Brovelli, S.; Galland, C.; Viswanatha, R.; Klimov, V. I. Tuning Radiative Recombination in Cu-Doped Nanocrystals via Electrochemical Control of Surface Trapping. *Nano letters* **2012**.
- [35] Sewall, S. L.; Cooney, R. R.; Anderson, K. E. H.; Dias, E. a.; Sagar, D. M.; Kambhampati, P. State-resolved studies of biexcitons and surface trapping dynamics in semiconductor quantum dots. *The Journal of chemical physics* **2008**, *129*, 084701.
- [36] Hassinen, A.; Moreels, I.; De Nolf, K.; Smet, P. F.; Martins, J. C.; Hens, Z. Short-chain alcohols strip X-type ligands and quench the luminescence of PbSe and CdSe quantum dots, acetonitrile does not. *Journal of the American Chemical Society* **2012**, *134*, 20705–12.
- [37] Liu, H.; Keuleyan, S.; Guyot-Sionnest, P. n- and p-Type HgTe Quantum Dot Films. *The Journal of Physical Chemistry C* **2012**, *116*, 1344–1349.

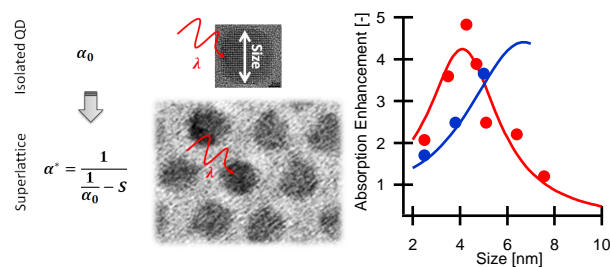
- [38] Kershaw, S. V.; Kalytchuk, S.; Zhovtiuk, O.; Shen, Q.; Oshima, T.; Yindeesuk, W.; Toyoda, T.; Rogach, A. L. Multiple exciton generation in cluster-free alloy  $\text{Cd}_x\text{Hg}_{1-x}\text{Te}$  colloidal quantum dots synthesized in water. *Physical chemistry chemical physics : PCCP* **2014**.
- [39] Yin, Y.; Alivisatos, P. Colloidal nanocrystal synthesis and the organic-inorganic interface. *Nature* **2005**, *437*, 664–70.
- [40] Wang, X.; Koleilat, G. I.; Tang, J.; Liu, H.; Kramer, I. J.; Debnath, R.; Brzozowski, L.; Barkhouse, D. A. R.; Levina, L.; Hoogland, S.; Sargent, E. H. Tandem colloidal quantum dot solar cells employing a graded recombination layer. *Nature Photonics* **2011**, *5*, 480–484.
- [41] Kim, T.-h.; Cho, K.-s.; Lee, E. K.; Lee, S. J.; Chae, J.; Kim, J. W.; Kim, D. H.; Kwon, J.-y.; Amaratunga, G.; Lee, S. Y.; Choi, B. L.; Kuk, Y.; Kim, J. M.; Kim, K. Full-colour quantum dot displays fabricated by transfer printing. *Nature Photonics* **2011**, *5*, 176–182.
- [42] Beard, M. C.; Midgett, A. G.; Hanna, M. C.; Luther, J. M.; Hughes, B. K.; Nozik, A. J. Comparing multiple exciton generation in quantum dots to impact ionization in bulk semiconductors: implications for enhancement of solar energy conversion. *Nano letters* **2010**, *10*, 3019–27.
- [43] Aubert, T.; Cirillo, M.; Flamee, S.; Van Deun, R.; Lange, H.; Thomsen, C.; Hens, Z. Homogeneously Alloyed CdSeS Quantum Dots: An Efficient Synthesis for Full Optical Tunability. *Chemistry of Materials* **2013**, *25*, 2388–2390.
- [44] Jenkins, A. Silicon Lasers: the Final Frontier. *Nature Photonics* **2007**, *1*, year.
- [45] Simply silicon. *Nature Photonics* **2010**, *4*, 491–491.
- [46] Chen, R.; Tran, T.-t. D.; Ng, K. W.; Ko, W. S.; Chuang, L. C.; Sedgwick, F. G.; Chang-Hasnain, C. Nanolasers grown on silicon. *Nature Photonics* **2011**, *5*, 170–175.
- [47] Klimov, V. I.; Mikhailovsky, A.; Xu, S.; Malko, A.; Hollingsworth, J.; Leatherdale, C.; Eisler, H.-J.; Bawendi, M. Optical Gain and Stimulated Emission in Nanocrystal Quantum Dots. *Science* **2000**, *290*, 314–317.
- [48] Dang, C.; Lee, J.; Breen, C.; Steckel, J. S.; Coe-Sullivan, S.; Nurmikko, A. Red, green and blue lasing enabled by single-exciton gain

- in colloidal quantum dot films. *Nature Nanotechnology* **2012**, 7, 335–339.
- [49] Klimov, V. I. Quantization of Multiparticle Auger Rates in Semiconductor Quantum Dots. *Science* **2000**, 287, 1011–1013.
- [50] García-Santamaría, F.; Chen, Y.; Vela, J.; Schaller, R. D.; Hollingsworth, J. a.; Klimov, V. I. Suppressed auger recombination in "giant" nanocrystals boosts optical gain performance. *Nano letters* **2009**, 9, 3482–8.
- [51] Grivas, C.; Li, C.; Andreakou, P.; Wang, P.; Ding, M.; Brambilla, G.; Manna, L.; Lagoudakis, P. Single-mode tunable laser emission in the single-exciton regime from colloidal nanocrystals. *Nature Communications* **2013**, 4, year.
- [52] Caruge, J. M.; Halpert, J. E.; Wood, V.; Bulović, V.; Bawendi, M. G. Colloidal quantum-dot light-emitting diodes with metal-oxide charge transport layers. *Nature Photonics* **2008**, 2, 247–250.
- [53] Digonnet, M. *Rare-Earth Doped Fiber Lasers and Amplifiers*; Marcel Dekker, inc., 2001.
- [54] Chuang, S. *Physics of Photonic Devices*; Wiley, 2009.

# 8

## Absorption Enhancement in 2D and 3D Quantum Dot Superlattices

The absorption cross section of colloidal quantum dots in close packed monolayers shows a 4 (CdSe) to 5-fold (PbS) enhancement as compared to quantum dots in a dilute dispersion. Quantitative agreement is demonstrated between the value and the size dependence of the enhancement and theoretical model predictions based on dipolar coupling between neighboring quantum dots. This collective optical behavior offers a new degree of freedom in the custom design of optical properties for electro-optical devices.



## 8.1 Introduction

Like atoms forming macroscopic crystals, nanoparticle superlattices (NSLs) can exhibit physical properties different from their individual constituents.<sup>1</sup> These properties can be tuned by means of the characteristics of the building blocks (size, shape, ferromagnetic, metallic, . . .), the lattice structure (particle separation, lattice symmetry, . . .) or the interparticle interactions (electromagnetic and/or quantum mechanical coupling, . . .). Lithographically defined arrays of metallic nanoparticles for example show collective optical properties based on coupling through near-field and/or long range dipolar interactions which strongly affect the single particle plasmon resonance<sup>2;3</sup>. Similarly long range electromagnetic interactions have recently been observed in ensembles of epitaxially grown, semiconducting quantum dots<sup>4</sup>. However, both the plasmonic and the epitaxial systems are limited by their fabrication process, which prevents the formation of heterogeneous superlattices or assemblies with high packing densities. An alternative to these lithography-based techniques is the bottom-up formation of NSLs by self-assembly of colloidal nanocrystals. These nanometer-sized metal, metal oxide or semiconductor crystals are synthesized with low size dispersion by a solution-based synthesis<sup>5</sup>. Single component, binary and even ternary close packed NSLs have been demonstrated<sup>1;6-8</sup>, in which crucial parameters such as the type of building block, the interparticle spacing and the superlattice symmetry can be adjusted. Although colloidal NSLs are of great fundamental and practical interest, few collective physical properties resulting from coupling between nanocrystals have been demonstrated so far, not least since NSLs are difficult to make over large areas. Using a more simple one-component, two dimensional (2D) array of PbSe quantum dots (QDs), electronic coupling has been demonstrated by means of scanning tunneling spectroscopy<sup>9</sup>. In the case of binary NSLs, single-phase like magnetization was observed with differently sized Fe<sub>3</sub>O<sub>4</sub> nanocrystals and attributed to magnetic dipole coupling<sup>10</sup>.

Here, we analyze the absorption cross section ( $\sigma_f$ ) of PbS and CdSe QDs in close-packed one component monolayers<sup>11;12</sup>. These materials have been chosen since CdSe is the most widely used colloidal QD and, as such, a reference material, while PbS QDs hold great promise for photovoltaics and infrared photodetection<sup>13;14</sup>, applications where light absorbance is a key material property. As compared to literature data on the absorption cross section in diluted dispersions ( $\sigma_{0,s}$ ) of both materials, we find that  $\sigma_f$  can be enhanced up to a factor of 4 (CdSe) or 5 (PbS). For example, in the case of PbS QDs, the enhancement  $\mathcal{E} = \sigma_f/\sigma_{0,s}$  shows a marked, resonance-like diameter dependence, with a maximum value for

QDs of around 4 nm. Similar results are obtained for CdSe. We also show a strong dependence on the superlattice parameters by studying the effect of the inter-particle spacing on fixed size CdSe nanocrystals. Moreover,  $\mathcal{E}$  is largely wavelength independent, which was validated for PbS. We show that the value and the layer parameter-dependence of  $\mathcal{E}$  for both PbS and CdSe can be quantitatively described by considering the dipolar coupling between neighboring QDs in the close packed film. According to this description, the resonance behavior results from the condition for optimal coupling, where the mutual enhancement of the electric fields of neighboring QDs is maximized. In this way, we demonstrate that light absorption by a close packed film of quantum dots is a joint property of the individual QDs and the QD superlattice, thereby showing for the first time a truly collective optical effect in colloidal nanocrystal superlattices

## 8.2 Experiment

### 8.2.1 Thin Film Formation

This work makes use of monodisperse batches of CdSe and PbS QDs stabilized by oleate ligands. They have been synthesized following literature recipes, with diameters  $d_{QD}$  ranging from 2.5 to 6.2 nm for CdSe and 2.5 to 8 nm for PbS. Ligand exchange was carried out on 4.4 nm CdSe QDs capped with oleic acid (OA). As substitute ligands (SL) we used carboxylic acids with different chain lengths from palmitic acid (C16) to dodecanoic acid (C12). A ligand exchange is typically performed by adding an excess of the SL to a toluene suspension of CdSe QDs in a molar ratio of 200:1 SL:OA. After precipitation with methanol (MeOH) and centrifugation, the QDs are resuspended in toluene. The exchange is repeated three times to ensure full exchange. Finally, the QDs are precipitated one more time with MeOH to remove any excess of the SL. In both cases, QD monolayers are formed by spreading a QD dispersion on a Langmuir trough, followed by the transfer of the Langmuir film to a glass substrate using Langmuir-Blodgett deposition.

To produce QD monolayers, we spread the QDs dissolved in chloroform on a water surface using a commercial Langmuir-Blodgett trough (Nima 310). The monolayers are transferred at a surface pressure of 12-30 mN/m to glass substrates by Langmuir-Blodgett deposition or to TEM grids by Langmuir-Schaeffer deposition. As shown in Figure 8.1, this results in homogeneous monolayers over  $\text{cm}^2$  areas, with typical surface coverages as determined by atomic force microscopy (AFM) of 95% or more. In addition, transmission electron microscopy (TEM) demonstrates that the

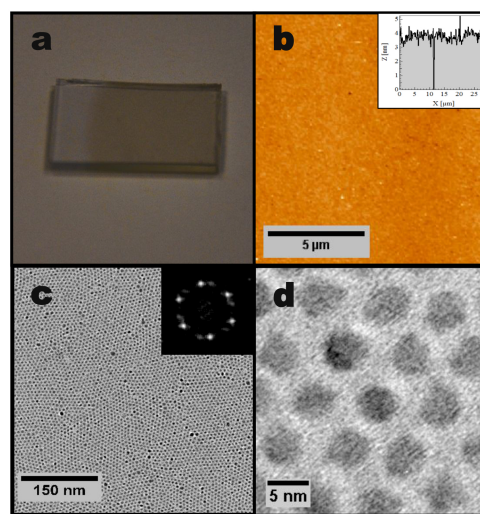


Figure 8.1: Langmuir-Blodgett monolayer of PbS quantum dots. (a) Contrast picture of a monolayer of PbS quantum dots ( $d = 5$  nm) on a glass surface ( $2$  cm  $\times$   $1$  cm) showing homogeneous  $\text{cm}^2$  coverage. (b) Atomic force microscope (AFM) scan of the same PbS monolayer indicating excellent area uniformity (inset: cross section). (c) Larger area TEM image showing the PbS quantum dot superlattice with local hexagonal ordering (inset: Fourier transform image). (d) Zoomed TEM image showing the individual quantum dots and their interdistance.

Oleic	1.45
Palmitic	1.29
Myristic	1.14
Dodecanoic	1.08

Table 8.1: Ligand length (in nm) for different carboxylic acids used.

monolayers have a locally hexagonal ordering.

### 8.2.2 Determination of the Absorption Cross Section

The absorption cross section  $\sigma_f$  of a QD in these close packed monolayers is calculated from the absorbance  $A$  and the reflectance  $R$ , combined with the surface density of absorbers ( $N_s$ ):

$$\sigma_f = \ln(10) \times \frac{A - R}{N_s} \quad (8.1)$$

In this expression, scattering is neglected since the wavelengths used ( $> 350$  nm) are much larger than the quantum dot diameter. The correction of the absorbance for reflection is typically very small ( $< 10\%$ ). The QD surface density ( $N_s$ ) is determined from TEM micrographs (see Figure 8.2), where the QD interdistance – written as  $d_{QD} + 2l$  where  $l$  denotes the thickness of the ligand shell – is obtained. The QDs are capped with organic long-chain molecules (typically carboxylic acids) for stability in solution, which is required for the Langmuir-Blodgett (LB) deposition. In the case of PbS, oleic acid is used. For CdSe, similar ligands but with different chain lengths were used (going from oleic (18 carbon atoms) to dodecanoic acid (12 carbon atoms), see table 8.1). To estimate the inter-particle spacing  $d_{ij}$  of the particles in the layer, we use TEM imaging of the monolayers. These images are obtained from carbon grids stamped on the nanocrystal layer after LB compression.

Note that the inter-particle spacing is crucial in determining the enhancement since it determines directly the surface density of absorbers, which appears in the denominator for the expression of  $\sigma_f$  !

Using the TEM images, we can obtain the (real) super-lattice parameters by taking a spatial FFT (Fast Fourier Transform) (software: ImageJ 1.44) of one 'monocrystalline' subdomain (see Figure 8.2). The latter are typically 200 nm in diameter containing up to 50 nanocrystals at a time. This allows us to do fast statistics on the inter-particle spacing. We confirm this by doing also spacing measurements on the real lattice directly.

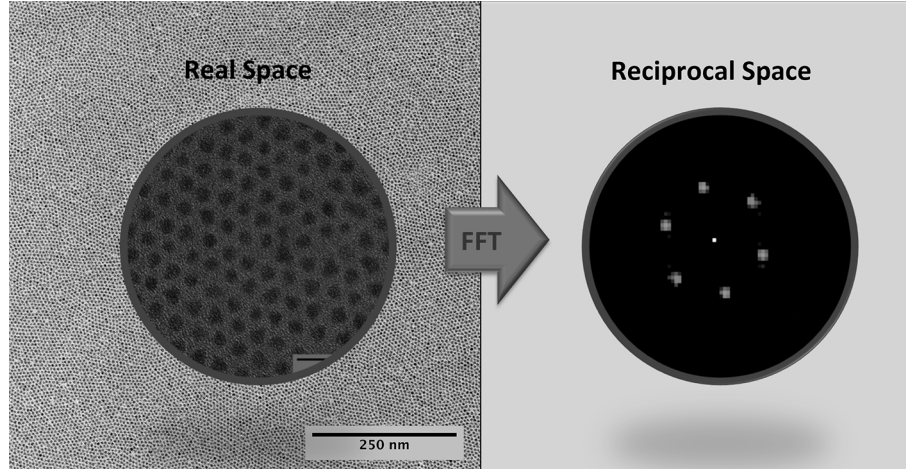


Figure 8.2: Packing density analysis based on TEM grids: (left) real lattice with zoom and (right) reciprocal lattice (first Brillouin zone) obtained through direct spatial FFT of the left image.

The absorption and reflection of the monolayers is measured using a commercial spectrophotometer (Perkin-Elmer Lambda 950 UV-VIS-NIR) equipped with an absolute reflectance measurement (URA) tool. Typically, three (absolute, *i.e.* no reference recorded before) spectra are recorded (both for absorption and reflection): an internal (instrument related) calibration, a bare glass sample and the glass sample covered with the monolayer under study. The quantities  $A$  and  $R$  are then obtained through subsequent subtraction procedures. Such procedures are valid for thin films where interference effects can be neglected. This method provided us with the best accuracy for weakly absorbing and reflecting samples.

The absorbance in a regular spectrophotometer always includes contributions of reflection. Especially for thin layers, these corrections can be quite substantial. Therefore, we collect absolute reflectance data (collection angle of incidence =  $8^\circ$ , note that  $\cos(8^\circ) \approx 1$ ) for all our samples. The corrections are quite small however in our case, typically around 10 % of the measured absorbance (see Figure 8.3) is due to net reflectance of the nanocrystal monolayer. Scattering is neglected since the particles are very small compared to the optical wavelengths used. For example, in simple Rayleigh scattering, the cross section is evaluated as:

$$\sigma_{scat,Ray} = \left(\frac{d}{\lambda}\right)^6 \pi^2 \left(\frac{n^2 - 1}{n^2 + 1}\right)^2 \approx 10^{-18} \text{cm}^2 \ll \sigma_{abs} \quad (8.2)$$

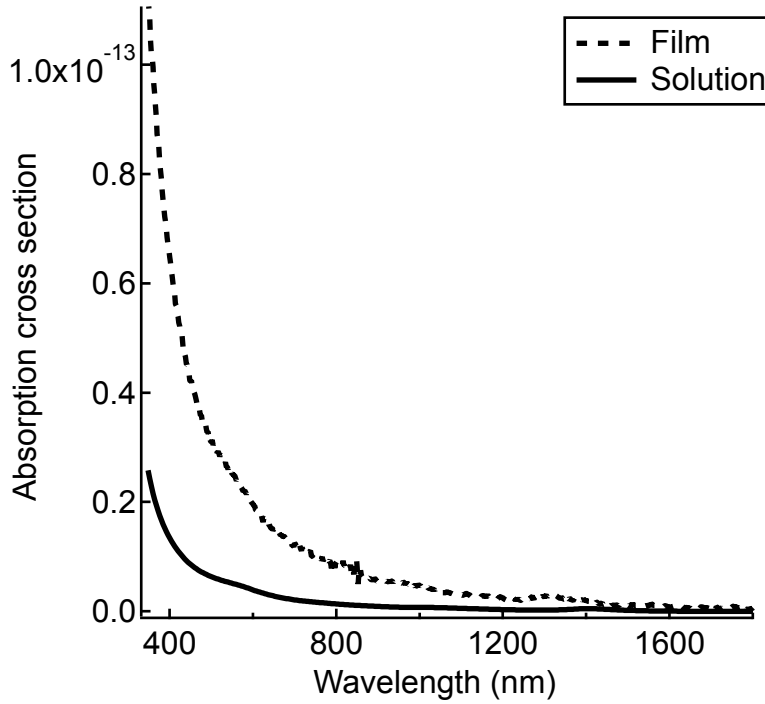


Figure 8.3: Absorption and reflection of a monolayer of PbS (4.3 nm) on glass.

where  $\sigma_{abs}$  is typically  $\sim 10^{-15} \text{ cm}^2$ , especially at high photon energies (or short wavelengths).

### 8.3 Observation of Enhancement

To calculate the absorption enhancement, we combine the experimental values of  $\sigma_f$  with published values<sup>15;16</sup> for  $\sigma_{0,s}$ , where we work at 400 nm for PbS and at 335 nm for CdSe:

$$\sigma_{0,s,\lambda_i} = 3.85e^{-15} \times \epsilon_{\lambda_i} \quad (8.3)$$

Figure 8.4(a) and (b) show the absorption enhancement  $\mathcal{E}$  for PbS and CdSe QDs as a function of their diameter at 400 and 335 nm, respectively. For PbS, we find that  $\mathcal{E}$  initially increases with increasing particle size up to a maximum of 5 at a core size of around 4 nm. For larger sizes,  $\mathcal{E}$  goes

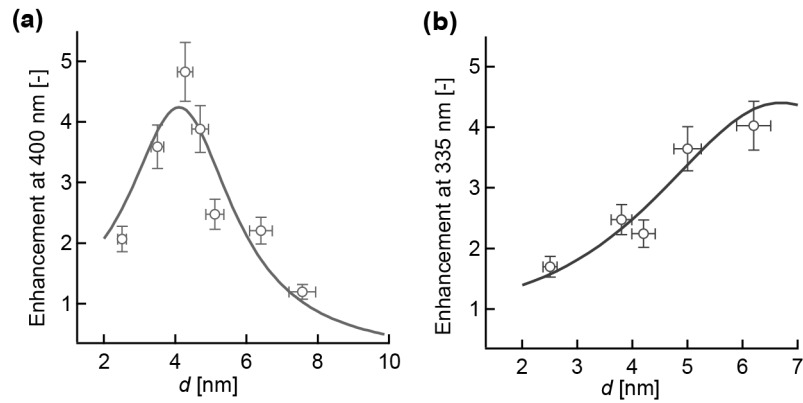


Figure 8.4: Absorption enhancement  $\mathcal{E}$  for (a) PbS quantum dots at 400 nm and (b) CdSe quantum dots at 335 nm as a function of QD diameter  $d$ . The markers indicate experimental values, while the solid lines represent the enhancement predicted by the coupled dipole model. The horizontal error bars are based on the particle size dispersion, which is typically 5–10%.

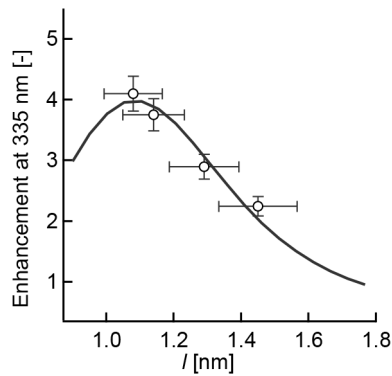


Figure 8.5: Absorption enhancement  $\mathcal{E}$  of CdSe monolayer for a fixed size (4.4 nm) varying only the length of the passivating ligand  $l$ . The latter influences interparticle spacing, but not the single particle polarizability. A clear decrease of the enhancement with increased ligand length (or equivalently interparticle distance) is observed.

down and reaches values of about 1 for 8 nm particles. In the case of CdSe,  $\mathcal{E}$  steadily increases within the diameter range studied to level off at a value of around 4 for a diameter of 6.2 nm. We also investigated the influence of the thickness of the ligand shell  $l$  (see Figure 8.5). In particular, for a fixed size of CdSe nanocrystal (4.4 nm), the ligand shell was exchanged from oleic acid to shorter chain carboxylic acids (palmitic, myristic and dodecanoic acid). We notice a steep decrease in  $\mathcal{E}$  for increasing ligand length (or equivalently 'interparticle spacing').

## 8.4 Maxwell-Garnett Model

To analyze the enhancement of  $\sigma_f$  relative to  $\sigma_{0,s}$ , including its remarkable diameter and ligand-length dependence, we start from the fact that light absorption by isolated QDs can be understood within the framework of the Maxwell-Garnett effective medium theory. This yields an absorption cross section  $\sigma_{0,s}$  given by ( $V_{QD}$ , QD volume;  $n_s$ , refractive index of the solvent;  $\varepsilon_s$ , dielectric constant of the solvent at the radiation frequency;  $\varepsilon_{QD}$ , dielectric function of the QD materials at the radiation frequency):

$$\sigma_{0,s} = V_{QD} \frac{2\pi}{\lambda n_s} \frac{9\varepsilon_s^2}{|\varepsilon_{QD} + 2\varepsilon_s|^2} \text{Im}(\varepsilon_{QD}) \quad (8.4)$$

Typically,  $|\varepsilon_{QD}|$  strongly exceeds  $|\varepsilon_s|$  for QDs dispersed in an apolar, organic solvent, a condition implying that the optical electric field in the QDs is strongly screened. An increase of  $|\varepsilon_s|$  and the concomitant reduction of this screening will therefore result in an enhancement of the absorption cross section (see equation 8.4). Hence, a first possible origin of the enhanced absorption of QDs in a close packed thin film is the reduced screening of the incident light by an increase of dielectric constant of the environment. This increase could, *e.g.*, be due to the presence of neighbouring particles in the film or due to the presence of the glass substrate. However, as is shown in 8.6a, not only is this effect size-independent, it also fails to account for the large enhancements (up to 5) measured experimentally. A similar conclusion is arrived at when explicitly taking the volume fraction of the absorbers into account in the Maxwell-Garnett expression for a given host permittivity (see 8.6b). This indicates that the Maxwell-Garnett mixing rule model breaks down in films of close packed nanocrystals.

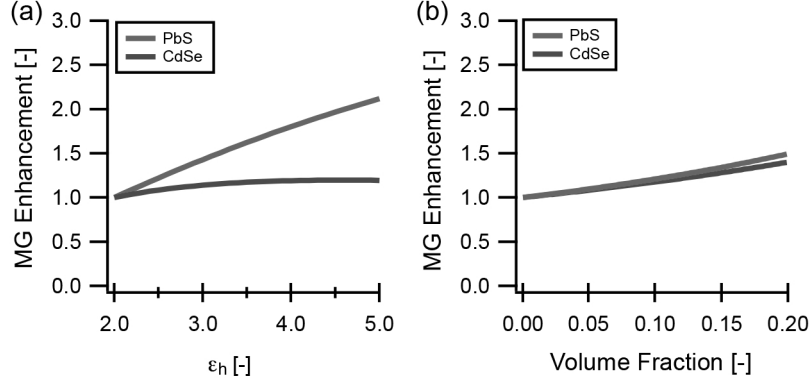


Figure 8.6: Absorption enhancement  $\mathcal{E}$  in the Maxwell-Garnett (MG) model for (a) increasing dielectric constant of the particle environment at a fixed volume fraction and (b) vice versa.

## 8.5 Beyond Maxwell-Garnett: The Coupled Dipole Model

An alternative approach to derive equation 8.4 is to see each QD as a polarizable point particle with a polarizability  $\alpha_{0,s}$  that depends on its volume,  $\epsilon_{QD}$  and  $\epsilon_s$ :

$$\alpha_{0,s} = 4\pi\epsilon_0 r^3 \epsilon_s \frac{\epsilon_{QD} - \epsilon_s}{\epsilon_{QD} + 2\epsilon_s} \quad (8.5)$$

Equation 8.4 is then recovered by the relation between the absorption cross section and the imaginary part of  $\alpha_{0,s}$ :

$$\sigma_{0,s} = \frac{2\pi}{\lambda n_s} \text{Im}(\alpha_{0,s}) \quad (8.6)$$

Describing QDs as polarizable point particles, the exceptional absorption enhancement in close packed QD monolayers can be intuitively understood by means of dipolar coupling between neighboring QDs. A polarized QD will induce a polarization field with dominant dipolar character<sup>17</sup>, decaying rapidly outside of the QD (see Figure 8.7). However, opposite from isolated QDs (*e.g.* in a dilute solution), neighboring QDs in a close packed layer will feel this additional field. Hence, their polarization by an external driving field will be different from that of an isolated QD, which results in a change in absorption cross section. Since the distance  $d_{ij}$  between two dipoles  $i$  and  $j$  in a close packed film increases linearly with the QD radius,

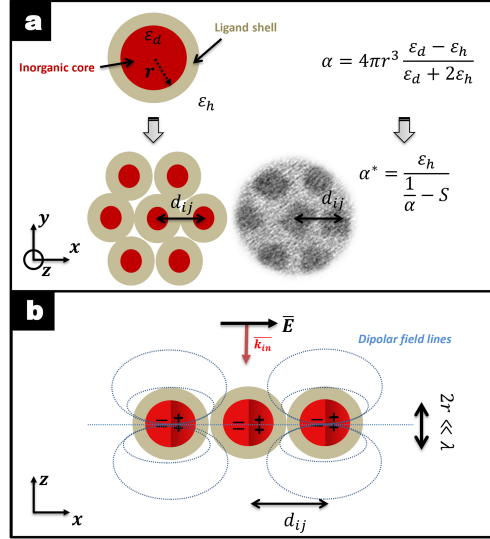


Figure 8.7: Side view schematic of monolayer subject to incident field polarized in-plane with induced depolarization fields. The relevant geometrical parameters are indicated by  $d_{QD}$ ,  $d$  and  $l$  as the (nearest-neighbor) interdot distance, QD size, and ligand length, respectively.

there is a trade-off in this dipolar coupling: larger particles show a larger polarizability but increased interparticle spacing. Apparently, this gives rise to an optimal separation or, equivalently, an optimal particle size for dipolar coupling, as follows from the experimental data in Figure 8.4.

This qualitative description can be quantified by the coupled dipole (CD) model, which was originally developed to explain collective resonance effects in arrays of metallic particles<sup>2,3;18</sup>. Such particles show distinct multipolar plasmon resonances in their single particle polarizability, thus differing fundamentally from the semiconducting QDs studied here. Within this model, we write the local field  $E_{L,i}$  polarizing a particular QD  $i$  as the sum of the incident external field  $E$  and the contribution from the polarization fields of all other QDs  $j$ :

$$E_{L,i} = E + \sum_{j \neq i} \beta_{i,j} E_{L,j} \quad (8.7)$$

Here, the coupling coefficients  $\beta_{i,j}$  describe the dipole field of QD  $j$  at the position of QD  $i$ . They are thus proportional to  $\alpha_{0,h}/\varepsilon_h$ , *i.e.*, the polariz-

ability of an individual QD screened by the host. More importantly, due to symmetry reasons, all QDs must experience the same local field  $E_L$ . Thus, we can rewrite equation 8.7 as:

$$E_L = E + \frac{\alpha_{0,h}}{\varepsilon_h} \sum_{j \neq i} S_{i,j} E_L = E + \frac{\alpha_{0,h}}{\varepsilon_h} S E_L \quad (8.8)$$

The quantity  $S$ , introduced in equation 8.8 is called the retarded dipole sum which includes the dipolar contributions from all neighboring particles to the internal field of the considered particle.

$$S = \frac{1}{4\pi} \sum_{j \neq i} (1 - ikd_{ij})(3 \cos^2(\theta_{ij}) - 1) \times \frac{e^{ikd_{ij}}}{d_{ij}^3} + k^2 \sin^2(\theta_{ij}) \frac{e^{ikd_{ij}}}{d_{ij}} \quad (8.9)$$

The first term of the dipole sum  $S$  relates to near-field electrostatic interactions, the second term to long range electrodynamic interactions. Since our particles are very small (2-10 nm) compared to the optical wavelengths used ( $\ll 335$  nm), we can neglect terms in  $k^2$  (with  $k = \frac{2\pi}{\lambda}$ ). Also, the interparticle spacing is so small that terms in  $kd$  are unlikely to be of importance. The term  $d_{ij}$  relates to the distance between particle  $i$  and  $j$ . This can be evaluated from the simple hexagonal packing obtained in our superlattices as evaluated by TEM analysis. The angle  $\theta_{ij}$  refers to the angle between the polarization of the incident light and the orientation vector from particle  $i$  to particle  $j$ . We can average out this angle for two reasons:

- The nanocrystals are ordered in hexagonally close packed layers. However, the crystal structure itself is not extended over the entire substrate (or equivalently the optical beam area) but is limited to small 'grains' (typically around 100 nm x 100 nm). This situation resembles a polycrystalline superlattice as can be seen in 8.1.
- Our experiments use unpolarized light under a 0 degree incidence angle. Experiments with polarized light gave no difference, most likely because of reason 1.

Both arguments indicate that the angle between the polarization and the lattice basis-vectors will be arbitrary, so we can write:

$$\langle \cos^2(\theta_{ij}) \rangle = \langle \sin^2(\theta_{ij}) \rangle = \frac{1}{2} \quad (8.10)$$

Using the above assumptions, we can write  $S$  in a simplified form:

$$S = \sum_{j \neq i} \frac{(1 - ikd_{ij})e^{ikd_{ij}}}{8\pi d_{ij}^3} \quad (8.11)$$

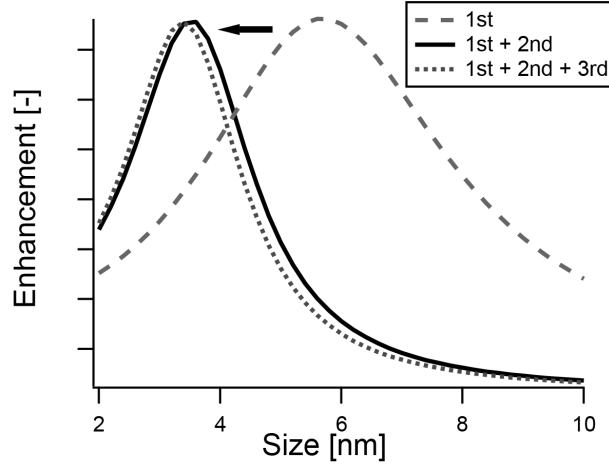


Figure 8.8: Calculated enhancement (PbS @ 400 nm) considering different degrees of nearest neighbors. The effect clearly saturates at the second nearest neighbors, allowing us to limit the dipole sum  $S$  numerically.

Note that there are no free parameters in this expression. Also, the expression for  $S$  does not depend on the used materials, only on the geometry of the lattice, *i.e.* particle size and ligand length. The inter-particle distance is fixed by the particle size  $d_{QD}$  because of the close packing in the monolayer:

$$d_{ij} = \gamma(d_{QD} + 2l) \quad (8.12)$$

The value for the ligand length  $l$  is obtained from TEM analysis (see part 3). An average value for oleic acid capped particles is ca. 1.5 nm. The scaling factor  $\gamma$  differs for the first ( $\gamma = 1$ ), second ( $\gamma = \sqrt{3}$ ), ... nearest neighbors in the hexagonal lattice. Note that the hexagonal packing is only important to accurately calculate the interparticle spacing between neighbors. The rotational symmetry is not important in our case.

Figure 8.8 shows the effect of the number of interactions considered in  $S$  on the enhancement  $\mathcal{E}$  for different sizes of PbS at 400 nm. The dipolar contributions clearly saturate at the second nearest neighbors. Taking more interactions into account will not substantially change the calculation. This allows us to limit the dipole sum numerically and gives a very clear indication that especially near-field interactions are important in our system. Note that the full expression for  $S$  was used, including the long range term.

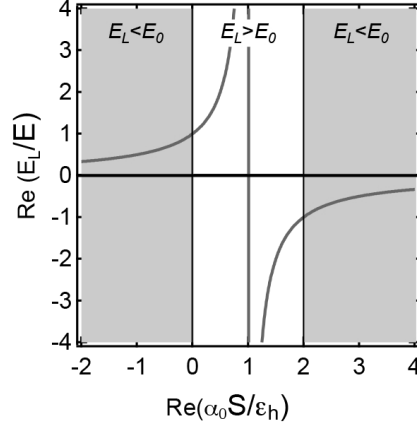


Figure 8.9: The ratio of the local driving field  $E_L$  and the external driving field  $E$  as a function of the coupling between neighboring QDs as expressed by equation 8.14.

Under the assumptions above, we can write:

$$S = \sum_{j \neq i} \frac{(1 - ikd_{ij}) e^{ikd_{ij}}}{8\pi d_{ij}^3} \quad (8.13)$$

Rewriting 8.8, we obtain an expression for the field locally driving an individual QD as a function of the incident electric field:

$$E_L = \frac{E}{1 - \frac{\alpha_{0,h}}{\epsilon_h} S} \quad (8.14)$$

Equation 8.14, which describes the local driving field  $E_L$  as a function of the incident field  $E$ , provides an excellent starting point to understand the occurrence of a maximum enhancement. It indicates that the ratio between  $E_L$  and  $E$  crucially depends on the product  $\alpha_{0,h}S/\epsilon_h$ , *i.e.*, on the combination of the polarizability of an individual QD and the coupling between the QDs. Based on the respective definitions of  $\alpha_{0,h}$  and  $S$ , it follows that this quantity changes depending on the QD material, the driving frequency (*via*  $\epsilon_{QD}$ ), the diameter of the QDs and the distance between neighboring QDs. Assuming for simplicity that  $\alpha_{0,h}S/\epsilon_h$  is a real number,  $E_L$  will be enhanced relative to  $E$  when  $0 < \alpha_{0,h}S/\epsilon_h < 2$  (see Figure 8.9). Moreover,  $E_L$  increases to infinity when  $\alpha_{0,h}S/\epsilon_h = 1$ . Returning to 8.8, this actually means that the system of dipoles can support a local driving field without

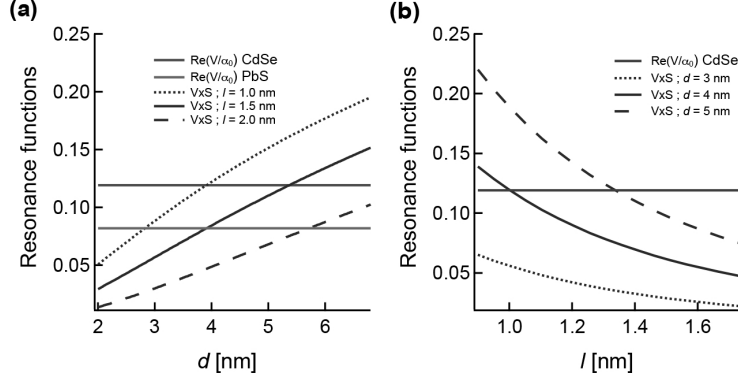


Figure 8.10: (a) Graphical representation of the optimal coupling condition (8.16) showing the term (full lines)  $\alpha_{0,h}/\varepsilon_h V_{QD}$  for PbS (bottom horizontal) QDs at 400 nm and CdSe (top horizontal) QDs at 335 nm, together with the term (dashed lines)  $1/(V_{QD}S)$  for ligand lengths  $l$  of (dotted) 1 nm, (solid) 1.5 nm and (dashed) 2 nm as a function of particle size. In (b), the same terms are plotted, now as a function of ligand length  $l$  for different particle sizes: (dotted) 3 nm, (solid) 4 nm and (dashed) 5 nm. Optimal coupling for a given material corresponds to the crossing of the respective dashed and full lines. Calculations done taking  $\varepsilon_h = 1.5$  and assuming local hexagonal ordering in the monolayers.

external driving field at the particular driving frequency where this condition holds. Hence, the condition  $\alpha_{0,h}S/\varepsilon_h = 1$  determines a resonance condition for the 2D array of coupled, oscillating dipoles. Obviously, we expect that around this resonance condition, the absorbance of the layer will be maximally enhanced, a situation we call optimal coupling. We note that neglecting the imaginary part of the denominator in 8.14 is useful for understanding the resonance condition. In reality, the imaginary part limits the increase of  $E_L$ , resulting in a damped resonance. For a quantitative comparison between the experimental results and the theory developed here, both the real and imaginary part of  $S$  and  $\alpha_{0,h}$  are to be taken into account.

**Effect of Size Dispersion** In the model, it is assumed that particles have fixed sizes and interparticle distances. In a real system however, there will always be a certain degree of 'size dispersion': either the ligands (due to over -or undercompression during Langmuir-Blodgett deposition) or the nanocrystals (due to inherent size fluctuations in the wet colloidal synthesis) will show a Gaussian distribution.

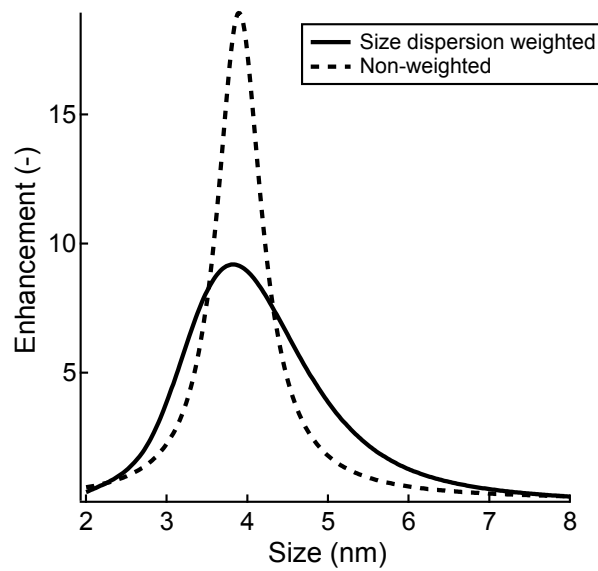


Figure 8.11: Calculated enhancement (PbS @ 400 nm, considering 1<sup>st</sup> and 2<sup>nd</sup> nearest neighbors) for different values of the considered relative size dispersion of 0.1 (weighted) and 0 (non-weighted).

Figure 8.11 shows the effect of size dispersion on the enhancement, taken into account as:

$$\mathcal{E}(r) = \int \mathcal{E}^*(r') \frac{e^{-\frac{(r-r')^2}{2\sigma_r(r')^2}}}{\sqrt{2\pi}\sigma_r(r')^2} dr' \quad (8.15)$$

where  $\mathcal{E}^*$  is the theoretical enhancement (red line, 8.11). By weighing the theoretical enhancement with the size dispersion (a typical value is  $\frac{\sigma_r(r)}{r} = 0.1$ ), we can predict the actual enhancement (black line, 8.11) of a realistic system and compare it with the experimental results. We can conclude that the large theoretical enhancements are not found experimentally because of the detrimental effect of size distribution.

## 8.6 Coupled Dipole Model and the Experiment

### 8.6.1 Nanocrystal Size and Ligand Length

In the experiments shown in Figures 8.4 and 8.5, we fix the driving frequency – and thus  $\varepsilon_{QD}$  – yet we change  $\alpha_{0,h}$  via the QD size and  $S$  via both the QD size and ligand length. To analyze the occurrence of optimal coupling in this case, we rewrite the resonance condition as:

$$\frac{\alpha_{0,h}}{\varepsilon_h \times V_{QD}} = \frac{1}{V_{QD} \times S} \quad (8.16)$$

In equation 8.16, the left hand side depends on the QD material and the driving frequency, but not on the QD size or the inter-particle spacing. On the other hand, the right hand side depends on the geometrical parameters of the close-packed layer, *i.e.*,  $d_{QD}$  and  $l$ . By varying  $d_{QD}$  or  $l$ , we thus only change  $1/(V_{QD} \times S)$ , and optimal coupling occurs when equation 8.16 holds. When  $l = 1.5$  nm – the experimentally determined ligand shell thickness in the close packed Langmuir-Blodgett films – Figure 8.10a shows that this results in optimal coupling for  $\approx 4$  nm PbS QDs. This value matches the experimentally observed diameter for maximum enhancement, confirming that the mutual dipolar coupling between adjacent QDs indeed accounts for the observed absorption enhancement. Equation 8.16 and Figure 8.10(a) also show that the lower polarizability of CdSe QDs makes that larger diameters are needed to reach optimal coupling, which is also confirmed experimentally (see 8.4). Also the dependence of the resonance on ligand length can be understood using the resonance condition described in equation 8.16. As plotted in 8.10(b), optimal coupling for a fixed size of

CdSe (4.4 nm) occurs for a ligand length of close to 1.1 nm, which is also suggested by the experimental data in 8.5.

For a more quantitative comparison between our experimental data and the coupled dipole model, we use equation 8.14 to obtain an effective polarizability  $\alpha_{film}$  of a QD in a close packed monolayer:

$$\alpha_{film} = \frac{\alpha_{0,h}}{1 - \frac{\alpha_{0,h}}{\varepsilon_h} S} \quad (8.17)$$

As a result,  $\sigma_f$  and the absorption enhancement read:

$$\sigma_f = \frac{2\pi}{\lambda n_h} \text{Im} \left( \frac{\alpha_{0,h}}{1 - \frac{\alpha_{0,h}}{\varepsilon_h} S} \right) \quad (8.18)$$

$$\mathcal{E} = \frac{\sigma_f}{\sigma_{0,s}} = \frac{n_s}{n_h} \frac{\text{Im} \left( \frac{\alpha_{0,h}}{1 - \frac{\alpha_{0,h}}{\varepsilon_h} S} \right)}{\text{Im}(\alpha_{0,s})} \quad (8.19)$$

Equation 8.19 shows that the condition for optimal coupling also controls the enhancement of  $\sigma_f$ . In Figure 8.10, the solid lines represent  $\mathcal{E}$  for PbS and CdSe QDs, calculated using 8.19 at 400 and 335 nm, respectively. As is common for the high energy dielectric function of semiconductor quantum dots, the respective bulk values are used for  $\varepsilon_{QD}$ . In addition, the film environment is modeled as  $\varepsilon_h = 1.5$ , which corresponds to an environment of low polarizability. This is a reasonable estimate for an environment consisting of organic ligands, glass and air. Assuming a size dispersion of 10%, we find that the experimental enhancement is in very good agreement with the enhancement that follows from the assumption of dipolar coupling between neighboring QDs. For both PbS and CdSe, the magnitude and the size-dependence of  $\mathcal{E}$  are correctly predicted with, for the particular example of PbS, a maximum enhancement for a diameter of around 4 nm. Also, for CdSe, the dependence of  $\mathcal{E}$  on the ligand length  $l$  is well reproduced.

### 8.6.2 The Wavelength Dependence of the Enhancement

In Figure 8.4, we pass through the condition of optimal coupling by changing  $d_{QD}$ . Alternatively, optimal coupling can also be obtained by changing the wavelength  $\lambda$  of the incident light. The color scale in 8.12a shows the optimal coupling condition – as determined by equation 8.16 – as a function of both variables. While changing  $d_{QD}$  results in a relatively narrow resonance, one sees that the condition for optimal coupling hardly depends

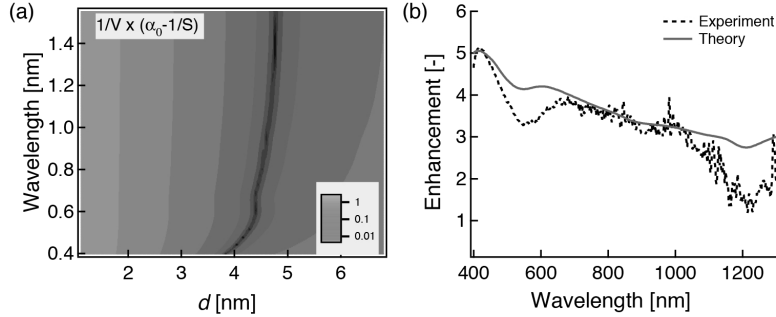


Figure 8.12: (a) Plot of  $(\alpha_{0,h}/\epsilon_h - 1/S)/V$  as a function of QD diameter and wavelength according to the indicated color code. Optimal coupling corresponds to a value of 0, indicated as dark brown ( $\epsilon_h=1.5$ ) (b) Spectrum of the absorption enhancement as (dotted) measured and (solid) calculated for 4.3 nm PbS QDs.

on  $\lambda$ . This minor wavelength dependence can be understood from the non-resonant polarizability of individual QDs in the wavelength range considered. Opposite from metal nanocrystals driven near their surface plasmon resonance, this leads to a limited change of  $\alpha_0$ . Importantly, this implies that for a fixed QD diameter, the absorption will be enhanced over a broad wavelength range. This prediction is confirmed by the spectrum of  $\mathcal{E}$  for 4.3 nm PbS QDs as represented in Figure 8.12b, where  $\mathcal{E}$  goes down gradually from a value of 5 around 400 nm to 3 around 1000 nm. This overall trend is well reproduced by the coupled dipole model, where we now use the frequency dependent dielectric function of PbS nanocrystals as obtained through the Kramers-Krönig relations<sup>19</sup>. Nanocrystal devices for photodetection or solar energy conversion typically face a trade-off between light absorption, which improves with thicker layers, and charge carrier extraction, where thinner films are preferred. Hence, the possibility to enhance the absorption over a broad wavelength range by tuning the nanocrystals size and the intra-nanocrystal spacing is very relevant for these applications.

### 8.6.3 Core/Shell Nanocrystals

By varying the ligand length  $l$ , we change the distance between two dipoles, but not their intrinsic polarizability. Vice versa, it would be interesting to see what happens if we change the intrinsic polarizability of the particle, but keeping them at a fixed distance. This was investigated using core/shell

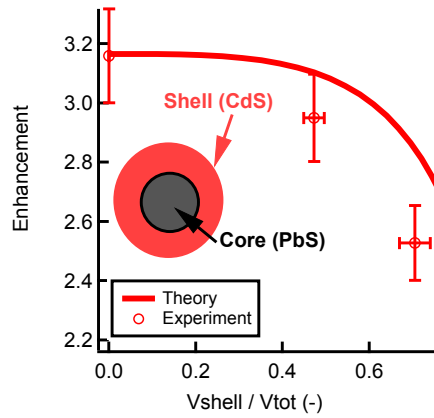


Figure 8.13: Enhancement (at 400 nm) for PbS/CdS core/shell QDs for varying core size, expressed through the ratio  $V_{shell}/V_{tot}$ . Note that the total size is fixed at 3.55 nm.

PbS/CdS nanocrystals. These QDs are synthesized through exposure of the PbS cores to a cation excess of cadmium (Cd) (see chapter 3) leading to partial cation exchange of Pb for Cd. Through this process, the total size of the particle does not change, but the composition of the QD changes (a 'shell' of CdS is formed around a core of PbS). The latter leads to a different polarizability for the particle (or dipole) but keeps them at the same interdistance in a layer as both size and ligand length are unaltered.

The addition of a shell reduces the polarizability of the particle (or dipole) and as such, we expect that increasing the shell thickness will lead to a reduction of the enhancement since nearest neighbours induce smaller fields onto each other. This is indeed observed in Figure 8.13 where the enhancement is shown for increasing shell thickness of a 3.55 nm PbS particle which is gradually exchanged (expressed through the ratio  $V_{shell}/V_{tot}$ , going from 0 (pure PbS) to 0.7 (PbS/CdS)). As such, the composition of a QD adds an additional degree of freedom in tuning the enhancement of a close packed QD lattice, apart from overall size and ligand length.

## 8.7 Beyond Single Component Monolayer

Whether this new phenomenon can play a role of interest in an actual device context depends on two additional issues: does it extend beyond the monolayer thickness and how does it depend on the polarization of the incident

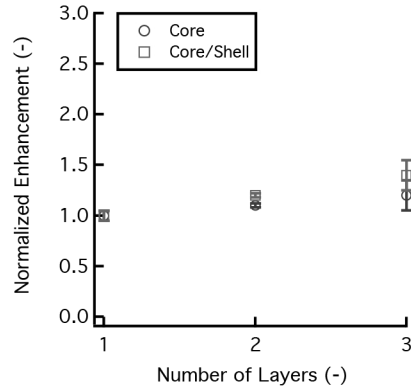


Figure 8.14: Enhancement (normalized to the number of layers) versus the number of layers of the multi-layer films.

light.

### 8.7.1 Multilayers

The amount of material needed to absorb a given fraction of incident light competes with the extraction of photo-generated carriers: thicker cells absorb more light, but do not allow for efficient carrier extraction and vice versa. The latter is known as the absorption-extraction compromise. Our absorption enhancement mechanism could offer part of the solution since it would allow fabrication of thinner cells with light absorption equal to that of non-optimized thicker cells. Our model can be extended to analyze these technologically relevant multilayers. It turns out the enhancement is also present in these stacked systems in an additive way (see Figure 8.14): Dipole coupling occurs between particles in the same layer, but does not occur between different layers in the stack. This allows us to stack the layers until a certain desired absorption is achieved, without losing the effect of the absorption enhancement.

### 8.7.2 Polarization Dependence

In the experiments discussed before, light was incident under  $0^\circ$  angle, forcing the polarization to be in-plane of the nanocrystal layer. Such a case could be noted as transverse electric (TE). One could envisage a situation where the light is polarized perpendicular to the nanocrystal plane, *i.e.* transverse magnetic (TM), for example in the case of oblique incidence

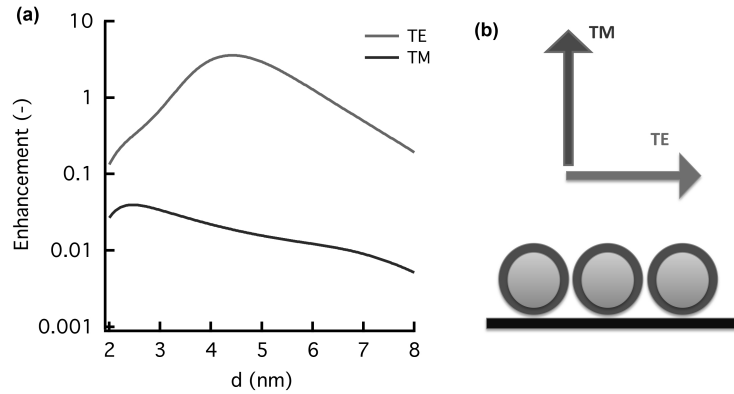


Figure 8.15: Polarization influence (a) Enhancement for varying PbS particle size for TE and TM polarized light (see (b)). A clear deenhancement is observed for the TM case, where light is polarized orthogonal to the layer plane.

or propagation in a guided mode of an SOI waveguide.

The delicate matching of depolarization fields at neighbouring particles completely changes when the dipoles are oriented perpendicular to the plane of the nanocrystal film (TM) instead of in-plane (TE) (see Figure

### 8.7.3 Dipolar Coupling and Spontaneous Emission

As introduced in chapter 2, the Einstein coefficients provide a semi-classical means to understand the link between the three fundamental light-matter interactions of spontaneous/stimulated emission and absorption. Absorption and stimulated emission essentially boil down to the same type of interaction between light and matter, expressed through the symmetry in the Einstein B coefficients ( $B_{12}$  and  $B_{21}$ ). Based on a simple detailed balancing argument, we can argue that modifying the rate of absorption  $B_{12}$  (or equivalently  $B_{21}$ ), will inevitably modify the rate for spontaneous emission  $A_{21}$ :

$$0 = A_{21}n_2 + (B_{21}n_2 - B_{12}n_1) \times \rho(\nu) \quad (8.20)$$

Indeed, the observed absorption enhancement provides a means to boost

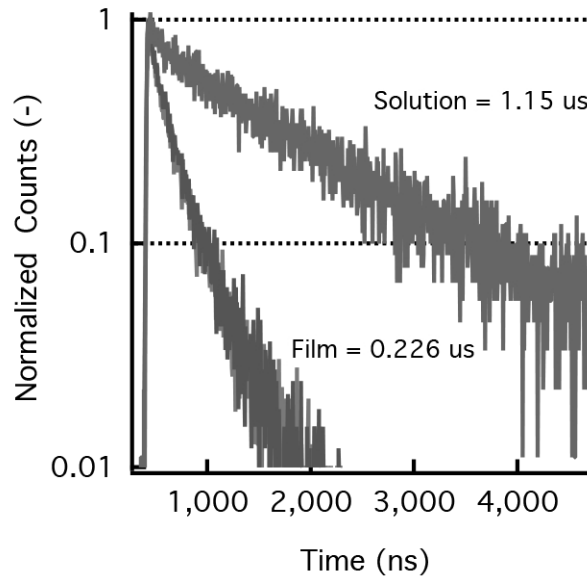


Figure 8.16: Decay of spontaneous emission of a 4.3 nm PbS close-packed layer on glass (blue) and silicon compared to the solution case.

$B_{12}$  (and  $B_{21}$ ), requiring also  $A_{21}$  to increase, *i.e.* by increasing the rate of spontaneous emission. We observe this effect in a monolayer of 4.3 nm PbS QDs deposited on glass or silica (glass) substrates as is shown in Figure 8.16 where the comparison between decay in close-packed film and in solution is presented. A clear reduction (up to 5) in the spontaneous emission lifetime is observed, both on glass and silicon. The latter indicates that the type of substrate (high or low refractive index) does not influence the lifetime.

#### 8.7.4 Phonon Dipolar Coupling

Just as is the case for frequencies resonant with the electronic interband excitations (typically NIR-VIS), one could also envisage electrostatic coupling in different frequency ranges such as the far infrared where the polarizability of semiconductors (e.g. nanocrystals) is determined by phonon oscillations and free carrier motion instead of electronic oscillations.

The typical dielectric function (*i.e.* response to an external driving field) of a semiconductor in the phonon-dominated far-infrared is given by :

$$\epsilon(\omega) = \epsilon_{phonon}(\omega) + \epsilon_{freecarrier}(\omega) \quad (8.21)$$

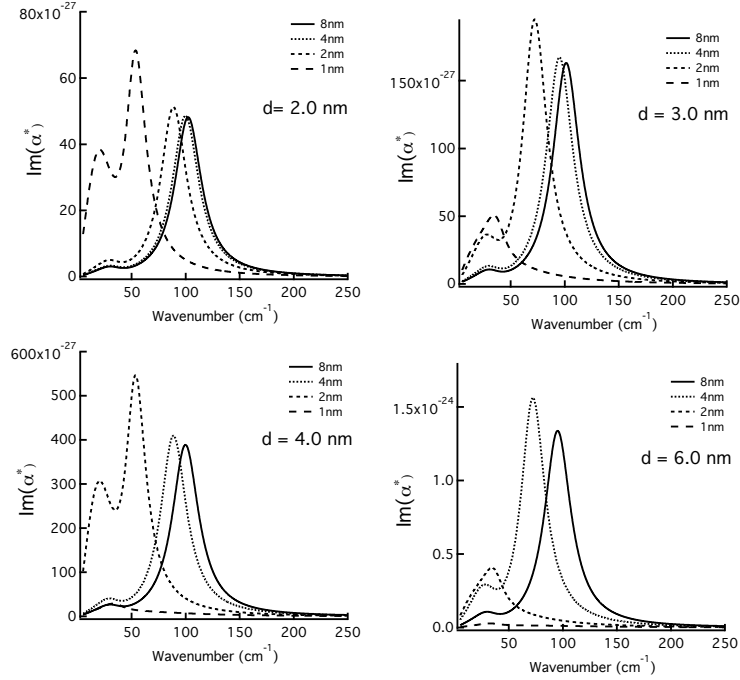


Figure 8.17: Imaginary part of the coupled polarizability for different sizes ( $d$ ) of PbSe and different ligand lengths  $l$  (8,4,2 and 1 nm). Note that the interparticle spacing is  $d + 2 \times L$

which can be written as :

$$\epsilon(\omega) = (\epsilon_0 - \epsilon_\infty) \frac{\omega_{TO}^2}{\omega_{TO}^2 - \omega^2 - i\Gamma\omega} - \frac{\omega_p^2}{\omega^2 + i\gamma\omega} + \epsilon_\infty \quad (8.22)$$

The coupling can be expressed through a near-field dipolar sum  $S$ , modifying the uncoupled polarizability  $\alpha_0$  to:

$$\alpha^* = \frac{\alpha_0}{1 - \alpha_0 \times S} \quad (8.23)$$

We study the imaginary part of this quantity as function of PbSe size and separation (expressed through ligand length). A clear effect is seen on the surface phonon mode, whereas the TO mode is not really affected.

## 8.8 Conclusion

We have demonstrated strong optical coupling phenomena in close packed monolayers of colloidal QDs, leading to giant enhancement of the absorbance per QD up to a factor of 5. The influence of the layer geometry (particle size and composition, ligand length), wavelength and polarization state were investigated. The results can be explained and quantified using a dipolar coupling model. On top of the cheap bottom-up fabrication and processing, a collective property like absorption enhancement makes colloidal QDs extremely suited for applications in photovoltaics and photo-detection, where a trade-off between layer thickness and light absorption restricts conversion efficiencies. The model presented here provides a general framework to further study the optical properties of the simple superlattices analysed here, where key questions are the difference between *s* and *p* polarized light and the impact optimal coupling has on the radiative lifetime. Moreover, it gives a basis to understand the optical properties of more complex, possibly hybrid superlattices, *e.g.*, containing nanocrystals of different sizes or different materials and even modifications of phononic effects at much longer wavelengths are predicted theoretically.

## References

- [1] Talapin, D. V.; Shevchenko, E. V.; Bodnarchuk, M. I.; Ye, X.; Chen, J.; Murray, C. B. Quasicrystalline order in self-assembled binary nanoparticle superlattices. *Nature* **2009**, *461*, 964–7.
- [2] Jensen, T.; Kelly, L.; Lazarides, A.; Schatz, G. C. Electrodynamics of Noble Metal Nanoparticles and Nanoparticle Clusters. *Journal of Cluster Science* **1999**, *10*, 295–317.
- [3] Zhao, L.; Kelly, K. L.; Schatz, G. C. The Extinction Spectra of Silver Nanoparticle Arrays: Influence of Array Structure on Plasmon Resonance Wavelength and Width. *The Journal of Physical Chemistry B* **2003**, *107*, 7343–7350.
- [4] Bogaart, E. W.; Haverkort, J. E. M. Anomalous exciton lifetime by electromagnetic coupling of self-assembled InAs/GaAs quantum dots. *Journal of Applied Physics* **2010**, *107*, 064313.
- [5] Yin, Y.; Alivisatos, P. Colloidal nanocrystal synthesis and the organic-inorganic interface. *Nature* **2005**, *437*, 664–70.

- [6] Shevchenko, E. V.; Talapin, D. V.; Kotov, N. a.; O'Brien, S.; Murray, C. B. Structural diversity in binary nanoparticle superlattices. *Nature* **2006**, *439*, 55–9.
- [7] Dong, A.; Ye, X.; Chen, J.; Murray, C. B. Two-Dimensional Binary and Ternary Nanocrystal Superlattices : The **2011**, 1804–1809.
- [8] Talapin, D. V.; Shevchenko, E. V.; Murray, C. B.; Titov, A. V.; Kral, P. Dipole-dipole interactions in nanoparticle superlattices. *Nano letters* **2007**, *7*, 1213–9.
- [9] Overgaag, K.; Liljeroth, P.; Grandidier, B.; Vanmaekelbergh, D. Scanning tunneling spectroscopy of individual PbSe quantum dots and molecular aggregates stabilized in an inert nanocrystal matrix. *ACS Nano* **2008**, *2*, 600–6.
- [10] Chen, J.; Dong, A.; Cai, J.; Ye, X.; Kang, Y.; Kikkawa, J. M.; Murray, C. B. Collective Dipolar Interactions in Self-Assembled Magnetic Binary Nanocrystal Superlattice Membranes. *Nano letters* **2010**, *10*, 5103–5108.
- [11] Justo, Y.; Moreels, I.; Lambert, K.; Hens, Z. Langmuir-Blodgett monolayers of colloidal lead chalcogenide quantum dots: morphology and photoluminescence. *Nanotechnology* **2010**, *21*, 295606.
- [12] Lambert, K.; Capek, R. K.; Bodnarchuk, M. I.; Kovalenko, M. V.; Van Thourhout, D.; Heiss, W.; Hens, Z. Langmuir-Schaefer deposition of quantum dot multilayers. *Langmuir* **2010**, *26*, 7732–6.
- [13] Sargent, E. H. Infrared photovoltaics made by solution processing. *Nature Photonics* **2009**, *3*, 325–331.
- [14] Clifford, J. P.; Konstantatos, G.; Johnston, K. W.; Hoogland, S.; Levina, L.; Sargent, E. H. Fast , sensitive and spectrally tuneable colloidal- quantum-dot photodetectors. *Nature Nanotechnology* **2009**, *4*, 40–44.
- [15] Moreels, I.; Lambert, K.; Smeets, D.; De Muynck, D.; Nollet, T.; Martins, J. C.; Vanhaecke, F.; Vantomme, A.; Delerue, C.; Allan, G.; Hens, Z. Size-dependent optical properties of colloidal PbS quantum dots. *ACS Nano* **2009**, *3*, 3023–30.
- [16] Karel Capek, R.; Moreels, I.; Lambert, K.; De Muynck, D.; Zhao, Q.; Van Tomme, A.; Vanhaecke, F.; Hens, Z. Optical Properties of

- Zincblende Cadmium Selenide Quantum Dots. *The Journal of Physical Chemistry C* **2010**, *114*, 6371–6376.
- [17] Jackson, J. *Classical Electrodynamics*, 3rd ed.; Wiley, 1999.
- [18] Haynes, C. L.; McFarland, A. D.; Zhao, L.; Van Duyne, R. P.; Schatz, G. C.; Gunnarsson, L.; Prikulis, J.; Kasemo, B.; Käll, M. Nanoparticle Optics: The Importance of Radiative Dipole Coupling in Two-Dimensional Nanoparticle Arrays . *The Journal of Physical Chemistry B* **2003**, *107*, 7337–7342.
- [19] Moreels, I.; Allan, G.; De Geyter, B.; Wirtz, L.; Delerue, C.; Hens, Z. Dielectric function of colloidal lead chalcogenide quantum dots obtained by a Kramers-Krönig analysis of the absorbance spectrum. *Physical Review B* **2010**, *81*, 1–7.



# 9

## Functionalizing Silicon Photonics with Colloidal Nanocrystals

### 9.1 Introduction

A suitable platform to combine the strength of photonic integration with that of solution processable photonic materials such as colloidal nanocrystals (QDs) is found in silicon photonics, more specifically the 'silicon-on-insulator' platform (SOI). SOI relies on the manufacturing backbone of modern CMOS to achieve cost-effective and compact on-chip photonic circuits with diverse functionalities. Although several of these are readily built on silicon (light guiding and passive routing/filtering), some highly desired features such as modulation and generation of light remain difficult. Hybridization of the SOI platform with novel materials is therefore considered a possible route to complete the photonic toolbox<sup>1;2</sup>.

In this chapter, we will demonstrate the potential of hybridising silicon photonics with QDs through numerical simulations and experiments. We demonstrate the ability of QDs to interact with the optical modes of both standard SOI waveguides and more advanced microcavities. Finally we evaluate the potential for integrating QDs with functional metal-oxides (*e.g.* as charge-injecting layers) using atomic-layer deposition.

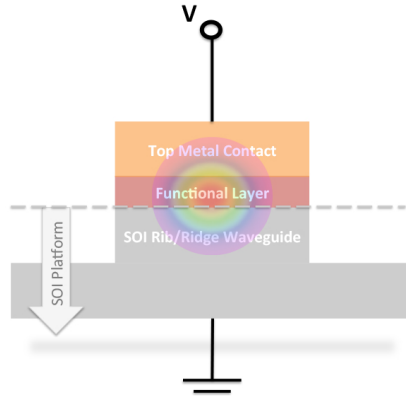


Figure 9.1: Generic structure considered for the simulations: functional layer (*e.g.* QDs squeezed between two conductive metal-oxides for an LED) on the SOI platform (rib or ridge silicon waveguide on silica) and a top electrical contact.

## 9.2 Hybrid Plasmonic-Dielectric Waveguides

In order to combine colloidal nanocrystals with silicon photonics (*i.e.* hybridize SOI), we investigated<sup>3</sup> the route of so-called hybrid plasmonic-dielectric waveguides<sup>4-7</sup>. Combining metals with dielectrics offers the advantage of high light confinement (due to plasmonic boundary effects at the metal-dielectric interface) with possibility of electrical contacting, a necessity for any opto-electronic device.

We consider a generic structure (see Figure 9.1) that could be used for light modulation<sup>8,9</sup>, detection and generation<sup>10,11</sup> (*e.g.* for integrated LEDs or lasers). A stack of functional layers (*e.g.* nanocrystals with insulating or transparent conductive oxides (TCO's) as cladding for electrical excitation<sup>12-14</sup>) is put on a standard silicon rib or ridge waveguide. An electrical top contact is added to provide light confinement much as a standard slot waveguide, with the added benefit of easy electrical contacting.

Due to strict boundary conditions imposed by Maxwell's equations, the metal-dielectric stack provides a so-called *slot mode* where light is confined to the region between the high index silicon waveguide and the top metal (see Figure 9.2), *i.e.* in the functional layer where high field intensity is required. We find that such a hybrid metal-dielectric slot waveguide offers a good compromise between plasmonic (metal induced, often lossy) and dielectric (lossless) confinement. Moreover, a possibility of electri-

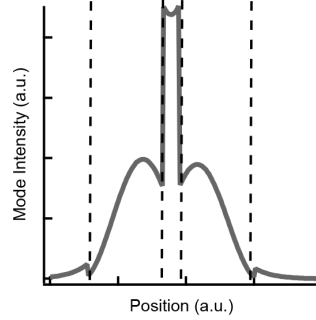


Figure 9.2: Normalized power density in a silicon-silica-silicon slot waveguide showing the 'slot' effect (*i.e.* an enhanced field intensity in the slot layer) due to discontinuity in the dielectric constants of silicon and silica.

cal contacting is a substantial benefit as it could be used to enable electrically addressable colloidal nanocrystals or other functional materials (*e.g.* transparent conductive oxides (TCO) such as ITO (Indium-Tin-Oxide) or zinc-oxide) onto the SOI platform.

### 9.2.1 Simulations

We used a commercial Finite-Element package (COMSOL MultiPhysics 3.5) to obtain the eigenmodes of the hybrid plasmon-dielectric waveguides. COMSOL solves the Helmholtz wave equation in 2 dimensions (transverse solutions, invariant in the propagation direction) to obtain the complex propagation constants (through the complex effective index) of the optical modes. In practice, the mode profile and the complex effective index  $n_{eff}$  are retrieved and used to evaluate the optical confinement in the active layer and the propagation loss respectively.

**Propagation Loss** The two main loss mechanisms for mode propagation are light absorption (*e.g.* due to metals) and scattering (*e.g.* through waveguide roughness). In its simplest form, the propagation of the electric field  $E$  (in a scalar form) along a direction  $x$  is described using the expression (see chapter 2):

$$E(x) = E(0)e^{ik_{eff}x} = E(0) \times e^{-\frac{2\pi}{\lambda_0}n_{eff,r}x} \times e^{-\frac{2\pi}{\lambda_0}n_{eff,i}x} \quad (9.1)$$

where  $k_{eff} = \frac{2\pi n_{eff}}{\lambda_0}$  was used. In general, the effective index will be a complex number  $n_{eff} = n_{eff,r} + in_{eff,i}$ , combining both propagation

(through  $n_{eff,r}$ ) and extinction (through  $n_{eff,i}$ ). The propagation length of an optical mode with free space wavelength  $\lambda_0$  is defined as the length over which the mode should propagate to experience an extinction of  $1/e^2$  in power density (proportional to  $|E|^2$ , note that this corresponds to  $1/e$  in the electric field  $E$ ) and can be written as:

$$L_p = \frac{4\pi n_{eff,i}}{\lambda_0} (= 1/\alpha_m) \quad (9.2)$$

**Nanocrystals under effective medium approach** For simplicity, the nanocrystal layer was modeled as a layer with a refractive index  $n$  of 2, similar to the surrounding dielectrics. This corresponds quite well to the Maxwell-Garnett value for  $n$ , leaving out the QD absorption (*i.e.*  $n$  is real). The latter is justified since we are looking at the spontaneous emission that is Stokes-shifted from the linear absorption, effectively reducing self-absorption of the emitted light. A more advanced approach could make use of the actual complex refractive index of the QDs, calculated *e.g.* through Kramers-Kronig analysis of the absorption spectrum, as was shown by Moreels *et al.*<sup>15</sup>.

**Spontaneous Emission Enhancement** To study the effect of QD spontaneous emission coupling to the hybrid waveguides, we invoke the Purcell factor  $F_p$ <sup>16</sup>:

$$F_p = \frac{3}{4\pi^2} \lambda^2 \frac{Q}{V_m} \quad (9.3)$$

which expresses the ratio between the rate of spontaneous emission of an emitter (placed at the field maximum) in the cavity relative to free space:  $F_p = \frac{k_{sp,cav}}{k_{sp,free}}$ . The Q-factor (quality factor) is a measure of the cavity quality as it can be seen as the number of oscillations of the (electric) field (before extinguishing by  $1/e$ ) created by a short excitation inside the cavity. As such, higher Q values correspond to higher quality cavities with the ability to confine light for longer periods. The Q of the total system (emitter and cavity) can be limited by the emitter  $Q_{em}$  (*e.g.* emitter with a wide (in)homogeneously broadened spectrum) or by the cavity  $Q_{cav}$ . In practice, using the 'worst' Q is appropriate in the expression for  $F_p$ <sup>16</sup> or in general:  $1/Q = 1/Q_{cav} + 1/Q_{em}$ .

In 2D, this Purcell factor can be rewritten as function of an effective area (instead of volume)<sup>17;18</sup>:

$$F_{p,2D} = \frac{3}{4\pi} \frac{c/n}{v_g} \frac{(\lambda_0/n)^2}{A_{eff}} \quad (9.4)$$

We can calculate the effective area as:

$$A_{eff} = 1/2 \iint \left\{ \epsilon_0 \frac{d(\epsilon\omega)}{d\omega} |E(\mathbf{r}, \omega)|^2 + \mu_0 |H(\mathbf{r}, \omega)|^2 \right\} d\mathbf{r} / (\epsilon\epsilon_0 |E(\mathbf{r}_e, \omega)|^2) \quad (9.5)$$

In this expression,  $E(\mathbf{r}_e, \omega)$  is the electric field at the position of the emitter,  $\epsilon$  is the permittivity (note that this is in general a quantity depending on both frequency and position) and  $\epsilon_0$  is the permittivity of vacuum.

**Figure of Merit** We will define a 'transparency gain'  $G$  as the modal gain required to compensate the loss of the cavity (dominated by material loss  $\alpha_m$ ), without mirror losses<sup>19</sup>:

$$G = \Gamma \times \alpha_m (= \Gamma/L_p) \quad (9.6)$$

where  $\Gamma$  is the mode confinement factor and  $L_p$  is the propagation length of the optical mode. Note that the real transparency gain will be higher as even highly reflective mirrors leak photons out of the cavity.

## 9.2.2 Hybrid structures

A variety of hybrid structures were considered, varying the contact type (metal or amorphous Si (a:Si)): the metal - dielectric - silicon (MDSi), silicon - dielectric - silicon (SiDSi) and the metal - dielectric - metal (MDM).

**MDSi** The first order guided mode in this structure is a quasi-TM mode with electric field mainly in the y-direction (orthogonal to the device plane) and magnetic field in the x-direction. The obtained propagation length and confinement factors for varying waveguide width and slot thickness are shown in Figure 9.3. Lower transparency gain is obtained for wider structures with thinner gaps. However, increasing the waveguide width will eventually make the structure multi-modal, with acrossover at around 300 nm in width. The optimum  $F_p$  of 7.1 is obtained for a 300 nm wide waveguide with 60 nm slot thickness.

**SiDSi** The use of metals implies large optical losses and as such, other materials should be considered for electrical contacting. Amorphous silicon (a:Si) is a good candidate as it can be deposited using (PE-)CVD under relatively mild conditions (low temperature and plasma power) compatible with the QD layers underneath. Recent reports show the potential of a:Si to extract carriers from CdSe QDs in a photovoltaic device<sup>20</sup> or generate light in an LED configuration<sup>21</sup>.

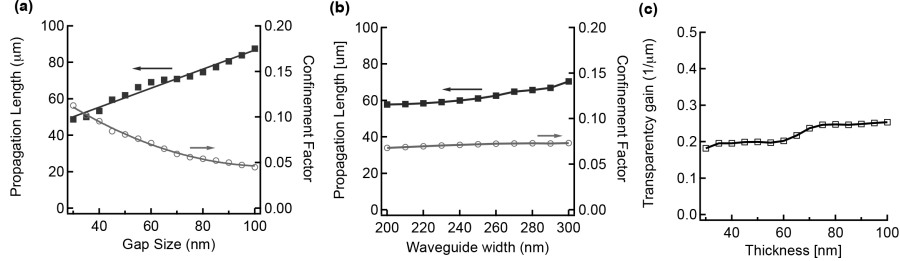


Figure 9.3: Simulation output for metal-dielectric-ridge configuration: (a) Propagation length and confinement factor as function of gap size for a waveguide width of 200 nm and (b) the same quantities for varying waveguide width with fixed gap of 60 nm. (c) Transparency gain in  $1/\mu\text{m}$  FOM for varying gap size (again with fixed 200 nm waveguide width).

Amorphous silicon has little intrinsic loss in the near-infrared, especially compared to common metals as gold or silver. As such, the main loss channel is scattering from surface roughness. This is evidenced from Figure 9.5a where the loss induced by both absorption (intrinsic loss) and scattering ( $\alpha_s$ ) is presented. The confinement factor is dependent on the top slab thickness (see Figure 9.5b) where an optimum around 200 nm is found. We can understand this by looking at Figure 9.5c where we see a clear change of mode profile with increasing slab thickness.

The influence of scattering from an interface of two dielectrics A and B is taken into account using the following expression:

$$\alpha_s = \frac{\sigma^2 k_0^2 h}{\beta} \times \frac{E_s^2}{\int E^2 dx} \times \Delta n^2 \quad (9.7)$$

where  $\Delta n$  is the refractive index difference between layer A and B,  $E_s$  is the surface electric field,  $\sigma$  is the standard deviation of the roughness (taken here as 0.5 nm from AFM measurements) in nanometer and  $\beta$  is the real part of the mode propagation constant.

**All metallic slot waveguides (MDM) for integrated plasmonics** In recent years the use of surface plasmons polaritons (SPPs) has gained much interest due to the potentially denser integration (no diffraction limit) and intricate plasmonic field enhancement effects (*e.g.* for sensing). SPPs are electromagnetic modes caused by interaction of TM polarized light with mobile surface electrons in the metals (or more generally 'conductors') that support them. For example, it has been shown that silicon nanocrystals in

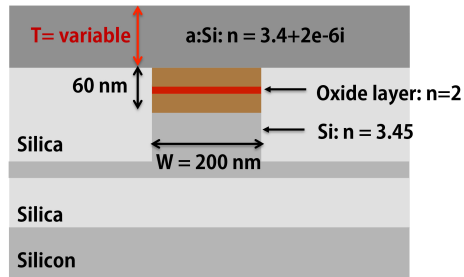


Figure 9.4: Schematic showing the use of amorphous silicon (a:Si) as the top contact instead of a metal.

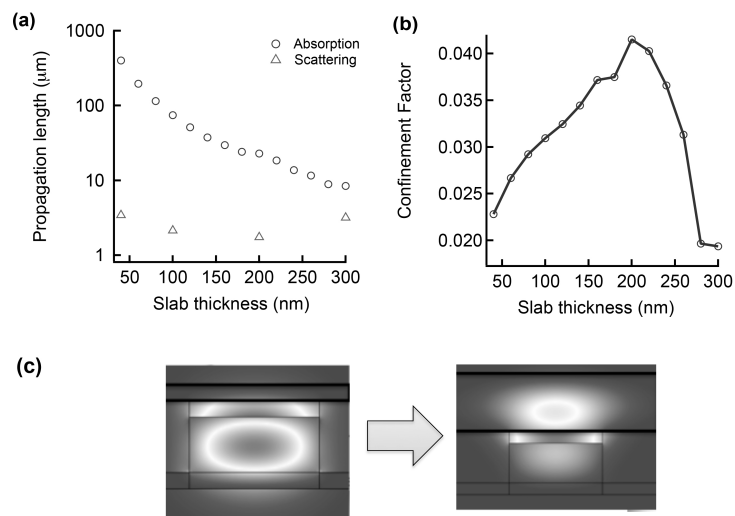


Figure 9.5: Propagation length (limited by light scattering at the many interfaces, and not by absorption as is the case for the metal caps) (a) and confinement factor (b) for the waveguide geometry shown in Figure 9.4.

(c) For increasing top silicon slab thickness (beyond *ca.* 200 nm), the optical mode jumps from the core waveguide to the top slab.

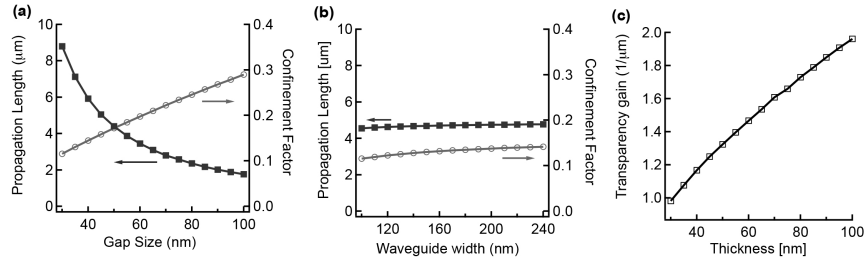


Figure 9.6: Simulation output for metal-dielectric-metal configuration: (a) Propagation length and confinement factor as function of gap size for a waveguide width of 200 nm and (b) the same quantities for varying waveguide width with fixed gap of 60 nm. (c) Transparency gain in  $1/\mu\text{m}$  FOM for varying gap size (again with fixed 200 nm waveguide width).

a metal-dielectric-metal (MDM) waveguide can be electrically excited and serve as an efficient source for SPPs<sup>22</sup>. Similar configurations were used by Melikyan *et al.*<sup>23</sup> to modulate light in extremely small footprint devices.

In our structure, we squeeze a nanocrystal-oxide stack between two metal plates: a silver cathode and gold anode. These two metals are generic, a wide variety of other conductors could be used for this purpose. The refractive index of the gold and silver (at a wavelength of  $1.55 \mu\text{m}$ ) are fixed at  $0.56 + 9i$  and  $0.14 + 11.36i$  respectively. The refractive index of both the oxides and the nanocrystal layer was fixed at  $n = 2$ . Hybrid mode analysis yielded a quasi-TM first order mode with high mode confinement in the slot layer. Varying both width and gap size (see Figure 9.6), we find that high confinement factors are accompanied by higher loss, yielding an overall increase of the transparency gain figure-of-merit. Such high transparency gains could be reached by epitaxial materials (e.g. III-V), whereas colloidal nanocrystals probably fall short in this respect.

Although lasing seems elusive with these structures, the spontaneous emission enhancement  $F_p$  reaches values up to 33.9, indicating the potential for compact and efficient light emitting diodes. As such, the results presented here give a first indication of the potential of NCs for integrated plasmonics.

**Conclusion** Table 9.1 summarizes the main parameters for the considered hybrid waveguide configurations<sup>3</sup>. The combination of a metal cap (e.g. silver) as cathode with a silicon waveguide as anode seems a good route to follow if the material gain provided by colloidal QDs can be sufficiently large. If the gain provided by the QDs is lower than roughly  $1000 \text{ cm}^{-1}$  (as

Cathode	Silver	Silver	a:Si
Anode	Gold	Si	Si
Confinement (%)	13.8	7.8	4.93
Propagation Length ( $\mu\text{m}$ )	4.9	51	6800
Transparency Gain ( $\text{cm}^{-1}$ )	$1.5 \cdot 10^4$	2500	30
Purcell factor (-)	34	8.9	5.8

Table 9.1: Overview of relevant parameters for different hybrid waveguide configurations.

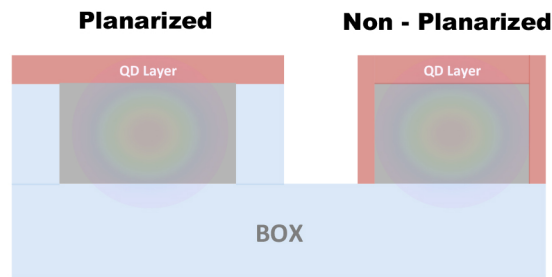


Figure 9.7: Difference between planarized and non-planarized (strip) silicon single-mode waveguides coated with QDs (red) on top of a buried oxide layer (BOX).

is the case for HgTe QDs), a route with a:Si seems more suitable.

### 9.3 Colloidal Nanocrystals on SOI Waveguides

A key question on combining colloidal nanocrystals with silicon photonics is whether the nanocrystals can interact with the optical modes of the SOI platform. Typical single mode waveguides confine the optical mode to the silicon core with high confinement and low optical loss<sup>24</sup> (see also Figure 9.8b). However, some part of the mode leaks into the environment (the so-called evanescent 'tail') allowing interaction with materials deposited on the waveguide. We studied two types of waveguides<sup>25;26</sup>: planarized rib waveguides and regular rib waveguides. Near-infrared active PbS/CdS core/shell nanocrystals are patterned on top of these waveguides through a combination of subsequent Langmuir-Blodgett depositions<sup>27</sup> and optical lithography.

**Planarized Waveguides** Planarized SOI waveguides start from the basic rib waveguide geometry but have an additional lateral cladding of silica ( $\text{SiO}_2$ ). The top surface is flat (see Figure 9.7), such that a layer of QDs is deposited in a layer-by-layer fashion, much as would be the case on any other flat substrate (see Figure 9.8a). The optical mode (see Figure 9.8b) can only interact with the quantum dots through the top part of the waveguide, as opposed to the regular rib waveguides (see further) where also lateral interaction is possible. Therefore, the planarized waveguide is a model system to understand the geometrically more complex standard rib waveguide.

The absorption coefficient of planarized SOI waveguides coated with close packed mono- and multilayers of colloidal PbS/CdS quantum dots (QDs) was determined through a series of power transmission experiments<sup>25</sup>: light is coupled in and out of the waveguides through grating couplers and the transmission loss is measured as function of the nanocrystal coverage (*i.e.* interaction length). The experimental data (see Figure 9.8c) clearly show the influence of the QDs on the waveguide absorbance around 1500 nm, where we find that QDs absorb stronger in thicker layers. To simulate the absorption coefficient  $\alpha_{QD}$  of QD functionalized waveguides, the QD layer is replaced by an effective medium with a dielectric function determined by dipolar coupling between neighbouring QDs ('coupled dipole' model from chapter 8):

$$\epsilon_{eff} = \epsilon_h \epsilon_0 \left( 1 + \frac{N_s}{L_t} \frac{a_{QD}}{1 - a_{QD} S} \right) \quad (9.8)$$

where  $L_t$  is the layer thickness and  $N_s$  the surface density of QDs.  $a_{QD}$  is the (complex) QD polarizability and  $S$  is the dipole sum (see Chapter 8).  $N_s$  is determined from SEM and TEM analysis. Using the host dielectric constant  $\epsilon_h$  as an adjustable parameter, excellent agreement with the experimental results is obtained (see Figure 9.8b, right tab). In this way, the increase in absorption cross section with layer thickness can be traced back to an increasing  $\epsilon_h$ . We argue that this reflects the decreasing influence of the surroundings on the  $\epsilon_h$  which therefore evolves from an extrinsic property for monolayers to a more intrinsic film property for multilayers.

**Strip waveguides** Through the analysis of the planarized waveguides, we demonstrated that (1) QDs interact with the optical modes of the SOI platform and (2) we can model their interaction with a coupled dipole (CD) model. Next, the geometrically more complex standard rib waveguide was studied<sup>26</sup>. In this case, the nanocrystals cover both the top surface and part

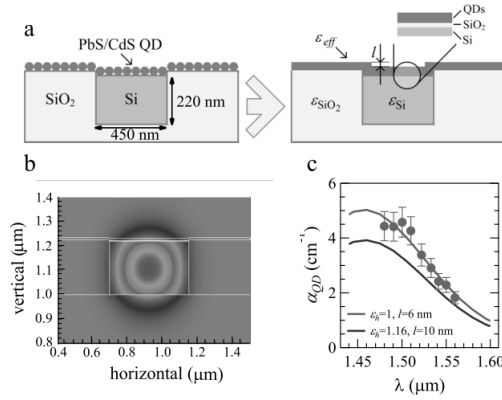


Figure 9.8: (a) Cartoon representation of the replacement of the QD film on top of an SOI planarized waveguide by an effective medium. (b) Cross-sectional representation of the simulated electric field for 1520 nm light guided by a waveguide coated by a QD monolayer. (c) Comparison of the experimental and simulated  $\alpha_{QD}$  QD absorbance spectrum of a QD coated waveguide for two different combinations of  $l$  and  $\epsilon_h$ .

of the sidewalls of the waveguide. Again the absorbance of the QDs is retrieved and modeled quite well with the CD model, indicating the validity of the model to study QD-waveguide interactions.

Having shown that the absorption of the QDs influences the optical modes, another linear property of QDs should be investigated: spontaneous emission (SE). Coupling this SE to the waveguide modes should be possible as was shown by other authors<sup>1,2</sup> and is a first step towards a fully integrated QD light source on silicon. We have simulated the coupling efficiency  $\eta$  of a QD (modeled as an oscillating dipole 5 nm above the waveguide top surface (a)/side wall (b) and averaged over all dipole orientations) for our standard rib waveguides. The results are shown in Figure 9.9: roughly 25 % of the emitted light will couple to the optical mode for this basic geometry. Correcting for quantum yield (QY) and one-sided facet out-coupling (a factor of 1/2 as light is only collected from one facet), this amounts to maximum 5% of extraction efficiency. Combined with the overall low power emitted by a mono - or multilayer of QDs (typically a few nW at best), the extraction and detection of generated light (*e.g.* through optical pumping) of QD monolayers (and even multi-layers) is quite difficult, especially in the near-infrared (where less sensitive detectors are available). Recent efforts

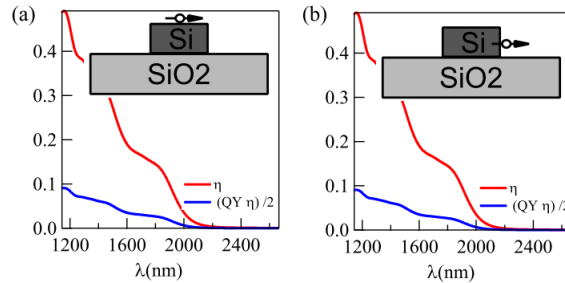


Figure 9.9: (a) Coupling efficiency  $\eta$  and  $\eta QY/2$  as a function of the wavelength for a dipole oscillator located 5 nm away from the top waveguide surface. (b) Wavelength dependency of  $\eta$  and  $\eta QY/2$  for a dipole oscillator located 5 nm from the edge WG-surface.

have shown this is possible in the visible with silicon-nitride waveguides covered with VIS emitting CdSe/CdS QDs<sup>28</sup>. More advanced geometries such as slot waveguides or ring resonators should allow for more interaction between the QDs and the optical modes, resulting in higher extraction efficiency of the QD spontaneous emission.

**Conclusion** We have shown that QDs interact with the optical modes of the SOI platform and have modeled the absorption of QD functionalized (planarized) rib waveguides, providing a toolbox to model other hybrid QD systems (slot waveguides, silicon nitride waveguides, microcavities, ...). The next step is to demonstrate coupling of SE in the near-infrared and to demonstrate non-linear QD properties (such as optical gain, wavelength conversion, ...) on-chip.

## 9.4 Microcavities

Confining optical modes to small volumes with high quality factors (so-called  $Q$ -factors) is a research field in its own right<sup>29</sup>. A wide variety of devices was demonstrated in recent years such as photonic crystals<sup>30–32</sup>, holey waveguides<sup>33</sup>, distributed feedback cavities<sup>34;35</sup>, plasmonic cavities<sup>8;36;37</sup>, ... To quantify the performance of a photonic cavity (or feedback structure), two quantities are important: the quality factor  $Q$  and the (effective) mode volume  $V_m$ . The former expresses the intrinsic quality of the structure, both in confining the light (radiative  $Q$ ) and its defects (usually light scattering from structural defects (*e.g.* edge roughness)). The latter relates

directly to the volume the optical mode occupies and is usually normalized to the cubic wavelength  $\lambda_0/n$  (with  $n$  the refractive index of the medium),  $V_{m,norm} = V_m/(\lambda_0/n)^3$ .

These quantities are elegantly combined in the Purcell factor  $F_p$ :

$$F_p = \frac{3}{4\pi^2} \lambda^3 \frac{Q}{V_m} \quad (9.9)$$

which expresses the ratio between the rate of spontaneous emission of an emitter (placed at the field maximum, in a host dielectric) in the cavity relative to free space (filled with a material of the same dielectric constant as the host):  $F_p = \frac{k_{sp,cav}}{k_{sp,free}}$ . The Purcell factor is combined into a 'spontaneous emission coupling factor'  $\beta$ , which expresses how much of the spontaneously emitted light contributes to a specific cavity mode, a relevant quantity for lasing thresholds.

$$\beta = \frac{F_p}{1 + F_p} \quad (9.10)$$

In this thesis two approaches were explored (in strong collaboration with other researchers<sup>1</sup>) with varying  $Q$  and  $V_m$ :

- DBR cavities: Moderate  $Q$  ; large  $V_m$
- Nitride Microdisks: Moderate  $Q$  ; moderate  $V_m$

#### 9.4.1 DBR cavities

A distributed Bragg reflector (DBR) consists of pairs of alternating layers of high ( $n_H$ ) and low ( $n_L$ ) refractive index dielectric materials (*e.g.* amorphous silicon (a:Si) and silicon oxide (SiO<sub>2</sub>), each a quarter wavelength ( $\lambda_0/n$ ) thick. The destructive interference between subsequent reflections on the alternating layers creates a so-called stop-band<sup>38</sup>: a spectral region of width  $\Delta\lambda$  where no light passes through, *i.e.* the DBR acts as a dielectric mirror but without the losses associated with the use of metals.

An approximate expression for the width of the stop-band is given by:

$$\frac{\Delta\lambda}{\lambda_0} = \frac{4}{\pi} \text{asin}\left(\frac{n_H - n_L}{n_H + n_L}\right) \quad (9.11)$$

The cavity length  $L$  and mirror reflectivity  $R$  will determine the mode spacing (or free spectral range (FSR)) and  $Q$  factor of the cavity, as the threshold gain  $g_{th}$  (neglecting cavity loss) for optical pumping:

<sup>1</sup>Dr. ir. Bram de Geyter, Dr. ir. Abdoulghafar Omari

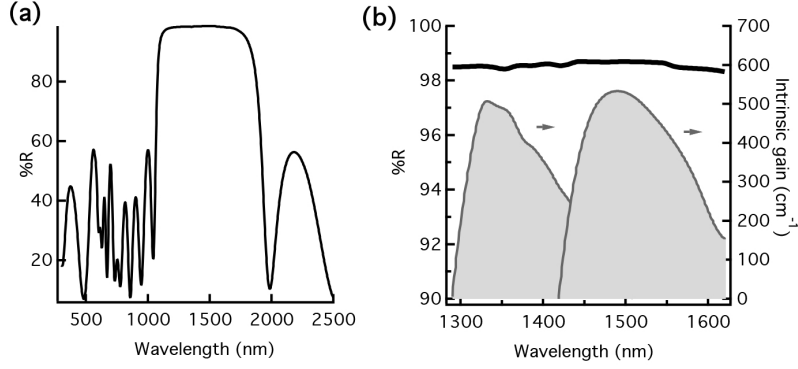


Figure 9.10: Overview of DBR cavities (a) Reflection of a 5-pair a:Si/SiOx DBR under 8 incidence. A clear stopband is observed of ca. 600 nm wide covering the entire telecom OESCL band. (b) Zoom of the stop band (giving up to 98.6% reflection over 600 nm) plotted with the intrinsic gain spectrum of 2 sizes of HgTe QDs (see also chapter 7).

$$g_{th} = \frac{\ln(\frac{1}{R})}{L} \quad (9.12)$$

$$FSR = \frac{\lambda^2}{2n_g L} \quad (9.13)$$

where  $n_g$  is the group index of the cavity medium (*e.g.* QDs with  $n_g \simeq 1.8$ ) and  $\lambda$  is the wavelength. The Q factor can be obtained as:

$$Q = \frac{2\pi n_g L}{\lambda} \frac{\sqrt{R}}{1-R} \quad (9.14)$$

For a cavity length of 50  $\mu\text{m}$  and a mirror reflection  $R = 0.98$ , this results in:  $g_{th} = 4\text{cm}^{-1}$  and a Q-factor of 20700. Note that these gain values should be achievable with HgTe QDs (see chapter 7) where 100  $\text{cm}^{-1}$  is achieved under close packing conditions of the QD film.

#### 9.4.2 Microdisks

The incorporation of colloidal QDs in dielectric microcavities was investigated using silicon-nitride (pillar-supported) microdisks<sup>39</sup>, fabricated through plasma-enhanced CVD (PE-CVD). These cavities offer moderate Q-factors (300-600) and mode volumes  $V_m$  (10-100  $\lambda^3$ ), resulting in Purcell factors

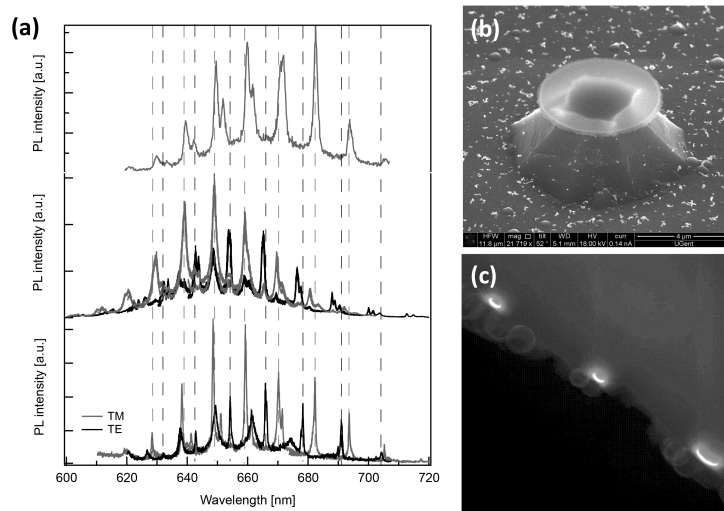


Figure 9.11: (a) TE (transverse electric) and TM (transverse magnetic) spectra of three  $6.5 \mu\text{m}$  disks (same sample) after  $532 \text{ nm}$  continuous wave (CW) excitation. (b) SEM micrograph of a microdisk and (c) Confocal microscope image of the disks under CW excitation.

of  $\approx 10$ . From fabrication point of view, a process was developed to incorporate QDs in insulating silicon-nitride matrices (see Figure 9.12), a platform that is now extended to linear nitride waveguides enhanced with QDs to achieve functional waveguides, *e.g.* for on-chip electroluminescence.

## 9.5 Incorporation of Nanocrystals in Functional Oxides

The potential use of QDs in electronic or electro-optic devices relies greatly on the ability to embed them into a functional host material. Indeed, isolated QDs serve no purpose as charge carriers cannot be extracted or created, unless through all-optical means (*e.g.* wavelength conversion). For example, a solar cell with QDs as absorbers requires the extraction of photogenerated electrons and holes. Vice versa, a light emitting diode (LED) based on QDs as phosphors typically requires either direct injection of charge or high field biasing, requiring n and p-type conductive layers or insulating layers around the QDs respectively.

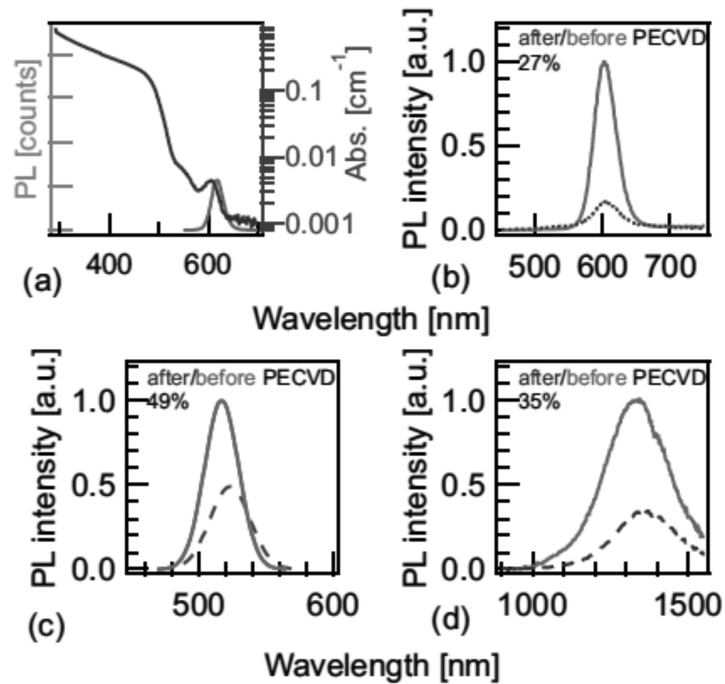


Figure 9.12: (a) Photoluminescence (PL) after 400 nm excitation (red) and absorption (blue) spectrum of 12 nm giant CdSe/CdS QDs used in the microdisk experiment shows the 12 nm Stokes shift between absorption and emission. (b) PL spectrum of spincoated CdSe/CdS QDs before (red) and after (blue) deposition of low-temperature silicon nitride shows that 27% of the emission remains after  $\text{Si}_3\text{N}_4$  deposition. (c) A similar experiment for type I CdSe/ZnS QDs illustrates that 49% of the PL remains after deposition, indicating the importance of a surface passivating layer (here ZnS) (d) Also for type I near-infrared emitting PbS/CdS QDs 35% of the PL is recovered after nitride deposition.

A potential route is the incorporation of QDs in so-called 'functional oxides': metal-oxides with controlled insulating, n or p-type charge conduction with sufficient optical transparency to serve in photonic devices. As opposed to organic host materials, oxides offer great tunability, higher carrier mobilities and increased stability under high external bias and/or current density. They are also able to withstand higher temperatures and are typically less prone to degradation under ambient conditions. Several routes were investigated during this thesis work to deposit these (metal-)oxides such as PE-CVD, DC (and RF) magnetron sputtering and atomic layer deposition (ALD). ALD was found to be the best candidate<sup>40</sup> as it offers mild deposition conditions (low temperature, no need for a plasma) combined with monolayer thickness control.

As a model system, we study the encapsulation of a monolayer of Cd-Se/CdS/ZnS core/shell QDs in a ZnO matrix by in situ synchrotron based x-ray fluorescence (XRF) and grazing incidence small angle x-ray scattering (GISAXS)<sup>41;42</sup>. The 10 nm QDs are terminated by oleic acid ligands, enabling Langmuir-Blodgett deposition of a hexagonally ordered monolayer on a silicon support. The GISAXS clearly shows the order present in the monolayer of QDs, both before and during the encapsulation process. The XRF data is used to monitor the amount of deposited material. No ZnO growth occurs directly on the QDs during the first 50 ALD cycles. Previous studies, however, have shown that it is possible to use thermal ALD of Al<sub>2</sub>O<sub>3</sub> (using water and trimethyl-aluminum (TMA)) to encapsulate similar QDs<sup>40</sup>. Therefore, a pretreatment of the QDs with TMA was used to facilitate the ZnO growth. During the exposure to TMA, a reduction of the Zn content is observed, indicating the etching of the ZnS shell of the QDs by the TMA. This pretreatment enables the subsequent growth of ZnO. However, a clear delay in nucleation is still present compared to the growth on SiO<sub>2</sub>. The results obtained here are the first steps in understanding the complex growth mechanism of ALD oxides on QDs.

## 9.6 Conclusion

In this chapter, combining QDs with an integrated photonic platform such as silicon-on-insulator to extend the functionalities of the latter. Through simulations and experiments, it was shown that QDs interact with the building blocks of the platform from simple waveguides to subwavelength microcavities. The incorporation of QDs in the functional or insulating layers (oxides, nitride, ...) that constitute these building blocks was investigated and it was shown to be possible to incorporate QDs with conservation of their linear optical properties (such as spontaneous light emission and ab-

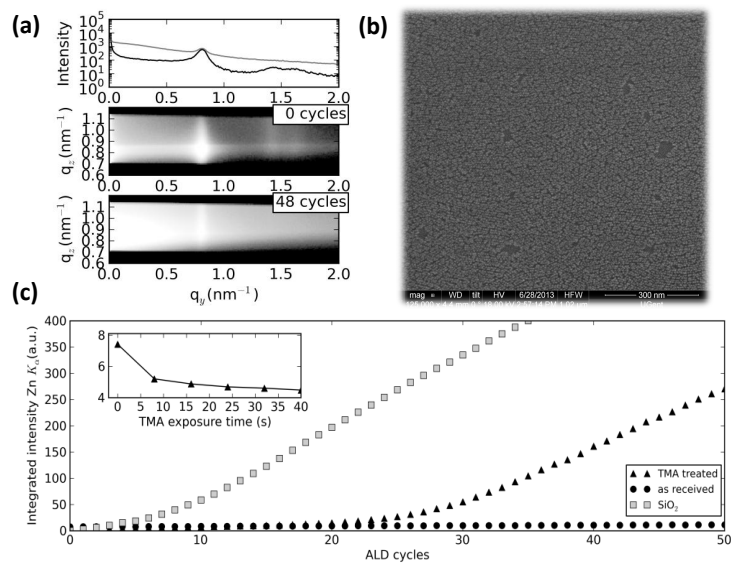


Figure 9.13: (a) Gisaxs pattern before and after 48 ALD cycles of ZnO growth and TMA treatment, showing the conservation of order during encapsulation. (b) SEM micrograph showing the QD monolayer (c) The integrated XRF intensity of the Zn-K line indicating the amount of deposited ZnO during the encapsulation process. The growth on  $SiO_2$  is added as a reference. The inset shows the loss of Zn from the ZnS shell of the QDs during TMA exposure, as measured using in-situ XRF.

sorption). Future work should focus on extending this to non-linear properties such as nanocavity lasing and on-chip wavelength conversion.

## References

- [1] Humer, M.; Guider, R.; Jantsch, W.; Fromherz, T. Integration , photostability and spontaneous emission rate enhancement of colloidal PbS nanocrystals for Si-based photonics at telecom wavelengths. *Optics Express* **2013**, *21*, 2457–2460.
- [2] Gaufrès, E.; Izard, N.; Noury, A.; Le Roux, X.; Rasigade, G.; Beck, A.; Vivien, L. Light emission in silicon from carbon nanotubes. *ACS Nano* **2012**, *6*, 3813–9.
- [3] Lu, Q.; Geiregat, P.; Hens, Z.; Thourhout, D. V. Design of integrated nanocrystal light sources. *Photonics Conference (PHO)*, 2011; pp 527–528.
- [4] Jayatilleka, H.; Nasrollahy-shiraz, A.; Kenyon, A. J. Electrically pumped silicon waveguide light sources. *Optics Express* **2011**, *19*, 24569–24576.
- [5] Briggs, R. M.; Grandidier, J.; Burgos, S. P.; Feigenbaum, E.; Atwater, H. a. Efficient Coupling between Dielectric-Loaded Plasmonic and Silicon Photonic Waveguides. *Nano letters* **2010**.
- [6] Song, Y.; Wang, J.; Li, Q.; Yan, M.; Qiu, M. Broadband coupler between silicon waveguide and hybrid plasmonic waveguide. *Optics express* **2010**, *18*, 13173–9.
- [7] Dai, D.; He, S. A silicon-based hybrid plasmonic waveguide with a metal cap for a nano-scale light confinement. *Optics express* **2009**, *17*, 16646–53.
- [8] Lu, Y.-J.; Kim, J.; Chen, H.-Y.; Wu, C.; Dabidian, N.; Sanders, C. E.; Wang, C.-Y.; Lu, M.-Y.; Li, B.-H.; Qiu, X.; Chang, W.-H.; Chen, L.-J.; Shvets, G.; Shih, C.-K.; Gwo, S. Plasmonic nanolaser using epitaxially grown silver film. *Science (New York, N.Y.)* **2012**, *337*, 450–3.
- [9] Liu, A.; Jones, R.; Liao, L.; Samara-rubio, D. A high-speed silicon optical modulator based on a metal oxide semiconductor capacitor. *Nature* **2004**, *427*, 615–618.

- [10] Barrios, C. A.; Lipson, M. Electrically driven silicon resonant light emitting device based on slot-waveguide. *Optics express* **2005**, *13*, 10092–101.
- [11] Hryciw, A.; Jun, Y. C.; Brongersma, M. L. Plasmon-enhanced emission from optically-doped MOS light sources. *Optics express* **2009**, *17*, 185–92.
- [12] Wood, V.; Panzer, M. J.; Bozyigit, D.; Shirasaki, Y.; Rousseau, I.; Geyer, S.; Bawendi, M. G.; Bulović, V. Electroluminescence from nanoscale materials via field-driven ionization. *Nano letters* **2011**, *11*, 2927–32.
- [13] Caruge, J. M.; Halpert, J. E.; Wood, V.; Bulović, V.; Bawendi, M. G. Colloidal quantum-dot light-emitting diodes with metal-oxide charge transport layers. *Nature Photonics* **2008**, *2*, 247–250.
- [14] Qian, L.; Zheng, Y.; Xue, J.; Holloway, P. H. Stable and efficient quantum-dot light-emitting diodes based on solution-processed multilayer structures. *Nature Photonics* **2011**, *5*, 543–548.
- [15] Moreels, I.; Allan, G.; De Geyter, B.; Wirtz, L.; Delerue, C.; Hens, Z. Dielectric function of colloidal lead chalcogenide quantum dots obtained by a Kramers-Krönig analysis of the absorbance spectrum. *Physical Review B* **2010**, *81*, 1–7.
- [16] Novotny, L.; Hecht, B. *Principles of Nano-Optics*; Cambridge University press, 2006.
- [17] Jun, Y. C.; Briggs, R. M.; Atwater, H. a.; Brongersma, M. L. Broadband enhancement of light emission in silicon slot waveguides. *Optics express* **2009**, *17*, 7479–90.
- [18] Jun, Y.; Kekatpure, R.; White, J.; Brongersma, M. Nonresonant enhancement of spontaneous emission in metal-dielectric-metal plasmon waveguide structures. *Physical Review B* **2008**, *78*, 1–4.
- [19] Robinson, J. T.; Preston, K.; Painter, O.; Lipson, M. First-principle derivation of gain in high-index-contrast waveguides. *Optics express* **2008**, *16*, 16659–69.
- [20] Sun, B.; Findikoglu, A. T.; Sykora, M.; Werder, D. J.; Klimov, V. I. Hybrid Photovoltaics Based on Semiconductor Nanocrystals and Amorphous Silicon. *Nano Letters* **2009**, *9*, 1235–1241.

- [21] Song, T.; Zhang, F.; Shen, X.; Zhang, X.; Zhu, X.; Sun, B. Amorphous silicon as electron transport layer for colloidal semiconductor nanocrystals light emitting diode. *Applied Physics Letters* **2009**, *95*, 233502.
- [22] Walters, R. J.; van Loon, R. V. A.; Brunets, I.; Schmitz, J.; Polman, A. A silicon-based electrical source of surface plasmon polaritons. *Nature Materials* **2009**, *9*, 21–25.
- [23] Melikyan, a. et al. High-speed plasmonic phase modulators. *Nature Photonics* **2014**, *8*, 229–233.
- [24] Vlasov, Y.; McNab, S. Losses in single-mode silicon-on-insulator strip waveguides and bends. *Optics express* **2004**, *12*, 1622–31.
- [25] Omari, A.; Geiregat, P.; Van Thourhout, D.; Hens, Z. Light Absorption in Hybrid Silicon-on-Insulator/Quantum Dot Waveguides. *Optics Express* **2013**, *21*, 23272.
- [26] Omari, A.; Xie, W.; Geiregat, P.; Van, D. Modeling the Optical Properties of Low-Cost Colloidal Quantum Dot Functionalized Strip SOI Waveguides. *Journal of Selected Topics in Quantum Electronics* **2013**, *XX*, 1–6.
- [27] Justo, Y.; Moreels, I.; Lambert, K.; Hens, Z. Langmuir-Blodgett monolayers of colloidal lead chalcogenide quantum dots: morphology and photoluminescence. *Nanotechnology* **2010**, *21*, 295606.
- [28] Zhu, Y.; Xie, W.; Verstuyft, S.; Aubert, T.; Hens, Z.; Van Thourhout, D. Colloidal quantum dot silicon nitride platform. *2013 Annual Symposium of the IEEE Photonics Society Belenux Chapter*, 2013; pp 175–178.
- [29] Vahala, K. J. Optical microcavities. *Nature* **2003**, *424*, 839–46.
- [30] Azzini, S.; Gerace, D.; Galli, M.; Sagnes, I.; Braive, R.; Lematre, A.; Bloch, J.; Bajoni, D. Ultra-low threshold polariton lasing in photonic crystal cavities. *Applied Physics Letters* **2011**, *99*, 111106.
- [31] Akahane, Y.; Asano, T.; Song, B.-s. High-Q photonic nanocavity in a two-dimensional photonic crystal. *Nature* **2003**, *425*, 4–7.
- [32] Pattantyus-Abraham, A. G.; Qiao, H.; Shan, J.; Abel, K. a.; Wang, T.-S.; van Veggel, F. C. J. M.; Young, J. F. Site-selective optical coupling of PbSe nanocrystals to Si-based photonic crystal microcavities. *Nano letters* **2009**, *9*, 2849–54.

- [33] Xie, W.; Fiers, M.; Selvaraja, S.; Bienstman, P.; Campenhout, J. V.; Absil, P.; Thourhout, D. V. High-Q Photonic Crystal Nanocavities on 300 nm Immersion Lithography. *Journal of Lightwave Technology* **2014**, *32*, 1457–1462.
- [34] Roh, K.; Dang, C.; Lee, J.; Chen, S.; Steckel, J. S.; Coe-Sullivan, S.; Nurmikko, A. Surface-emitting red, green, and blue colloidal quantum dot distributed feedback lasers. *Optics express* **2014**, *22*, 18800–6.
- [35] Chen, Y.; Guilhabert, B.; Herrnsdorf, J.; Zhang, Y.; Mackintosh, A. R.; Pethrick, R. a.; Gu, E.; Laurand, N.; Dawson, M. D. Flexible distributed-feedback colloidal quantum dot laser. *Applied Physics Letters* **2011**, *99*, 241103.
- [36] Khajavikhan, M.; Simic, a.; Katz, M.; Lee, J. H.; Slutsky, B.; Mizrahi, a.; Lomakin, V.; Fainman, Y. Thresholdless nanoscale coaxial lasers. *Nature* **2012**, *482*, 204–7.
- [37] Noginov, M. a.; Zhu, G.; Belgrave, a. M.; Bakker, R.; Shalae, V. M.; Narimanov, E. E.; Stout, S.; Herz, E.; Suteewong, T.; Wiesner, U. Demonstration of a spaser-based nanolaser. *Nature* **2009**, *460*, 1110–2.
- [38] Saleh, B.; Teich, M. *Fundamentals of Photonics*, 2nd ed.; John Wiley & Sons Ltd., 2007.
- [39] De Geyter, B.; Komorowska, K.; Brainis, E.; Emplit, P.; Geiregat, P.; Hassinen, A.; Hens, Z.; Van Thourhout, D. From fabrication to mode mapping in silicon nitride microdisks with embedded colloidal quantum dots. *Applied Physics Letters* **2012**, *101*, 161101.
- [40] Lambert, K.; Capek, R. K.; Bodnarchuk, M. I.; Kovalenko, M. V.; Van Thourhout, D.; Heiss, W.; Hens, Z. Langmuir-Schaefer deposition of quantum dot multilayers. *Langmuir* **2010**, *26*, 7732–6.
- [41] Devloo-Casier, K.; Dendooven, J.; Ludwig, K. F.; Geiregat, P.; Hens, Z.; Detavernier, C. Nanoscale area selective ZnO growth between a monolayer of nanocrystals Sample description Growth analysis through in situ XRF Zn K $\alpha$  intensity as monitored during ALD growth of ZnO. *12th International conference on Atomic Layer Deposition (ALD 2012)*, 2012.

- 
- [42] Devloo-casier, K.; Dendooven, J.; Geiregat, P.; Ludwig, K.; Detavernier, C. In-situ synchrotron based XRF and GISAXS study of ALD encapsulation of supported nanocrystals. *Baltic Conference on Atomic Layer Deposition*, 2011.



# 10

## General Conclusion

### 10.1 Conclusion

In this thesis, the potential for colloidal nanocrystals or quantum dots (QDs) to enhance the functionalities of (silicon) photonics was explored. We started from the basic linear properties of lead-chalcogenide QDs in solution, showing size-tuneable absorption and emission throughout the entire near-infrared region. We developed a platform to characterize the highly luminescent (spherical) PbS and PbS/CdS QDs in terms of size and composition and unraveled the electronic structure of the core/shell system (through a combination of tight binding modeling, radiative lifetime and absorption experiments combined with elemental analysis), proving that the PbS/CdS QDs are a type I heterostructure where both electron and hole are confined to the PbS core. The latter is consistent with their increased stability and processability over their core PbS counterparts. More advanced near-infrared active nanostructures with shape anisotropy were synthesized by means of cation exchange of CdS nanorods to obtain PbS rods. The rods were shown to be luminescent and subsequent cationic exchange with cadmium led to peculiar dot-in-rod heterostructures: a chain of PbS/CdS dots fused together with the potential for interdot coupling. The latter was not found experimentally but simulations indicate that using PbSe/CdSe, which have a band alignment inbetween type I and II, could offer a way to show interdot coupling in a single nanostructure. The ultrafast optical properties

of lead-chalcogenides were briefly investigated for applications in optical gain, where it was found that the material is inadequate for this purpose, mainly due to the high band edge degeneracy and strong photo-induced absorption.

Next, we explored the fascinating world of the ultrafast and non-linear response of QDs in solution. When QDs are pumped with a very short and high energy (short wavelength) laser pulse, excitons are created with excess energy to the QD band gap. These so-called *hot* excitons induce both strong spectral shifts (due to Coulomb interactions) and strong intraband absorption. When carriers condense to the band edge by fast ( $\sim 1ps$ ) cooling (*e.g.* through phonon emission in the continuum or Auger-assisted relaxation from P to S states), they become so-called *cold* excitons, occupying band edge states. The latter induce a bleach of the absorption spectrum as electronic transitions get blocked by the presence of carriers in these levels. We show that this can give rise to optical gain and, in the case of HgTe QDs, this gain was shown to be extremely long-lived and thresholdless, making these QDs the first to show potential for electrically pumped lasing. Moreover, we showed that the common lead-chalcogenide QDs are limited in their gain performance by short Auger lifetimes of the excited states and strong sub-gap intraband absorption. The latter process was later used to our advantage as the compensation of this intraband absorption by bleach at a particular energy (wavelength) leads to strong and ultrafast absorption bursts without any residual background. This mechanism can be used to convert information between different wavelengths or modulate a light stream with low power consumption (order of 10 - 100 fJ/bit) using devices only a few 10 - 100  $\mu\text{m}$  in length.

If the hot carriers in the QDs are sufficiently energetic, they can also undergo a process called *carrier multiplication*, where a single hot exciton condenses into two excitons. In this multiple-exciton generation (MEG) mechanism, carriers have to remain 'hot' for sufficiently long time. Up till now, people have not directly studied the rate at which high energy carriers dissipate their energy. Studies were limited to the P-S cooling step near the band-edge. However, carriers have already lost too much energy at that transition to be relevant for MEG (*i.e.* the energy conservation threshold is twice the band gap energy). We show, through both theory and experiments, that a cooling bottleneck for hot carriers exists in polar semiconductors with a saddle point in their energy band dispersion such as the lead-chalcogenide QDs. We assign this to a phonon scattering bottleneck where the carrier momentum has to be changed by intervention of a specific phonon (lattice vibration). In the case of lead-chalcogenide QDs, carriers are shown to accumulate shortly (with roughly 1 ps retention) at the so-called  $\Sigma_c$  criti-

cal saddle point. This allows us to study the hot carrier cooling rates for the first time in this technologically relevant material. Indeed, understanding the cooling rate which competes with MEG and hot carrier extraction in detectors or solar cells, should allow for a more profound theoretical understanding of processes such as MEG, but at the same time allow the design of new materials with increased or decreased cooling rates for respectively faster modulators and more efficient carrier extraction in solar cells.

Next, we aimed at transferring the exciting properties of QDs measured in solution to thin films. Close-packed monolayers of (near-infrared active) PbS QDs and CdSe/(CdS/ZnS) QDs, active in the visible, were deposited using Langmuir-Blodgett deposition and spincoating and the basic optical properties, such as absorption (cross section) and spontaneous emission lifetime, were evaluated. We found strong enhancement (up to 4 for CdSe and 5 for PbS) of the absorption cross section and reduction of the spontaneous emission lifetime. A so-called 'coupled dipole' model was developed which includes the near-field electrostatic contributions of neighboring QDs in a thin film on the polarizability of a single QD. The model requires only a single fit parameter (the dielectric constant of the film environment) to explain the size, ligand length and wavelength dependence of the observed enhancement. By demonstrating this 'collective' optical effect, we showed that the simple transfer of solution measured properties to thin films is often incorrect and misses out on a whole new field of physics related to these near-field phenomena.

Finally, having characterized and modeled the linear and ultrafast nonlinear response of the QDs in solution and thin films, we aimed at demonstrating the potential for QD integration on SOI. We showed that QDs interact with the optical modes of the SOI platform, *i.e.* the propagating guided modes of waveguides and the confined resonant modes of microcavities and sub-wavelength nanocavities.

## 10.2 Perspectives

In this section a short perspective is given based on the observations and experience built up in this thesis. It is by no means a complete transcript, but rather a train of thought on how to proceed with QDs for integrated photonics. The ever elusive goal (a 'holy grail', if you want) to build an electrically pumped nanocrystal (or more general solution-processable) laser on silicon was not fully reached in this work, but in every aspect of this 'holy grail', major steps forward were achieved, both in terms of understanding the ultrafast dynamics underlying QD lasing and its integration with (silicon) photonics. The potential for QDs to enhance this platform was demon-

strated using simple waveguides and more advanced microcavities. We showed that the QDs interact with the optical modes (either through showing traces of the absorption or coupling their (spontaneous) emission to the cavities). However, the measurements were restricted to linear properties (spontaneous emission and absorption). Although already quite exciting, we should move forward to show that also the rich field of ultrafast nonlinearities explored in this thesis could be translated to the SOI platform: on-chip ultrafast wavelength conversion, thresholdless gain and hot carrier extraction are waiting to be demonstrated.

### 10.2.1 Light Conversion and Modulation

The use of nanocrystals in silicon photonics might see its greatest use in light modulation and conversion. This is very much a story of thinking outside of the box, in the sense that both Auger recombination, carrier cooling and intraband absorption are typically deemed as horrendous material properties: they block out lasing and limit extraction efficiencies of detectors and solar cells. We have shown that these properties are actually superb to modulate light on ultrafast timescales with high extinction ratio and little or no insertion loss. Only PbS was investigated but the basic idea of matching inter - and intraband transitions is valid for almost any type of QD material. For example, HgTe shows similar behavior with even higher figure-of-merits but some slower dynamics. Combining it with the extreme size tunability of the latter, modulation and/or conversion could be achieved over decades of wavelengths (*e.g.* near-infrared to mid and long wave infrared). Another field of non-linearities that remains unexplored is the change of refractive index of QDs upon photo-excitation, which could find applications in all-optical switching or wavelength conversion. This change could be determined from the usually measured change in absorption through a Kramers-Krönig analysis of the broadband TA spectrum.

### 10.2.2 Optical Gain

The thresholdless gain in HgTe QDs was assigned to a surface related trap state with empty energy levels mid-gap, *i.e.* above the Fermi level. As such, it should be possible to control the number of active surface sites by controlling the Fermi level, *e.g.* through electrochemical gating. The combination of electrochemistry and transient absorption was shown to be feasible by researchers at the TU Delft recently. Not only would this reveal the nature of the surface state, but it would allow for active control of the optical gain itself. One route to win from Auger was not explored in this

work: build a cavity that builds up sufficient optical gain faster than Auger can quench the population inversion sustaining it. For example, a roundtrip time of a couple of picoseconds enables multiple passes through the gain medium before bi-exciton Auger (10-100 ps) can quench the inverted population. This notion was put forward by Klimov *et al.* already in the year 2000. We did not explore this route for the simple reason that winning from Auger and achieving (single pass) amplification (or ASE, amplified spontaneous emission) is not a free ticket for electrically pumped lasing. Indeed, even if your gain builds up faster than Auger quenches it, you still need to provide this multi-X state every Auger lifetime of 10-100 ps. With an average dot density of  $10^{11} - 10^{12} \text{ cm}^{-2}$ , this requires minimal current densities of  $0.1 - 10 \text{ kA/cm}^2$ . Although possible through short pulse optical excitation, these current levels are too high to compete with existing epitaxial technologies (even if the price of a solution processable QD laser is probably lower) and are highly incompatible with current state-of-the-art electrical pumping schemes for QD based LEDs.

As such, we stress that the only way forward is to reduce the transparency density and increase the gain lifetime, much as was shown with HgTe QDs in this work. Although HgTe is showing these requirements in solution, it is still unclear whether the properties measured in solution can be translated to thin films. Much effort is needed in understanding the clustering and stability, and the role of the mercury-thiolates in this process. An additional route that might be followed is that of *polariton* lasing: the strong coupling between an exciton and a photonic mode leads to the occurrence of a new regime, that of the 'polariton'. An intriguing field of solid state physics, it offers the possibility to achieve 'lasing' in a regime where no population inversion of the QD would be required. This peculiarity arises from the strong coupling, rendering the familiar ideas we have of each isolated system inadequate.

We have shown theoretically that structural relaxation of the excited electronic state of QDs can make them very efficient laser dyes (much as is the case for molecular laser dyes). We should explore this field by synthesizing extremely small QDs from materials with strong electron-phonon coupling. In this approach we are entering the realm of so-called molecular clusters of only a few tens of atoms. Such clusters were demonstrated to be extremely stable and can be made from Cd or Hg based systems. Characterization of these novel nanostructures could make use of ultrafast spectroscopy combined with structural characterization (*e.g.* using the pulsed IR light of a synchrotron).

### 10.2.3 Hot Carrier Cooling

The carrier accumulation observed at the  $\Sigma_c$  saddle point in the Pb-chalcogenide QDs was used to explain and measure hot carrier cooling rates and those results were invoked to discuss the nature of the MEG mechanism. However, the obtained hot carrier cooling rates ( $2 - 3ps^{-1}$ ) are very close to the convolution of the 180 fs pulse width of pump and probe pulses. This work would greatly benefit from measurements with reduced pulse width, *e.g.* 25-50 fs, achievable with recent types of ultrafast oscillators. From a theoretical point of view, it is interesting to look both at other nanomaterials with saddle points as to obtain materials with reduced cooling rates, *e.g.* for MEG and to use the hot carrier cooling rates as input for more advanced models on the MEG mechanism itself.

### 10.2.4 Absorption Enhancement

Although only a limited study of the modification of spontaneous emission (SE) in superlattices is presented in this thesis, the ability to modify SE through near-field coupling of QDs in close-packed films should be studied more detail. For example, using an optical microscope, one could look at completely ordered sublattices of a Langmuir film (typically on the order of half a micron to 1 micron), looking at polarization dependence (relative to the crystal symmetry) of the enhancement compared to the 'bulky' average measurements presented here. The modification of spontaneous emission shown here might be a first in the direction of true super- and subradiance of colloidal QD superlattices, an effect only observed in epitaxial QDs so far. The application of the coupled dipole framework to phonon resonances is another exciting field which could be explored through Raman analysis of the lattices, again possibly showing that the individual vanishes in the collective.

### 10.2.5 SOI integration

The development of a platform combining amorphous silicon (a:Si) and near-infrared QDs could be of great interest as a:Si offers high index contrast with the QDs, allowing *e.g.* for efficient slot waveguide fabrication. Moreover, combining a:Si with silica gives the ability to create VCSEL like cavities with QDs, grown directly on silicon.

Using metals in photonic devices is usually detrimental because of the large optical losses associated with them. However, the use of metals offers the possibility to confine light in subwavelength dimensions because of the plasmonic effect. The latter might outweigh the losses if strong field

localization and enhancements are required, *e.g.* for sensing or in nanocavities. During this thesis, we explored this by looking at so-called 'metallic nanopatches': a nanoscale structure consisting of a thin ( $\leq 200$  nm) metal-dielectric-metal stack, etched in a circular pillar of subwavelength diameter ( $d \leq 200$  nm). The dielectric layer consists of colloidal QDs sandwiched between two silicon nitride layers of 50 nm thickness. The ambition here is to couple to the strongly confined optical mode of the cavity. As mentioned, the use of metals limits the performance due to high optical loss which is evidenced by the low Q factor of the cavity (in the order of 10). However, due to the plasmonic confinement effect, the mode is squeezed in a volume roughly 1000 times smaller than the cubic wavelength, *i.e.*  $V_m \approx 10^{-3} - 10^{-4} \lambda^3$ . This should allow, despite the low Q, to attain Purcell factors in the order of 10 – 100. Combined with the directional emission, this could lead to interesting nanoscale source of light, maybe even subwavelength QD based lasers.

